CIVIL ENGINEERING STUDIES
Transportation Engineering Series No. 126
Illinois Cooperative Highway and Transportation Series No. 287

UILU-ENG-2003-2006

ISSN-0197-9191

HIGH PERFORMANCE CONCRETE FOR TRANSPORTATION STRUCTURES

by

D. A. Lange
J. R. Roesler
M. D. D'Ambrosia
Z. C. Grasley
C. J. Lee
D. R. Cowen

A report of the findings of
Enhancements to Illinois Pavement Management

Project IHR-R29
Illinois Cooperative Highway Research Program

Conducted by the

Department of Civil and Environmental Engineering
University of Illinois at Urbana-Champaign
and the
Illinois Department of Transportation
in cooperation with the
U.S. Department of Transportation
Federal Highway Administration

July 2003

FINAL REPORT

IHR-R29
High Performance Concrete
For Transportation Structures

Prepared for

Illinois Department of Transportation
Bureau of Materials and Physical Research

Prepared by

David A. Lange
Jeffery R. Roesler
Matthew D. D'Ambrosia
Zachary Grasley
December Cowen
Chang Joon Lee

Department of Civil and Environmental Engineering
The University of Illinois at Urbana-Champaign
Urbana, IL

June 30, 2003
2nd Revision October 18, 2003

Abstract:

The use of High Performance Concrete (HPC) for IDOT transportation structures was the subject of a three-year study that involved field investigation, laboratory experiments, analysis and modeling work. The field study was based on IDOT projects and involved instrumentation and analysis of six HPC bridge decks. The laboratory component used methods developed at UIUC for characterizing early age thermal, shrinkage, creep, and cracking behavior. Modeling included the use of material models to analyze and predict creep and shrinkage behavior and a finite element model to investigate structural and material interaction in IDOT bridges.

Acknowledgement

The authors gratefully acknowledge the valuable input and assistance of the Technical Review Panel (TRP) throughout the course of this project. Special thanks go to David Lippert, Doug Dirks, Brian Pfeifer, Melinda Winkelman, Russ Gotschall (BMPR), and Thomas Domagalski (BBS).

The contribution of Dr. Salah A. Altoubat and Dr. Cheolwoo Park is also greatly appreciated. Although they were not present on the research team at the end of the project, their initial input and involvement in the research was significant and should be noted.

Additional thanks goes to IDOT resident engineers and personnel at the individual bridge construction sites in Districts 5, 6 and 7, as well as the contractors for their patience and understanding during the installation process.

TABLE OF CONTENTS

LIST OF TABLES

II. LABORATORY STUDY

LIST OF FIGURES

I. INTRODUCTION

High Performance Concrete (HPC) offers compelling advantages for transportation structures such as bridge decks and substructures. HPC has high strength to resist applied load, low permeability to protect reinforcing steel from corrosion, improved durability to extend the service life of the surface and structure, and lower life cycle cost for many applications. One persistent problem with HPC is its early age performance, particularly early age cracking. HPC has a low *w/c*, utilizes mineral and chemical admixtures, and often has high cement content and higher mortar fraction. The result of these mixture characteristics can include a faster set, faster strength gain, faster increase in elastic modulus, higher heat evolution, higher thermal stresses, higher autogenous shrinkage, and greater potential for surface and through-slab cracking within the first few days after placement.

IDOT initiated field projects that use HPC for transportation structures starting in 2000. Six structures that were built with HPC and one conventional deck were instrumented and analyzed. The three-year study conducted by UIUC had a field component, a laboratory component, and an analysis/modeling component. The field component included instrumentation and analysis of HPC bridge decks to study deformation and cracking potential due to volume change of the concrete materials. The laboratory component used methods developed at UIUC for characterizing early age thermal, shrinkage, creep, and cracking behavior.

II. LABORATORY STUDY

1. INTRODUCTION

Concrete experiences volumetric changes due to external drying, temperature changes, and autogenous shrinkage. Volumetric changes are critical during early ages when the concrete is most vulnerable to cracking. Drying shrinkage and tensile creep are especially important because if concrete is restrained, tensile stress will develop and may cause cracking. Tensile creep is beneficial as a stress relaxing mechanism, relieving part of the tensile stress that develops due to shrinkage. Furthermore, creep and shrinkage are coupled phenomena. Additional tensile creep associated with drying has been observed and is commonly referred to as drying creep or the Pickett effect [1].

High performance concrete (HPC) has gained popularity in recent decades in part due to the increasing desire to build more durable concrete structures. Although high performance is often associated with high strength, the terms are not interchangeable. High performance concrete, as defined by the American Concrete Institute (ACI) is "concrete meeting special combinations of performance and uniformity requirements that cannot always be achieved routinely using conventional constituents and normal mixing, placing, and curing practices." [2]. Concrete designed to have enhanced properties over ordinary portland cement concrete (OPC) should be considered high performance. HPC commonly has a lower *w/c* ratio than normal concrete. Chemical and mineral admixtures are often added to enhance or control properties such as strength, workability, and setting time [3]. As a result, the material could have drastically different creep and shrinkage behavior than normal concrete, not just with regard to strength. Sometimes adverse side effects may negatively influence durability if shrinkage and creep are not properly accounted for in the design of a structure.

One of the most common reasons for the engineer to specify high performance concrete is to improve durability. Many concrete durability mechanisms involve the ingress or migration of water containing aggressive ions. Therefore, a material with low permeability is desired to improve concrete durability and lengthen the service life of a structure. A reduction in material permeability is easily achieved with HPC by lowering the *w/c* ratio or adding chemical and mineral admixtures that improve consolidation or create a dense microstructure. Unfortunately, a dense microstructure does not always mean a reduction in permeability of the reinforced concrete structure. Cracking may counteract the reduction in permeability provided by HPC, and could eventually lead to a higher overall permeability and reduce the durability of a structure. Cracks provide interconnected channels that are necessary for infiltration of water and aggressive ions. The relationship between crack width and permeability has been studied by Aldea *et al* [4]. The water permeability of cracked normal and high strength concrete increased significantly with increasing crack width. For cracks less than 200 μm, the permeability coefficient increased within an order of magnitude compared with that corresponding to uncracked material, whereas for crack widths greater than 200 μm, water permeability increased rapidly. The effect of cracking on durability is significant due to this rapid increase in permeability. If crack width is limited, by reducing shrinkage or using fiber reinforced concrete, then the impact of cracking on durability is limited. For this reason, both steel and synthetic fibers are becoming popular for use in concrete structures.

Cracking of HPC has been attributed to the combined effects of drying shrinkage, autogenous shrinkage, and lower tensile creep. The effect of autogenous shrinkage is normally not important under drying conditions for normal portland cement concrete, but is more significant when considering HPC [5]. Structural restraint increases the tendency for cracking to occur, so a high degree of restraint is a cause for cracking as well. Thermal changes cause

cracking in concrete structures, especially after heat evolution due to hydration has peaked and the ambient temperature drops rapidly, or when a large temperature gradient is present, such as in mass concrete.

REFERENCES

1. Pickett, C., "The effect of change in moisture content on the creep of concrete under a sustained load", *ACI Journal,* V. 38, 1942, pp. 333-356

2. Russell, H. G. (1999). "ACI Defines High Performance Concrete" Concrete International (21) 2, 56-57.

3. American Concrete Institute (ACI) 363R-92 (Re-approved 1997). State-of-the-Art Report on High-Strength Concrete Reported by ACI Committee 363, Farmington Hills, MI.

4. Aldea, C. –M., Shah, S. P., Karr, A. (1999) "Effect of Cracking on Water and Chloride Permeability of Concrete", ASCE Journal of Materials in Civil Engineering, (11) 3, 181-187

5. Jensen, O. M., Hansen, P. F. (1996). "Autogenous Deformation and Change in the Relative Humidity in Silica Fume-Modified Cement Paste" ACI Mat. J. (93) 6, 539-543.

2. SHRINKAGE AND CREEP MECHANISMS

Concrete undergoes volumetric shrinkage during external and internal drying. Aggregate in concrete does not shrink significantly and the total shrinkage is a function of the volume of cement paste. The mechanisms of shrinkage are not completely understood, as they depend on the composition and microstructure of cement hydration products. The current theories for shrinkage in cement paste depend on the internal relative humidity. For internal relative humidity down to 50%, which represents a standard laboratory condition, only two mechanisms are proposed. Capillary stress is a mechanism that occurs in micropores (~1μm) and disjoining pressure acts on particles in very close proximity (~2 nm) when attraction results from van der Waals' forces.

2.1 Shrinkage Mechanisms

The primary mechanism of shrinkage behavior is described by the model of capillary tension in cement paste. Hydrostatic tension develops when a meniscus forms in a capillary as shown in Figure 1. The resulting differential pressure depends on surface tension and the radius of the meniscus. The developing pressure is given by the Gauss-Laplace equation according to

$$P_c = \frac{2\gamma}{R}, \tag{1}$$

where P_c is the capillary pressure, R is the meniscus and pore radii respectively, and γ is the surface tension of the pore fluid [1]. As the internal relative humidity decreases during drying, the radius of the meniscus decreases. This in turn increases the internal capillary pressure and draws the pore walls together. Shrinkage is also affected by disjoining pressure created by water adsorbed on the surface of the C-S-H gel. As the internal relative humidity decreases, the

adsorbed water layer decreases in thickness, decreasing the disjoining pressure and allowing the pore surfaces to come closer together due to attraction by van der Waals' forces.

The driving mechanisms for shrinkage are controlled by internal relative humidity, which changes as a function of time due to hydration and external drying. The rate of drying is a diffusion-controlled process, which is highly dependent on the pore microstructure of hardened cement paste. Therefore, any change in the hardened cement paste that affects the pore microstructure, consequently affects drying shrinkage. Early age concrete has a microstructure that is continuously evolving. Shrinkage rates can change over time, allowing materials with high early shrinkage to have lower long-term shrinkage and vice versa. Therefore, it is important to study early age shrinkage behavior in addition to long-term behavior.

2.2 Creep Mechanisms

The mechanism of concrete creep is divided into short-term and long-term. Short-term creep describes the deformation of a linear viscoelastic solid due to applied stress [1]. This behavior in concrete is attributed to the redistribution of capillary water under a constant load. Long-term creep describes behavior that does not necessarily resemble that of a linear viscoelastic solid and may be attributed to movement or bond slip of gel particles, interlayer water movement, or diffusion of solid material. The study of early age concrete does not consider the mechanism of long-term creep. Many of the same concrete properties that effect shrinkage also effect creep, such as internal moisture content, drying rate, and temperature. Creep mechanisms are divided into separate components for drying creep and basic creep. The two components can then be separated by experimental methods [2,3].

From a durability viewpoint, creep is beneficial because it reduces stress development that leads to cracking. Admixtures or proportioning methods that reduce creep capacity could

have a negative impact on a structure in terms of durability. The opposite is sometimes true in structural engineering, especially for prestressed concrete structures. Creep deformation over time leads to larger deflections and loss of prestressing force, so it may be unfavorable for structural serviceability requirements.

REFERENCES

1. Wittmann, F.H., "Creep and shrinkage mechanisms" in *Creep and Shrinkage in Concrete Structures,* Ed, Z. Bazant, F. Wittmann, Wiley, 1982, pp. 129-161

2. Kovler, K., "Testing System for Determining the Mechanical Behavior of Early Age Concrete under Restrained and Free Uniaxial Shrinkage," Materials and Structures, V. 27, 1994, pp. 324-330

3. Altoubat, S. A. (2000). "Early age stresses and creep-shrinkage interaction of restrained concrete", Ph.D. Thesis, Department of Civil and Environmental Engineering, University of Illinois at Urbana-Champaign, Urbana, IL.

FIGURES

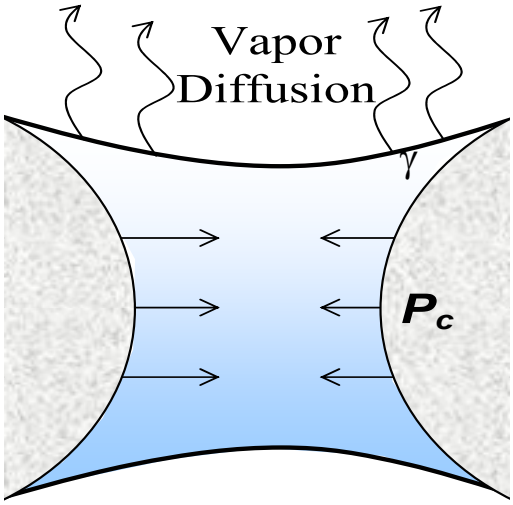

Figure 1. Capillary pressure mechanism for drying shrinkage in concrete

3. HIGH PERFORMANCE CONCRETE

3.1 Water to Cement Ratio and Cement Content

A common characteristic of high performance concrete is a low water to cement ratio. As the *w/c* ratio is decreased, paste capillary porosity decreases, and strength and impermeability increase [1]. The rate of diffusion is highly dependent on the paste porosity, and this is one explanation for shrinkage reduction. Drying shrinkage can be reduced as the pore microstructure is densified, but according to many sources, shrinkage is mostly dependent on the total water content. Total water content represents the amount of water that could potentially evaporate from the paste as a portion of the total concrete mixture. This parameter is therefore combining the effect of *w/c* ratio with paste content. The cement content has been shown to have an insignificant effect on shrinkage behavior unless the water content is also changed [2].

The effects of paste proportions on creep are less understood. As the water content is reduced, there should be less water available to redistribute within the paste, which could reduce the total amount of creep strain. This theory is based on the assumption that part of the creep mechanism is due to redistribution of capillary water. In fact, the amount of creep for a given stress level has been shown to increase as water to cement ratio increases in cement paste [1].

Reducing the cement paste content will reduce shrinkage because a higher portion of the concrete will consist of aggregate. Aggregate acts to restrain both shrinkage and creep mechanisms since it is volumetrically stable. Hard and strong aggregates provide the greatest reduction in shrinkage and creep. However, after the *w/c* ratio has been reduced, it is often common mix design procedure to increase the paste content to maintain the same level of concrete workability in HPC. To minimize shrinkage, workability should be maintained without increasing paste content. Possible solutions are to improve the gradation of coarse aggregate through optimization methods or to add superplasticizing admixtures.

Autogenous shrinkage, sometimes referred to as self-desiccation, plays a part in the total shrinkage behavior, particularly in low *w/c* ratio concrete mixtures (theoretically below 0.42 *w/c* ratio). The effect of autogenous shrinkage is particularly evident at early age, when the greatest percentage of cement hydration occurs. In reality, self-desiccation can occur at higher ratios because diffusion through C-S-H limits access to unhydrated cement. However, autogenous shrinkage is usually not a problem unless the *w/c* ratio is extremely low or mineral admixtures are used at high rates of addition to cement.

3.2 Water Reducers and Superplasticizers

Various researchers have studied the effects of water reducers and superplasticizers on concrete creep and shrinkage [3, 4, 5]. The results of various types of testing performed are sometimes conflicting, but generally water reducers and superplasticizers are associated with increased amounts of creep and shrinkage of concrete. To the extent that the purpose is also to allow for a lower *w/c* ratio, the effect is probably offset somewhat by the development of a dense microstructure. The magnitude of this effect also varies depending on the admixture type. Normal and mid-range water reducers were associated with higher shrinkage than superplasticizer. The reason for this difference is not fully understood, but can possibly be attributed the molecular size and the thickness of the layer that forms around each cement particle during the dispersion process. This layer may then have an effect on pore structure or composition of hydration products.

The effect of water reducers and superplasticizers on creep is not well understood. Khan *et al*. observed that creep of concrete containing superplasticizer was much more sensitive to the age of loading than plain concrete [6]. Therefore, even though a higher shrinkage potential exists, the increase in early age creep could reduce the possibility of cracking.

Common practices may include a combination of admixtures to provide the greatest reduction in slump at the lowest cost [7]. Other admixtures are often used to control setting time and other concrete properties. Such practice makes the effects virtually impossible to predict and testing must be performed to ensure sufficient quality is met.

3.3 Mineral Admixtures

The effects of fly ash, silica fume, ground granulated blast furnace slag, and metakaolin on creep and shrinkage of concrete have been evaluated. Many sources report conflicting data of the effect of mineral admixtures on creep and shrinkage. Some researchers reported increases in drying shrinkage due to silica fume [4, 8, 9, 10]while other claim a significant decrease due to silica fume [5, 11, 12]. The possible explanation for the discrepancy is that several competing mechanisms are affecting the shrinkage behavior. At lower *w/c* ratio, autogenous shrinkage plays a much greater role in the overall shrinkage behavior. Silica fume increases the amount of autogenous shrinkage considerably when compared to plain portland cement [13]. Silica fume also leads to the development of finer capillary pores in mature concrete, which can increase the capillary stress and lead to higher shrinkage over long periods. However, the smaller pores also reduce the drying rate and shrinkage. Other mineral admixtures can be expected to have similar tendencies since they all serve the same purpose of densifying the cement paste with secondary C-S-H according to the pozzolanic reaction. Silica fume differs from other mineral admixtures mainly in particle size and rate of reactivity. Consequently, the effect of mineral admixtures on shrinkage can vary depending on the *w/c* ratio and curing method. Mineral admixtures affect creep mechanisms in a similar fashion. In some cases an increase in creep behavior is reported, while in other cases a decrease is observed. The same arguments can be made about why this discrepancy exists as were made in the case of shrinkage mechanisms.

3.4 Shrinkage Reducing Admixtures

The driving force for cracking in concrete can be reduced with shrinkage-reducing admixtures (SRA). The mechanism of shrinkage reduction is attributed to a reduction in the surface free energy of the liquid/solid interface in a partially saturated pore structure, which then causes a reduction in the stress generated by capillary tension during the drying process. This mechanism can be demonstrated using Equation 1. It can be observed that as the surface free energy (σ) decreases, the capillary pressure (P_c) decreases proportionally. Uniaxial, free shrinkage and ring type restrained tests have demonstrated that SRA reduces the driving force for cracking [14, 15, 16]. The results of a recent study at UIUC indicate that the addition of an SRA was effective in reducing the early age unrestrained shrinkage of concrete. Shrinkage reduction of up to 60% was measured in the first week after casting with the manufacturers recommended dosage of SRA. Shrinkage reduction was not proportional to weight loss measurements and SRA did not have a significant effect of the rate of weight loss of concrete. This is consistent with the theory of the mechanism of shrinkage reduction with SRA, which contends that SRA causes a reduction in shrinkage by reducing the surface tension of the pore solution. Reduction in unrestrained shrinkage was greater for mixtures with a lower *w/c* ratio, indicating that SRA reduces autogenous shrinkage in addition to external drying shrinkage. The suppression of drying and autogenous shrinkage revealed expansion after demolding, that persisted for up to 24 hours. The expansion could have been due to thermal changes, pressure from the formation of hydration products, or both.

Stress development due to drying under restrained conditions was reduced when SRA was added to the concrete mixture. Initial stress development was delayed in some cases due to early expansion of concrete containing SRA. Split tensile strength of concrete containing SRA

was only slightly reduced and hydration kinetics were not affected. A reduction in stress without loss of strength delayed or prevented cracking of concrete containing SRA.

SRA reduced the tensile creep strain of concrete, but did not appreciably reduce the creep coefficient. Concrete containing SRA developed lower stress, and as a result had less creep strain. The results of this study indicate that creep coefficient is independent of stress level, but does depend on loading age for concrete of roughly the same stiffness. A slight reduction in creep coefficient with SRA in the 0.40 *w/c* mixtures may be attributed to a delay in initial loading from early expansion and the reduction of drying shrinkage stress.

SRA reduced concrete stress due to suppression of drying shrinkage. Strength and creep coefficient were only slightly affected. These effects combined to delay or prevent cracking of early age concrete. A reduction in cracking produces concrete that is more durable and increases the service life of concrete structures.

3.5 Fiber Reinforcement

Instead of reducing the driving forces for shrinkage, it is possible to distribute the stresses that build up due to shrinkage and subsequently reduce crack width and propagation. This is the reasoning behind the use of fiber reinforcement in concrete. Fiber reinforcement does not have a significant effect on the shrinkage mechanisms that cause cracking, but it does affect creep thereby reducing cracking and crack width. Crack width has been shown to have a significant effect on permeability, and therefore durability of concrete structures [17]. Steel fibers have also been shown to delay the time of cracking [18]. As concrete creeps, tensile stress is transferred to the fiber and the stress concentrations in capillary pores that cause cracks are reduced. This can result in a significant improvement in durability for a concrete structure. One practical limitation

is the adverse effect that fibers have on the workability of fresh concrete. Regardless of this limitation, the use of fiber reinforced concrete for durability is increasing.

3.6 HPC Summary

Cracking of HPC is attributed to the combined effects of increased autogenous shrinkage and reduced creep. Autogenous shrinkage can be significant when considering HPC with low *w/c* ratio and silica fume. Shrinkage and creep mechanisms were summarized, followed by an analysis of each specific component of HPC and its relationship to shrinkage, creep, and cracking. Lowering the *w/c* decreases the amount of drying shrinkage and creep, but increases autogenous shrinkage, adding to total shrinkage. Superplasticizers and water reducers may increase creep and shrinkage of concrete, but conflicting results have been observed. Mineral admixtures do not have a general trend with respect to shrinkage and creep behavior. Instead, the results seem to vary with *w/c* ratio and curing procedures. Shrinkage reducing admixtures will significantly reduce shrinkage, but their influence on creep is minimal. Fiber reinforced concrete is an alternate approach to improve durability. Fibers can distribute restrained shrinkage tensile stresses to reduce cracking.

It is evident from this review that the design of HPC to reduce cracking is not trivial. A balance must be obtained when selecting materials and dosages of chemical and mineral admixtures. SRA and fiber reinforcement are proven methods for crack reduction, but are not always cost effective. So in order to improve the crack resistance of HPC, laboratory testing is required to evaluate a concrete mixture for performance.

REFERENCES

1. Mindess S., and Young, J. F. (1981). Concrete. Prentice-Hall, NJ

2. Kosmatka, S., Panarese, W. (1988). Design and Control of Concrete Mixtures, Portland Cement Association, Skokie, IL

3. Brooks, J.J., Megat Johari, M.A. "Influence of mix proportions, plasticizers, and superplasticizers on creep and drying shrinkage of concrete," Magazine of Concrete Research, V. 41, No. 148, 1989, pp. 145-153

4. Bloom, R. and Bentur, A. (1995) "Free and Restrained Shrinkage of Normal and High Strength Concretes." ACI Mat. J, (92) 2, 211-217.

5. Alsayed, S. H. (1998). "Influence of superplasticizers, plasticizers, and silica fume on the drying shrinkage of high strength concrete subjected to hot dry field conditions." Cem. Conc. Res., (28) 10, 1405-1415.

6. Khan, A., Cook, W., Mitchell, D. (1997). "Creep, Shrinkage and Thermal Strains in Normal, Medium, and High-Strength Concretes During Hydration." ACI Mat. J, (94) 2, 156-163.

7. American Concrete Institute (ACI) 363R-92 (Re-approved 1997). State-of-the-Art Report on High-Strength Concrete Reported by ACI Committee 363, Farmington Hills, MI.

8. Al-sugair, F. H. (1995). "Analysis of Time Dependant Volume Reduction of Concrete Containing Silica Fume." Mag. Con Res, (47) 170, 77-81.

9. Ravindrajah R., Mercer, C.M., Toth, J. (1994) Proceedings of the International Conference on High Performance Concrete, (ACI SP-149), Singapore, 475-476.

10. Wiegrink, K., Marikunte, S., Shah, S. (1996) "Shrinkage Cracking of High Strength Concrete." ACI Mat. J, (93) 6, 409-415.

11. Tazawa and Yonekura (1986). "Fly ash, Silica Fume, Slag, and Natural Pozzolans in Concrete." CANMET/ACI, Intl. Conference (ACI SP-91), Madrid, Spain

12. Jianyong, L., Yan, Y. (2001). "A study on creep and drying shrinkage of high performance concrete." Cem. Conc. Res., (31),1203-1206.

13. Jensen, O. M., Hansen, P. F. (1996). "Autogenous Deformation and Change in the Relative Humidity in Silica Fume-Modified Cement Paste" ACI Mat. J. (93) 6, 539-543.

14. Shah, S. P., Karaguler, M. E., Sarigaphuti, M. (1992). "Effects of shrinkage reducing admixtures on restrained shrinkage cracking of concrete" ACI Mat. J., 89, 88-90.

15. Weiss, J. and Shah, S. P. (1998). “Shrinkage cracking of restrained concrete slabs”, J Eng. Mech., ASCE, (124) 7, 765-774.

16. D’Ambrosia, M., Altoubat, S., Park, C., and Lange, D. (2002) “Early Age Tensile Creep and Shrinkage of Concrete with Shrinkage Reducing Admixtures”, Submitted for publication, Cement and Concrete Research

17. Aldea, C. –M., Shah, S. P., Karr, A. (1999) “Effect of Cracking on Water and Chloride Permeability of Concrete”, ASCE Journal of Materials in Civil Engineering, (11) 3, 181-187

18. Altoubat, S. A. (2000). “Early age stresses and creep-shrinkage interaction of restrained concrete”, Ph.D. Thesis, Department of Civil and Environmental Engineering, University of Illinois at Urbana-Champaign, Urbana, IL.

4. MATERIALS

The concrete materials and mixture proportions used in this study reflect current IDOT practice for HPC and conventional (OPC) projects. In the first year of the study, IDOT BMPR identified five mixtures representing the current use of HPC as well as one OPC conventional deck mixture. These mixtures are presented in Table 4-1. The mixtures are denoted with codes IHPC-1 through IHPC-4 and then I-STD to represent a standard concrete mixture. IHPC-1 and IHPC-2 are the same mixture except that silica fume was used in place of high reactivity metakaolin (HRM). IHPC-3 had lower cementitious materials content, higher fine aggregate proportion, and a higher percentage of silica fume by weight of cementitious materials. IHPC-4 had more cement and no fly ash, with a slightly higher proportion of fine aggregate. High performance mixtures contained air entraining agent (Grace Daravair 1400), Type A water reducer (Grace Daracem 65), Type D water reducing retarder (Grace Daratard 17) and, Type F superplasticizer (Grace Daracem 19) in the amounts shown in Table 1. The conventional mixture, ISTD, did not contain mineral admixtures, water reducer, or superplasticizer. IHPC-1 and IHPC-2 were used in the construction of two concrete bridge decks on US-51 in IDOT District 5 (Macon, IL). UIUC retrieved the cement, mineral admixtures, and aggregates used in the bridge projects for laboratory testing. Chemical admixtures were obtained directly from the supplier and not from the field source. Specimens tested using field materials were given the designation IHPC-1F or IHPC-2F.

In the second and third year of the study, IDOT BMPR identified concrete mixtures for testing after their use in bridge deck projects. The bridge projects consisted of the Duncan Rd bridge over I-72 in IDOT District 5 (Champaign, IL), the I-55 bridge over Lake Springfield in IDOT District 6 (Springfield, IL), the I-70 bridge over Big Creek in IDOT District 5 (Clark Co.),

and the US-51 bridge over the Kaskaskia River in IDOT District 7 (Vandalia, IL). Bridge project details are discussed further in the field portion of this report. The mixtures are shown in Table 1 and are coded to distinguish mixture and testing conditions. As an example, IDL44R1 represents IDOT – Duncan Rd – Laboratory (or Field) materials – 0.44 *w/c* ratio – Restrained test – 1 day cure. In the other codes, B represents Big Creek, K represents Kaskaskia, and S represents Lake Springfield. Repeat specimens are denoted as "- 2" at the end of the code.

The Duncan Rd mixture was a conventional design containing fly ash and did not contain silica fume or superplasticizer. The Lake Springfield mixture had a lower cementitious material content and contained silica fume in addition to cement. Big Creek and Kaskaskia mixtures were optimized aggregate mixtures, with improved aggregate gradation of the field materials. Coarse aggregate was required to contain 50% material passing the ½ sieve. Improving the aggregate gradation improves workability and allows lower cementitious materials content to achieve the same slump. The mixtures in this portion of the study did not contain a set retarding admixture. This admixture, when used in practice, allows more time for placement and finishing, especially in warmer weather. However, when used at the same dosage in laboratory conditions, problems arose with low early strength gain. Hydration and strength gain were more severely retarded in the laboratory, due to the lower temperatures (~73°F) compared to the field conditions during some bridge deck installations (80-90°F). Early shrinkage stress development exceeded tensile strength in the first hours of testing and the specimens fractured. The decision was made to compare the remaining mixtures without retarder to avoid early test failure.

The laboratory mixing procedure followed the sequence recommended by IDOT BMPR. The sequence is used by IDOT for microsilica or HRM mixtures, but for this study it was used for all laboratory mixtures. The procedure varies from AASHTO T 126 (3 minute mixing, 3 minute rest, and 2 minute mixing) to simulate the sequence of mixing in the field and to ensure

that the microsilica/HRM is thoroughly distributed. The UIUC concrete laboratory uses a 3 cubic foot Lancaster pan mixer. The following procedure was followed for each batch of concrete:

IDOT BMPR Microsilica / HRM Mixing Sequence

- ◊ **Add CA, FA, and most of mixing water, and mix for 30 seconds to allow water to be absorbed into any aggregate that may be drier than SSD. This prevents AEA from being absorbed into dry aggregate**
- ◊ **Add AEA and wash out beaker with mix water, then mix for 30 seconds**
- ◊ **Add cement and mix for 3 minutes**
  - **Within first 1½ minutes, add water-reducer, retarder and wash out beakers (if applicable)**
- ◊ **Rest for 3 minutes**
- ◊ **Resume mixing**
  - **Begin adding microsilica or HRM at 30 seconds**
  - **Mix for 1 minute**
  - **Add superplasticizer *SLOWLY* until desired slump is attained**
  - **Mix for additional 2 minutes**
- ◊ **Take air content and slump readings and record**
- ◊ **Adjust as necessary; if water or admixtures are added, then mix for additional 1 – 2 minutes**

Concrete mixtures produced two uniaxial specimens, three 3×3×11in. prisms, and six 4×8 in. cylinders for each batch. Fresh concrete properties such as air content and slump were measured for each batch, although no corrective action was taken to adjust for incorrect slump or air content. This was for the purposes of direct comparison between admixture dosages and water contents. Fresh concrete properties for each mixture are given in Table 2.

The aggregates and cementitious materials used in this study were characterized in the laboratory at UIUC and the data are presented in Appendix A. The measured gradations for laboratory and field aggregate are given in Table 8 through Table 10. The chemical oxide compositions were determined by X-ray fluorescence for cement, fly ash, silica fume, and high reactivity metakaolin and are shown in Table 11.

TABLES

Table 1. IDOT Concrete Mixture Summary

Bridge Name		Macon NB	Macon SB	n/a	n/a	n/a	Duncan Rd	L. Springfield	Big Creek	Kaskaskia
Mix Code	SG	IHPC-1	IHPC-2	IHPC-3	IHPC-4	I-STD	IDL44R1	IS(L,F)44R1	IB(L,F)44R1	IK(L,F)44R1
Cement (Type I)	3.15	465	465	445	565	605	515	465	545	445
Fly Ash	2.65	120	120	90			140	145		90
Silica Fume	2.20		25	25	25			25	25	25
Metakaolin	2.50	27								
Coarse Aggregate	2.67	1820	1820	1820	1820	1820	1863	1866	1820	1811
Fine Aggregate	2.60	1095	1095	1200	1150	1130	1108	1130	1240	1230
Water	1.00	269	268	246	260	266	288	279	251	246
w/c ratio		0.44	0.44	0.44	0.44	0.44	0.44	0.44	0.44	0.44
AEA *(Grace Daravair 1400)*	oz/cwt	0.5	0.5	0.5	0.5	0.2	0.72	1.01	1.01	1.01
	oz/cy	**3.1**	**3.1**	**2.8**	**3.0**	**1.2**	**4.7**	**6.4**	**5.8**	**5.7**
Type A WR *(Grace Daracem 65)*	oz/cwt	2.9	2.9	2.9	3.5			1.51	1.51	1.51
	oz/cy	**17.7**	**17.7**	**16.2**	**20.7**			**9.6**	**8.6**	**8.5**
Type D WR+R *(Grace Daratard 17)*	oz/cwt	4.3	4.3	4.3	4.3	3				
	oz/cy	**26.3**	**26.2**	**24.1**	**25.4**	**18.2**				
Type F HRWR *(Grace Daracem 19)*	oz/cwt	4.6	5	5	5			6.19	6.19	6.19
	oz/cy	**28.2**	**30.5**	**28.0**	**29.5**			**39.3**	**35.3**	**34.7**
Cementitous content by wt		612	610	560	590	605	655	635	570	560
Paste % by vol		28.1%	28.0%	25.7%	26.8%	27.2%	29.9%	29.3%	25.8%	25.7%
Paste % by wt		23.2%	23.1%	21.1%	22.3%	22.8%	24.1%	23.4%	21.2%	21.0%

Units are lb/yd^3 unless otherwise noted

Table 2. IDOT Fresh Concrete Properties

Designation	Slump	Air %
IHPC1F	7.5"	3.0%
IHPC2F	8"	3.5%
IHPC1	8", 7.5"	4.5%, 1.5%
IHPC2	8", 4"	3%, 3.5%
IHPC3	3"	2.0%
IHPC4	5.75"	4.5%
ISTD	3"	1.75%
IDL44R1	6.5", 7.5", 8"	4.5%, 5%
IDL41R1	6", 7"	5%, 5%
ISL39R1	2"	3.5%
ISF39R1	1"	4.0%
ISL44R1	7"	3.0%
IKL44R1	5"	4.0%
ISF44R1	9"	4.5%
IBL44R1	2"	5.0%
IBF44R1	8"	8.0%
IKF44R1	1"	3.0%
ISL50R1	9"	3.0%

5. UNIAXIAL SHRINKAGE AND CREEP TESTING OF EARLY AGE CONCRETE

Experimental methods to study the material properties and behavior of concrete can be classified into several categories: Qualitative, Quantitative-Passive, and Quantitative-Active. Qualitative test methods for evaluating creep and shrinkage behavior of concrete such as the un-instrumented restrained ring test and uniaxial restrained tests are based on the observation of cracking (time to cracking, number of cracks, crack width). They are useful for making comparisons between different materials or environmental conditions, but they provide little information about the actual magnitude of stress or strain during the test. This type of testing is widespread and has been used since the 1950's [1,2]. Quantitative-passive testing of concrete creep and shrinkage behavior involves the measurement of a physical property, such as strain, during a test. Restrained concrete behavior has been measured extensively using this type of testing approach. Examples include the instrumented ring test [3,4,5,6] and the instrumented uniaxial test [7,8,9,10]. Instrumented uniaxial tests are rigid frames that have a load cell or strain gages attached to measure shrinkage stress. Instrumented testing reveals more about the actual physical behavior of the material and permits more than simple rank comparison. Mechanical analysis may further enable the separation of creep from the restrained test measurements. A drawback of an instrumented rigid frame test is that the level of restraint is difficult to determine. Nevertheless, measured restrained shrinkage strain, standardized using AASHTO PP34, enables comparison relative to other published work. Knowledge of acceptable strain and stress measurements has been achieved due to this type of testing. Material models for physical behavior have been developed based on the experimental results of quantitative-passive testing and are available in the literature [11,12,13].

Quantitative-active testing represents the highest level of advancement in material testing. Active tests are capable of changing the conditions of the test, such as the amount of applied load, based on the measured feedback from instrumentation of a test specimen. Testing of this type is possible with advances in computers, analog to digital signal processing, and servo-hydraulic systems. Quantitative active testing allows for carefully controlled conditions such as load control to simulate a restrained condition, or displacement control of a crack opening. Simulating a restrained condition is necessary to understand shrinkage and creep of restrained concrete, as it behaves differently than a constant load condition.

A widely accepted method to measure early age concrete behavior is to use a uniaxial test specimen in a frame that is capable of simulating restraint or applying load based on the feedback of the test specimen. Paillere *et al*. developed a system to measure the stress developed due to restrained shrinkage [14]. A uniaxial specimen with dovetail ends was cast into a frame that applied a restraining force by means of an air jack. The tensile stress generated was then measured with a load cell. The deformation was monitored and the load was applied manually to produce a restrained condition. This test was performed both vertically and horizontally depending on the age of the specimen. It was determined that a vertical test was problematic due to the dead load of the specimen. Bloom and Bentur developed a similar system in which a step motor was used to apply the restraining load [15]. Two flared end specimens were measured for simultaneous determination of free shrinkage and stress development. Creep was calculated as the difference in strain accumulation between the two specimens. Kovler further modified this system to include a closed-loop computer control system, and measured deformation with LVDT sensors instead of conventional dial gages [16]. When the load reached a predefined threshold, a restraining force was applied automatically to move the specimen to its original position. An experiment developed by Pigeon *et al*., based on Kovler's system, measured the stress due to

restrained autogenous shrinkage [17]. This system also used a computer controlled loading system. Deformation was measured using a direct current displacement transducer for greater precision. Springenschmid *et al*. developed the Temperature Stress Testing Machine (TSTM) to measure the tensile stress in concrete due to the heat generated of hydration [9]. Attached to one end of a uniaxial concrete specimen was an adjustable crosshead. A computer controlled step motor applied a load to control the deformation of the concrete specimen as it reached a threshold of 0.001 mm. Van Breugel and de Vreis developed a TSTM similar to Springenschmid, except that it used a hydraulic actuator to apply load [18]. The device was used in conjunction with an autogenous deformation testing machine (ADTM) to optimize high performance concrete mixture proportions based on creep and shrinkage performance.

Altoubat developed a uniaxial system currently in use at the University of Illinois at Urbana-Champaign [19]. It was an improvement over the systems developed previously for several reasons. The 3x3" cross-section was large enough to allow for concrete with coarse aggregate. The applied load generated using a servo-hydraulic actuator had superior load stability and was capable of high load application. In addition, a new deformation measurement technique avoided grip-specimen interaction by anchoring an extensometer directly into the concrete.

5.1 Uniaxial Experiment Procedures

The uniaxial test technique developed by Altoubat allowed for simultaneous measurement of free shrinkage and deformation under restrained tension [19]. Two companion specimens were tested simultaneously in a temperature and humidity controlled environmental chamber. The dimensions of each specimen are given in Figure 2. The steel formwork was removed from the sides of the specimen at 24 hours. The steel end grips, which were used for

applying load, remained in place for the duration of the test. A sealed barrier of self-adhesive aluminum foil was applied to the top of each specimen immediately after demolding to impose the condition of symmetric drying from two sides of the specimen. To avoid the effect of evaporative cooling associated with formwork removal, the specimens were allowed to equilibrate to room conditions for one hour after demolding. Evaporative cooling has been shown to cause deformation during early age testing, which may lead to misinterpretation of test data [19,20] and premature restrained load application.

The rounded shape of the specimen produces stress development in the center region, where deformation is more accurately measured. Previous work by Altoubat has shown that measurements taken from the end grips or including the end grips are less accurate due to grip specimen interaction [21]. Stress concentrations and interactions between the specimen and the end grip were minimized through a rounded transition in specimen geometry.

The applied load was measured using a 5-kip capacity load cell in line with a servo-hydraulic actuator. Friction between the concrete specimen and the bottom surface was minimized with a thin polymer sheet. Deformation was measured using an extensometer that consisted of a linear variable differential transformer (LVDT) and a steel rod positioned on the top of the concrete specimen for a total gage length of 24.5". The measurement assembly was attached with steel brackets supported by bolts anchored into the concrete specimen. The uniaxial tests were performed under controlled environmental conditions of 50% RH and 23 ºC for a period of seven days.

5.1.1 Restrained Test Procedure

A restrained load condition was simulated by allowing the specimen to deform within a threshold strain value of 8 με and then applying a load to compensate for this deformation once

the threshold value is reached. The applied load was feedback controlled and stopped once the specimen had returned to its original length. The threshold value was determined by preliminary experiments to be the minimum value that could effectively be used within the limitations of the measuring equipment.

5.1.2 Supplemental Testing

Test cylinders (4"x 8") were sampled from each concrete mixture and split tensile strength measurements were performed in accordance with ASTM C496 at ages of one, three, and eight days. Concrete prisms were cast for measurement of free shrinkage and weight loss due to drying. The prism dimensions were 3"x3"x11.25" and they were measured in accordance with ASTM 490 with a standard length change comparator as shown in Figure 5. The prisms were subject to the same environmental conditions and volume to surface ratio as the test specimens.

The internal temperature of a 3"x3"x11.25" concrete prism was measured using a computer controlled temperature measurement system. Thermocouple probes were placed a various depths in the specimen, as shown in Figure 6. Measurements were sampled every ten minutes from the time of casting. The internal specimen temperature was used to observe the effect of evaporative cooling after demolding, which was discussed previously as a potential problem. Semi-adiabatic temperature of concrete was measured in an insulated container to determine the approximate setting time and evaluate changes in hydration kinetics.

5.2 Results and Discussion

The results presented in the following sections will be organized in several ways. The experiments were performed on nine different IDOT concrete mixtures. The mixtures were

previously presented and the code designation defined in Chapter 4. Five mixtures containing set retarding admixture were tested in the first year of the study and will be grouped together for comparison purposes. The remaining mixtures did not contain set retarder. The *w/c* ratio was varied for the Lake Springfield and Duncan Rd. materials, and these comparisons will be presented separately. Finally, the mixtures containing laboratory materials will be compared directly with mixtures containing field materials to study the effect of material source.

5.2.1 Unrestrained Shrinkage

Unrestrained shrinkage is often described as a potential driving force for cracking in concrete. The unrestrained shrinkage results for IDOT concrete mixtures from the first year of the study are shown in Figure 7. The HPC mixtures containing laboratory materials performed similarly and had slightly higher shrinkage than the conventional mixture after one week of drying. The *w/c* ratio was 0.44 for all mixtures in this group and the paste content was similar, therefore the increase in shrinkage can possibly be attributed to the presence of mineral admixtures (fly ash, silica fume, HRM). Pozzolanic mineral admixtures cause an increase in autogenous shrinkage that is most pronounced at early age [22]. The pozzolanic reaction consumes additional water as the silica reacts with the hydration product calcium hydroxide to form secondary C-S-H. Mixtures containing silica fume (IHPC2, IHPC4) had slightly higher shrinkage than IHPC1, which contained HRM. Silica fume has the greatest impact on autogenous shrinkage due to its high silica content, which chemically uses a greater amount of water, and due to a smaller particle size, which speeds up the hydration process and the rate of autogenous shrinkage.

Unrestrained shrinkage of the remaining IDOT concrete mixtures from years two and three with laboratory materials are shown in Figure 8 with a consistent *w/c* ratio of 0.44. These

mixtures had similar free shrinkage behavior despite changes in cementitious materials, aggregate composition, and paste percentage. The free shrinkage after one week of drying correlated with the portland cement content for these mixtures. All mixtures in this group contained a pozzolan, so this relationship may be related to autogenous shrinkage. Overall magnitudes after one week of drying are similar for all IDOT concrete mixtures at the same *w/c* ratio. In Figure 10, the *w/c* ratio was varied for the Duncan Rd and Lake Springfield concrete mixtures. The change from 0.44 to a lower *w/c* ratio, 0.39 in the case of Lake Springfield or 0.41 in the case of Duncan Rd, did not produce much change in the free shrinkage result. Additional benefit of reduced drying shrinkage from a *w/c* ratio lower than 0.44 is probably counteracted by the increase in autogenous shrinkage. Therefore, it may be stated that the balance between autogenous shrinkage and drying shrinkage is optimized in this range. Increasing the *w/c* ratio from 0.44 to 0.50 produced an increase in shrinkage, as expected.

The mixtures containing field materials consistently exhibited lower shrinkage than mixtures containing laboratory materials. The comparisons can be observed in Figure 7 and Figure 9. It is reasonable to attribute this difference to the source of cementitious materials, since the aggregates were similar (crushed limestone). The role of aggregate as a restraint to volumetric changes indicates that if they are similar materials, they should not change shrinkage behavior significantly. The cement and fly ash combination was chemically different for the laboratory and field sources and the subsequent hydration products that form had different shrinkage potentials. The chemical oxide compositions are given in Table A-2 of the Appendix.

Long-term shrinkage measurements of 3" standard prism specimens are presented in Figure 11 through Figure 14. Most of the specimens were measured up to 40 days and many were measured for longer periods up to a maximum of almost three years, as shown in Figure 5-14. Trends that were apparent in the early age (8 day) measurements are not always consistent

when considering the longer-term (40 day) measurements. The mechanisms of shrinkage change over time as the pore structure densifies and autogenous shrinkage ceases to play a role in the overall shrinkage behavior. The prism measurements also do not always have the same magnitude of free shrinkage as the uniaxial specimens. This may be attributed to the somewhat higher experimental error in the prism tests relative to the more sensitive uniaxial measurement. Other experimental differences such as time of first measurement and location in the environmental chamber may cause this difference. The concrete mixtures made with field materials no longer have lower shrinkage in the long-term measurements. This is not surprising if the difference is attributed to the cement and fly ash sources. As the microstructure develops, the shrinkage becomes more dependent on the pore structure, rather than the composition of hydration products. Microstructures that may develop slowly in the first week tend to catch up later in the hydration process as the mechanisms of hydration change. The pore size dependence can be closely linked to *w/c* ratio and the presence of pozzolans. The conventional concrete mixture, which did not contain pozzolans eventually reaches higher levels of shrinkage than the HPC mixtures.

5.2.2 Weight Loss and Drying Rate

The initial amount of water in a concrete mixture influences how much shrinkage potential exists for that material. Simple weight loss measurements can be performed to measure the amount of water that evaporates from a concrete specimen. Both the rate of weight loss and the amount of weight loss per unit of shrinkage relate to the shrinkage potential of the material. Pozzolanic mineral admixtures generally increase the amount of autogenous shrinkage, which may cause an increase in the amount of shrinkage per unit of weight loss. The rate of weight loss results are shown in Figure 15 and Figure 16 and weight loss per unit of shrinkage is shown in

Figure 17 and Figure 18. Strong trends are not evident from the measured data, despite the presence of mineral admixtures. The conventional concrete mixture has significantly less weight loss and more shrinkage per unit weight loss than the HPC mixtures. This may indicate that this mixture has more remaining shrinkage potential and could have significantly higher long-term shrinkage.

5.2.3 Tensile Strength Development

The split tensile strengths of 4"x8" cylinders were measured during the first week after casting. The specimens were sealed for one day, then cured at 50% RH and 23°C for the remainder of the week. Tensile strength was measured as opposed to compressive strength because of the relationship of tensile stress to shrinkage cracking in concrete. It may be assumed that the tensile strength is 10% of compressive strength for estimation purposes. Tensile strength results of mixtures from the first year of the study are shown in Figure 19. This group of concrete mixtures contains a set retarding admixture, which has reduced the early age tensile strength in some instances. The HPC mixtures do not have higher early age tensile strength than the IDOT conventional mix, ISTD. The presence of fly ash can be expected to reduce the early strength gain. Therefore, higher strengths may be expected from the HPC mixtures at later ages. The early age strengths were unaffected by the proportioning of mineral admixtures. The mixtures containing field materials has higher initial strengths than the corresponding mixtures with laboratory materials indicating the retarder may have interacted differently with the cement. Retarder effectiveness depends on the C_3A content of the cement. When the C_3A content of cement is high, more retarder is consumed by the C_3A and becomes unavailable to slow C_3S hydration [23]. As shown in Table 11, the C_3A contents are similar for the laboratory and field cements, with the laboratory cement slightly higher, which does not support the argument.

Sulfate content also may alter the effectiveness of retarder by changing C_3A hydration [23]. The presence of mineral admixtures further complicates this relationship. The importance of testing cement-admixture interactions is illustrated by these results. Chemical analysis may not be able to predict an interaction problem, but the strength testing of any combination of admixtures will reveal the true material behavior.

Figure 20 shows the tensile strength measurements for the remaining mixtures with laboratory materials and a 0.44 *w/c* ratio. The materials have similar strengths except IDL44R1 (Duncan Rd), which had lower strength due to the addition of retarding admixture. The decision to stop using retarder in the laboratory was made after this mixture was tested. The results of these tests showed that the use of retarding admixture in the laboratory was unwarranted and caused difficulty in determining early age behavior. Laboratory specimens were not wet cured, as was the case in actual bridge deck applications. Stress developed in the laboratory specimens much earlier and thus the need for higher early strengths. Low strengths often meant early failure (less than 2 days) in the uniaxial test, prohibiting the measurement of early age creep.

Figure 21 shows the strength comparisons of laboratory and field materials for all mixtures after the first year of the study. The field materials did not have a consistent relationship to the laboratory materials, indicating a probable dependence on cement composition different from the first year mixtures.

Figure 22 shows the strength comparisons of different *w/c* ratio mixtures from Lake Springfield and Duncan Rd. Lowering the *w/c* ratio produced the expected result of increasing strength in both mixtures. Although additional tensile strength is beneficial to resist cracking, the strength may not reflect the cracking potential of the material. Strength is related to creep and the reduction in creep that usually occurs with an increase in strength may counteract a

resistance to cracking. A strong concrete material that also has high creep capacity is ideal to resist cracking due to shrinkage stress.

Early age tensile strength plays a critical role in the long-term durability of concrete structures. Shrinkage stresses that develop at early age will cause cracking much sooner if sufficient strength has not been achieved. High strength usually means low creep, which is detrimental to crack resistance. The importance of wet curing for as long as possible is reinforced here as well. Not only does wet curing delay the start of drying shrinkage, but also the strength of the material continues to develop, which further reduces the risk of cracking. Concrete will continue to gain strength over time, so if shrinkage stress development is prevented during the very early age when the concrete is one or two days old, the risk for cracking is greatly diminished.

5.2.4 Thermal Stress and Hydration Kinetics

Supplemental laboratory tests were performed to monitor the internal temperature of concrete. The internal temperature of a 3”x3”x11” prism, cast with each concrete batch, was measured by embedding polymer tubes in the top of the fresh concrete, and then placing temperature probes into the straws. Five probes were placed in each temperature prism, as shown in Figure 6. The temperature prism was sealed until an age of 23 hours, at which time it was demolded with the other lab specimens. Throughout the test, the temperature prisms were maintained in a climate controlled environment.

Once the internal relative humidity (RH) measurement system became available, the system was utilized to measure the internal temperature as well. The probe system was no longer used. The only differences between the two temperature measurement systems are that the old probe system involved placing straws in the top of a concrete prism with probes inside

whereas the new system involved sensors embedded in ¼ diameter PVC tubes projecting into the prism from the sides. The RH-temperature prism shown in Figure 96 was also 2 inches longer, but this had little effect on the measured temperature data.

The main purpose of this experiment was to monitor the internal temperature of the concrete just after the forms were removed. Removal of the forms from the moist concrete induced evaporative cooling. This evaporative cooling most likely causes thermal contraction. Since the uniaxial test involves monitoring shrinkage until a certain strain threshold is reached (8 με), this thermal contraction could induce stress. The purpose of the uniaxial test is to measure drying shrinkage, creep, and stress rather than any displacements caused by thermal events. Therefore, the start of the uniaxial data-acquisition was delayed one hour after demolding to ensure that most of the thermal contraction from evaporative cooling had occurred before the test began. Figure 23 shows the internal temperature data, illustrating the evaporative cooling that occurred after demolding each specimen. Figure 23 also indicates most of the cooling was complete within one hour of form removal.

In addition to measuring the internal temperature in the prism, the hydration kinetics were monitored using a small sample (0.44 lbs ~ 200 g) of concrete enclosed in a thermos, which created semi-adiabatic conditions. Some typical semi-adiabatic internal temperature curves are shown in Figure 24. This was a supplemental test used mainly for quality control purposes.

5.2.5 Restrained Stress Development

Stress development due to shrinkage is shown for IDOT concrete mixtures in Figure 25 through Figure 28. All mixtures of like *w/c* and material source developed similar magnitudes of stress (within a range of 100 psi). No significant trends were observed, leading to the conclusion that changing mixture proportions and mineral admixtures within in the range of this study did

not have much effect on stress development. It should also be noted that stress development did not follow the same trends as free shrinkage, emphasizing the importance of creep when considering stress. The stress development followed the tensile strength development trends in many cases. Creep of concrete is known to closely relate to strength, so this relationship was expected. In Figure 27, a trend is visible where higher stress develops in low *w/c* ratio mixtures. This relationship is also related to strength.

Failure due to fracture of the uniaxial concrete specimen is indicated in each figure with a black "X". Average shrinkage stress levels were on average approximately 80% of the concrete tensile strength at the time of failure. Previous work by Altoubat and others has shown that specimens in direct tension typically fail below their measured tensile strength. In his work, the rate of tensile strength gain was documented by split tensile strength measurements. Part of the difference may be attributed to this method for tensile strength measurement. The split cylinder test is an indirect measurement of tensile strength that is dependent on test conditions and may be as much as 5 to 12% higher than direct tensile strength [23]. Another factor in the stress at failure is the presence of a drying stress gradient in the specimen. As drying occurs, stress develops due to capillary tension in the pore microstructure. The stress, which is assumed constant in this study, is actually much greater at the surface where drying has occurred. The surface stress results in microcracking and causes damage to the specimen, which results in failure when the cracks propagate. The proper analysis for failure of concrete in direct tension should probably be based on a fracture energy approach. Comparison of the stress with the tensile strength at the macro level does not account for micro-mechanical processes that govern failure and the quasi-brittle nature of concrete [24].

5.2.6 Evolution of Elastic Modulus at Early Age

The elastic modulus was measured for concrete mixtures tested with the restrained test method each time the applied load was incremented. Stress-strain diagrams taken from test data of each uniaxial test are shown in Figure 29. The evolution of the elastic modulus for all IDOT concrete mixtures is shown in Figure 30. Each loading increment results in a finite amount of elastic strain as the specimen returns to original length from the threshold strain of 8 μstrain. The elastic modulus was calculated as from the summation of accumulated stress divided by the summation of elastic strain according to

$$E = \frac{\sum \sigma}{\sum \varepsilon_{el}} = \frac{\sum P / A}{\sum \varepsilon_{el}}, \tag{2}$$

where σ is the total average stress in the concrete, ε_{el} is the summation of measured elastic strain, P is the summation of load applied at each increment, and A is the cross sectional area, which was equal to 9 in^2 for all specimens. The elastic modulus measurement decreases after the initial measurement for most mixtures. The initial measurements represent the initial tangent modulus of elasticity, which is expected to be higher than the subsequent tangent or secant modulus. The measurements either level out or begin to increase slightly over the test period of one week. The ACI equation was used to predict the elastic modulus, also shown in Figure 30, according to

$$E = 57{,}000\sqrt{f'_c}\sqrt{\left(\frac{t}{4+0.85t}\right)}, \tag{3}$$

where f'_c is the compressive strength and t is the age of concrete [23]. The measured values for elastic modulus correlate well with the magnitude or evolution of the ACI equation. The initial measurement of the elastic modulus from the first load application during the test, which is at relatively low stress and strain, corresponds to the initial tangent modulus, E_1 shown in Figure 31. At higher stress levels, the measurement corresponds to the chord modulus, shown as E_2 in

Figure 31 since it represents a linear slope of the current stress-strain measurements. Slope E_3 is a chord modulus at higher stress-strain levels, where the concrete exhibits highly nonlinear behavior. The initial tangent modulus is expected to be greater than the chord modulus. At higher levels of stress, the chord modulus decreases due to the non-linear behavior of concrete. In this testing program, stress levels frequently exceeded 40% of the measured tensile strength, which is cited by many researchers as the point at which nonlinear behavior typically begins [23]. Some elastic modulus measurements showed a gradual increase in stiffness after an initial drop. This behavior is specific to early age concrete in which the microstructure is continuously developing stiffness and strength, causing the stress-strain curve to increase over time. To illustrate this point, two hypothetical cases of stress-strain curves for early age concrete are presented. In case I, shown in Figure 32, the measured stiffness decreases with time, despite the increase in the stress strain curve with evolving microstructure. In case II, shown in Figure 33, the opposite effect is measured. By changing the rate of stiffness evolution over time, the elastic modulus appears to increase despite the nonlinear behavior at later measurements. Therefore, measurements depend on the rate of stiffness evolution, stress level at measurement, and the shape of the stress strain curve.

5.2.7 Early Age Tensile Creep

Creep of concrete has been studied extensively for mature concrete under compressive loading. The importance of creep in concrete was first established from structural concerns about long-term deformation and prestress loss. Creep coefficient and specific creep are parameters that usually describe creep under sustained loading. They were originally single values that were used in structural design to account for long-term deformation. The typical

range for long-term creep coefficient of mature concrete in compression is 1.5 to 3.0 and specific creep ranges from 0.1 to 0.4 με/psi (25 to 50 με / MPa) [23].

Recent research focuses on tensile creep of concrete, since it relates to the ability to resist cracking by relaxation of stress. Early age concrete in particular is sensitive to volumetric changes such as drying and autogenous shrinkage or thermal deformation. Stress relaxation is critical at early ages, since the material has not achieved full strength and is more susceptible to cracking. At early ages, the creep coefficient changes over time and is best represented as a curve. The shape of the curve depends on the evolution of microstructure and environmental conditions. Furthermore, the creep coefficient is not the same in tension as it is in compression. The initial rate of creep is higher in tension, which results in greater creep for relatively short durations of load [23]. At later ages, compressive creep may exceed tensile creep, as the creep function appears to stabilize sooner in tension.

5.2.8 Discussion of Creep Parameters

Strain measurements from the unrestrained specimen were compared to the measured deformation of either the restrained or constant load specimen to obtain creep deformation. The procedure for calculating creep from raw test data is illustrated in Figure 34 for both the restrained and constant load tests. A chart of typical deformation data from a restrained test is displayed in Figure 35. The difference in deformation between the unrestrained and the loaded specimen is attributed to creep. The total tensile creep strain was calculated as the difference between the accumulated restrained deformation and the free shrinkage according to

$$\varepsilon_{cr} = \varepsilon_r - \varepsilon_f, \tag{4}$$

where, $\varepsilon_{cr,}$ is total creep strain, ε_r is restrained deformation and ε_f is unrestrained deformation.

Creep experiments are often performed using a constant load rather than simulating restraint. A constant load relates to structural conditions where external loads are applied for long periods. It is simpler to perform a constant load test, but a constant load does not simulate the creep that occurs due to restrained shrinkage stresses. The creep is different between the tests because of the aging and strength development of the material. Creep strain for the constant load test is initially higher than the restrained test and then levels off since there is no accumulation of stress. Creep strain from a restrained test will eventually surpass the constant load test as it reaches higher stress. Figure 36 shows the typical difference in creep strain measurements for a constant stress test and a restrained stress test. Creep at early age is highly sensitive to loading age, so as load is applied at later age during the restrained test, the additional creep due to increasing restrained load is proportionally lower. Therefore, instead of evaluating creep behavior according to strain, it is common to normalize the creep strain, $\varepsilon_{cr,}$ by the elastic strain, $\varepsilon_{el,}$ at the time of loading according to

$$\phi = \frac{\varepsilon_{cr}}{\varepsilon_{el}}. \tag{5}$$

The creep coefficient, $\phi,$ applies to constant load creep tests where the elastic strain is measured during initial load application. It has been modified for restrained creep testing [16,19] where creep strain under restrained conditions is normalized with the measured elastic strain at each load compensation cycle. At early age, the creep coefficient evolves over time and reflects the developing microstructure stiffness, which represents the ability of concrete to relax stresses. Early age tensile creep coefficient values in the literature are limited, but are typically in the range of 0.3 to 0.5 initially and then increase to 0.5 to 1.5 after the first week. These values are comparable to compressive creep after 100 days of loading [23].

Specific creep is a similar parameter to creep coefficient. The creep strain, $\varepsilon_{cr,}$ is divided by applied stress, σ, instead of elastic strain according to

$$c = \frac{\varepsilon_{cr}}{\sigma}. \tag{6}$$

When comparing concrete mixtures of the same stiffness, the creep coefficient and specific creep will give similar results. However, when comparing materials of different strength and stiffness, specific creep is more appropriate, as it does not include elastic deformation.

5.2.9 Restrained Tensile Creep Strain

The calculated creep strain for IDOT materials is shown in Figure 36. Trends related to material composition, *w/c* ratio or material source are not apparent when comparing the mixtures. Creep is dependent on the stress level, so creep strain is not an effective measure of creep behavior between tests at different stress levels. Specific creep and creep coefficient are more appropriate parameters than strain for comparison of creep capacity.

The creep strain can be related to free shrinkage strain as the Creep-Shrinkage ratio. This value can be used as a measure of how much of the developing shrinkage stress is relaxed by creep. This is a useful estimate when calculating the impact of creep and shrinkage on concrete structures. The creep-shrinkage ratio for IDOT concrete mixtures, shown in Figure 38, converges to about 0.5 after 1 week for most mixtures. Previous research has shown that the value is not very sensitive to material proportions or *w/c* ratio, but it may be affected by sealed or wet curing [19].

5.2.10 Restrained Tensile Creep Coefficient and Specific Creep

The tensile creep coefficients for IDOT mixtures from the first year of the study are shown in Figure 39. The results do not indicate a trend relating creep coefficient to either mixture proportions or pozzolans, but the field material mixtures had lower creep coefficient than mixtures containing laboratory materials. The relationship is similar to the differences in strength. The specific creep for the first year mixtures is shown in Figure 43. The specific creep was similar for all mixtures when compared relative to the applied stress level.

Figure 40 shows the creep coefficient for remaining 0.44 *w/c* mixtures with laboratory materials, all of which had similar strength. The creep coefficient is similar for these materials, indicating little dependence on mixture proportioning of aggregates and cementitious material, within the range of this study. The mixture with the highest creep coefficient in both cases also has the lowest strength. The creep coefficient seems to be unaffected by changes in mixture proportioning or cementitious materials, as long as the strength of the material does not change. Specific creep, shown in Figure 44 was similar for materials containing silica fume and higher for the Duncan Rd mixture IDL44R1, which did not contain silica fume, only fly ash.

In Figure 41, the creep coefficient does not correlate with changes in *w/c* ratio for Duncan Rd and Lake Springfield mixtures. This may again be due to differences in strength between the materials, changing the amount of elastic strain accumulated in each load cycle. The specific creep, shown in Figure 45, shows that as *w/c* ratio decreases, the amount of creep decreases, as expected.

The creep coefficients for laboratory and field material sources are shown in Figure 42, and the specific creep is shown in Figure 46. Similar to the first year mixtures, all field material mixtures had lower creep than the laboratory mixtures, indicating that creep is dependent on cementitious material source. The relationship of creep to cement composition is similar to

shrinkage. Increasing C_3A content or decreasing C_3S content produces higher creep [23]. The combination of cement and pozzolans from different sources makes the prediction of shrinkage and creep potentials difficult in this study, but it is evident that the combination used in the UIUC laboratory has high shrinkage and creep relative to cement/pozzolan combinations tested from other IDOT sources.

The practice of wet curing for concrete under field conditions has important implications for creep behavior. Wet curing may help to reduce cracking by reducing shrinkage, suppressing early shrinkage stress development, and increasing tensile strength, but tensile creep will be reduced. Creep is lower for mature concrete, particularly when compared to very early age concrete that is one day old. Tensile creep decreases over time once drying starts, as moisture is lost from the pore system. Østergaard performed basic creep tests concrete at different ages and the results in Figure 47 show that significantly higher creep is measured when load is applied at one day rather than three days [25]. A reduction in creep capacity will reduce the ability of concrete to relax tensile drying shrinkage stresses and resist cracking.

5.3 Creep and Shrinkage Modeling

The accurate prediction of early age cracking in concrete is essential for evaluating the durability of structures. Cracking reduces durability by providing a path for water and aggressive ions to penetrate the material and induce corrosion of reinforcing steel. To predict cracking, it is necessary to understand how early age volume changes, such as drying shrinkage, produce stress and how creep mechanisms act to relax part of the stress. Analytical models have been developed that evaluate the creep and shrinkage behavior of concrete. Some current models include ACI 209 and RILEM B3, and CEB-FIP Model Code 90 [11, 12, 13]. The experimental data used to construct and validate these models was primarily based on

compressive creep results from constant load tests on mature concrete. However, to predict early age cracking in concrete, we should consider tensile creep of early age concrete under restrained conditions. The ACI and RILEM models have been examined for their usefulness at evaluating early age tensile creep at variable stress levels.

5.3.1 Creep and Shrinkage Model Implementation

The models for concrete creep and shrinkage developed by ACI 209R-92 consist of simplified empirical equations based on laboratory test data. The creep coefficient is given by

$$v_t = \frac{t^{\Psi}}{d + t^{\Psi}} v_u ,$$

where t is the time after loading in days, and d, and Ψ are constants. The parameter v_u is the ultimate creep coefficient for a given material. Recommendations are given for each constant, based on standard test conditions. There are recommended modifications to each parameter for deviations from standard conditions.

The ACI equation for creep coefficient was applied to a concrete mixture with a *w/c* of 0.50. Creep, drying shrinkage, compressive and tensile strength, and elastic modulus were measured for this mixture. Compressive strength measurements were also taken from Altoubat, who studied the same mixture. A comparison between creep strain measurements from a constant load test and the ACI model prediction is shown in Figure 48 using two different values for the v_u parameter. The lower curve reflects the ACI recommended constants modified for test conditions, and the other uses an ultimate creep coefficient v_u of 13.5, which is beyond the recommended range of the parameter. Modifying the ultimate creep coefficient was the only way to fit the data with the ACI equation. The other parameters affect the shape of the curve more than the overall magnitude. The prediction fits the experimental data quite well –

demonstrating that even early age creep can be modeled with the ACI equation – but only after the v_u parameter has been modified beyond a realistic range. Clearly, an ultimate creep coefficient of 13.5 would not be expected from this material. Test data for early age tensile creep have not been know to exceed 2.0. ACI 209 allows for a minimum loading age of 7 days, which is reasonable for structural loads. For earlier loading ages due to drying and autogenous shrinkage or temperature change, modifications of some kind are necessary to apply this prediction.

The RILEM B3 prediction model developed by Bažant *et al*. [26] is based in part on the solidification theory for concrete creep [27]. Total strain is calculated according to

$$\varepsilon(t) = J(t,t')\sigma + \varepsilon_{sh}(t) + \alpha\Delta T(t)$$

where $J(t,t')$ is the compliance function, t is the age of concrete, and t' is the age at loading. $J(t,t')$ can be subdivided further into

$$J(t,t') = q_1 + C_o(t,t') + C_d(t,t')$$

where q_1 is the instantaneous compliance, $C_o(t,t')$ is the basic creep component, and $C_d(t,t')$ is the drying creep component. $C_o(t,t')$ and $C_d(t,t')$ are given by

$$C_o(t,t') = q_2 Q(t,t') + q_3 \ln[1+(t-t')^n] + q_4 \ln(t/t'),$$

$$C_d(t,t') = q_5[\exp\{-8H(t)\} - \exp\{-8H(t')\}]^{1/2},$$

$$\text{and } H(t) = 1 - (1-h)\tanh[(t-t_o)/\tau_{sh}],$$

where q_1 through q_5 are constant parameters, and τ_{sh} is a constant representing size dependence.

At first glance, this model is more attractive for describing early age tensile creep simply because is it based on real phenomena. However, application of the basic creep portion of this model to early age tensile basic creep by Østergaard *et al*. for a 0.50 *w/c* material has shown that the unmodified RILEM B3 model does not give accurate prediction at loading ages of one day or

less [25]. To account for this discrepancy, an additional parameter was proposed to capture very early creep. The additional parameter was incorporated into parameter q_2 according to

$$q_2 = q_2' \left[\frac{t'}{t' - q_6} \right].$$

[Note: The new coefficient was originally called q_5, but has been renamed q_6 here to avoid confusion with the drying creep parameter q_5.] The improvement to the model is illustrated in Figure 7, which shows a comparison between experimental data and the model before and after modification.

5.3.2 Model Results

The modified RILEM B3 model was used to predict creep and shrinkage for several IDOT mixtures under restrained load. The model predictions were used in later work to develop a finite element model for the corresponding bridge decks. The model prediction for tensile creep fits adequately to the experimental data, as shown in Figure 49, with the same model coefficients used by Østergaard *et al*. To adapt the B3 model to a variable stress case, as seen in a restrained test condition, the model was applied incrementally and the stress was increased at each load step. For the restrained test, the elastic modulus was measured at each load step, so no approximation was necessary. Actual measured values of elastic modulus were used in the model. The additional benefit of using the measured elastic modulus is that it incorporates the effect of damage due to microcracking during the test. Overall, the model is capable of predicting early age tensile creep when employing the proposed modification by Østergaard.

Drying shrinkage predictions were made using the B3 model for the IDOT concrete mixtures. The results are shown in Figure 50. The model predicted the drying shrinkage strains with reasonable accuracy for IDOT materials. When the model is used to predict early shrinkage

data, the curve does not fit well with longer-term data, so the best fit between the two curves led to the current result. This indicates that the influence of pozzolans on long-term shrinkage is not represented well in the model and an additional shrinkage term may be needed to consider this material. More shrinkage data representing a wide range of pozzolan additions and *w/c* ratios will be needed and is not available at this time.

5.3.3 Modeling Conclusions

Incremental restrained load cases for measurement and modeling of early age tensile creep and shrinkage of concrete were considered. The following conclusions were drawn:

- Early age tensile creep can be modeled with the ACI equation – but only after the v_u parameter (ultimate creep coefficient) has been modified beyond an acceptable range. The modified RILEM B3 model represents a more realistic and accurate approach.
- The modified B3 model was successfully used to model early age tensile creep under restrained load conditions. A variable stress state due to restrained drying shrinkage was applied and the elastic modulus at each loading step was used to incorporated damage at higher stress levels.
- RILEM B3 predicted the drying shrinkage strains with reasonable accuracy at early age. The model prediction did not fit as well at later ages, possibly due to the presence of pozzolans.
- RILEM B3 modifications for basic creep were implemented to capture special behavior at early age. Further modification to account for pozzolans is suggested, but more data is needed to formulate an additional term.

5.4 Conclusions of Uniaxial Creep and Shrinkage Tests

The early age stress and creep and shrinkage interaction of IDOT concrete mixtures was investigated using a uniaxial creep and shrinkage measurement system developed at UIUC. The IDOT HPC mixtures of like *w/c* containing laboratory materials performed similarly to each other and had slightly higher shrinkage than the conventional mixture after one week of drying. The increase in shrinkage was attributed to greater autogenous shrinkage from silica fume that was most pronounced at early age. Lowering *w/c* ratio did not produce much change in free shrinkage. Additional benefit of reduced drying shrinkage from a *w/c* ratio lower than 0.44 was probably counteracted by the increase in autogenous shrinkage. The balance between autogenous shrinkage and drying shrinkage was optimized in this range of *w/c*. Increasing the *w/c* ratio produced an increase in shrinkage, as expected. The mixtures containing field materials consistently had less shrinkage than mixtures containing laboratory materials, at early ages, but this trend did not continue to later ages, beyond 40 days. These differences were attributed to the source of cementitious materials. Trends that were apparent in the early age (8 day) measurements are not always consistent with longer-term (40 day) measurements. The mechanisms of shrinkage change over time as the pore structure densifies and autogenous shrinkage ceases to play a role in the overall shrinkage behavior. Microstructures that may develop slowly in the first week tend to catch up later in the hydration process as the mechanisms of hydration change. A significant trend was not evident from the weight loss measurements, possibly due to internal autogenous drying that occurred before the first measurement.

The HPC mixtures did not have significantly higher early age tensile strength than the IDOT conventional mix, ISTD. The mixtures containing field materials sometimes had higher initial strengths than the corresponding mixtures with laboratory materials indicating the retarder

may have interacted differently with the various cement sources. Lowering the *w/c* ratio produced the expected result of increasing strength. Although additional tensile strength is beneficial to resist cracking, the strength does not indicate the cracking potential of the material. Strength is related to creep and the reduction in creep that occurs with an increase in strength may counteract a resistance to cracking. A strong concrete material that also has high creep capacity is ideal to resist cracking due to shrinkage stress.

Early age tensile strength plays a critical role in the long-term durability of concrete structures. Shrinkage stresses that develop at early age will cause cracking much sooner if sufficient strength has not been achieved. High strength usually means low creep, which is detrimental to crack resistance. The importance of wet curing for as long as possible is reinforced here as well. Not only does wet curing delay the start of drying shrinkage, but also the strength of the material continues to develop, which further reduces the risk of cracking. Concrete will continue to gain strength over time, so if shrinkage stress development is prevented during the very early age when the concrete is one or two days old, the risk for cracking is greatly diminished.

Thermal characteristics of each concrete mixture were measured and the results indicate that HPC designs developed by IDOT do not have higher heat evolution or faster setting time when compared to standard IDOT concrete mixtures. The HPC mixtures in this study are unlikely to display an increase in cracking potential from early age thermal stresses.

All mixtures developed similar magnitudes of stress when compared at the same water cement ratio and with the same materials source, leading to the conclusion that changing mixture proportions and mineral admixtures within in the range of this study did not have much effect on stress development. Stress development did not follow the same trends as free shrinkage, emphasizing the importance of creep when considering stress. Average shrinkage stress levels

were on average approximately 80% of the concrete tensile strength at the time of failure. The difference may be attributed to the split tensile method for tensile strength measurement or the presence of a drying stress gradient in the specimen. The stiffness of each concrete mixture, indicated by the elastic modulus, did not follow any observed trends.

The creep-shrinkage ratio for IDOT concrete mixtures converges to about 0.5 after 1 week for most mixtures. The results do not indicate a trend relating creep coefficient to either mixture proportions or pozzolans, but the field material mixtures had lower creep coefficient than mixtures containing laboratory materials. The relationship is similar to the differences in strength. The specific creep was similar for mixtures of the same *w/c* ratio and material source when compared relative to the applied stress level. The creep coefficient was similar for constant *w/c* and materials source, indicating little dependence on mixture proportions, within the range investigated in this study. Field material mixtures had lower creep than the laboratory mixtures, indicating that creep is dependent on cementitious material source. The combination of cement and pozzolans from different sources makes the prediction of shrinkage and creep potentials difficult in this study, but it is evident that the combination used in the UIUC laboratory has high shrinkage and creep relative to cement/pozzolan combinations tested from other IDOT sources.

The practice of wet curing for concrete under field conditions has important implications for creep behavior. Wet curing may help to reduce cracking by reducing shrinkage, suppressing early shrinkage stress development, and increasing tensile strength, but tensile creep will be reduced. Creep is lower for mature concrete, particularly when compared to very early age concrete that is one day old. Tensile creep decreases over time once drying starts, as moisture is lost from the pore system. A reduction in creep capacity will reduce the ability of concrete to relax tensile drying shrinkage stresses and resist cracking.

Creep and shrinkage behavior were modeled with ACI 209 and modified RILEM B3. Results show that early age tensile creep can be modeled with the ACI equation – but only after the v_u parameter (ultimate creep coefficient) has been modified beyond an acceptable range. The modified RILEM B3 model represents a more realistic and accurate approach. A variable stress state due to restrained drying shrinkage was applied and the elastic modulus at each loading step was used to incorporated damage at higher stress levels. RILEM B3 predicted the drying shrinkage strains with reasonable accuracy at early age. The model prediction did not fit as well at later ages, possibly due to the presence of pozzolans. RILEM B3 modifications for basic creep were implemented to capture special behavior at early age. Further modification to account for pozzolans is suggested, but more data is needed to formulate an additional term.

REFERENCES

1. Banthia, N., Yan, C., Mindess, S., "Restrained shrinkage cracking in fiber reinforced concrete: a novel test technique," *Cement & Concrete Research,* V. 26, No. 1, 1996, pp. 9-14

2. Shah, S.P., Weiss, W.J. and Yang, W., "Shrinkage cracking-Can it be prevented?", *Concrete International*, V. 20, No. 4, 1998, pp. 51-55

3. Gryzbowski, M., Shah, S.P., "Shrinkage cracking of fiber reinforced concrete," *ACI Materials Journal*, V. 87, No. 2, 1990, pp. 138-148

4. Gryzbowski, M., Shah, S.P., "Model to predict cracking in fiber reinforced concrete due to restrained shrinkage," *Magazine of Concrete Research*, V. 41, No. 148, 1989, pp. 125-135

5. Weiss, W.J., Shah, S.P., "Restrained shrinkage cracking: the role of shrinkage reducing admixtures and specimen geometry," *Materials and Structures*, V. 35, 2002, pp. 85-91

6. Kovler, K., Sikuler, J., and Bentur, A., "Restrained shrinkage tests of fiber reinforced concrete ring specimens: effect of core thermal expansion," *Materials and Structures*, V. 26, 1993, pp. 231-137

7. Alexandrovsky, S.V., "Analysis of concrete and reinforced concrete structures for temperature and humidity change with consideration of creep," *Stroyizdat*, Moscow, 1966

8. Kasai, Y., Yokohama, K., and Matsui, T., "Tensile properties of early age concrete," in *Proceeding of the International Conference on the Mechanical Behavior of Materials*, Kyoto, Japan, 1971, Vol. IV, The Society of Materials Science Japan, 1972, pp. 288-298

9. Springenschmid, R., Breitenbücher, R., and Mangold, M., "Development of Thermal Cracking Frame and the Temperature-Stress Testing Machine," in *Thermal Cracking in Concrete at Early Ages*, Proceedings of the International RILEM Symposium, Munich 1994, Ed. by R. Springenschmid, 1995, pp. 137-144

10. Bissonnette, B., Pigeon, M., "Tensile creep at early ages of ordinary, silica fume and fiber reinforced concretes," *Cement and Concrete Research,* V. 25, No. 5, 1995, pp. 1075-1085

11. American Concrete Institute (ACI) 209R-92 (Reapproved 1997), "Prediction of Creep Shrinkage and Temperature Effects in Concrete Structures", Farmington Hills, MI, 2001

12. RILEM Draft Recommendation, TC 107-GCS Guidelines for the Formulation of Creep and Shrinkage Prediction Models, "Creep and Shrinkage Prediction Model for Analysis and Design of Concrete Structures – Model B3", prepared by Bažant, Z.P. and Baweja, S., *Materials and Structures*, V. 28, 1995, pp. 357-365

13. CEB-FIP Model Code 1990, Comitè Euro-International Du Beton, Bulletine D' Information No. 203, 1991

14. Paillère, A.M., Buil, M., Serrano, J.J., "Effect of Fiber Addition on the Autogenous Shrinkage of Silica Fume Concrete," *ACI Materials Journal*, V. 86, No. 2, 1989, pp. 139-144

15. Bloom, R. and Bentur, A., "Free and Restrained Shrinkage of Normal and High Strength Concretes," *ACI Materials Journal,* V. 92, No. 2, 1995, pp. 211-217

16. Kovler, K., "Testing System for Determining the Mechanical Behavior of Early Age Concrete under Restrained and Free Uniaxial Shrinkage," *Materials and Structures*, V. 27, 1994, pp. 324-330

17. Pigeon, M., Toma, G., Delgrave, A, Bissonnette, B., Marchand, J., and Prince, J.C., "Equipment for the analysis of the behavior of concrete under restrained shrinkage at early ages," *Magazine of Concrete Research*, V. 52, No. 4, 2000, pp. 297-302

18. van Breugel, K., de Vries, J., "Mixture optimization of HPC in view of autogenous shrinkage," *Proceeding of the Fifth International Symposium on Utilization of High Strength/High Performance Concrete,* Sandefjord, 1999, pp. 1017-1026

19. Altoubat, S.A., "Early age stresses and creep-shrinkage interaction of restrained concrete", *Ph.D. Thesis*, Department of Civil and Environmental Engineering, University of Illinois at Urbana-Champaign, 2000

20. Kovler, K., "Shock of evaporative cooling of concrete in hot dry climates", *Concrete International,* V. 10, 1995, pp. 65-69

21. Altoubat, S.A. and Lange, D.A. "Grip-specimen Interaction in Uniaxial Restrained Test," *Concrete: Material Science to Application - A Tribute to S P. Shah*, *ACI SP-206,* 2002

22. Jensen, O. M., Hansen, P. F. (1996). "Autogenous Deformation and Change in the Relative Humidity in Silica Fume-Modified Cement Paste" ACI Mat. J. (93) 6, 539-543.

23. Mindess S., Young, J.F., and Darwin, D., *Concrete*, 2ed, Prentice-Hall, NJ, 2003

24. van Mier, J.G.M., *Fracture Processes of Concrete*, CRC Press, Boca Raton, FL, USA, 1997

25. Østergaard, L., Lange, D.A., Altoubat, S.A., Stang, H., "Tensile basic creep of early-age concrete under constant load," *Cement and Concrete Research*, V. 31, No. 12, 2001, pp. 1895-1899

26. Bažant, Z. P. and Baweja, S., "Creep and Shrinkage Prediction Model for Analysis and Design of Concrete Structures – Model B3", *Structural Engineering Report 94-10/603c*, Northwestern University, 1994

27. Bažant, Z. P. and Prasannan, S., "Solidification Theory for Concrete Creep I: Formulation and II: Verification and Application," *J. of Eng. Mech. (ASCE)*, V. 115, No. 8, 1691-1725, 1989

TABLES

Table 3. Uniaxial Test Results

Designation	w/c	Cement Content	Cementitous Content	Failure Age	Maximum Stress	Tensile Strength at Failure	Tensile Strength (8 day)	Stress-Strength Ratio	Creep Coefficient	Specific Creep	Free Shrinkage after 1 week of drying	Creep-Shrinkage Ratio
HPC1	0.44	465	612	5.2	208	250	312	0.83	1.52	0.57	215	0.60
HPC1F	0.44	465	612	8.0	325		400	0.81	0.81	0.32	217	0.47
HPC2	0.44	465	610	3.1	218	165	272	1.32	0.85	0.46	306	0.46
HPC2F	0.44	465	610	8.0	262		428	0.61	0.94	0.42	223	0.49
HPC4	0.44	565	590	7.8	327	409	409	0.80	1.18	0.49	294	0.54
ISTD	0.44	605	605	8.0	397		400	0.99	1.43	0.35	240	0.45
IDL41R1	0.41	515	655	3.3	245	310	340	0.79	1.02	0.40	309	0.51
IDL44R1	0.44	515	655	8.0	254		321	0.79	1.43	0.65	303	0.56
ISL39R1	0.39	465	635	4.3	345	400	455	0.86	1.12	0.35	262	0.54
ISF39R1	0.39	465	635	4.8	327	440	440	0.74	0.70	0.22	181	0.42
ISL44R1	0.44	465	635	7.9	335	390	390	0.86	0.94	0.36	261	0.48
ISL50R1	0.50	465	635	8.0	208		281	0.74	1.60	0.80	348	0.60
ISF44R1-2	0.44	465	635	8.0	352		347	1.01	0.60	0.23	200	0.35
IKL44R1	0.44	545	560	6.7	315	360	380	0.88	1.00	0.60	269	0.35
IKF44R1	0.44	545	560	8.0	266		411	0.65	0.84	0.39	225	0.42
IBL44R1	0.44	445	570	3.5	237	370	471	0.64	0.87	0.47	309	0.46
IBF44R1	0.44	445	570	8.0	321		374	0.86	0.99	0.45	275	0.58
Average		**492**	**610.8**	**6.5**	**290.8**	**343.8**	**378.3**	**0.83**	**1.05**	**0.44**	**261**	**0.49**
Standard Dev		**47**	**31**	**2**	**57**	**88**	**58**	**0.17**	**0.29**	**0.15**	**47**	**0.08**

(stress and strength in psi, cement content in lbs/yd^3, shrinkage in με)

FIGURES

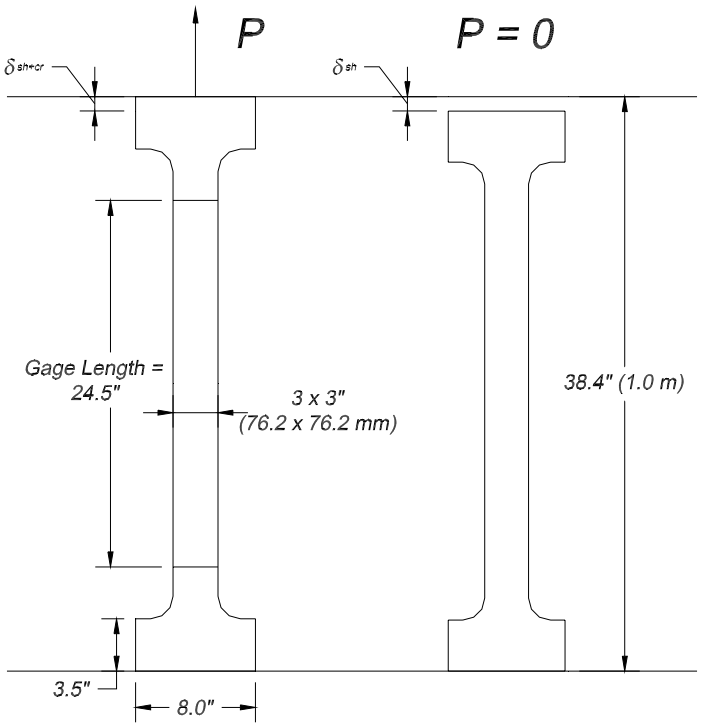

Figure 2. Companion specimen diagram for uniaxial creep and shrinkage tests

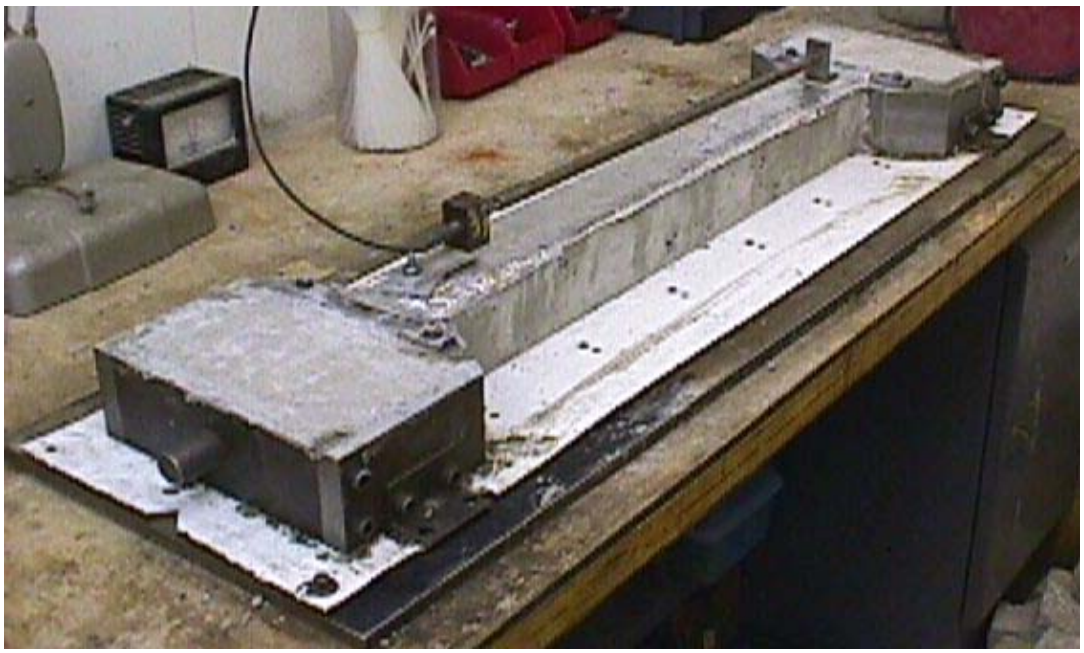

Figure 3. Unrestrained test specimen in environmental chamber

Figure 4. Restrained test specimen and hydraulic system

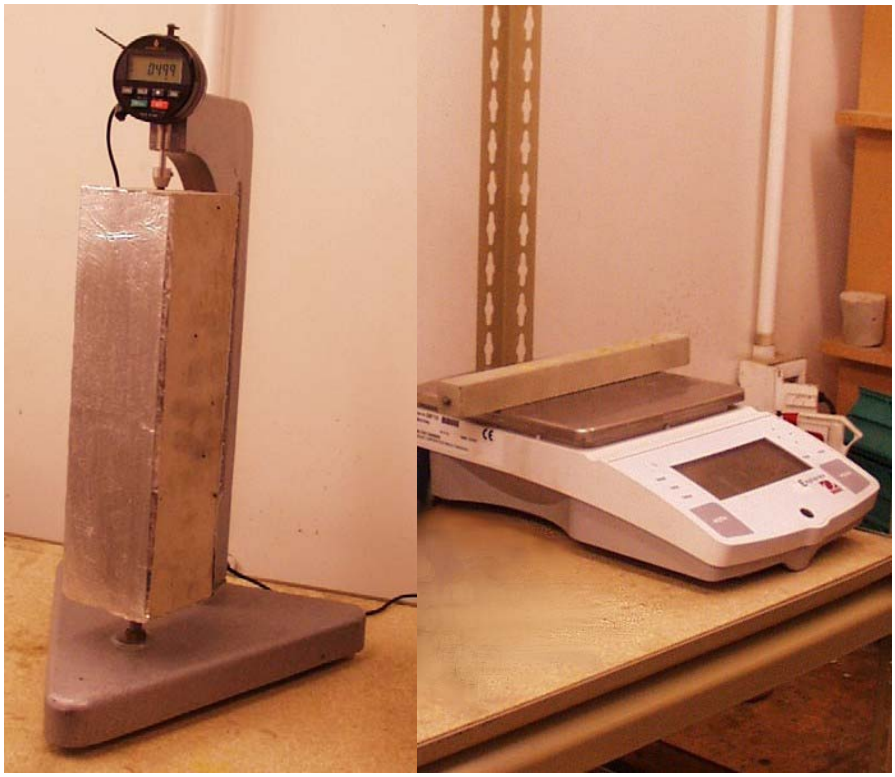

Figure 5. Concrete prism in length change comparator and analytical balance

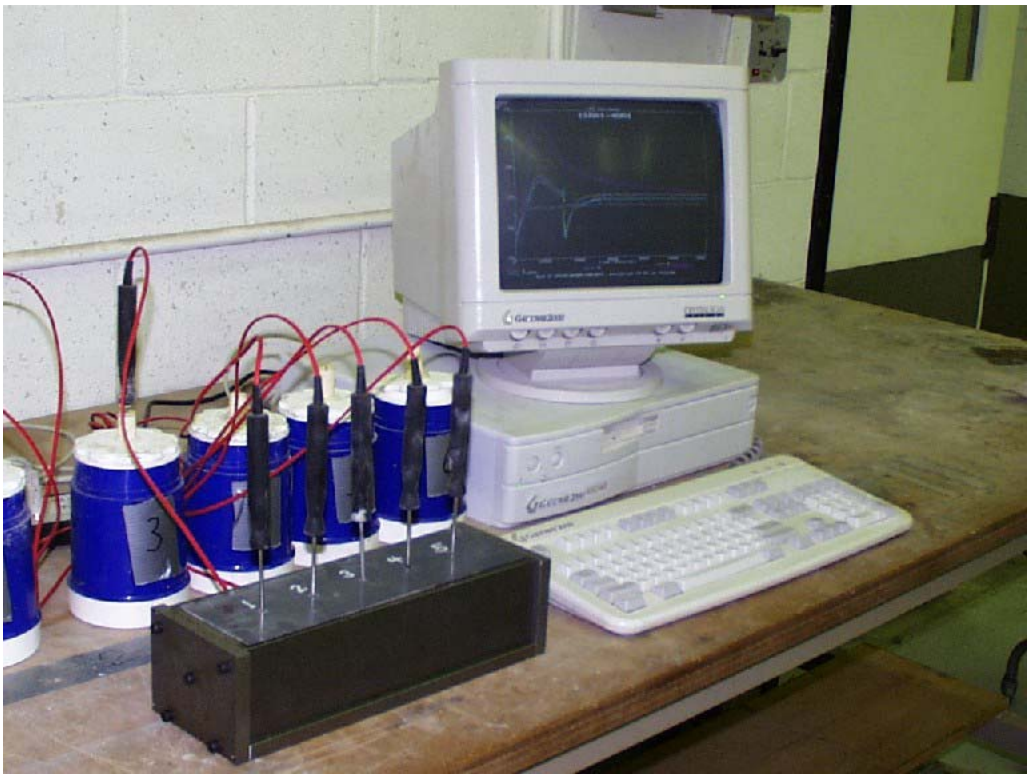

Figure 6. Internal temperature test system and semi-adiabatic containers

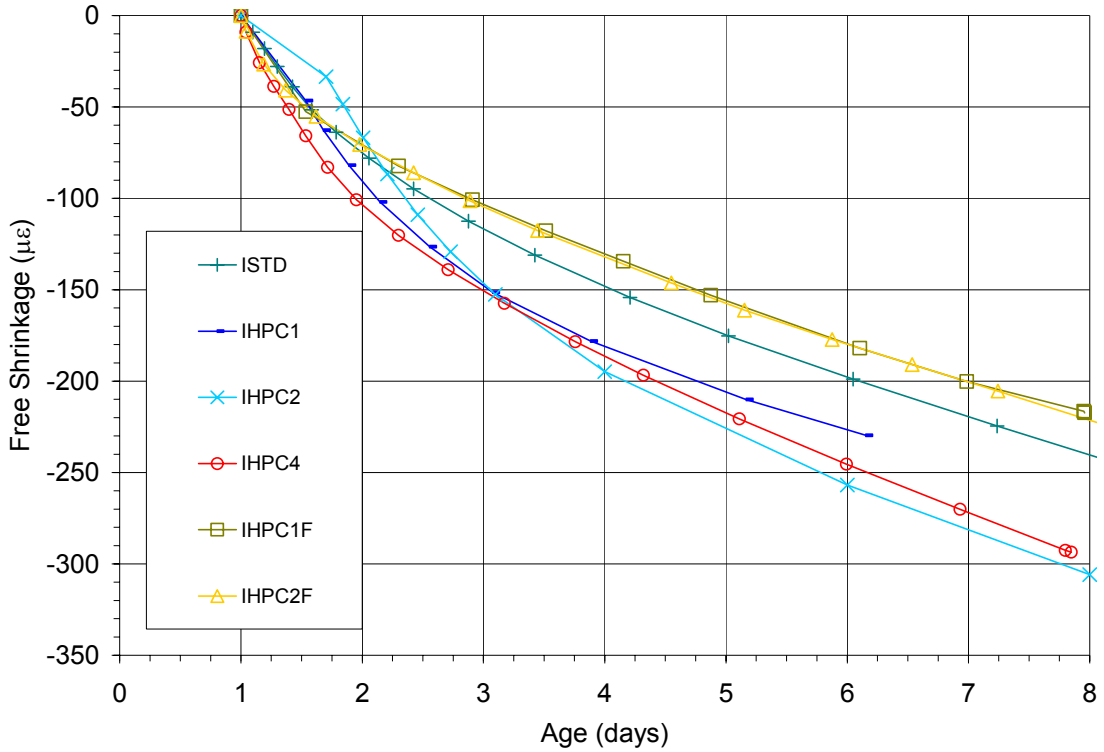

Figure 7. Free shrinkage of uniaxial specimens, *w/c* = 0.44

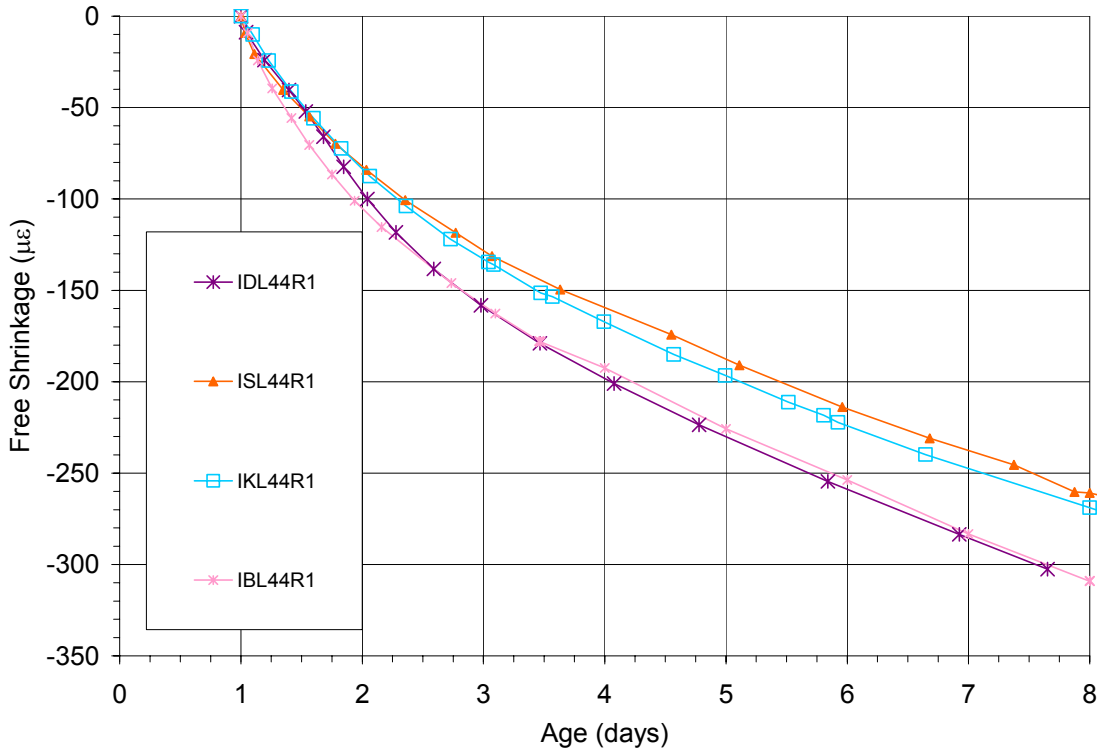

Figure 8. Free shrinkage of uniaxial specimens, *w/c* = 0.44, laboratory materials only

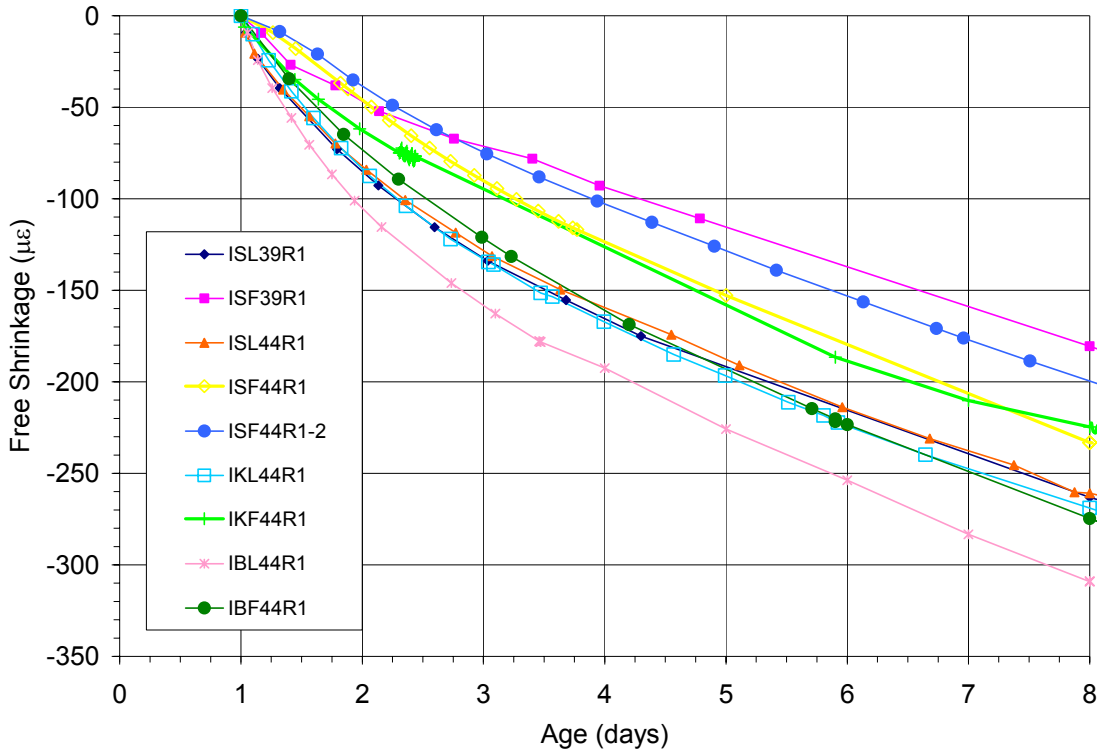

Figure 9. Free shrinkage of uniaxial specimens, laboratory vs. field materials

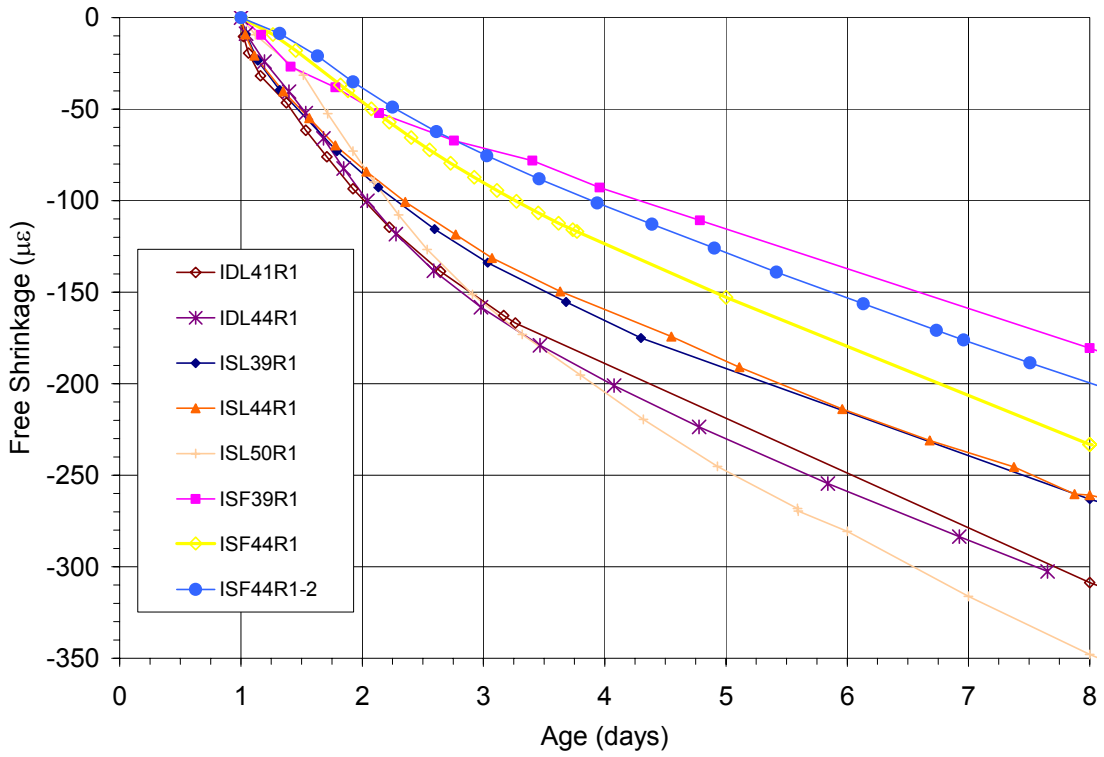

Figure 10. Free shrinkage of uniaxial specimens, variations in *w/c*

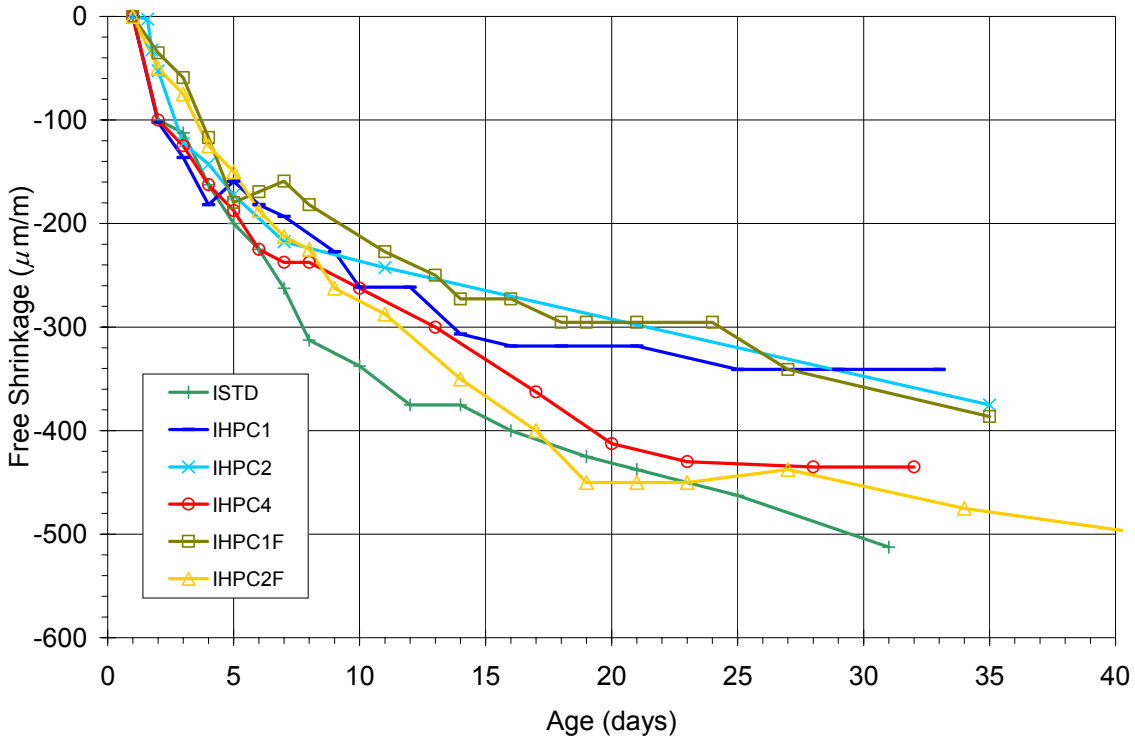

Figure 11. Long-term free shrinkage of prisms, *w/c* = 0.44

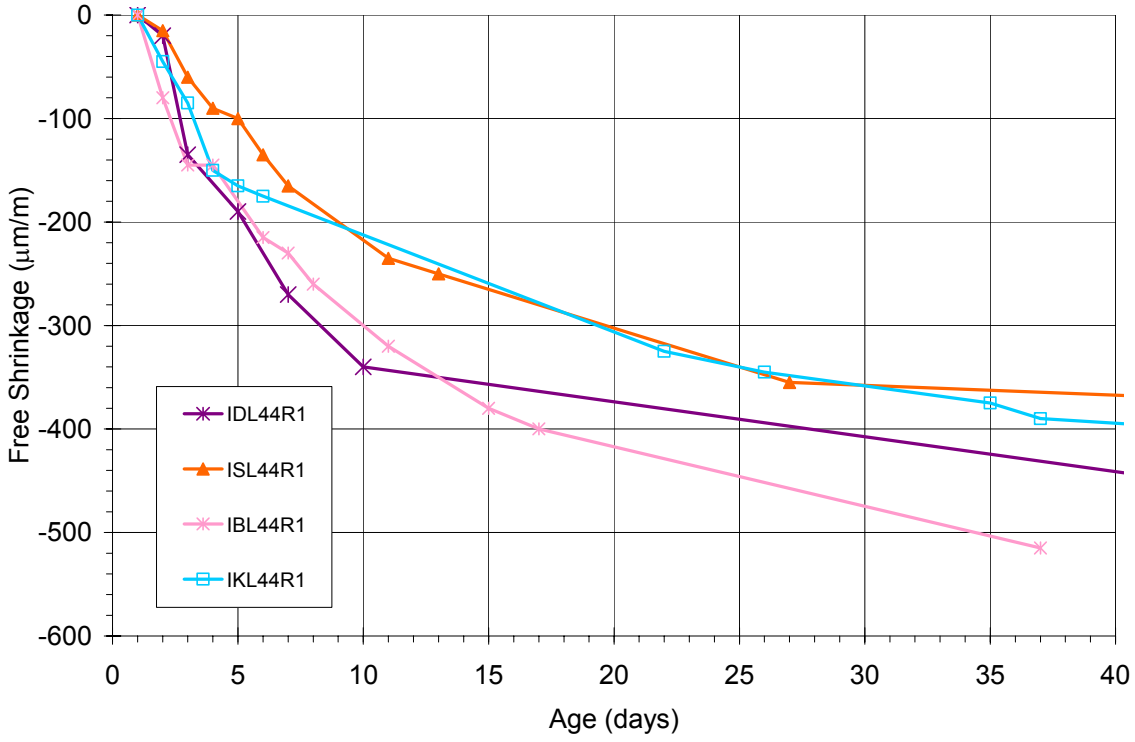

Figure 12. Long-term free shrinkage of prisms, *w/c* = 0.44, laboratory materials

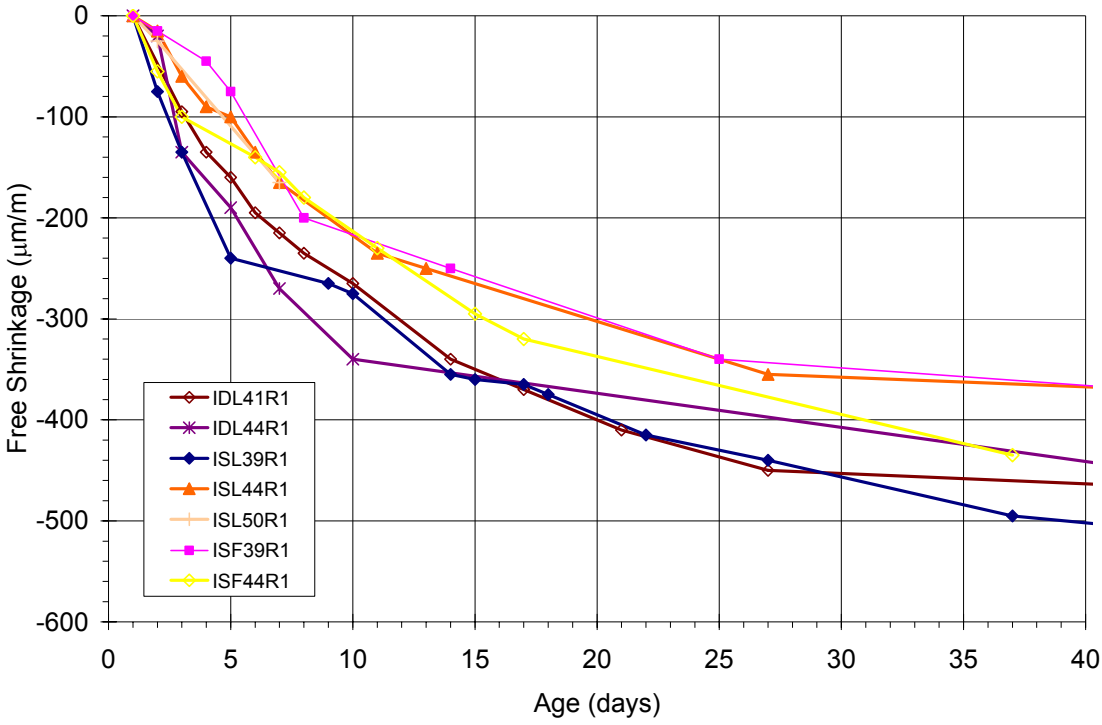

Figure 13. Long-term free shrinkage of prisms, variation in *w/c*

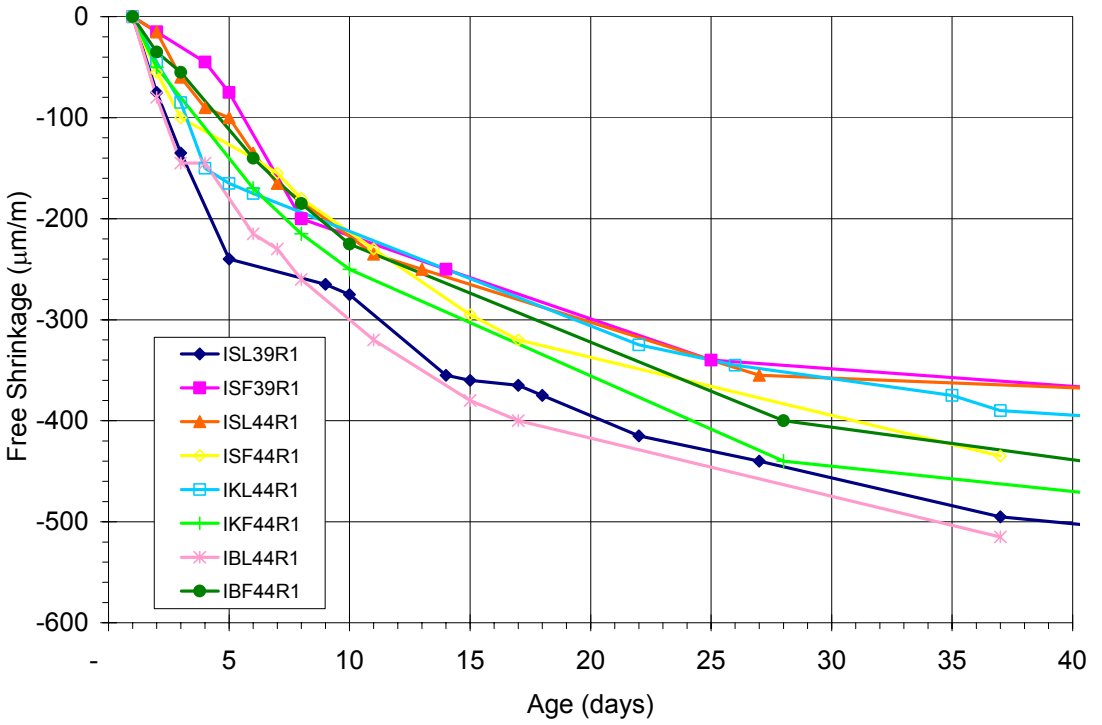

Figure 14. Long-term free shrinkage of prisms, laboratory vs. field materials

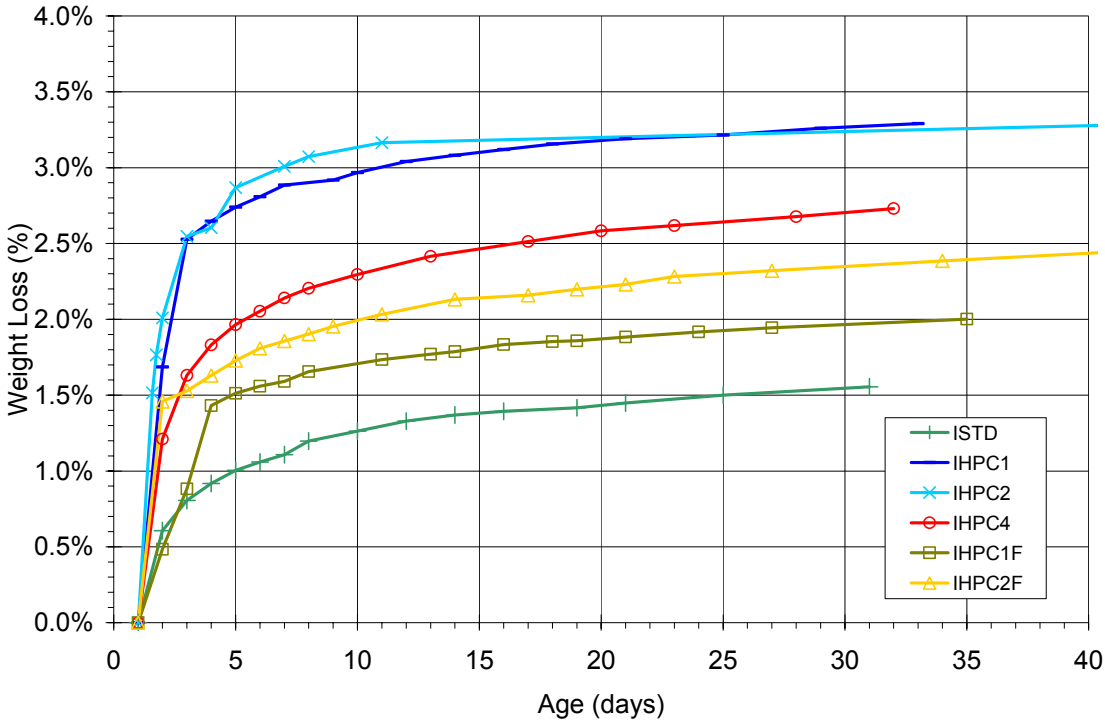

Figure 15. Weight loss of concrete prisms, *w/c* = 0.44

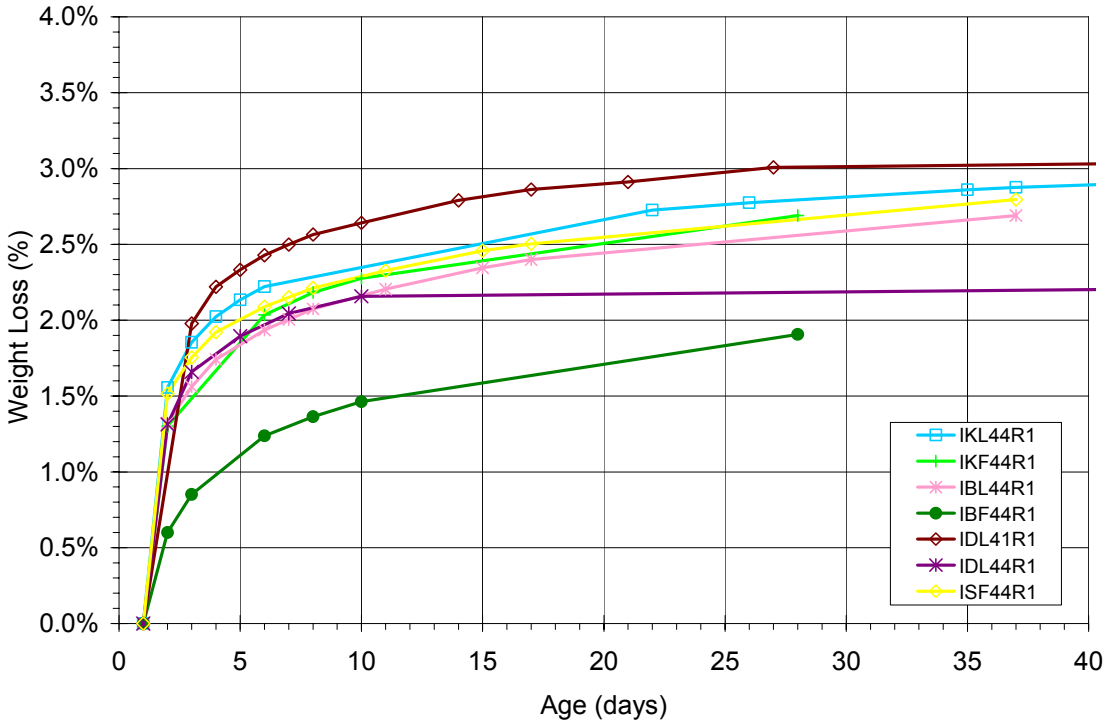

Figure 16. Weight loss of concrete prisms, laboratory vs. field materials

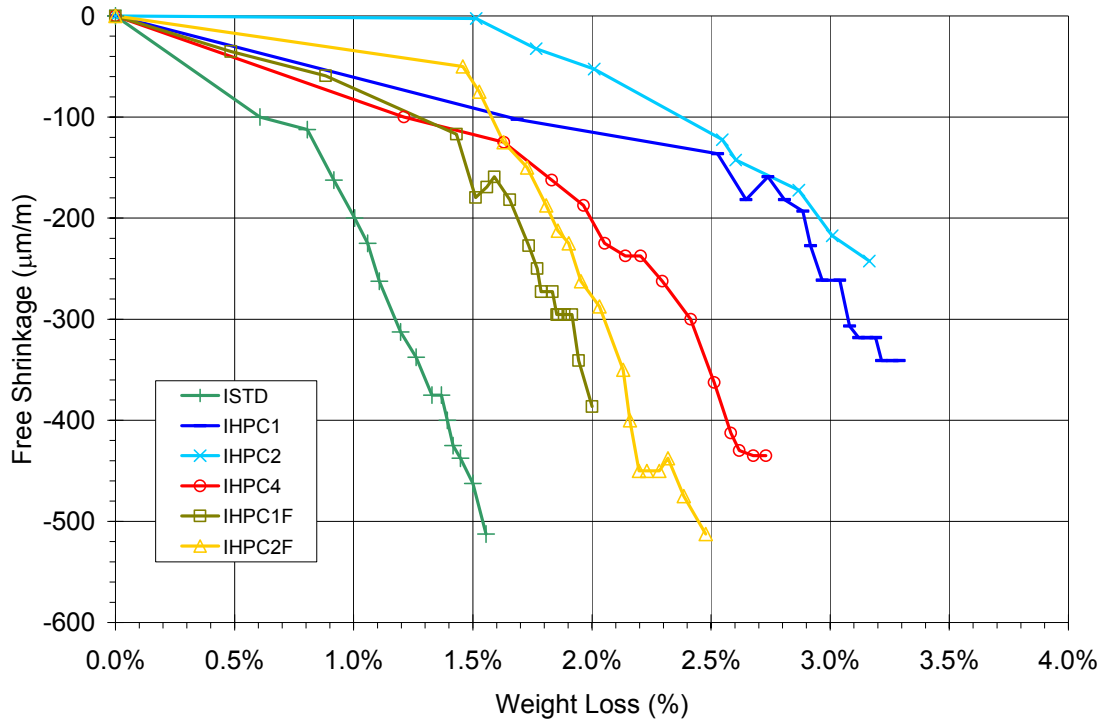

Figure 17. Free shrinkage vs. weight loss, *w/c* = 0.44

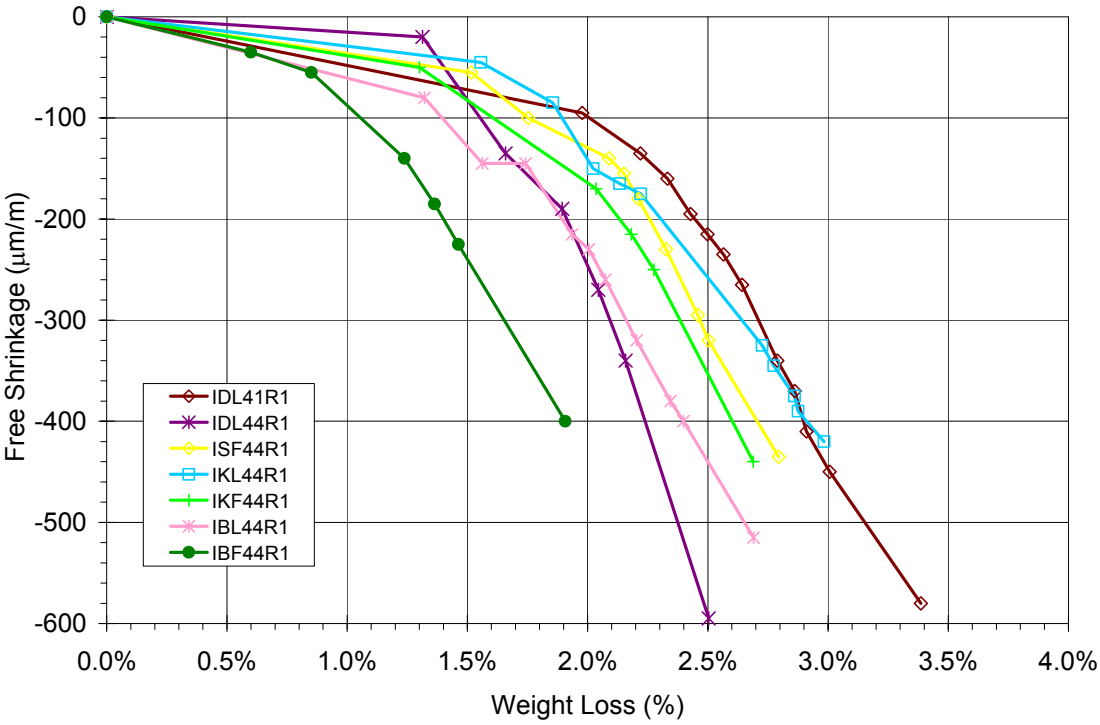

Figure 18. Free shrinkage vs. weight loss, laboratory vs. field materials

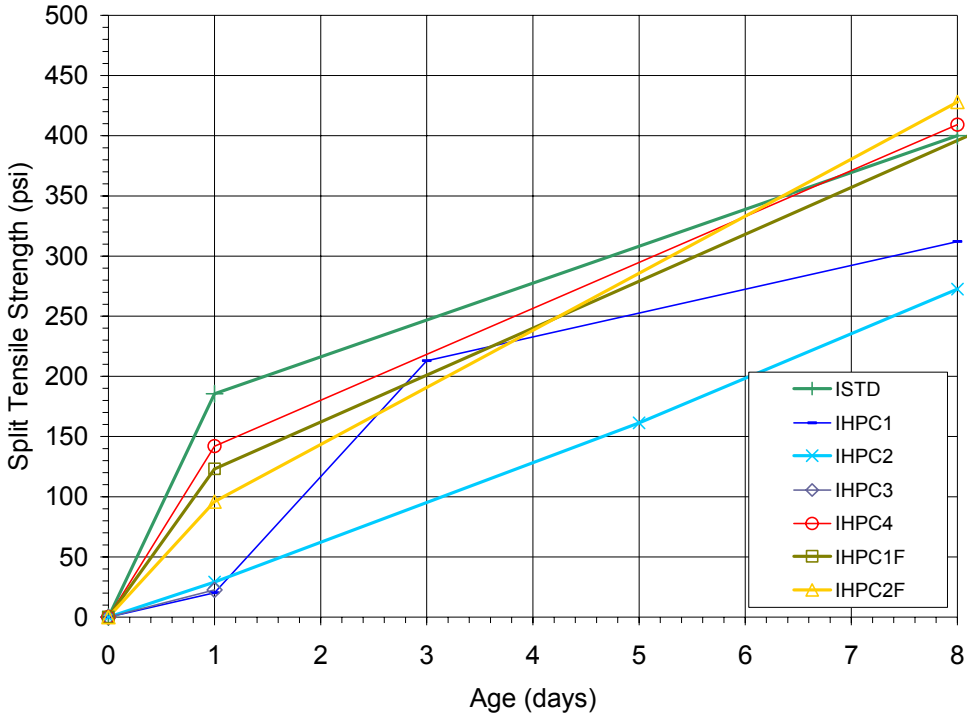

Figure 19. Split tensile strength, *w/c* = 0.44

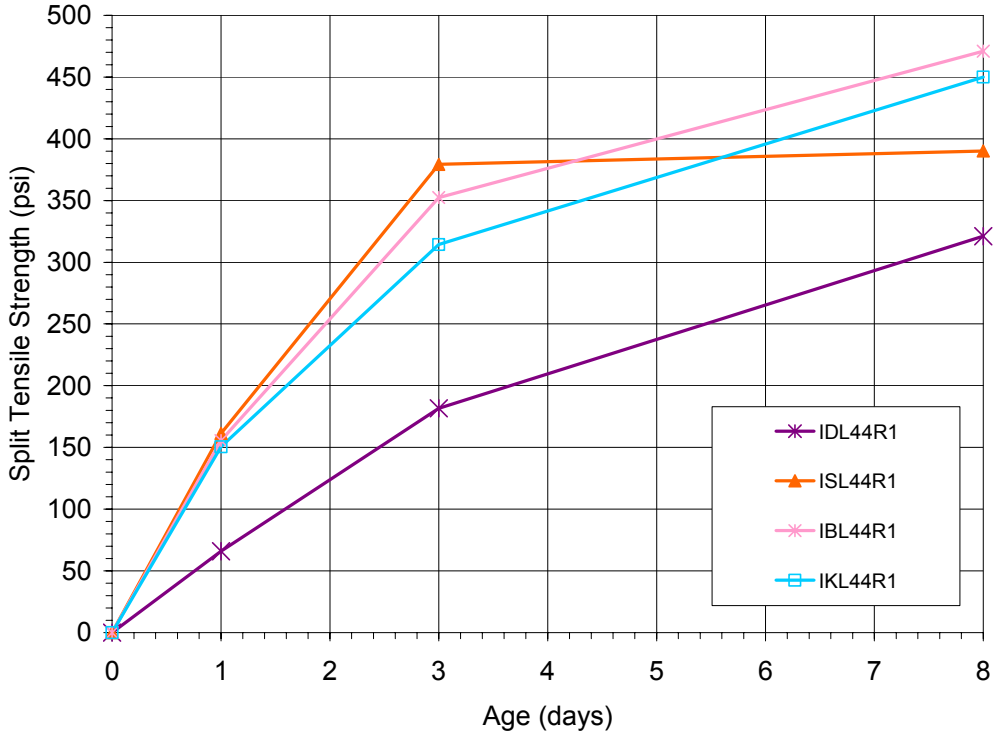

Figure 20. Split tensile strength, *w/c* = 0.44, laboratory materials only

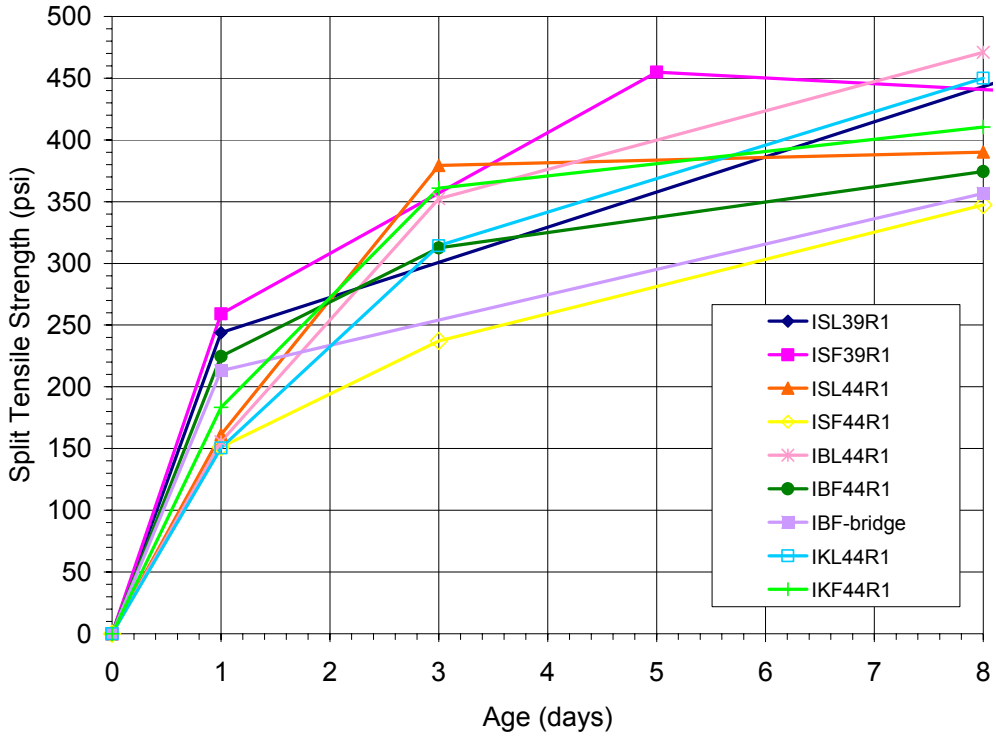

Figure 21. Split tensile strength, laboratory vs. field materials

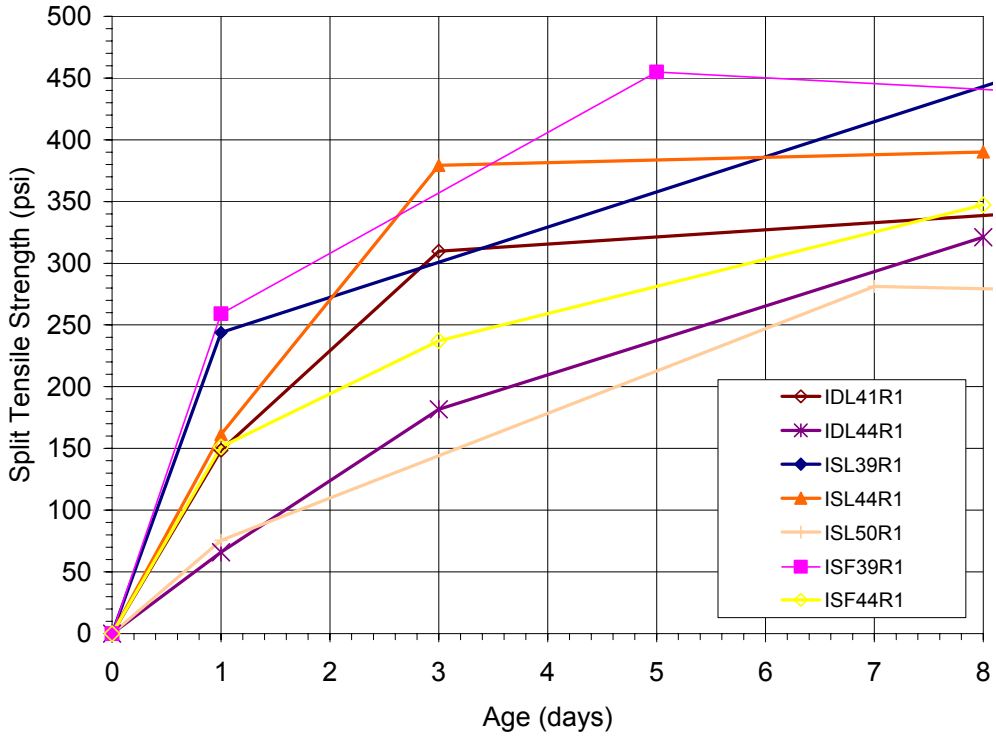

Figure 22. Split tensile strength, variations in *w/c* ratio

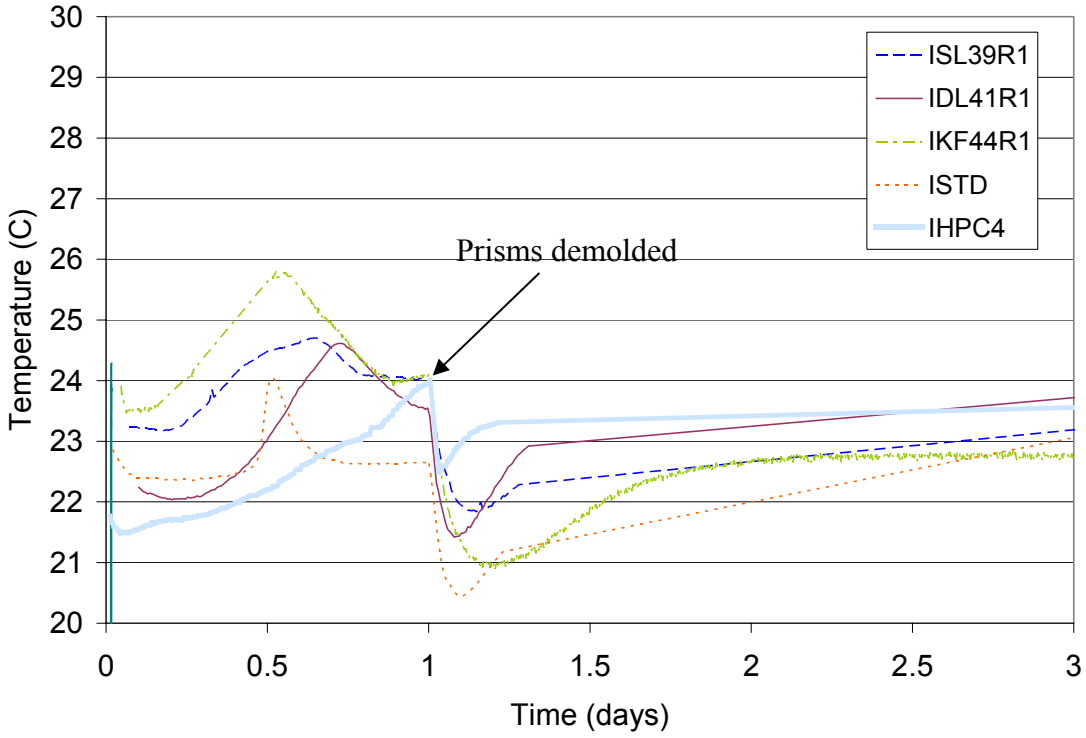

Figure 23. Internal temperature of concrete prisms during demolding

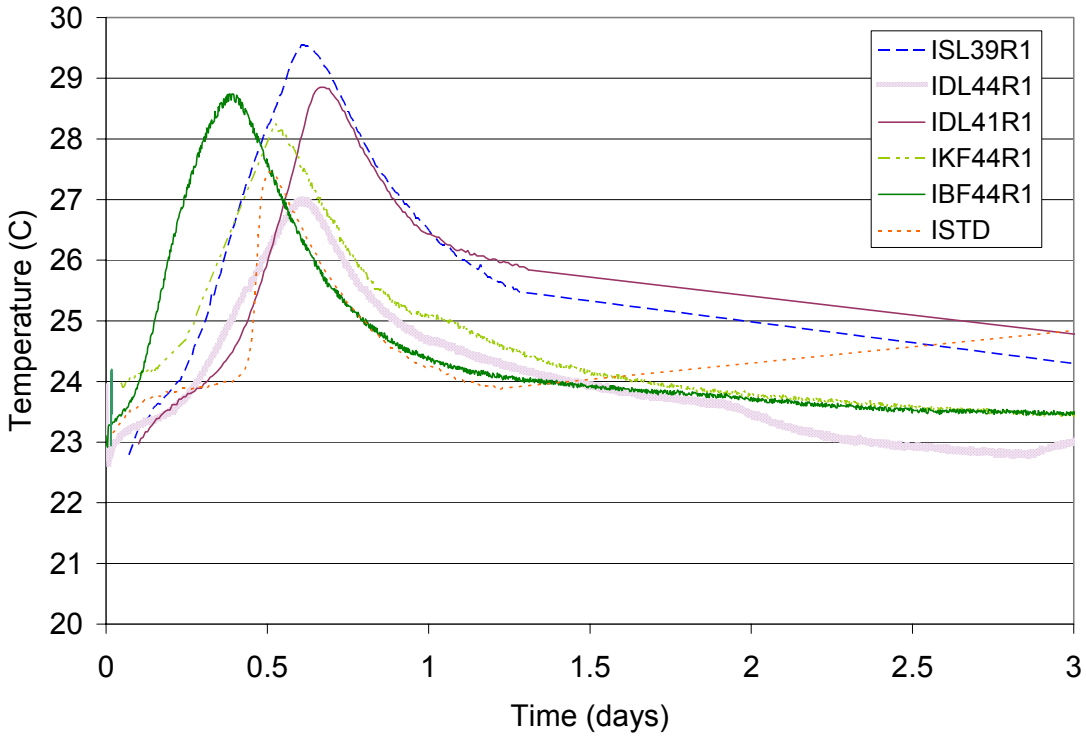

Figure 24. Internal concrete temperature under semi-adiabatic conditions

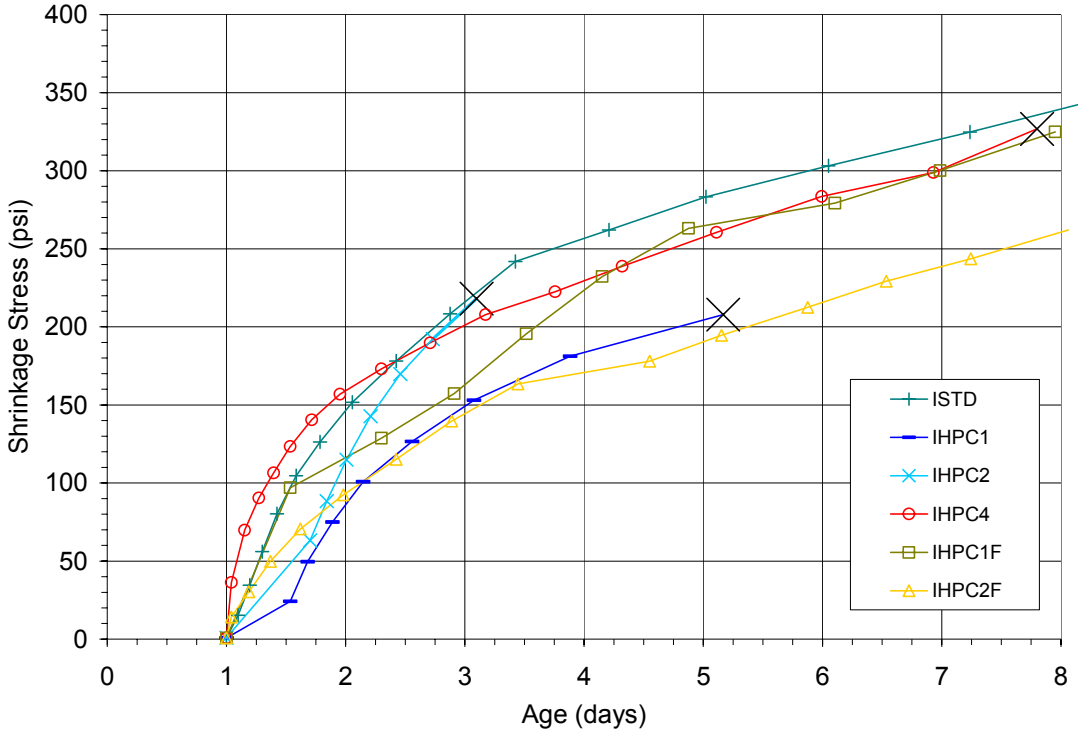

Figure 25. Shrinkage stress development, *w/c* = 0.44

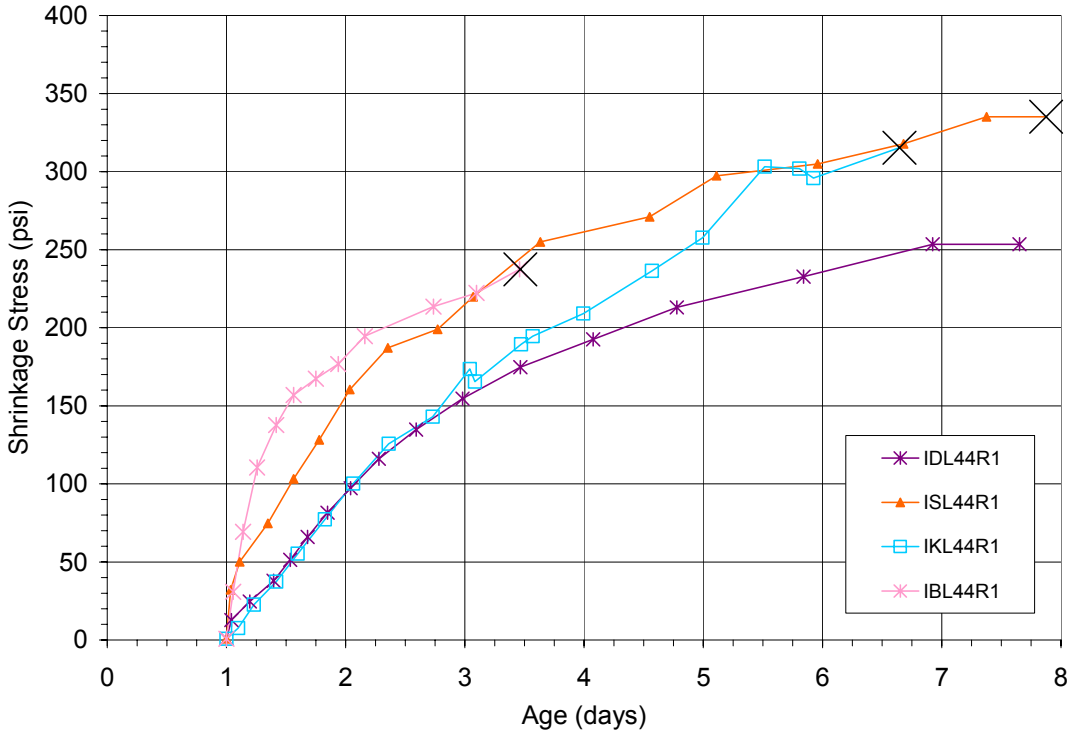

Figure 26. Shrinkage stress development, *w/c* = 0.44, laboratory materials only

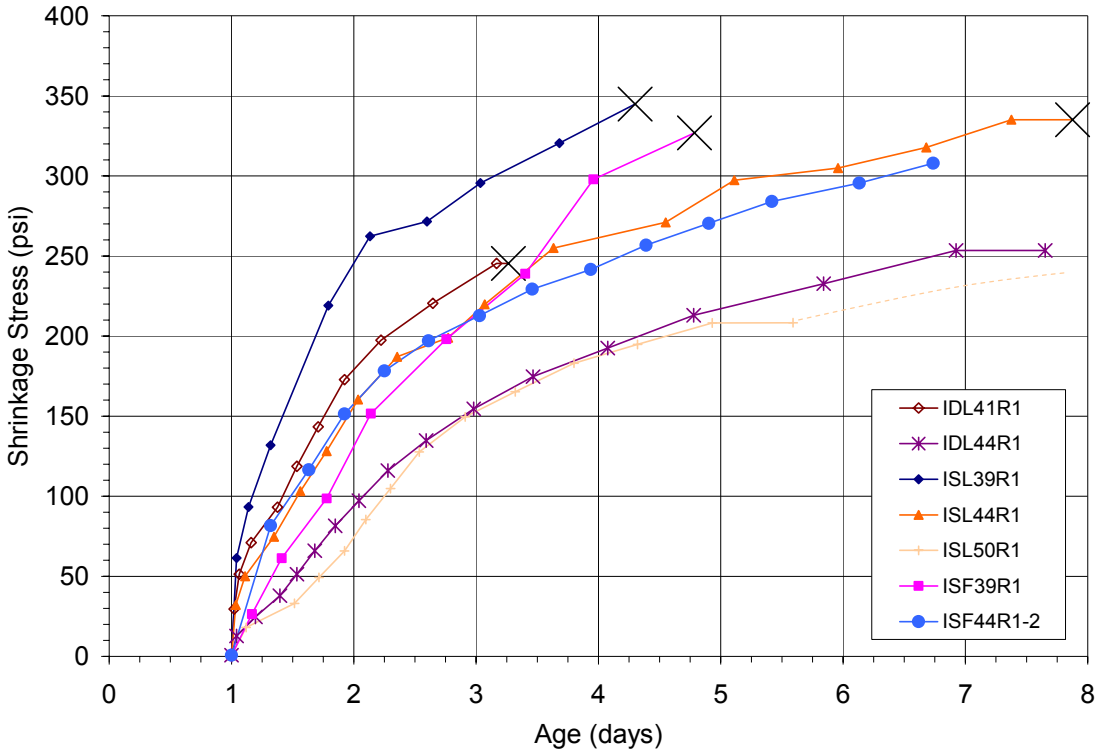

Figure 27. Shrinkage stress development, variation in *w/c* ratio

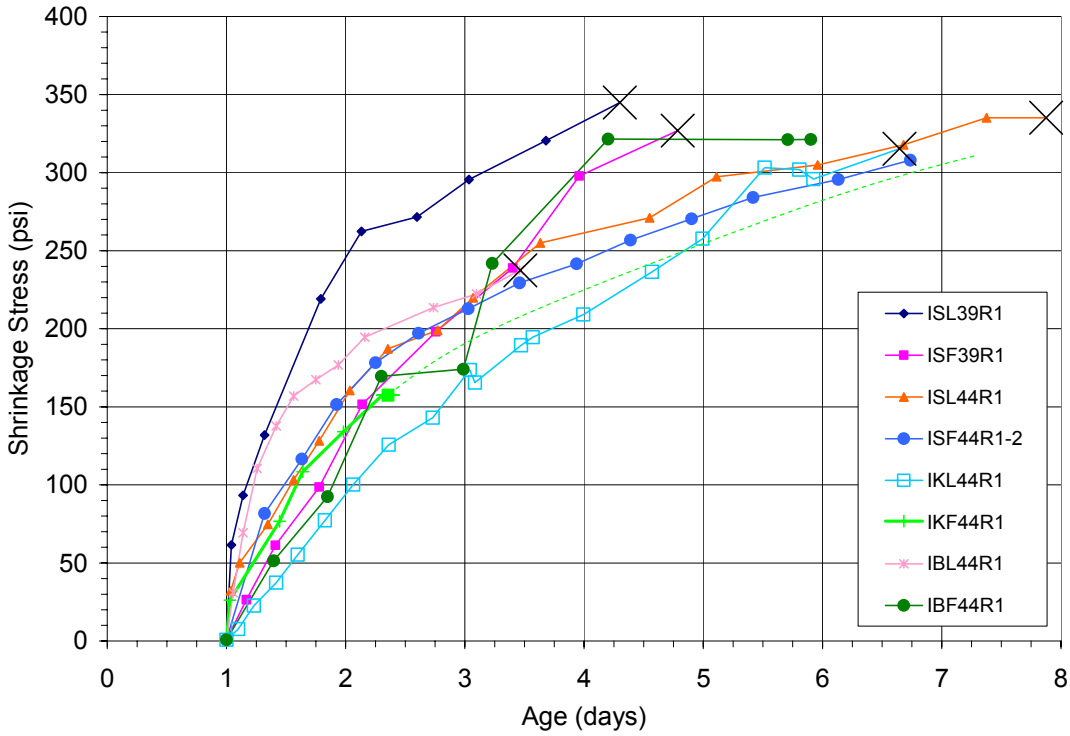

Figure 28. Shrinkage stress development, laboratory vs. field materials

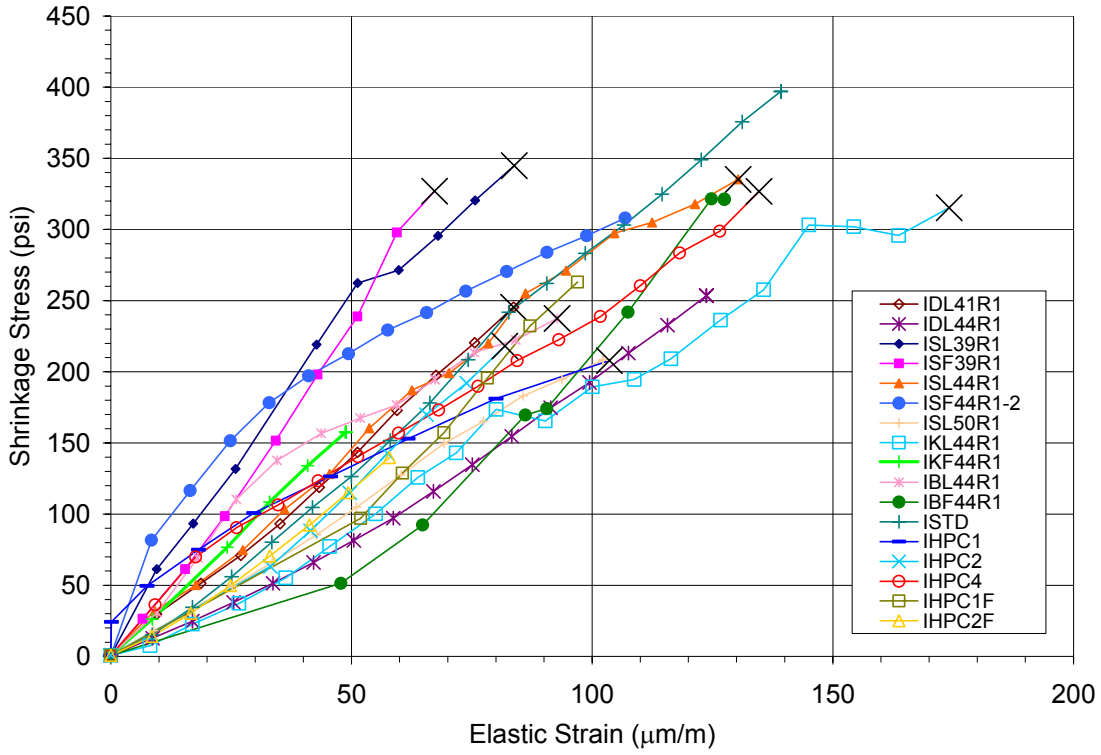

Figure 29. Stress strain diagram for uniaxial tests, all materials

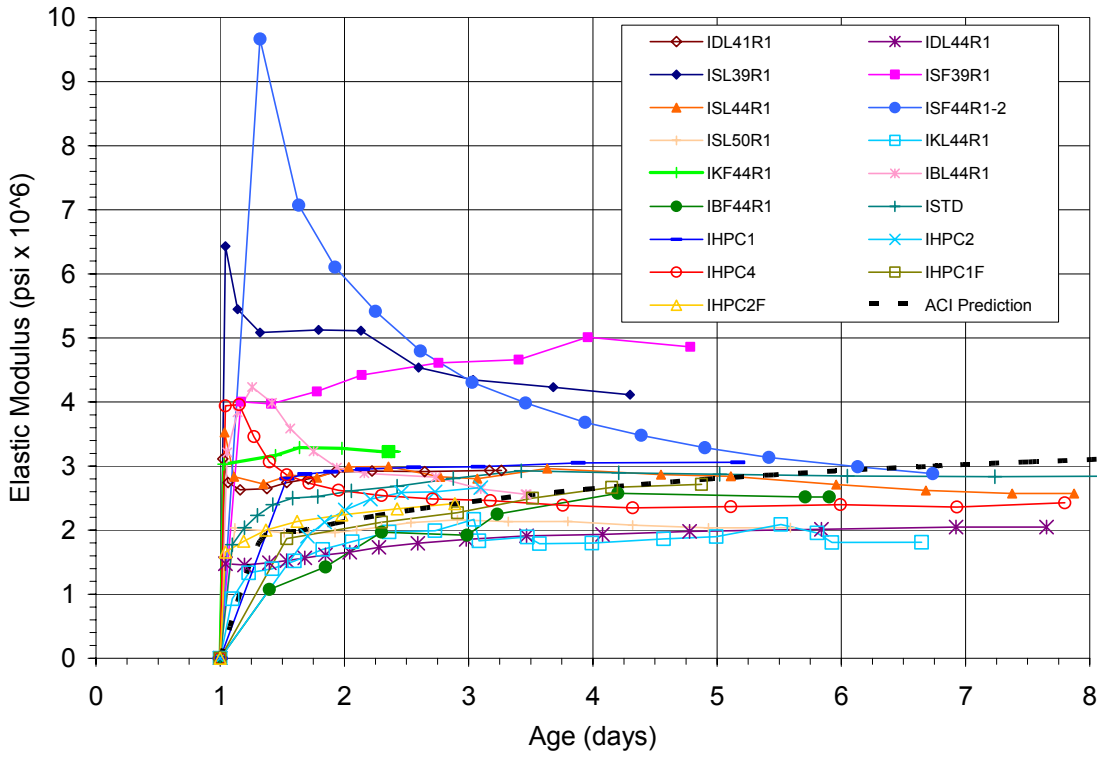

Figure 30. Elastic modulus (secant) for all materials

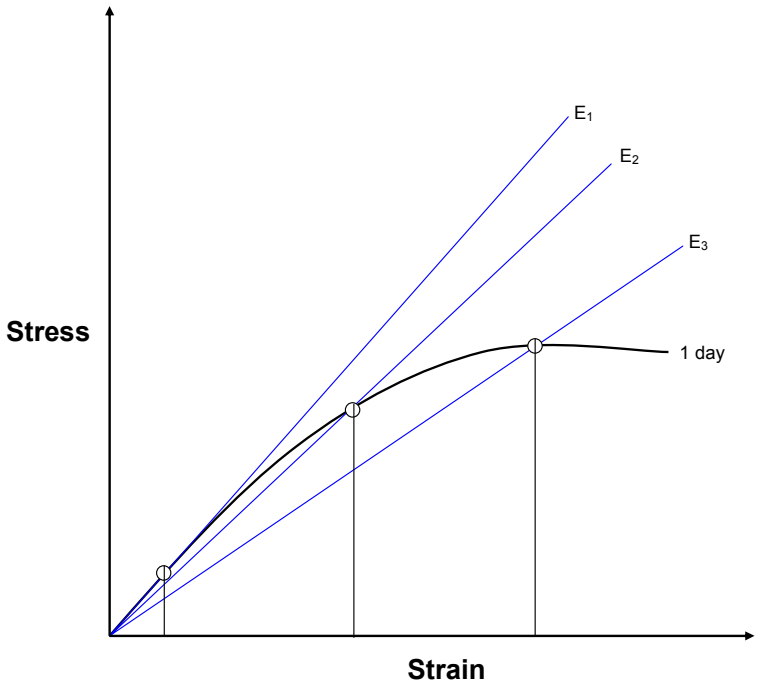

Figure 31. Schematic diagram for measurement of elastic modulus

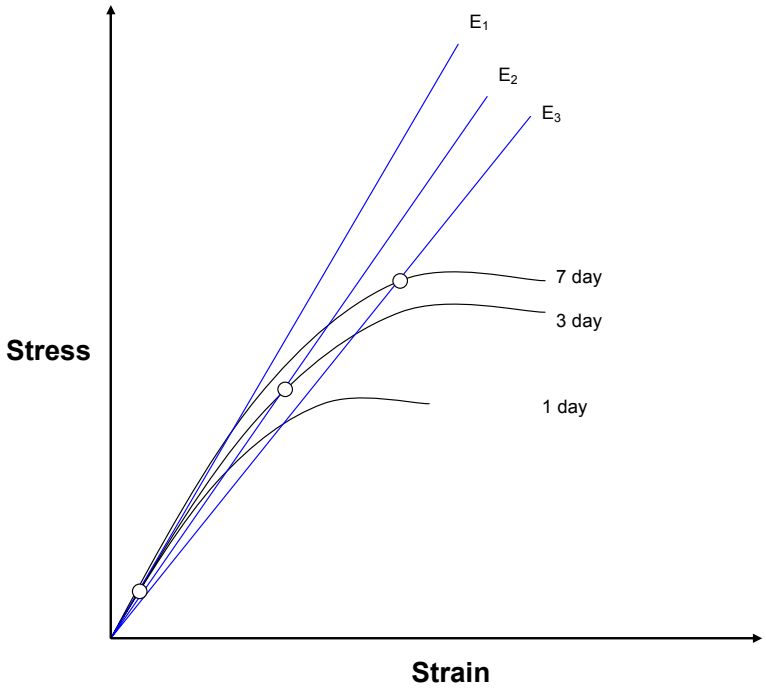

Figure 32. Measurement of elastic modulus at early ages, case 1

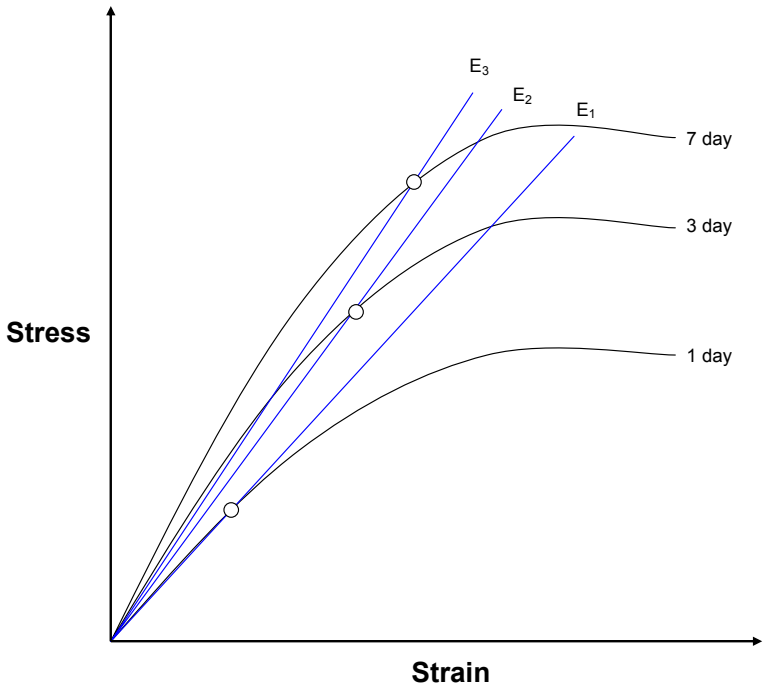

Figure 33. Measurement of elastic modulus at different ages, case 2

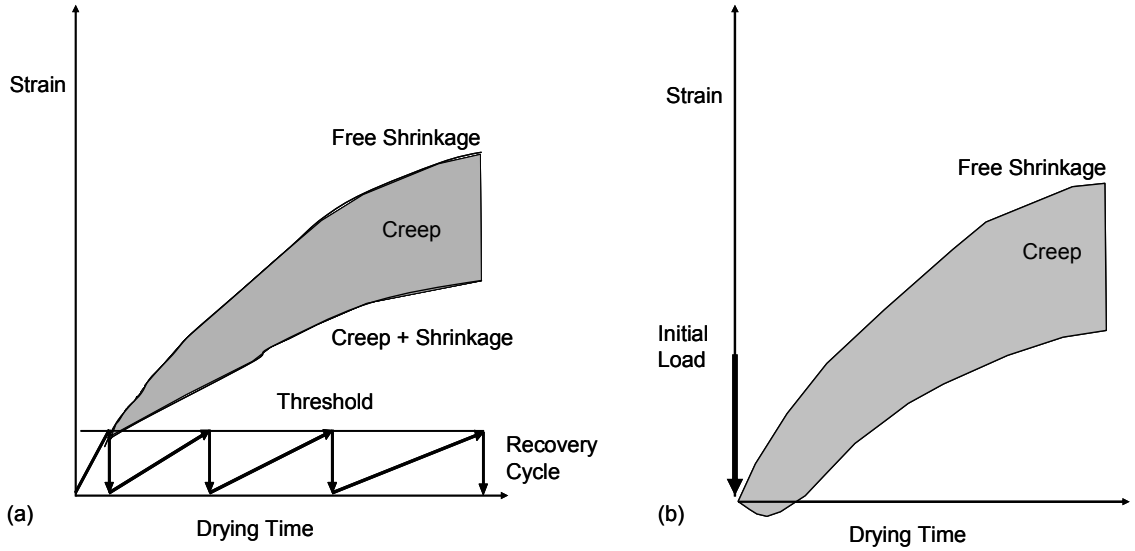

Figure 34. Schematic for determination of creep for restrained (a) and constant load test (b)

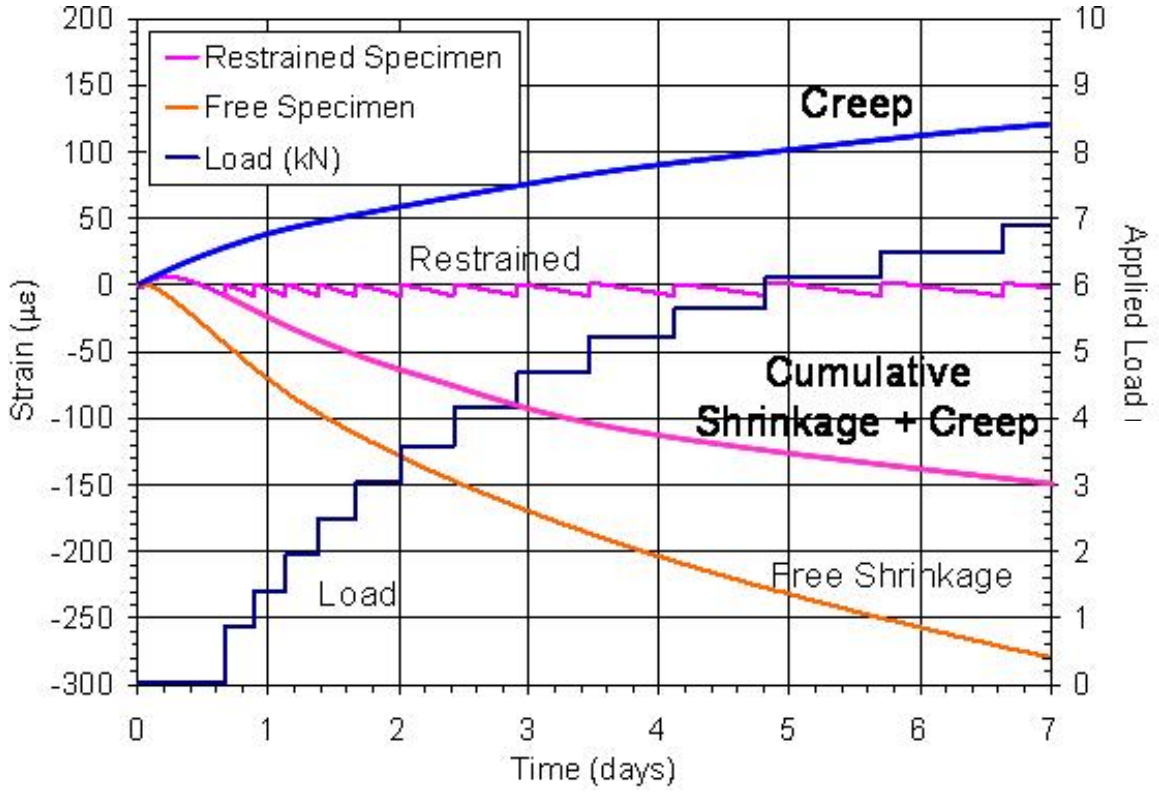

Figure 35. Typical restrained test data

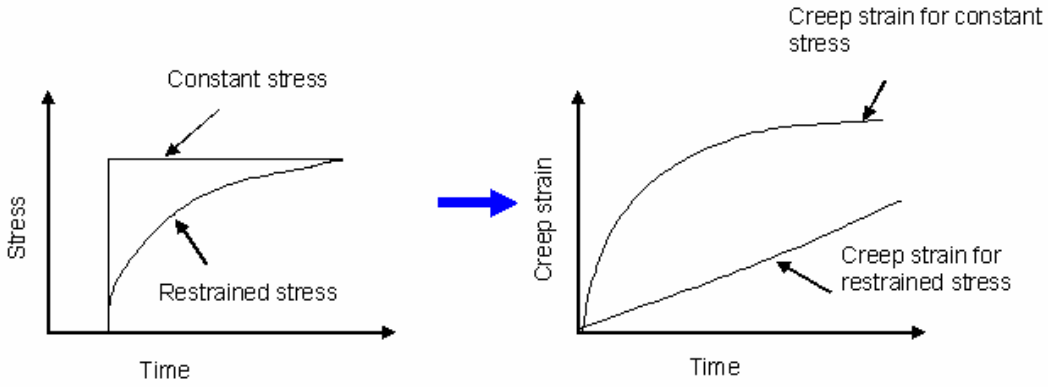

Figure 36. Creep strain measurements for constant and restrained tests

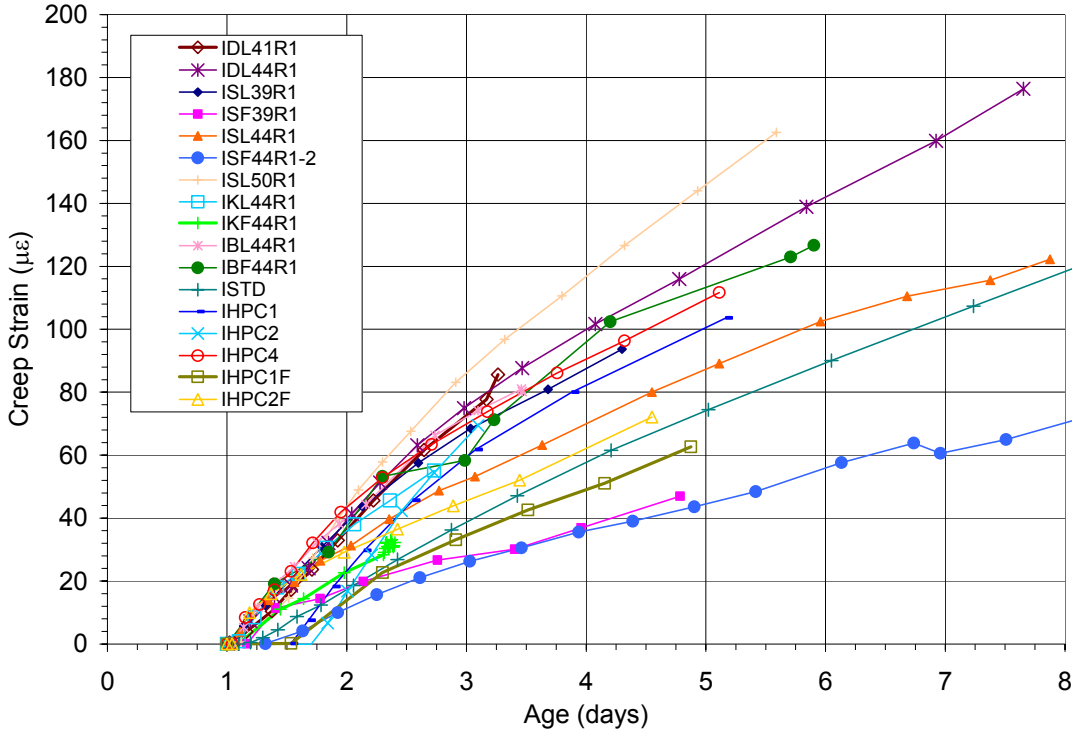

Figure 37. Tensile creep strain due to restrained shrinkage stress, all materials

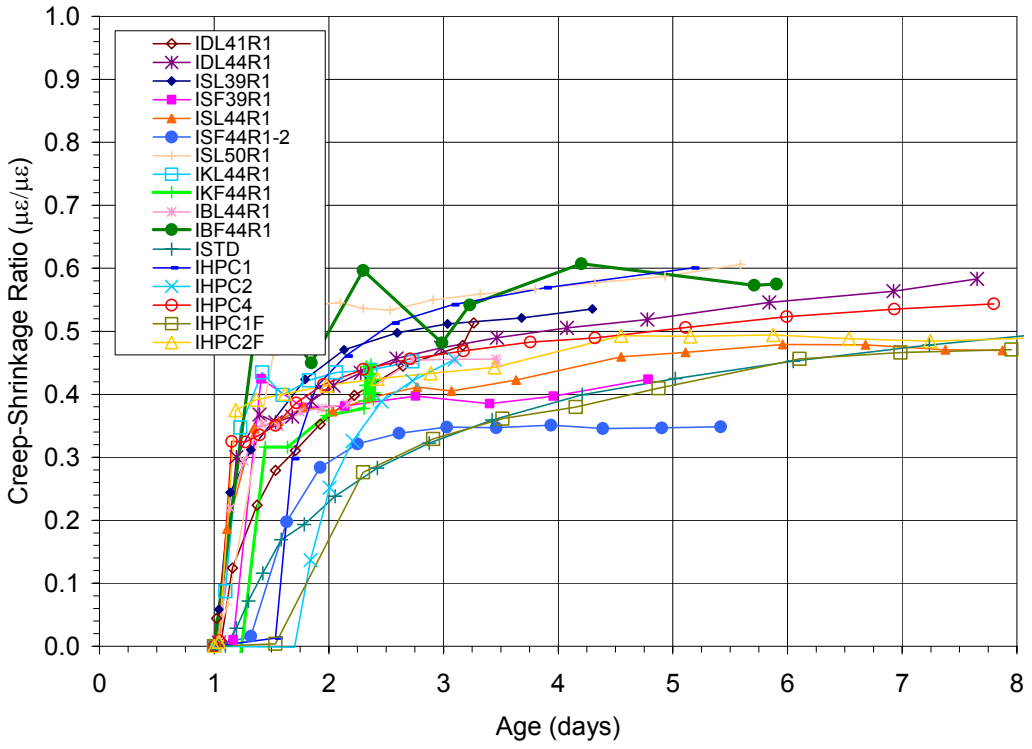

Figure 38. Tensile creep shrinkage ratio at early age, all materials

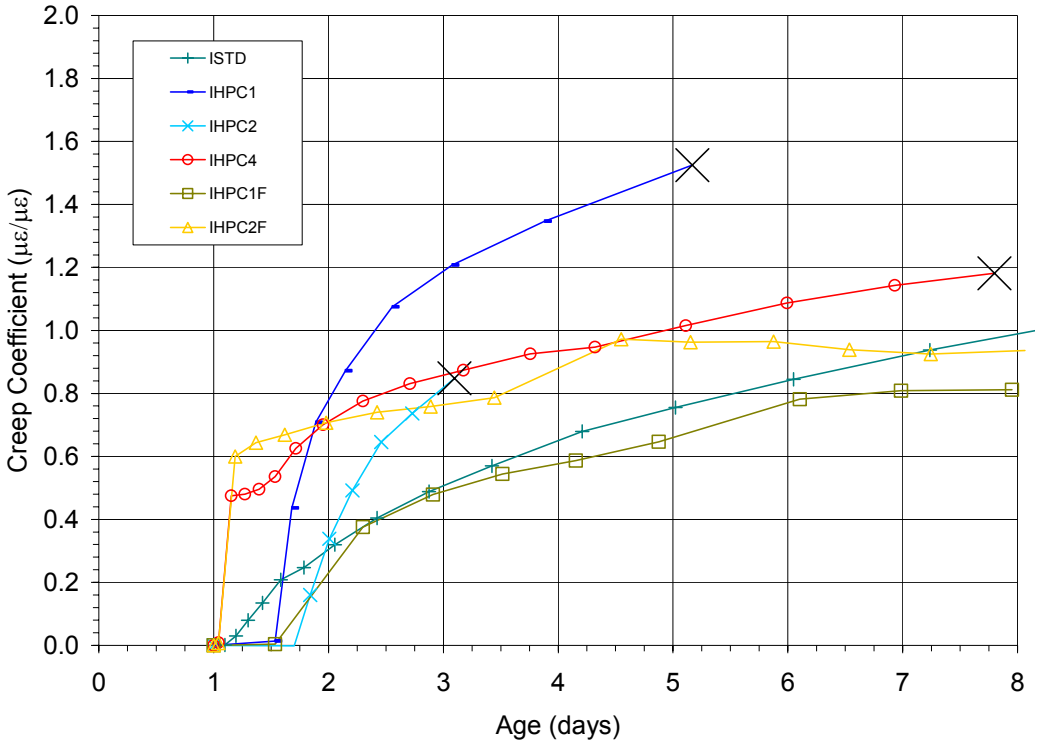

Figure 39. Tensile creep coefficient evolution, *w/c* = 0.44

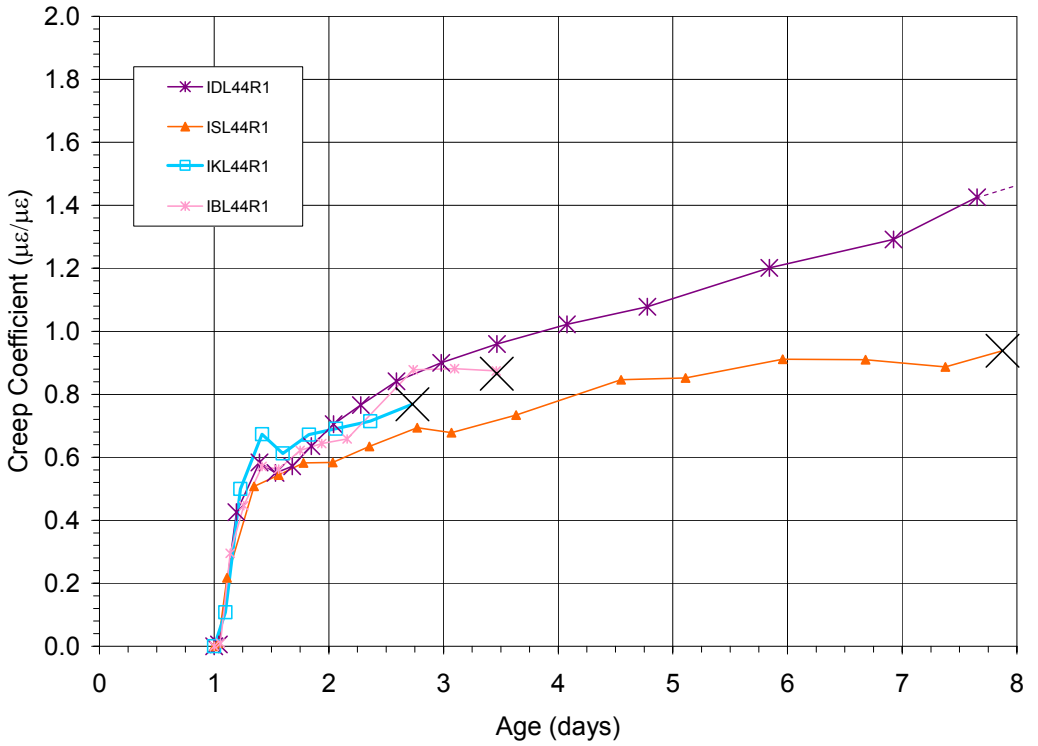

Figure 40. Tensile creep coefficient evolution, *w/c* = 0.44, laboratory materials only

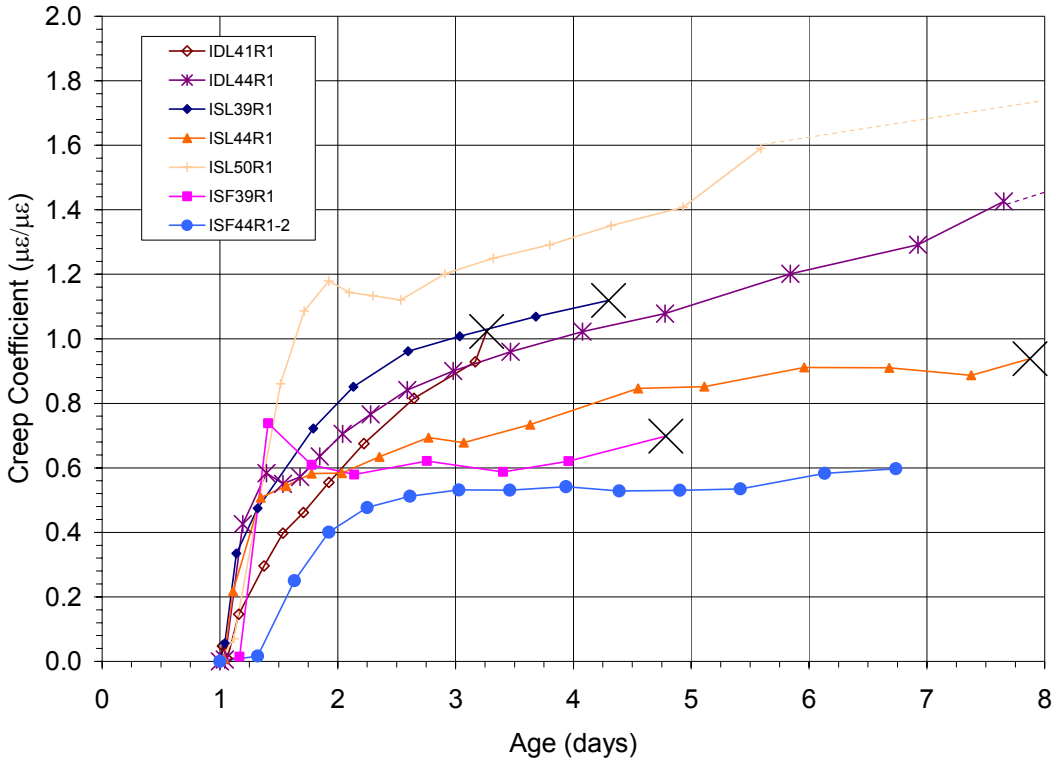

Figure 41. Tensile creep coefficient evolution, variation in *w/c*

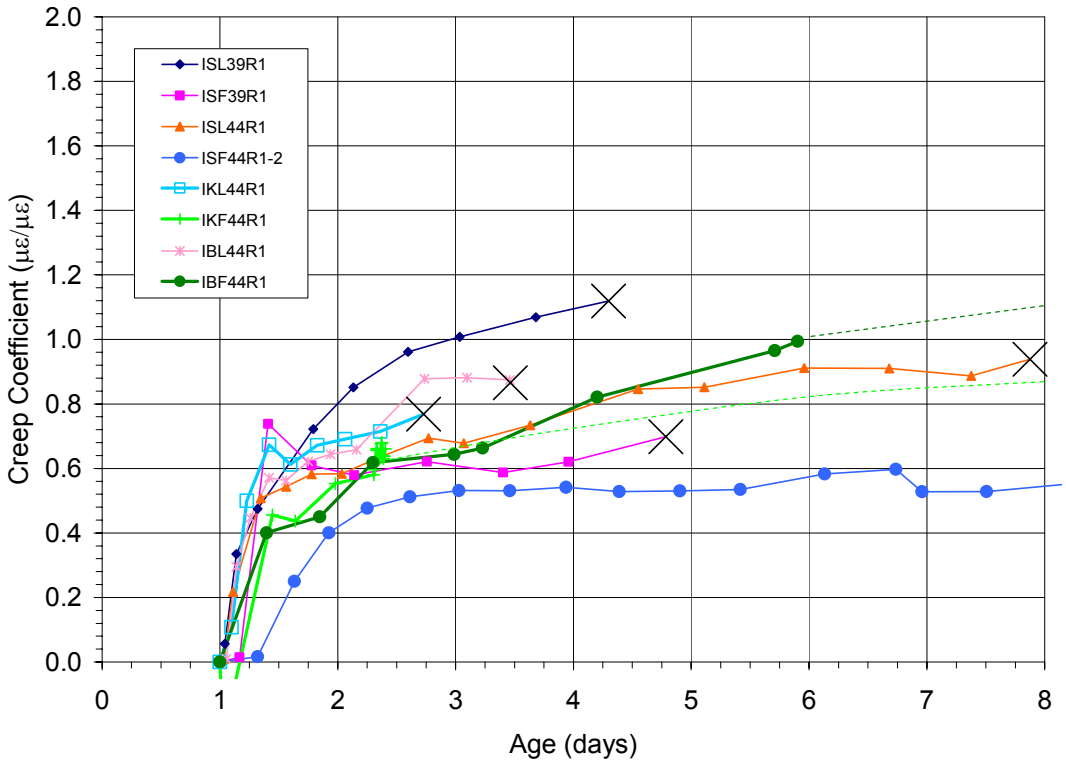

Figure 42. Tensile creep coefficient evolution, laboratory vs. field materials

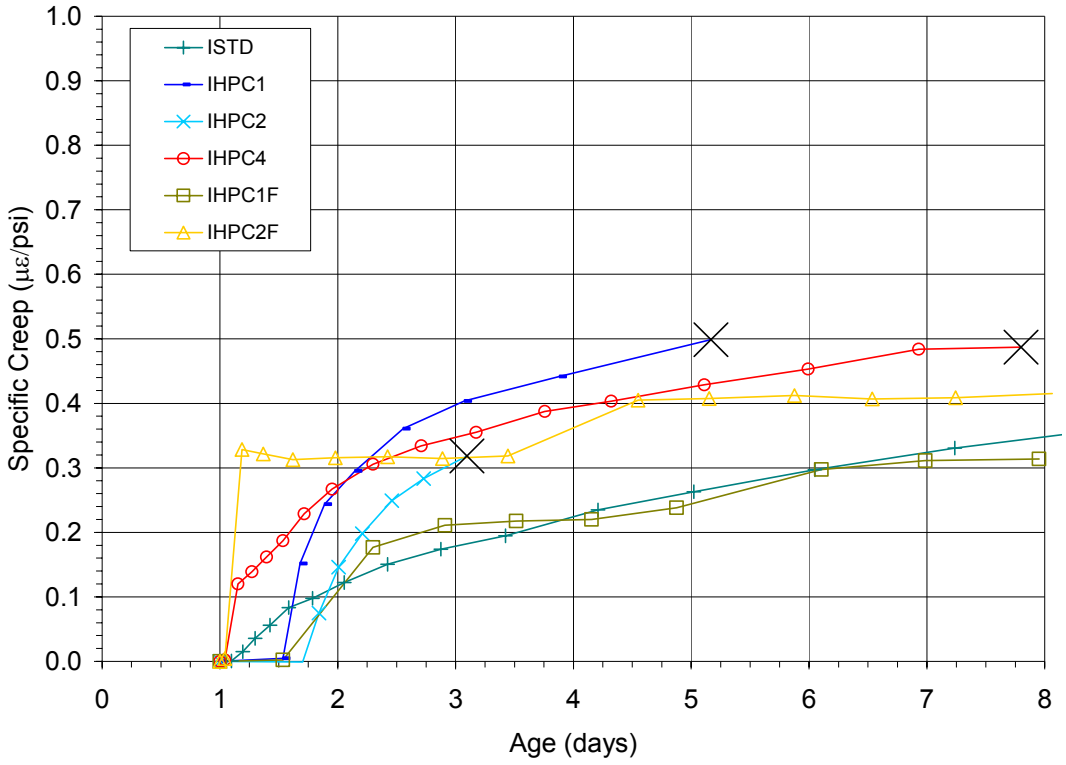

Figure 43. Tensile specific creep, *w/c* = 0.44

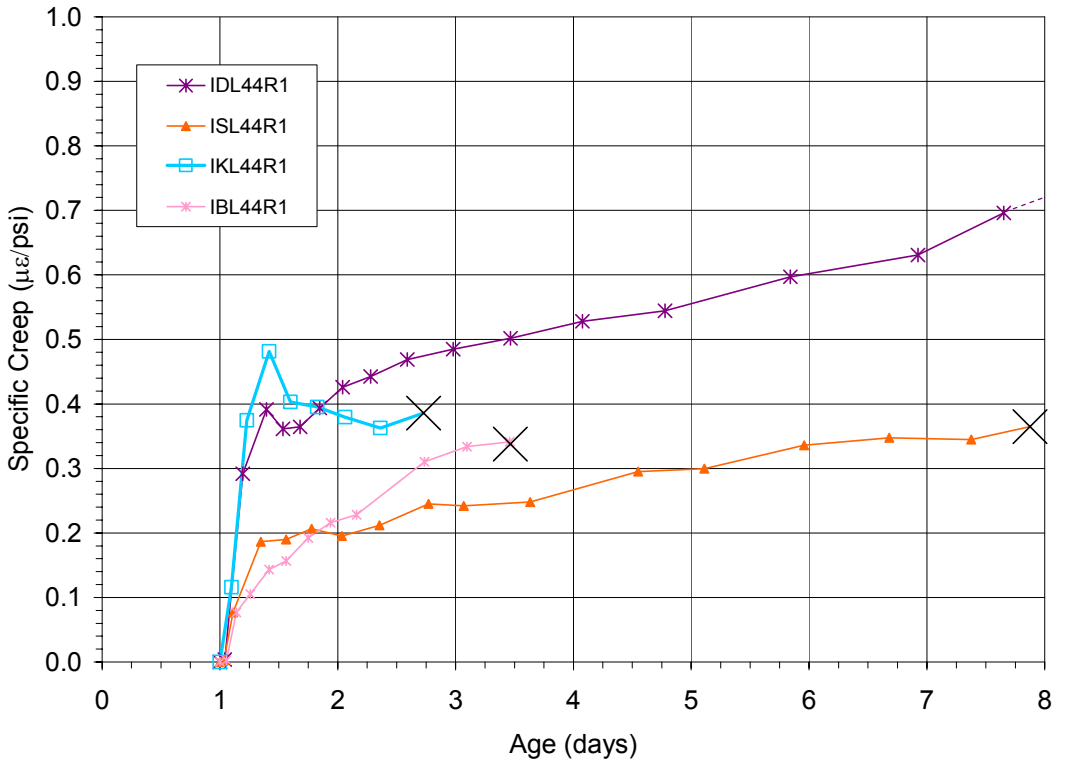

Figure 44. Tensile specific creep, *w/c* = 0.44, laboratory materials only

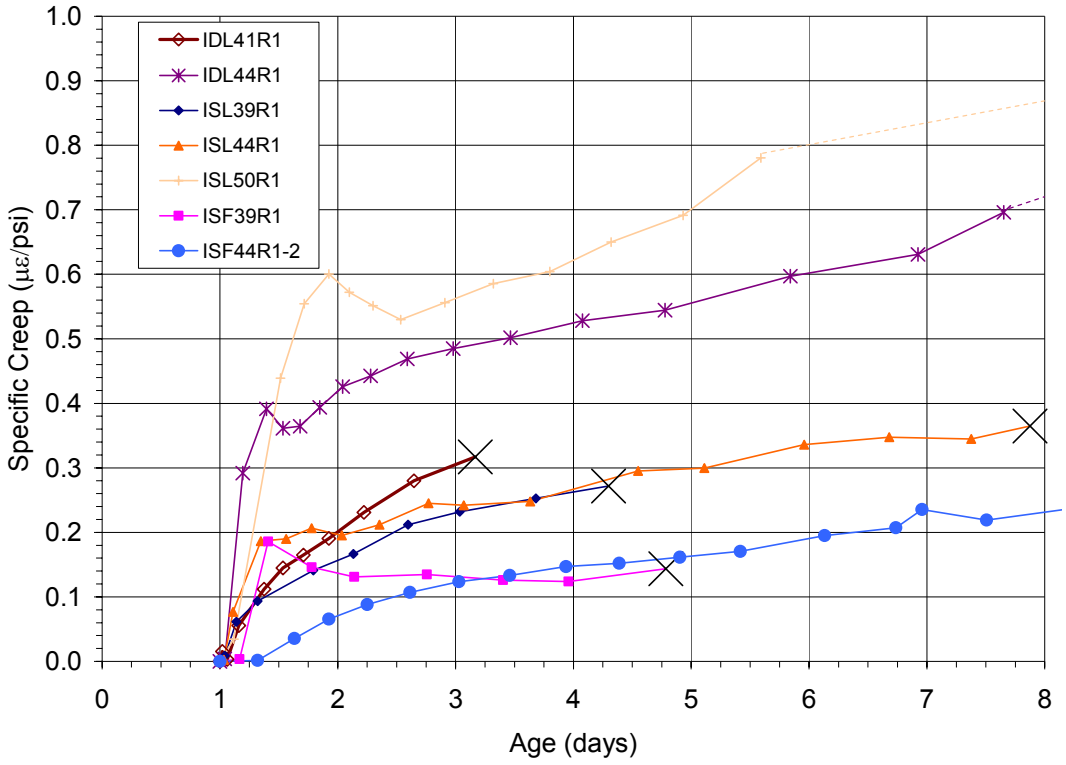

Figure 45. Tensile specific creep, variations in *w/c*

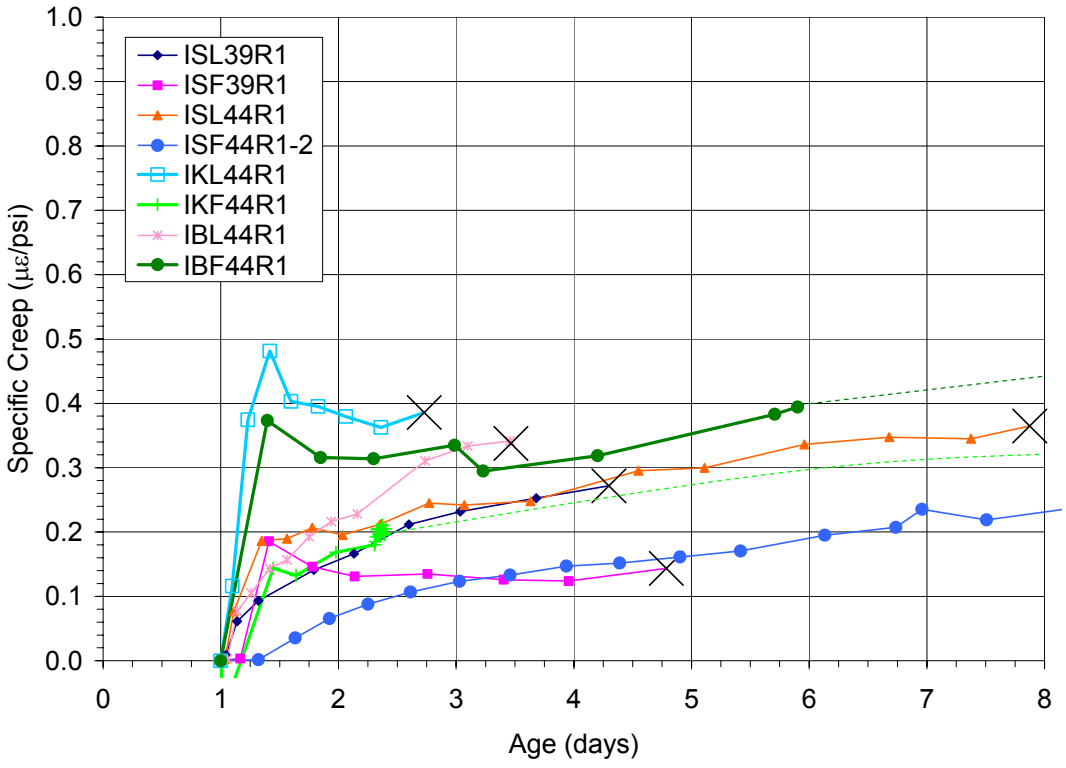

Figure 46. Tensile specific creep, laboratory vs. field materials

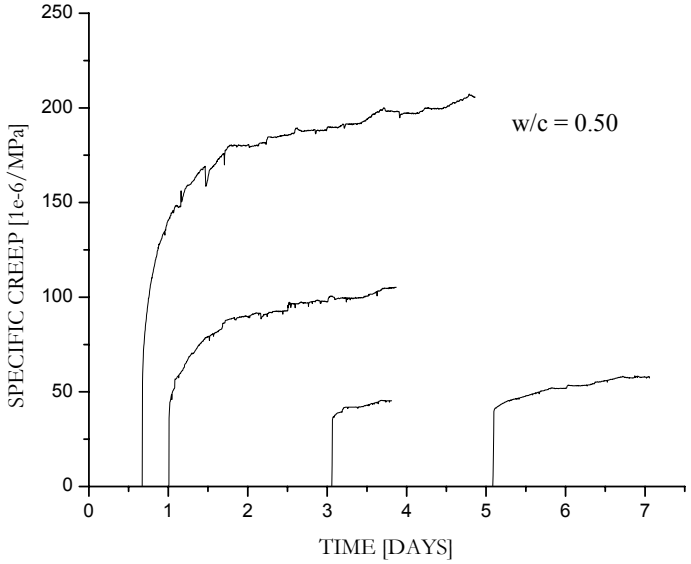

Figure 47. Effect of loading age on early age tensile creep [25]

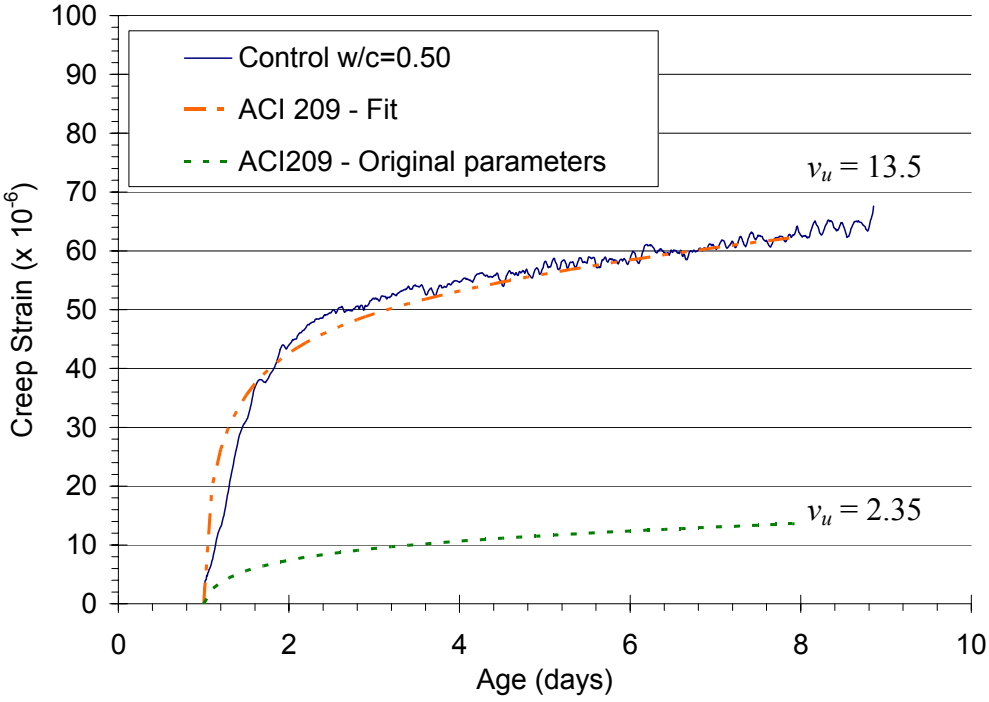

Figure 48. Prediction of creep strain with ACI 209 equation and different values for v_u

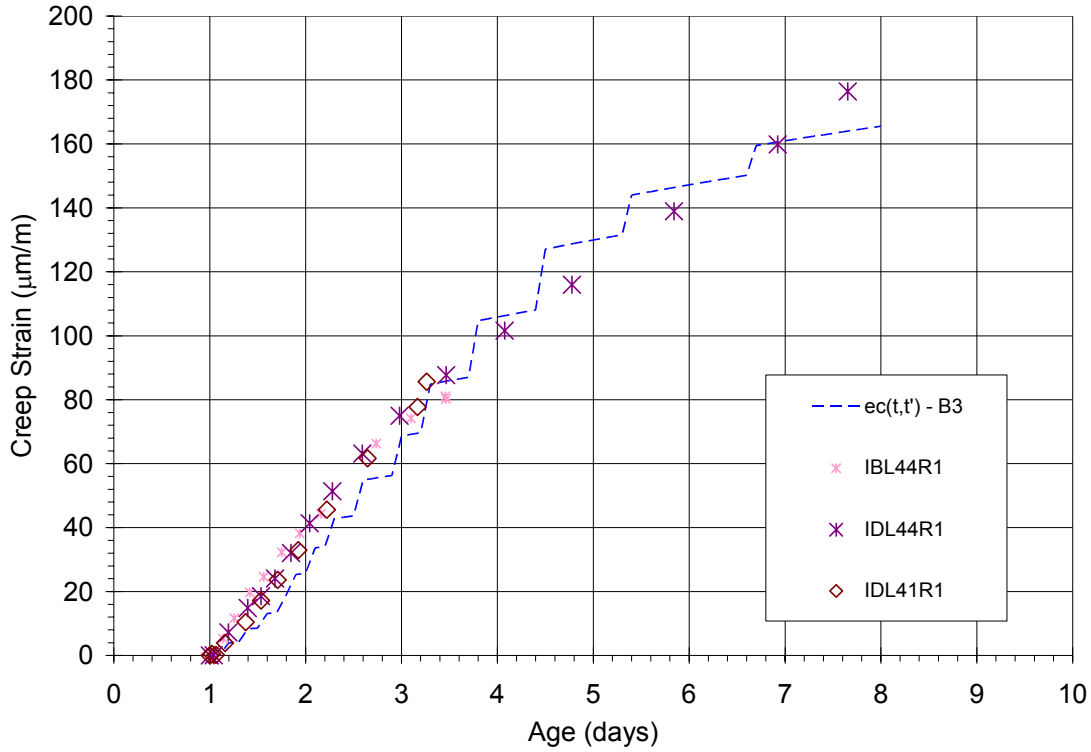

Figure 49. Modeling results for early age restrained tensile creep

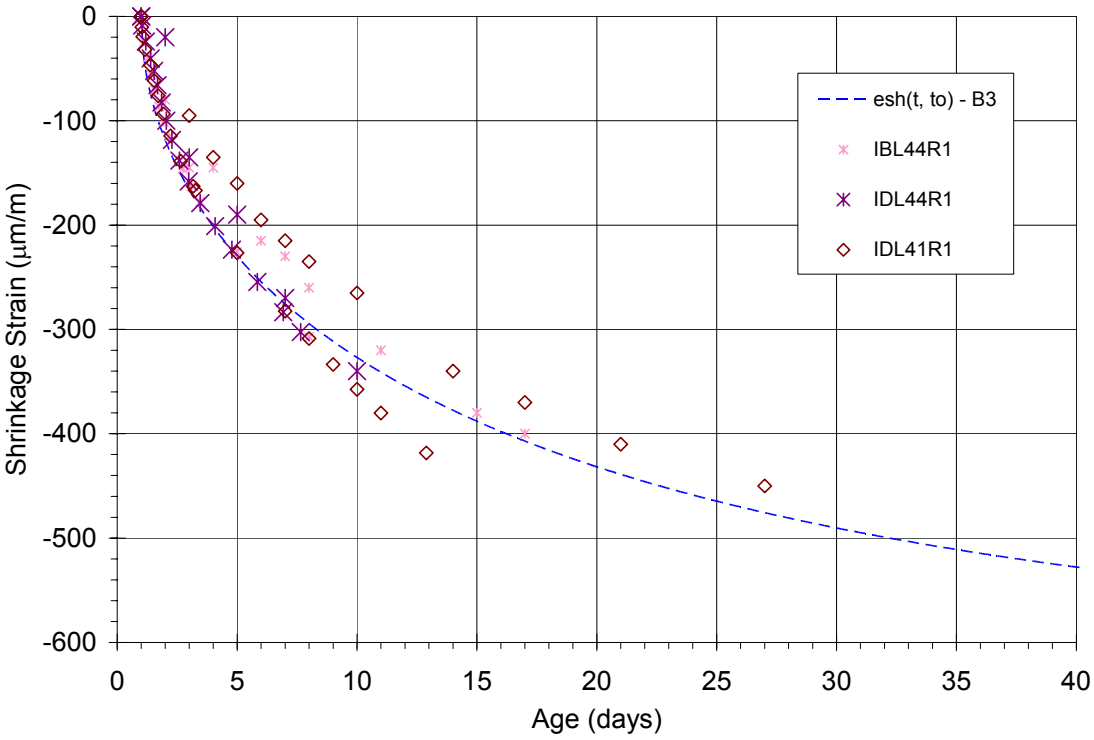

Figure 50. Modeling results for early age unrestrained shrinkage

6. RESTRAINED CONCRETE RING TESTING

6.1 Introduction

Concrete structures are susceptible to cracking caused by drying shrinkage, especially when they have large exposed surfaces, such as slabs and bridge decks. When drying shrinkage is restrained by structural boundaries, residual stresses are imposed on the concrete and may cause cracking. This phenomenon has been observed in bridge decks at fairly early ages [1-6]. It would be valuable to develop a testing method that could determine the susceptibility of a particular concrete mixture to drying shrinkage and associated cracking. The American Association for State Highway and Transportation Officials (AASHTO) has proposed a ring test method (AASHTO PP34-99) that could indirectly measure the drying shrinkage of concrete and qualitatively assess the capability of the material by the time when cracking would occur. This testing method is simple in design and data acquisition, which lends it to be advantageous for field and laboratory applications. This chapter of the report will describe the laboratory program conducted with the ring test and the provided IDOT bridge deck mix designs. However, this chapter can also serve as a manual for interpreting data and approximating the stress distribution in the concrete for future mixture designs.

The work performed by previous researchers has been applied in developing the analysis used to approximate the stresses in the concrete ring in the ring test. The experimental program carried out at the University of Illinois at Urbana-Champaign (UIUC) is described in detail. A method for interpreting the data collected and using that data to determine the stresses in the concrete is also outlined. The results from the tests done on the IDOT bridge deck mixtures are included with a discussion comparing the results and offering assertions to explain the observed behavior. Finally, a model based on the free shrinkage and tensile strength of the concrete and the measured strains of the ring test is proposed to determine the stresses that develop because of

drying in the concrete ring. This model can be used to determine the acceptance criterion of future, proposed mixture designs.

6.2 Literature Review

Concrete structures that have a low volume to surface area ratio are susceptible to drying shrinkage cracking. This cracking in itself is undesirable, but also allows for the ingress of aggressive agents into the concrete material that can lead to durability problems. When the use of HPC became more prevalent, it was observed that the cracking did not disappear even though lower *w/c* ratios and water contents were being utilized. These observations spurred researchers to investigate the affects of material constituents and structural constraints on shrinkage behavior and the cracking that may follow.

Different tests were developed to measure the shrinkage of concrete. The most common and easiest to implement is to measure the free shrinkage of standardized prisms. This type of test can measure the shrinkage behavior of the material, but does not explain the cause for cracking. Concrete structures present boundary conditions and reinforcement that resist the shrinkage of concrete and impose a "residual stress" on the material. The addition of the residual stress to the stress in the concrete caused by drying can exceed the capabilities of the material and cause cracking. Researchers have tried to capture this behavior by developing testing methods that could restrain drying shrinkage. Two predominant types of tests were developed; uniaxial and ring setups.

Ring tests are able to evaluate the effects of material composition and time dependent properties that affect the magnitude and rate of shrinkage. This test also introduces a boundary that resists the shrinkage of the concrete and imposes a residual stress in the specimen. Figure 51 is a diagram that shows the general setup for the ring test. A concrete ring is cast around a

hollow steel ring and shrinkage strains are measured by strain gages on the inner steel surface or by comparators measuring radial displacement.

6.2.1 Materials

Drying shrinkage is a product of concrete losing moisture to the environment as the material equilibrates with the relative humidity of the surroundings. The mechanisms by which that moisture moves vary at different relative humidities within the material and are affected by material composition [7]. Pozzolans and high-range water reducers are the most common admixtures used to achieve HPC and are believed to affect the moisture transport associated with drying shrinkage [8]. Various researchers used the test to compare the shrinkage behavior and cracking tendency of HPC to normal strength concrete [1,8-18]. Generally, HPC has shown to be more susceptible to shrinkage cracking than normal strength concrete [1,18,19]. There are some conflicting arguments among researchers as to how different admixtures used in HPC affect shrinkage. However, these discrepancies could be related to other testing parameters in the studies that also varied and could affect the drying shrinkage of the concrete [13,18]. Ring tests are also used to test the efficacy of admixtures and fibers in reducing shrinkage and associated cracking. Numerous tests have been conducted to measure the reduction in the magnitude and rate of shrinkage that can be achieved by using shrinkage-reducing admixtures [11,19,20,21,22,23]. The ring test is also used to examine how well fiber-reinforced concrete can arrest shrinkage cracks [1,5,9,24]. Researchers have shown that the shrinkage reducing admixtures and fibers reduced the magnitude of shrinkage and the occurrence of shrinkage cracking.

6.2.2 Variations in Test Setup

A quick examination of the literature will show many variations of the ring test. Reasons for these differences are as numerous as the variations themselves. Availability of supply materials can determine the testing configuration. The desired end result may dictate a preferred geometry or drying gradient. The analysis and modeling of these tests can be simplified if the geometry and drying gradient are altered. Some researchers have looked at the affect of altering the geometry to explore the size effect of concrete and the degree of restraint provided by the steel ring [1, 25]. AASHTO PP34-99 proposes the use of a ½" thickness ring. A standardized testing configuration makes comparisons between published studies more direct and useful.

The geometry of the test setup is generally altered by a change in the concrete or steel radii and/or the height of the system. Changing the thickness of the concrete would alter the rate of shrinkage and occurrence of cracking. If the concrete ring thickness is reduced, then the internal relative humidity will equilibrate with the environment more quickly and the time to cracking is reduced [26,27,28]. The thickness of the steel determines the degree of restraint provided and the amount of stress relaxation (creep) that the specimen will feel. As the steel thickness increases, the degree of restraint and relaxation will also increase [25]. Modifying the height of the specimen is only advantageous when the drying occurs from the top and bottom of the specimen rather than through the outside surface. If the specimen is dried from the top and bottom it will equilibrate more quickly (two parallel surfaces exposed to drying) and there will be no drying gradient in the radial direction of the specimen [25,28]. Reducing the height of the system will decrease the distance between the two parallel drying surfaces. This is advantageous for a researcher to decrease the amount of time needed to complete a test. The calculations for the actual stress distribution in the concrete specimen are simplified when there is no longer a drying gradient in the radial direction and only the residual stress need to be considered. The

manner in which the restrained shrinkage data is obtained can also vary. Strain gages can be applied to the inner steel surface and measure the strains applied to the steel by the concrete as it shrinks. The other method is to cast studs into the concrete and measure the radial displacement between the studs. Both methods are correct and only alter the approach used to solve for the residual stress.

The degree of restraint provided by the steel ring has not been given an appropriate amount of attention in the research community given the purpose of this test is to observe the effects of restrained drying shrinkage. Varying the steel thickness would demonstrate the effect the degree of restraint has on the magnitude of the residual stress and the time to cracking seen in the concrete ring.

6.2.3 Calculating Stress Distributions

The literature includes many studies that present methods by which to calculate the residual stress imposed on the concrete specimen. Some of these investigations then use fracture mechanics to predict the time to cracking based on the calculated residual stress [27,28]. Other researchers have used boundary element methods to predict the width of cracks [1]. For brevity, this discussion will focus on the analytical methods that pertain to the ring setup used in this investigation.

For the case where drying occurs from the sides, two different stresses are being applied to the concrete specimen. There is a drying stress caused by the loss of moisture and the residual stress imposed on the concrete due to the restraint provided by the steel ring. When the two stresses are combined the actual state of stress through the cross-section of the concrete can be determined. The residual stress field has been given a great deal of attention, and sufficient methods have been developed to solve for and model the residual stress. A solution for the

drying stress field has received less attention. Some researchers avoid the need to model the drying gradient by utilizing top and bottom drying and thereby create a vertical gradient, not a radial gradient. However, most ring tests (including the proposed AASHTO standard) allow drying from the ring perimeter, and thus a radial drying gradient must be modeled to accurately estimate the full stress field. The methods used to calculate the residual stress by other researchers will be presented here. The drying stress calculated for the tests in this investigation will be addressed in the analysis and modeling sections of this chapter as well as in 7.1.

The simplest approach to solve for the residual stress distribution is to consider the steel ring and concrete ring separately. During the test, the concrete is undergoing drying shrinkage and that shrinkage is applying a pressure to the steel ring. The pressure applied to the steel ring is directly related to the strain or radial displacement measurements recorded during the test. Lame's solution for thick–walled, cylindrical pressure vessels can be used to solve for the pressure that would cause the measured strain or radial displacements in the steel and use that pressure to determine the residual stress distribution in the concrete [1,6,25,29,30]. This method is used in the analysis of the tests conducted in this investigation and will be discussed in greater detail in the analysis section of this chapter.

Several researchers have proposed models to predict the residual stress distribution based on the free shrinkage of the material in hopes that these models could replace the ring test and/or predict the behavior of full scale structures given a certain geometry and degree of restraint. These models incorporate the free shrinkage strains of an unrestrained specimen (with equal volume to surface area ratio as the ring setup) and empirical relationships for strength gain, creep, and the modulus of elasticity in an effort to predict the residual stress [1,5,25,27]. The empirical relationships come from standardized material tests and must be performed each time a

model is developed for a new material. The equations in these models are not universal and must be altered for each different material tested.

The analytical solutions presented in the literature do not accurately capture the effect of the degree of the restraint of the system [1,25,5]. In most cases, it is considered that the steel ring provides 100% restraint [1,25]. If this were the case, all of the concrete shrinkage would be restrained and no strains would be measured in the steel ring. Other solutions try to capture the relative stiffness of the concrete ring and steel ring by comparing the differing moduli [1]. However, the modulus of each material is not sufficient. The geometry (thickness of the ring and ring) needs to also be considered to truly consider the relative stiffness.

6.3 Experimental

6.3.1 Formwork

The test set up was comprised of the following materials:

- Teflon and plywood base (20" x 20" x ¾")
- Steel Rings (6" tall, varying thicknesses: $^{3}/_{8}$", ½", and 1")
- Coated Cardboard Rings (6" tall, ¼" thickness, 18" inside diameter)
- Wooden Dowels (3" tall, ½" diameter)
- Plywood anchors (2" x 2" x ¾")
- Plastic Wrap
- Foil tape

Figure 51 and Figure 52 are diagrams of the testing setup. The steel and cardboard rings are secured to the base by the wooden dowels and plywood anchors.

6.3.2 Data Acquisition

The data acquisition system used at UIUC consists of strain conditioning units and a computer operating LabView. Strain conditioning units were used to balance each individual strain gage and then transmit the data signal to the computer. The software program, LabView, controlled the rate of acquiring strain data and stored the data to a permanent file. Figure 53 is a photograph of the data acquisition system at UIUC.

6.3.3 Testing Procedure

The raw materials were combined using the mixing procedure provided by IDOT (Chapter 4). The concrete was then cast in the forms in three equal lifts and rodded to sufficient compaction. The setup was then covered in plastic wrap and allowed to cure. The forms and plastic wrap were removed at 24 hours (+/- 1 hour) and the top surface was sealed with foil tape. The environmental conditions for the specimens were 23^{o}C (+/- 2^{o}C) and a relative humidity of 50% (+/- 4%). Strain measurements were taken up to 7 days of drying. Data acquisition began at the time of casting or the onset of drying. Figure 54 shows a ring during testing.

6.4 Analysis

This section of the chapter addresses how the measured data was used to calculate an approximate stress distribution in the concrete ring. This analysis should only be used to compare results from rings with the same steel ring thickness. A brief review of the test and the processes that occur within the specimen during the test outlines the analysis of the measured data. The concrete was cast around a steel ring that has four, equidistant strain gages attached to the inner steel surface at mid-height. The concrete was allowed to cure under a plastic cover for 24 hours and then is demolded. The top surface of the concrete ring was covered with foil tape

at the time of demolding. Data acquisition began as soon as the specimens are demolded and the foil tape was secured.

As the concrete specimen experiences drying shrinkage, two different stress distributions are developing within the specimen. The first is the drying stress caused by the loss of moisture from the concrete to the surrounding environment. The second stress is the residual stress that is imposed on the concrete specimen by the steel ring which is resisting the drying shrinkage of the concrete. The calculations for these two stresses is presented below. They were superimposed to give the actual stress distribution across the thickness of the concrete ring. Figure 55 shows a general representation of these stress distributions.

6.4.1 Drying Stress Distribution

The theory and calculations for the drying stress distribution are described in detail in 7.1, therefore, only a brief overview will be presented here. Drying shrinkage occurs as the relative humidity within the concrete equilibrates with the relative humidity of the environment by losing moisture to the surroundings. Therefore, relative humidity measurements are related to drying shrinkage strains and thus the stress caused by drying. Relative humidity measurements were taken at varying depths in a concrete prism exposed to drying. The relative humidity data was used in the Kelvin-Laplace equation to calculate a hydrostatic compressive stress in the pore fluid of the concrete. Equation 1 is the Kelvin – Laplace Equation

$$p = \frac{\ln(RH)RT}{v} \tag{1}$$

where, p is the hydrostatic compressive stress in the pore fluid, RH is the internal relative humidity, R is the universal gas constant, T is the temperature (Kelvins), and v is the molar volume of water. This stress is then converted into a shrinkage strain using Equation 2

$$\varepsilon_{sh} = \frac{Sp}{3}\left(\frac{1}{k} - \frac{1}{k_o}\right)\frac{V_{paste}}{V_{concrete}} \tag{2}$$

where, ε_{sh} is the potential free shrinkage occurring at the microscale, S is the degree of saturation within the concrete, p is the hydrostatic compressive stress in the pore fluid, k is the elastic modulus for the paste, k_o is the elastic modulus of the solid paste material, V_{paste} and $V_{concrete}$ are the volumes of the paste and concrete respectively. This equation was first developed by Mackenzie and then later modified by Bentz [31,32]. The drying stress is then calculated as

$$\sigma_{drying} = E_{concrete}\left(\varepsilon_t - \varepsilon_{sh}\right) \tag{3}$$

where, σ_{drying} is the drying stress, $E_{concrete}$ is the modulus of concrete calculated from ACI equations, ε_t is the macroscale free shrinkage measured in a specimen, and ε_{sh} is the potential free shrinkage occurring at the microscale. Figure 56 is a flow chart summarizing these calculations.

6.4.2 Residual Stress Distribution

The residual stress distribution was solved by applying Lame's solution for thick-walled, cylindrical pressure vessels [29,30]. The solution assumes that the material is homogeneous, linear elastic. These assumptions are reasonable for this investigation because the early age properties of the material are being explored and stress relaxation is considered with the estimated creep strain. As the concrete undergoes drying shrinkage a drying stress develops within the material. In turn, as the concrete shrinks against the steel ring, some of that shrinkage is restrained and imposed back onto the concrete as a residual stress. It is important to appropriately identify the associated strains for all of these phenomena in order to correctly calculate the residual stress in the concrete.

Figure 57 is a diagram showing the different strains associated with the uniaxial and ring tests. The uniaxial test represents a fully restrained test and the ring tests represent partially restrained tests. For both types of tests, the concrete experiences a shrinkage strain, ε_{SH}, this is then relaxed to some extent by creep, ε_{cr}. For the case of the uniaxial test, the remaining strain is the elastic component in the concrete, ε_{el}. There are two components to the elastic strain in the ring test. The first is the strain in the steel that occurs as the concrete is allowed to shrink. This is the measured strain from the gages on the inner steel surface and is denoted as ε_{ring}. The remaining elastic component is the strain imposed on the concrete as the steel resists the shrinkage of the concrete and is denoted as ε_{el}. This is the strain to calculate a residual stress in the concrete caused by the restraint of the steel ring.

ε_{sh} was determined by measuring the free shrinkage of prisms with the same volume to surface area ratio as the concrete ring in the ring test. Prisms of the same volume to surface area ratio as the concrete ring were shown to be equivalent to free shrinkage rings by Grybowski and Shah [5]. ε_{cr} was estimated from experimental findings found with the uniaxial test. The amount of creep to occur was dependent upon material composition as well as the degree of restraint provided by a structure. A large database of cementitious materials tested at UIUC has been created, and with that database it is seen that with time the degree of restraint has a dominant effect on the amount of creep occurring in a test specimen. In the case of the uniaxial test, the creep to shrinkage stress ratio averages 0.5 for a wide variety of materials. The uniaxial test (restrained test mode) is considered to provide 100% restraint as it allows the concrete to shrink to a very low threshold and then pulls the specimen back to the original position by a hydraulic actuator. A similar creep to shrinkage stress ratio (relaxation factor) could be applied to the ring tests for a given degree of restraint. The difficulty is in determining how to appropriately determine the degree of restraint provided by the ring tests in comparison to the uniaxial test and

a free shrinkage specimen (0% restraint). Several different equations are presented in the literature. One method for determining the degree of restraint is by calculating the ratio of the modulus and area of the steel ring by the combined moduli and area of the concrete and steel rings [6]. This is shown as

$$R = \frac{E_s A_s}{E_s A_s + E_c A_c}, \tag{4}$$

where, R is the degree of restraint provided by the steel ring, E_s and E_c are the elastic modulus for steel and concrete respectively, and A_s and A_c are the cross-sectional areas of the steel and concrete. This equation works well when comparing different ring tests, but makes a difficult comparison to the uniaxial test. Another restraint calculation looks at the ratio of free shrinkage displacements to restrained shrinkage displacements as shown as [25].

$$\psi = \frac{U_{SH} - U_s}{U_{SH}} \times 100\% \tag{5}$$

where, Ψ is the degree of restraint provided by the steel ring, U_{SH} is the displacement measured from a free shrinkage specimen, and U_S is the displacement measured on the outside of the steel ring. This type of relationship is better suited to drawing comparisons between different restrained shrinkage tests. A similar equation has been developed to determine the degree of restraint for the ring setups as compared to the uniaxial and free shrinkage prisms such that

$$R = 100 - \left(\frac{\varepsilon_s}{\varepsilon_{SH}} \times 100 \right) \tag{6}$$

where, R is the degree of restraint provided by the steel ring, ε_s is the measured steel strain, and ε_{sh} is the free shrinkage strains measured from prisms of a similar volume to surface area ratio. Equation 6 was applied to the ring configurations used in this investigation. Once the degree of

restraint was calculated, the relaxation factor for the different ring configurations was determined by a similar relationship shown as

$$\xi = 0.5 - \left(\frac{\varepsilon_s}{\varepsilon_{SH}} \times 100 \right) \tag{7}$$

Using Equation 7 the relaxation factor is used to calculate the appropriate creep strain by

$$\varepsilon_{CR} = (1 - \xi)\varepsilon_{SH} \tag{8}$$

ε_{Ring} is taken from the strain gages adhered to the inner steel surface. The constitutive strain relationship is shown below in Equation 9 solving for ε_{el}.

$$\varepsilon_{Elastic} = (1 - \xi)\varepsilon_{SH} - \varepsilon_{Ring} \tag{9}$$

This elastic strain is associated with the residual stress on the inner surface of the concrete ring. Using Hooke's Law and ε_{el} the residual stress on the inner surface of the concrete ring can be found.

$$\sigma_{ic} = E_c \varepsilon_{Elastic} \tag{10}$$

where, σ_{ic} is the residual stress in the concrete at the inner surface, E_c is the elastic modulus found using an empirical ACI equation (ACI 8.5.1-99), where the compressive strength was measured for each material. Using σ_{ic} and Lame's solution for a thick-walled pressure vessel, the residual stress in the concrete can be found for any point along the cross-section of the ring [30,30]. σ_{ic} is composed of tangential and radial stress components. Each stress component is a function of the internal pressure on the concrete caused by the steel ring and the inner and outer radii of the concrete ring. By solving for the internal pressure, the tangential and radial stresses can be found at any point along the cross-section of the concrete ring. The tangential or hoop stress is the component of importance in this investigation and will be referred to as the residual stress calculated in this analysis. The following equations display these relationships,

$$\sigma_{ic} = \sigma_{\Theta residual} - \upsilon\sigma_{rresidual}, \tag{11}$$

$$p_i = \frac{\sigma_{ic}\left(b_c^2 - a_c^2\right)}{(1-\upsilon)a_c^2 + (1+\upsilon)b_c^2}, \tag{12}$$

$$\sigma_{residual} = \frac{a_c^2 p_i}{b_c^2 - a_c^2}\left(1 + \frac{b^2}{r^2}\right), \tag{13}$$

where $\sigma_{\theta residual}$ and $\sigma_{\rho residual}$ are the tangential and radial components of $\sigma_{ic,}$ p_i is the internal pressure applied to the concrete by the steel ring as the steel ring resists the shrinkage of the concrete, a_c and b_c are the inner and outer radii of the concrete ring, υ is Poisson's ratio of the concrete, and r is the radius at any point in the concrete thickness.

6.4.3 Actual Stress Distribution

The drying stress and residual stress can be superimposed to give the actual state of stress in the concrete. By summing the stresses at different points along the thickness of the concrete, the actual stress distribution in the concrete can be found. This relationship is

$$\sigma_{actual} = \sigma_{drying} + \sigma_{residual} \tag{14}$$

The drying stress calculated from RH measurements exhibits a very high tensile stress at the outer concrete surface that in turn gives a high actual stress at the same location when the residual and drying stresses are superimposed. Often this calculated value exceeds the measured tensile strength of the material and yet no macrocracks are visible on the specimen surface. With time the tensile stress at the inner surface of the concrete increases and will exceed the tensile strength of the concrete. It is believed that microcracking is occurring at these locations in the concrete and relaxes the high tensile stresses. [33-37]. Therefore, when calculating the actual state of stress using Equation 14, the result is limited to the tensile strength of the concrete.

6.5 Results

This section of the chapter presents the experimental results of the IDOT mixtures tested in the rings. First, the different types of results that can be generated with the ring test will be discussed. Then the results for each of the IDOT mixtures will be presented.

The first result is the relationship between the corrected, measured strain data and the specimen age. Figure 58 through Figure 62 illustrate this relationship for the various mixtures. This plot can be used as a check for faulty strain gages, measure of the ultimate measured values, and a comparison of the relative strain values for the different steel rings.

The second result to examine is the residual stress distribution across the thickness of the concrete ring for any given age of the specimen. For this investigation, the residual stress is plotted versus the thickness of the concrete ring at 3, 5, and 7 days. Figure 63 through Figure 76 illustrate these results. This result can be used to make material comparisons over time and study how the level of restraint provided by different rings will affect the magnitude of residual stresses imposed on the concrete.

The final result to examine is the actual stress distribution across the thickness of the concrete ring for any given age of the specimen. These plots are also taken at 3, 5, and 7 days. The actual stress distribution can be used to determine whether a concrete mixture is acceptable in terms of early age drying shrinkage. Figure 77 through Figure 90 display this result for the various mixtures.

6.6 Discussion

This section of the chapter will examine the results found for the various IDOT mixtures and compare the behavior seen in the rings. The relative magnitudes for the residual and actual

stresses for each mixture will be compared and explained by the differences in the material compositions.

6.6.1 Residual Stress Distribution

The magnitude of the residual stress distribution is dependent upon the degree of restraint provided by the steel rings and the magnitude and rate of drying shrinkage that the concrete undergoes. The magnitude and rate of drying shrinkage is determined by the composition of the material. The *w/c* ratio, water content, and presence of high-range water-reducers and pozzolanic materials can affect the shrinkage behavior of a material [1, 8-18].

With time, the residual stress distribution continues to increase. By examining the curves in these figures it can be seen that in general, as the *w/c* ratio and water content of the mixtures did not alter the restrained stress values. All of the calculated stress values fall within the range of experimental error because the *w/c* ratio, water contents, and pozzolanic additions do not vary greatly. By comparing the mixture compositions of equal *w/c* ratios and similar water contents, the effects of fly ash and silica fume on the residual stress distribution can be examined.

6.6.2 Actual Stress Distribution

The actual stress distribution is a summation of the residual and drying stress distributions that has been relaxed by creep and microcracking. The factors affecting the residual stress also pertain to the actual stress distribution in addition to the environmental conditions surrounding the material. In the case of this investigation, the environmental conditions were held constant, therefore, the degree of restraint and material composition are the sole parameters affecting the actual stress distribution.

Generally, the average stress across the concrete ring increases with time. These figures also show that the tensile stress on the inner concrete surface increases with time. Comparisons can not be made between the different mixtures because the results fall within the range of experimental error. Further testing should be done varying the *w/c* ratios and water contents, and the additions of the pozzolanic admixtures across a broad range to properly investigate the efficacy of these parameters on drying shrinkage.

6.6.3 Simplified Modeling

If the early age behavior of the material caused by the drying gradient is of interest a simpler approach needs to be implemented to determine the drying stress across the cross-section. The ability to calculate a drying stress from RH measurements is not always possible due to a limitation in developing a proper system to measure the internal relative humidity of concrete. A good, empirical relationship can be developed between the measured free shrinkage of the concrete to the outer drying stress that will develop when exposed to drying for the materials used in this study. Utilizing the free shrinkage data from the uniaxial test, an empirical relationship can be used to determine the drying stress in the outer concrete fiber. For the mixtures tested in this investigation, that empirical relationship is shown as

$$\sigma_{drying}(t) = -0.0315\varepsilon_{SH}^{2}(t) - 9.547 \tag{14}$$

where, ε_{sh} is the free shrinkage measured from the uniaxial test and t is the age of the specimen. This relationship was found by averaging fitted curves of plots of the outer drying stress versus the free shrinkage measured in the uniaxial. The free shrinkage from the uniaxial test can be substituted for free shrinkage measurements made with prisms that have the same volume to surface area ratio as the ring setup. These measurements will be less accurate, but within acceptable tolerances.

The curve of the stress distribution can be simulated by a fourth order polynomial curve. For the mixes tested in this investigation, the drying stress distribution is such that the outer region is under relatively high tensile stress and the inner region is under relatively low compression. The absolute magnitude of the inner drying stress is usually 20% that of the absolute magnitude of the outer drying stress. Using the inner and outer drying stress values, a polynomial can be fit to represent the drying stress distribution across the thickness of the concrete ring. This approximation can be used to calculate the actual stress distribution in the concrete ring.

The long-term restrained shrinkage behavior could be of interest and a simpler model could be used to characterize the average stress in the concrete for any ring configuration rather than carrying out the rigorous calculations discussed in 6.4. At later ages, the drying gradient is reduced considerably and the actual state of stress in the concrete can be assumed to be uniform through the cross-section. Such behavior allows for the assumption that if the stress through the concrete specimen is equal to the actual stress value calculated at the inner surface of the concrete ring. This concept could be used with a concrete mixture of known, acceptable behavior in the field to begin to determine an acceptable criterion for future test mixtures. For example, if Mixture A performed well in a recent bridge deck, then a ring test could be run with Mixture A and serve as a guideline. . If a future mixture behaves similar to Mixture A in the ring test, it would be reasonable to assume that the future mixture would perform well in an actual structure (so long as the future structure does not deviate greatly from the structure constructed with Mixture A).

6.6.4 Acceptance Criterion

The experimental scope of the tests conducted in this investigation was limited to the early age behavior of the materials. The ring test can be used to estimate the performance of a concrete mixture in terms of the tendency to develop high stress under drying conditions that lead to cracking. It has been previously mentioned that at the onset of drying, high tensile stresses develop on the outer surface of the concrete and local stresses can exceed the tensile strength of the concrete. With time, the average tensile stress distribution in the concrete ring will continue to increase. The tensile stresses at the inner surface of the concrete will also increase in tension with time. Any region of high tensile stress may initiate microcracking in the concrete. Microcracking that develops in the concrete will limit the capacity of the material to carry load. Once a region of microcracking is created, the damage is not restored even though the tensile stress may be reduced with time. Although high stresses on the outer surface of the concrete may reduce with time, the initial damage caused by the early microcracking still exists and can later contribute to the failure of the ring specimen. As microcracking extends into the concrete ring from the inner and outer boundaries, the material will no longer be able to withstand the stress caused by drying and will develop macrocracks that will lead to failure of the concrete ring. This behavior is depicted in Figure 91.

The size of the concrete core with tensile stresses below the tensile strength may be used as a failure criterion for the ring test. For example, it is reasonable to suggest that the viability of the ring is lost when greater than 20% of the ring is developed into a microcracked zone. As long as this condition does not occur within the first 30 days, the mixture will most likely perform well (in terms of drying shrinkage) in an actual structure. If over 20% of a concrete ring is dominated by microcracking before 30 days, then that material will most likely not be able to resist full- depth cracking from drying shrinkage in an actual structure.

6.7 Conclusions

Overall, it has been shown that a satisfactory approximation of the state of stress in the concrete ring can be constructed. At later ages, the rigorous stress calculations can be simplified and approximations about the average stress in the concrete can be made. This approximation can also be used to estimate the performance of the material in terms of drying shrinkage. A possible, future performance criterion based on damage from microcracking was proposed to determine the suitability of a mixture for placement in a full-scale structure.

From the types of materials tested in the ring test in this investigation, little can be said as to the effect of the *w/c* ratio and water contents can have on the stresses associated with the ring test. These parameters need to be varied more in order for those types of assertions to be made. The effects of the pozzolanic admixtures could not be adequately determined because of the little variance between the amounts used in the different mixtures. In order to determine the effect of the pozzolanic admixtures on the shrinkage behavior of the materials, a study that varies the addition of pozzolans over a broad range needs to be carried out.

REFERENCES

1. Kovler, K., Sikuler, J., Bentur, A., "Restrained Shrinkage Tests of Fibre-Reinforced Concrete Ring Specimens: Effect of Core Thermal Expansion," Materials and Structures, v 26, (1993)

2. Hossain, A., Pease, B., Weiss, J., "Quantifiying Early-Age Stress Development and Crackig in Low *w/c* Concrete Using the Restrained Ring Test with Acoustic Emission," Submitted for publication to the Transportation Research Board, July 2002

3. Li, Z., Qi, M., Li, Z., Ma, B., "Crack Width of High-Performance Concrete due to Restrained Shrinkage," Journal of Materials in Civil Engineering, v 11, (1999)

4. Shah, S., Ouyang, C., Marikunte, S., Yang, W., Becq-Giraudon, E., "A Method to Predict Shrinkage Cracking of Concrete," ACI Materials Journal, (July – August 1998)

5. Grzybowski, M., Shah, S., "Shrinkage Cracking of Fiber Reinforced Concrete," ACI Materials Journal, (March – April 1990)

6. See, H., Attiogbe, E., Miltenberger, M., "Shrinkage Cracking Characteristics of Concrete Using Ring Specimens," ACI Materials Journal, v 100, (May – June 2003)

7. Mindess, S., Young, J.F., Darwin, D., Concrete, Prentice Hall, Upper Saddle River, NJ, 2003

8. Alsayed, S., "Influence of Superplasticizer, Plasticizer, and Silica Fume on the drying shrinkage of High-Strength Concrete subjected to hot-dry field conditions," Cement and Concrete Research, v 23, no 10, (June 1998)

9. Lim, Y., Wu, H.C., Li, V., "Development of Flexural Composite Properties and Dry Shrinkage Behavior of High-Performance Fiber Reinforced Cementitious Composites at Early Ages," ACI Materials Journal, (January – February 1999)

10. Wiegrink, K., Marikunte, S., Shah, S., "Shrinkage Cracking in High Strength Concrete," ACI Materials Journal (September – October 1996)

11. Folliard, K., Berke, N. "Properties of High-Performance Concrete Containing Shrinkage – Reducing Admixture," Cement and Concrete Research, v 27, no 9, (July 1997)

12. Rao, G., "Long-term drying shrinkage of mortar-influence of silica fume and size of fine aggregate," Cement and Concrete Research, v 31, (2001)

13. Jianyong, L., Yan, Y., " A study of creep and drying shrinkage of HPC," Cement and Concrete Research, v 31, (2001)

14. Haque, M. N., " A discussion of the paper 'Influence of Superplasticizer, Plasticizer, and Silica Fume on the drying shrinkage of High-Strength Concrete subjected to hot-dry field conditions," Cement and Concrete Research, v 30, (2000)

15. Xie, Y., Liu, B., Yin, J., Zhou, S., "Optimum mix parameters of high-strength self-compacting concrete with ultrapulverized fly ash," Cement and Concrete Research, v 32, (2002)

16. Persson, B., "Eight-year exploration of shrinkage in high-performance concrete," Cement and Concrete Research, v 32, (2002)

17. Bloom, R., Bentur, A., "Free and Restrained Shrinkage of Normal and High-Strength Concretes," ACI Materials Journal, v 92, (March-April 1995).

18. Khatri, R. P., Sirivivatnanon, V., "Effect of different supplementary cementitious materials on mechanical properties of HPC," Cement and Concrete Research, v 25, no1, (1995)

19. Shah, S., Weiss, J., Yang, W., "Shrinkage Cracking – Can it be Prevented?" ACI Materials Journal, (April 1998)

20. Shah, S., Karaguler, M. Sarigaphuti, M., "Effects of Shrinkage – Reducing Admixtures on Restrained Shrinkage Cracking of Concrete," ACI Materials Journal, (May-June 1992)

21. D'Ambrosia, M., Altoubat, S. Park, C., Lange, D., "Early Age Tensile Creep and Shrinkage of Concrete with Shrinkage Reducing Admixtures, " Creep, Shrinkage, and Durability Mechanics of Concrete and other Quasi-Brittle Materials, Elsevier Science, Ltd., New York, (2001).

22. Bentz, D., Geiker, M., Hansen, K., "Shrinkage-reducing admixtures and early-age dessication in cement pastes and mortars," Cement and Concrete Research, v 31, (April 2001)

23. Gettu, R., Roncero, J., Martin, M., "Evaluation of the Performance of Concretes Incorporating a Shrinkage Reducing Chemical Admixture," Creep, Shrinkage, and Durability Mechanics of Concrete and other Quasi-Brittle Materials, Elsevier Science Ltd., New York, (2001)

24. Sarigaphuti, M., Shah, S., Vinson, K., "Shrinkage Cracking and Durability Characterisitics of Cellulose Fiber Reinforced Concrete," ACI Materials Journal, (July – August 1993).

25. Hossain, A., Weiss, J., "Assessing Residual Stress Development and Stress Relaxation in Restrained Concrete Ring Specimens," to appear in Cement and Concrete Composites.

26. Schiebl, A., Weiss, J., Shane, J., Berke, N., Mason, T., Shah, S., "Assessing the moisture profile of drying concrete using impedance spectroscopy," Concrete Science and Engineering, v 2.

27. Weiss, J., Shah, S., "Restrained shrinkage cracking: the role of shrinkage reducing admixtures and specimen geometry," Materials and Structures, v 35, (March 2002)

28. Weiss, J., Yang, W., Shah, S., "Influence of Specimen Size/Geometry on Shrinkage Cracking of Rings," Journal of Engineering Mechanics, (January 2000)

29. Harvey, J., Theory and Design of Modern Pressure Vessels, Van Nostrand Reinhold Company, New York, (1974)

30. Burgreen, D., Pressure Vessel Analysis, C.P. Press, New York, (1979).

31. MacKenzie, J., "The Elastic Constants of a Solid Containing Spherical Holes," Proc. Phys. Soc., v 63, (1950)

32. Bentz, D., Garboczi, E., Quenard, D., "Modeling drying shrinkage in reconstructed porous materials: application to porous Vycor glass," Modeling Simul. Mater. Sci. Eng., v 16, (1998)

33. Bisschop, J., Drying shrinkage microcracking in cement-based materials, DUP Science, Delft, Netherlands, (2002)

34. Bazant, Z., Raftshol, W., "Effect of Cracking in Drying and Shrinkage Specimens," Cement and Concrete Research, v 12, (1982)

35. Mihashi, H., "Microcracking and Tension-Softening Properties of Concrete," Cement and Concrete Composites, v 14, (1992)

36. Ansari, F., "Mechanism of Microcrack Formation in Concrete," ACI Materials Journal, v 86, (September – October 1989)

37. Hori, H., Ichinomiya, T., "Observation of fracture process zone by laser speckle technique and governing mechanism in fracture of concrete," International Journal of Fracture, v 51, (1991)

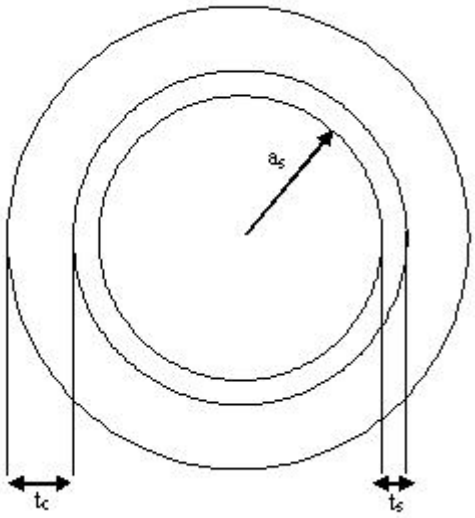

- a_s ~ internal radius of the steel ring
- t_s ~ thickness of the steel ring, t_c ~ thickness of the concrete ring
- h ~ height of the steel concrete rings

Figure 51. General setup for the ring test (plan view)

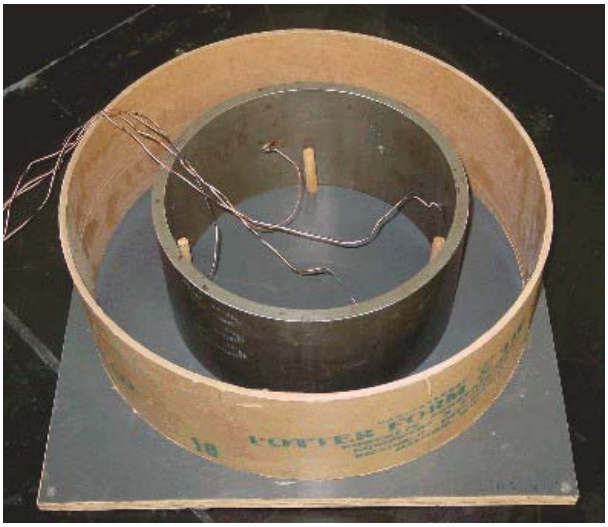

Figure 52. Formwork for ring test

Figure 53. Data acquisition and computer system

Figure 54. A ring test in progress at UIUC

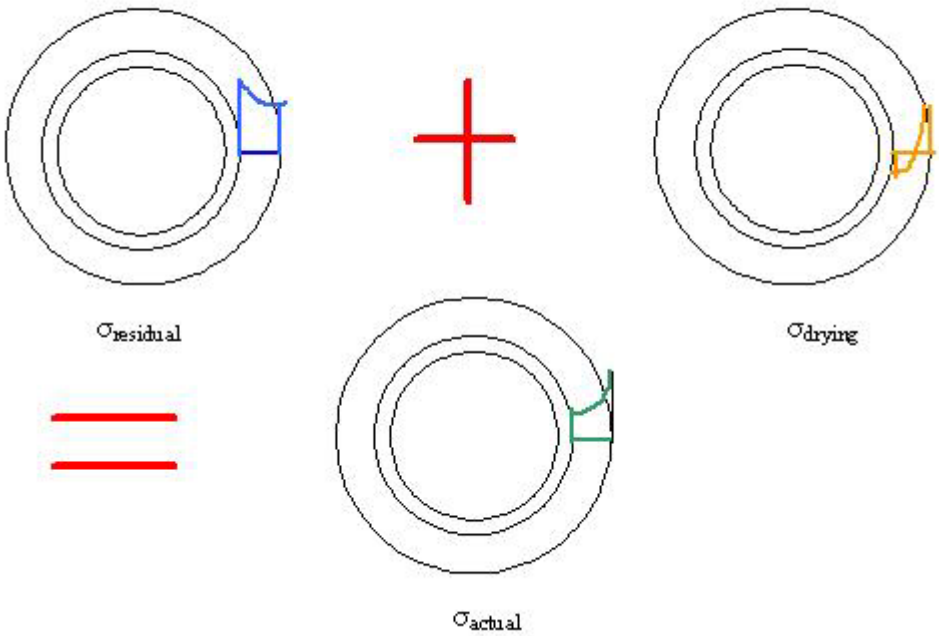

Figure 55. Idealized representation of stress distributions in the concrete ring

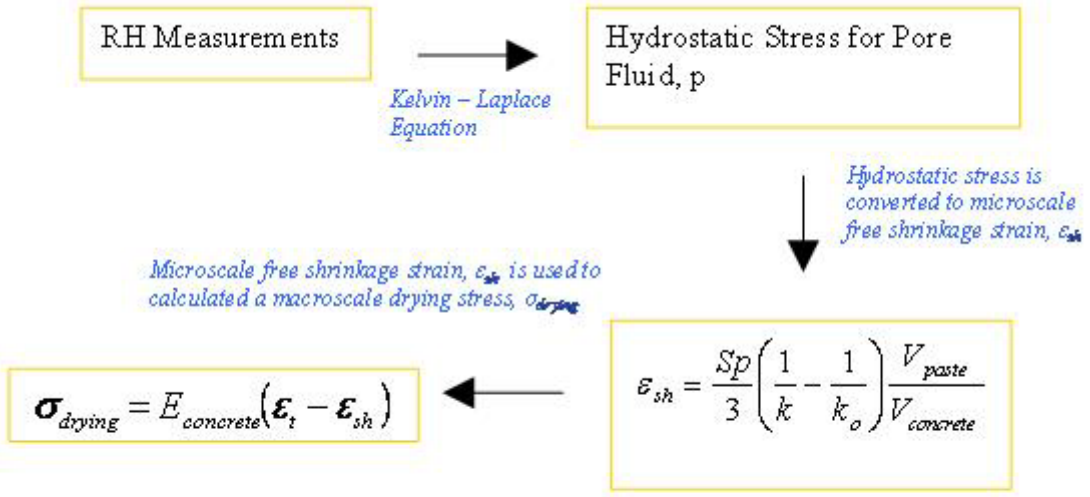

Figure 56. Flow chart summarizing the calculations for the drying stresses

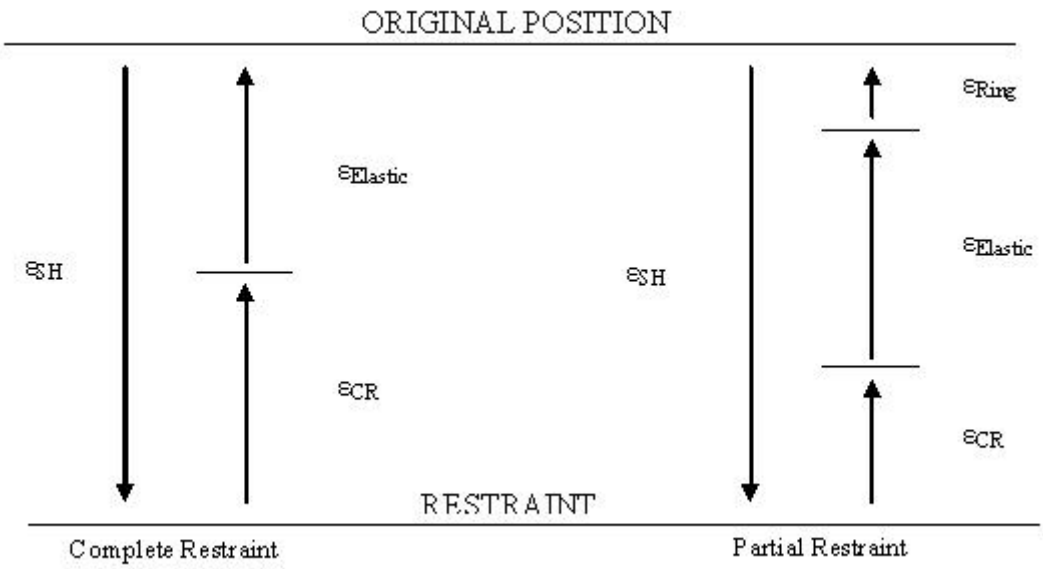

Figure 57. Various strain relationships for restrained shrinkage tests

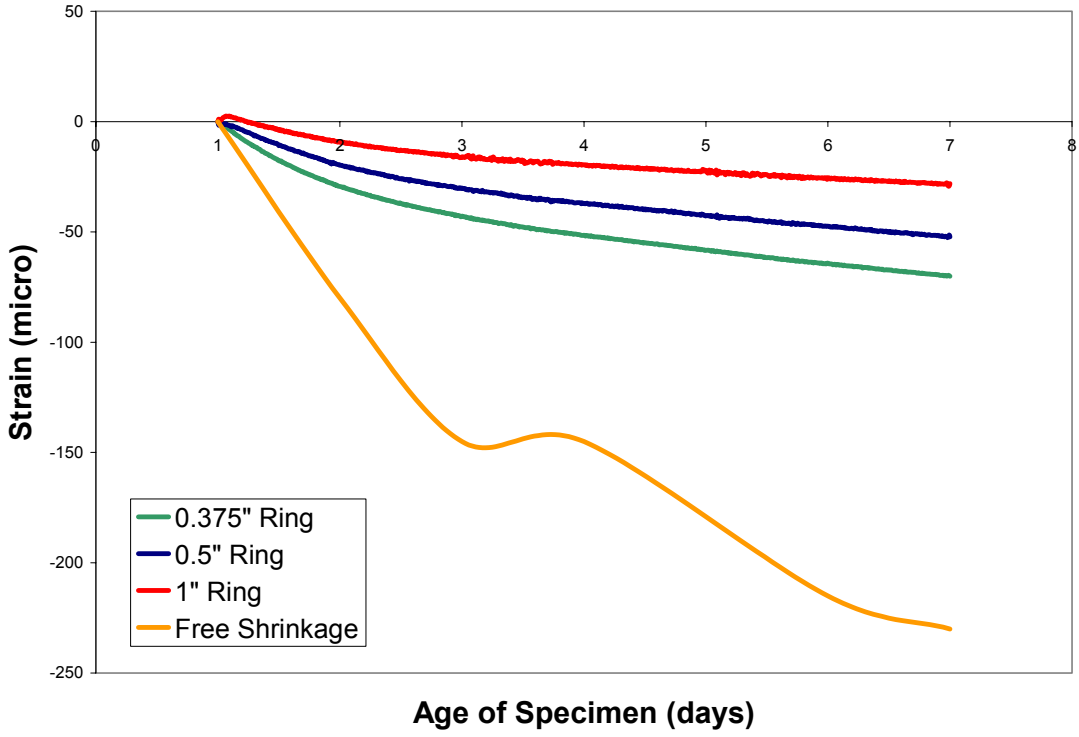

Figure 58. Measured steel strains for IBL44R1

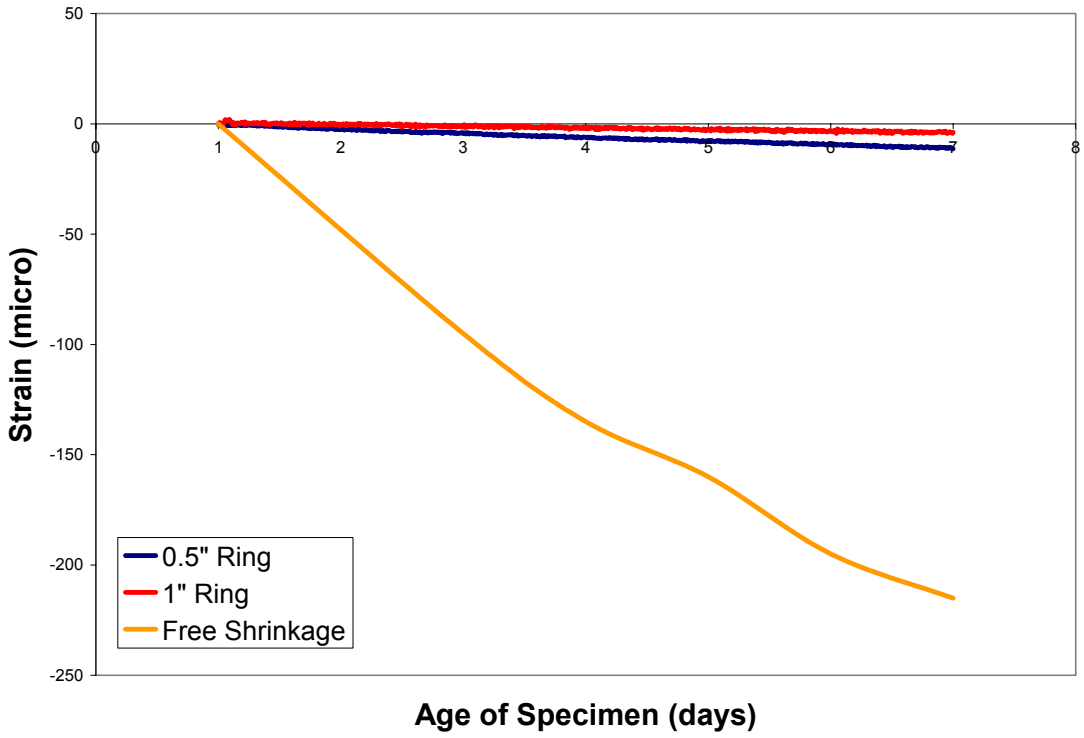

Figure 59. Measured steel strains for IDL41R1

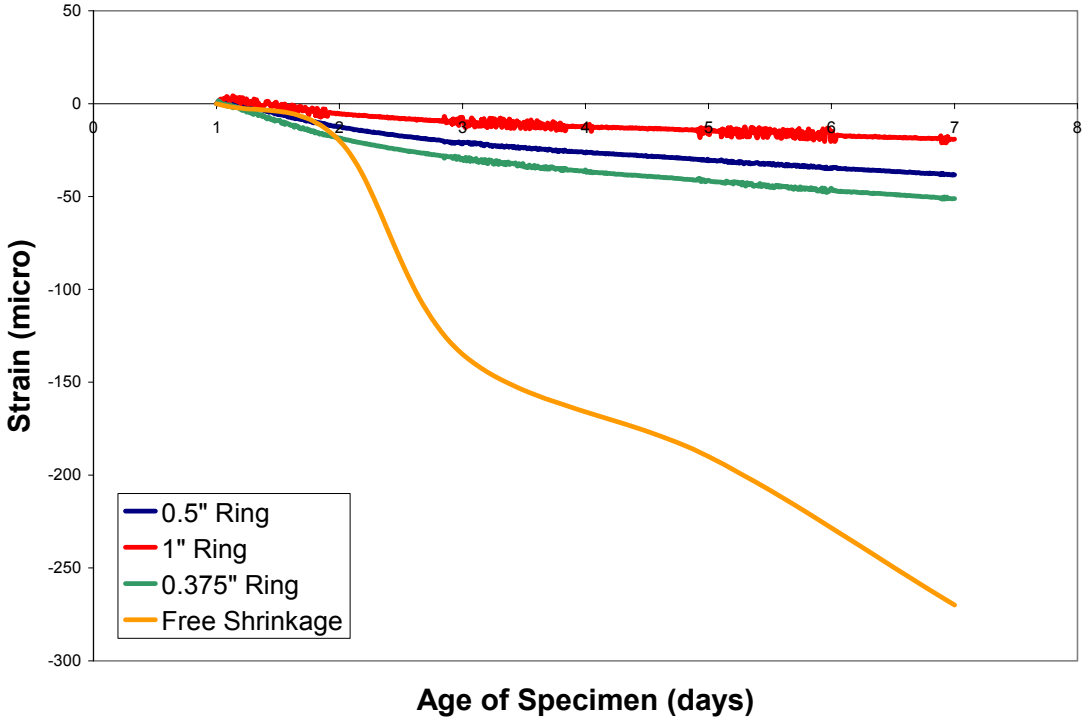

Figure 60. Measured Steel Strains for IDL44R1

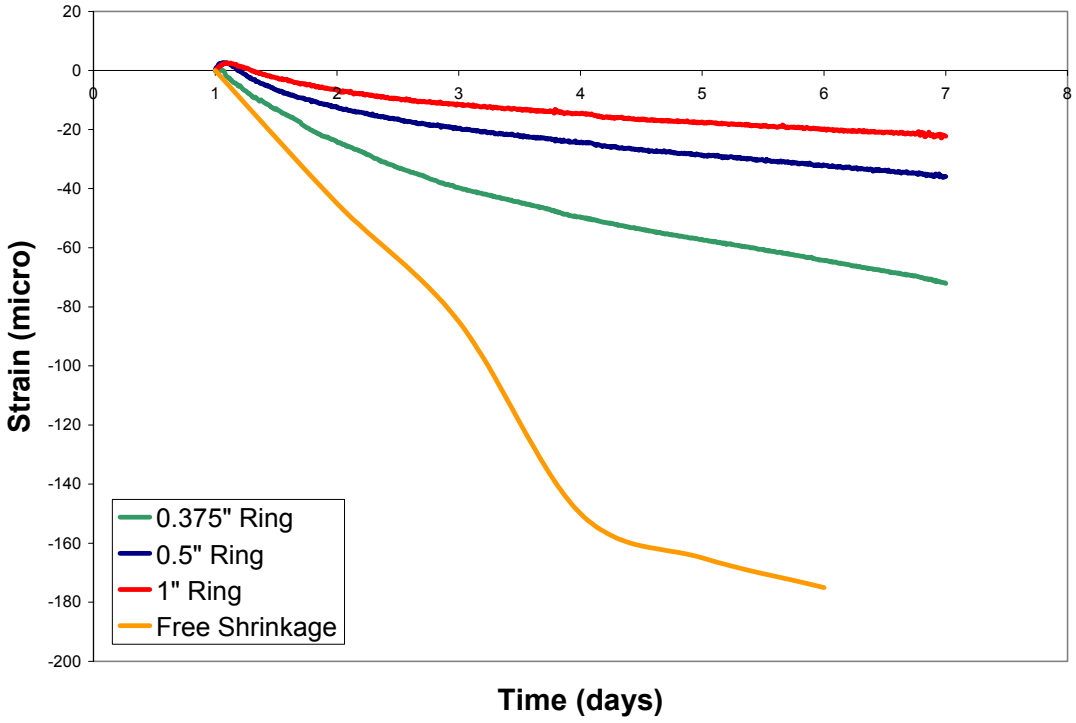

Figure 61. Measured Steel Strains for IKL44R1

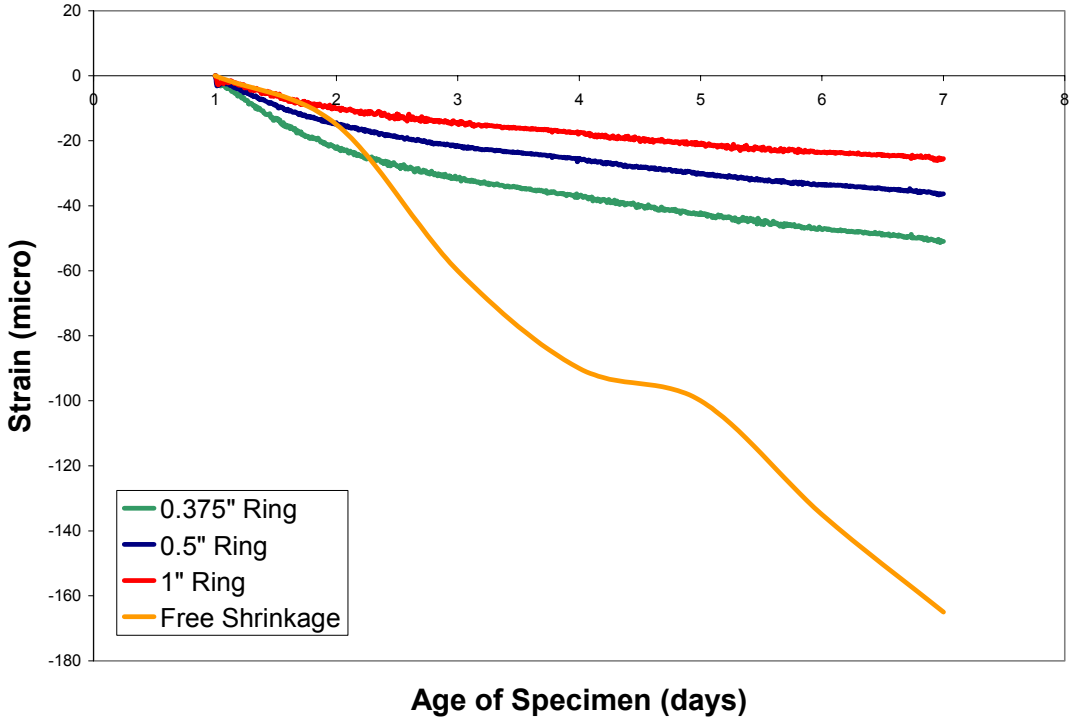

Figure 62. Measured Steel Strains for ISL44R1

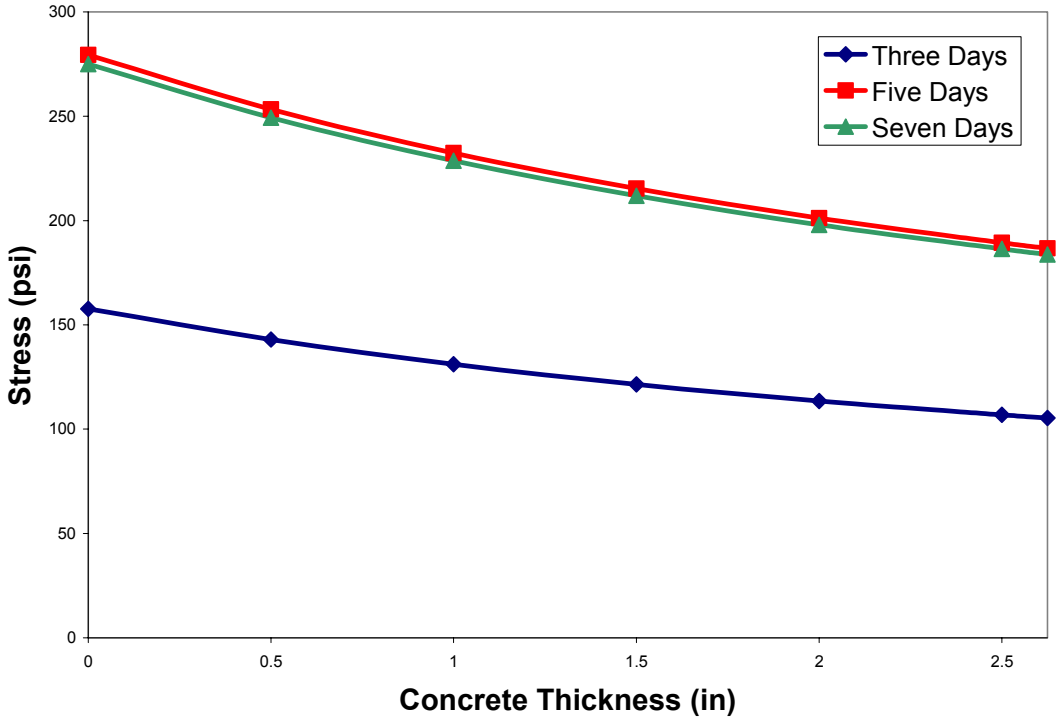

Figure 63. Residual Stress Distribution - IBL44R1 (0.375")

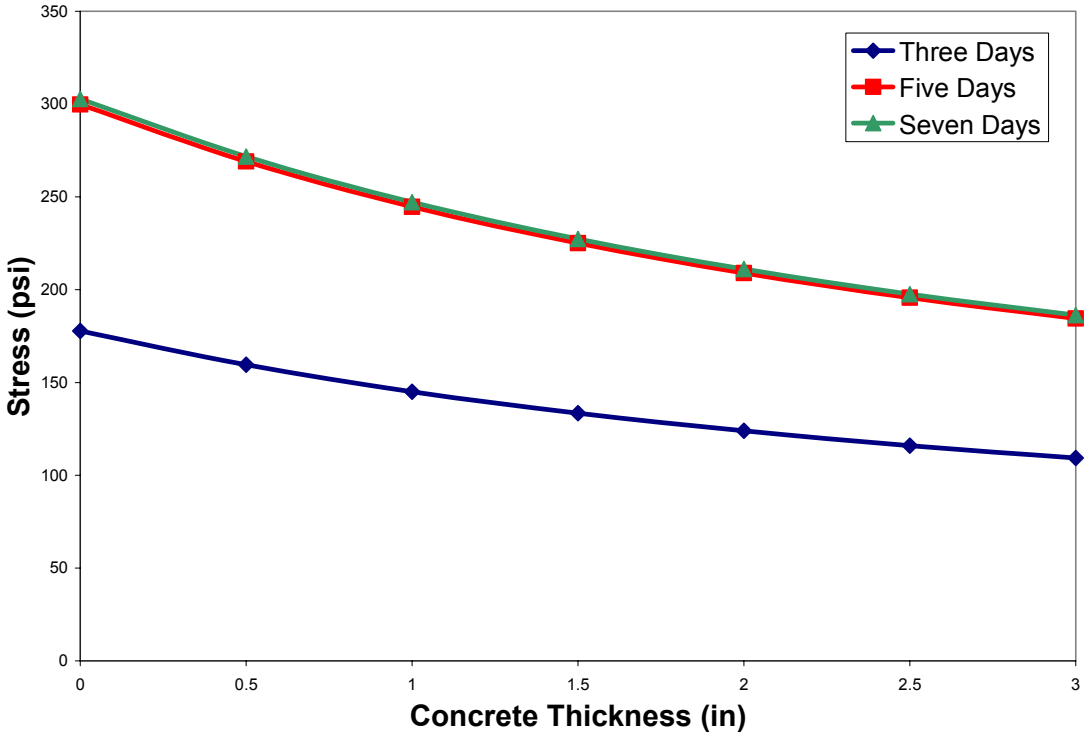

Figure 64. Residual Stress Distribution - IBL44R1 (0.5")

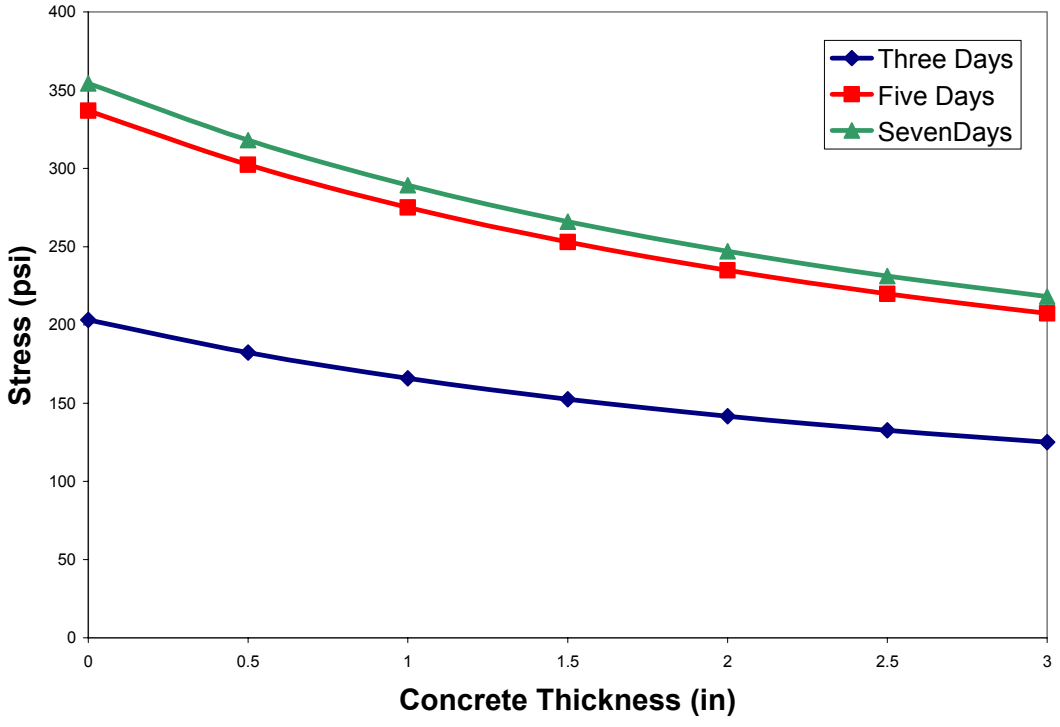

Figure 65. Residual Stress Distribution - IBL44R1 (1")

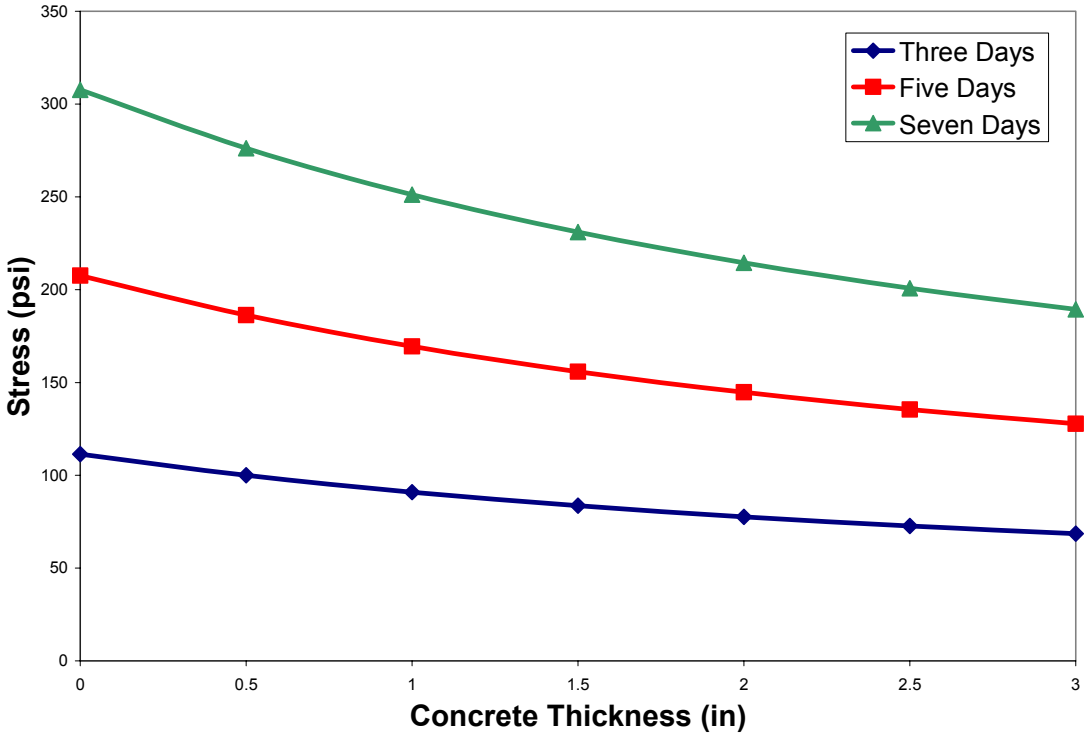

Figure 66. Residual Stress Distribution - IDL41R1 (0.5")

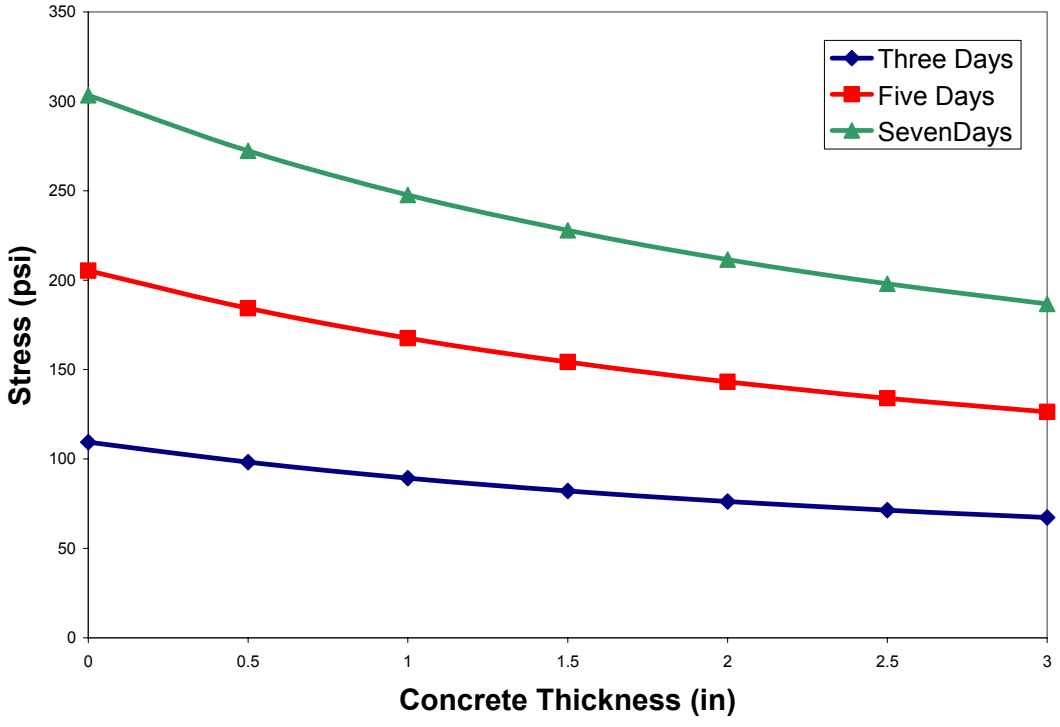

Figure 67. Residual Stress Distribution - IDL41R1 (1")

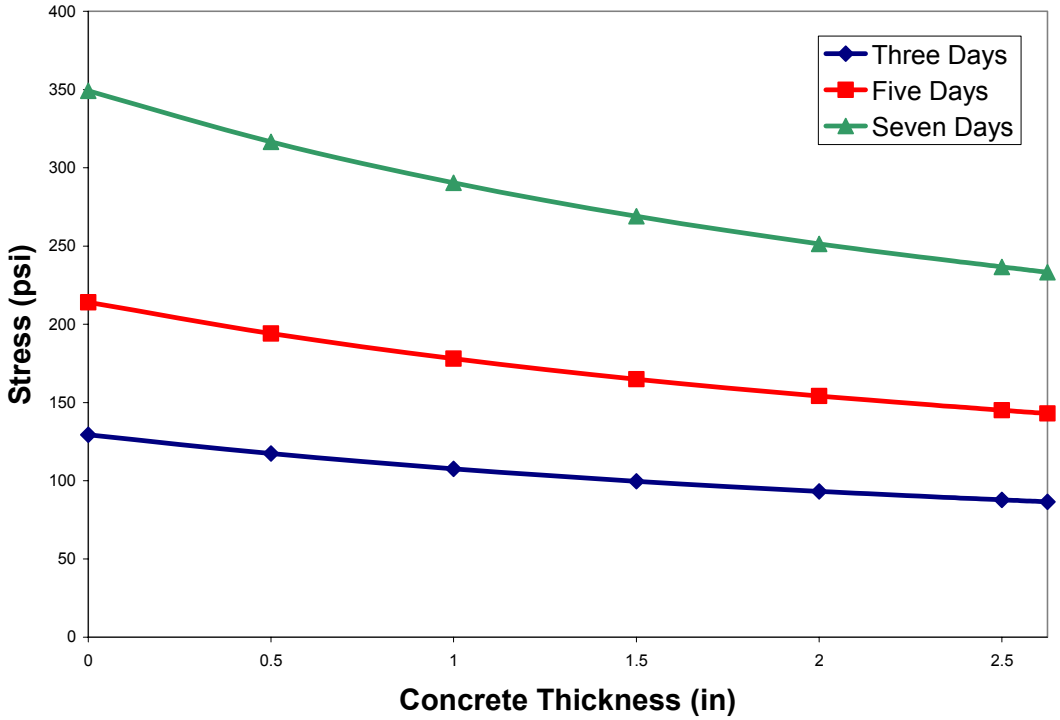

Figure 68. Residual Stress Distribution - IDL44R1 (0.375")

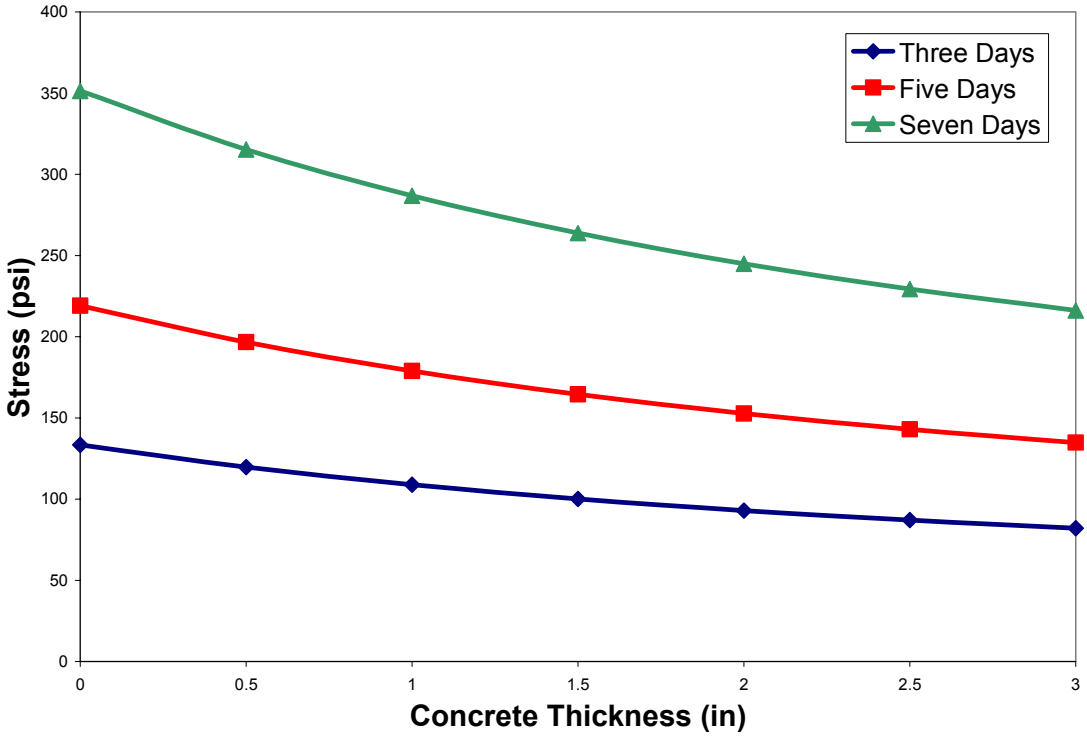

Figure 69. Residual Stress Distribution - IDL44R1 (0.5")

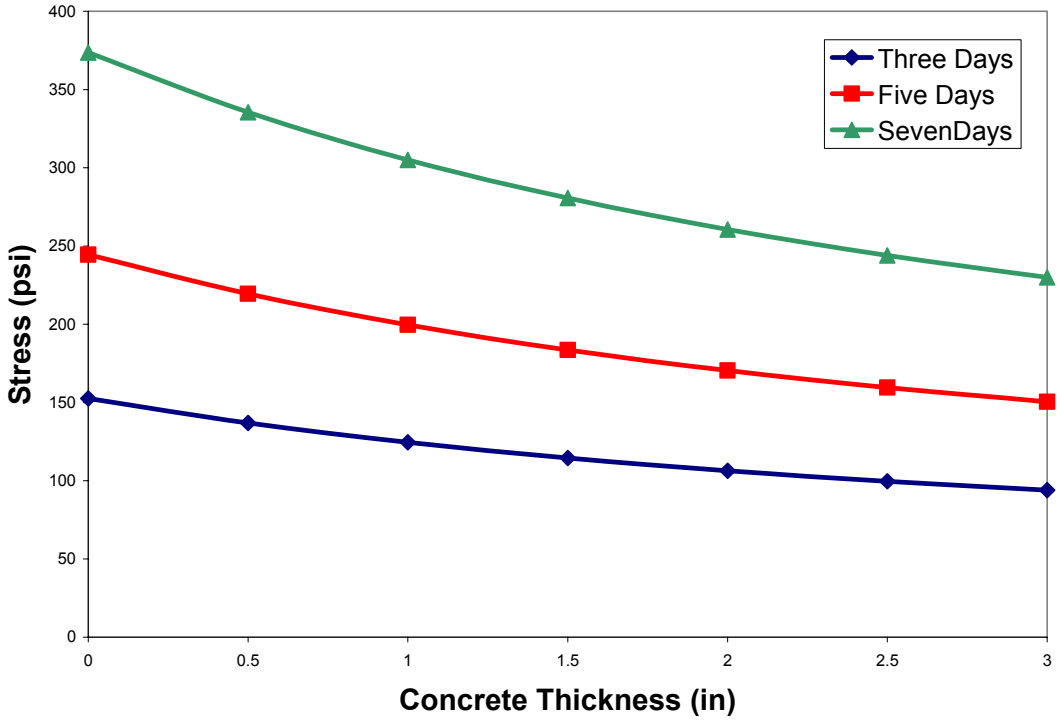

Figure 70. Residual Stress Distribution - IDL44R1 (1")

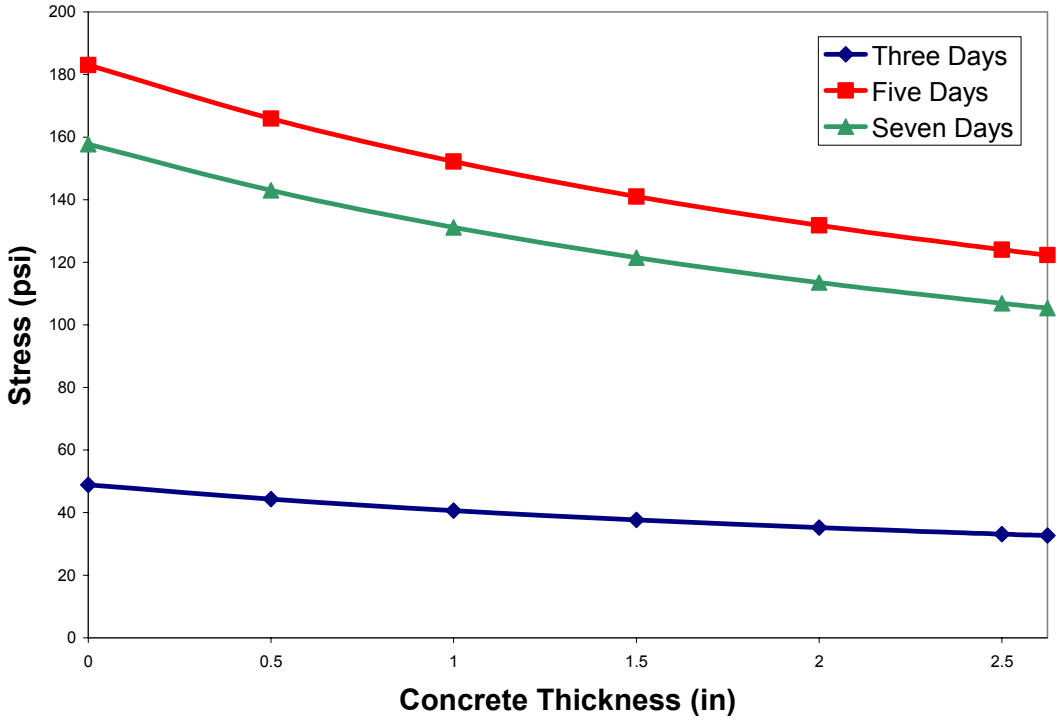

Figure 71. Residual Stress Distribution - IKL44R1 (0.375")

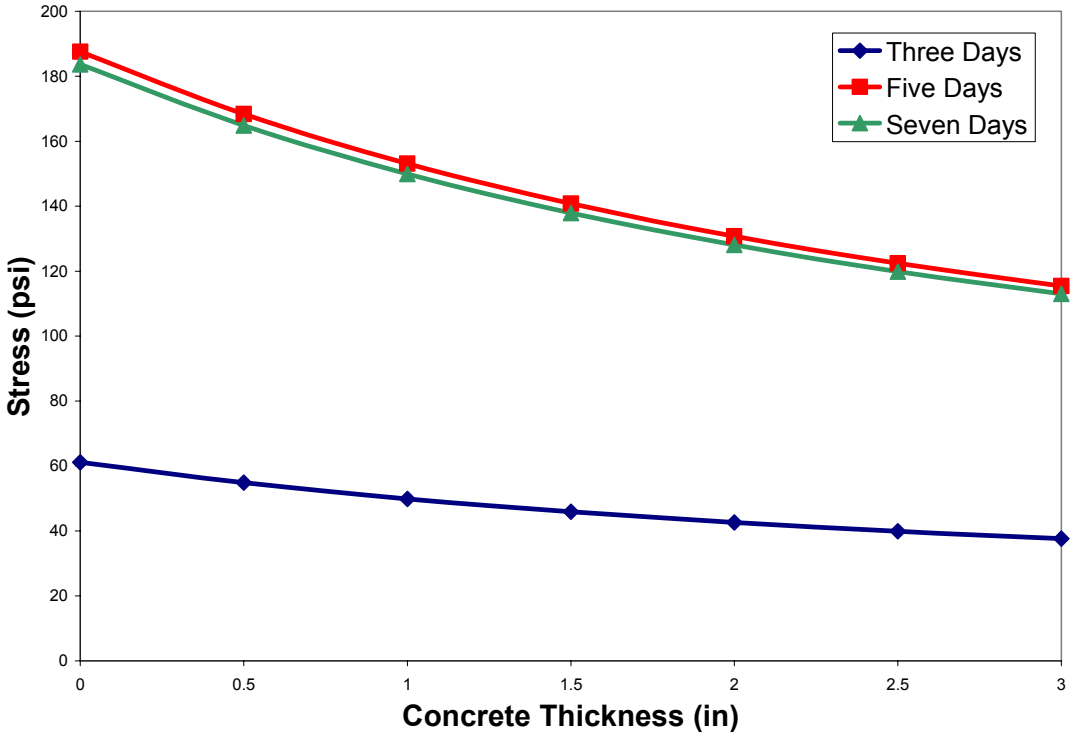

Figure 72. Residual Stress Distribution - IKL44R1 (0.5")

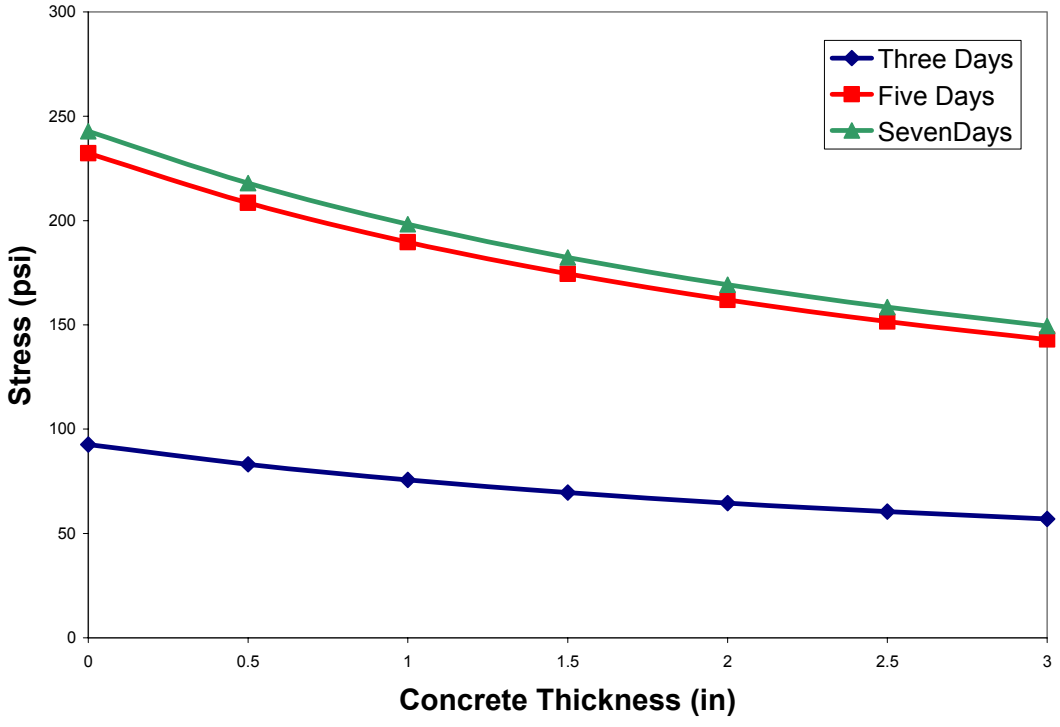

Figure 73. Residual Stress Distribution - IKL44R1 (1")

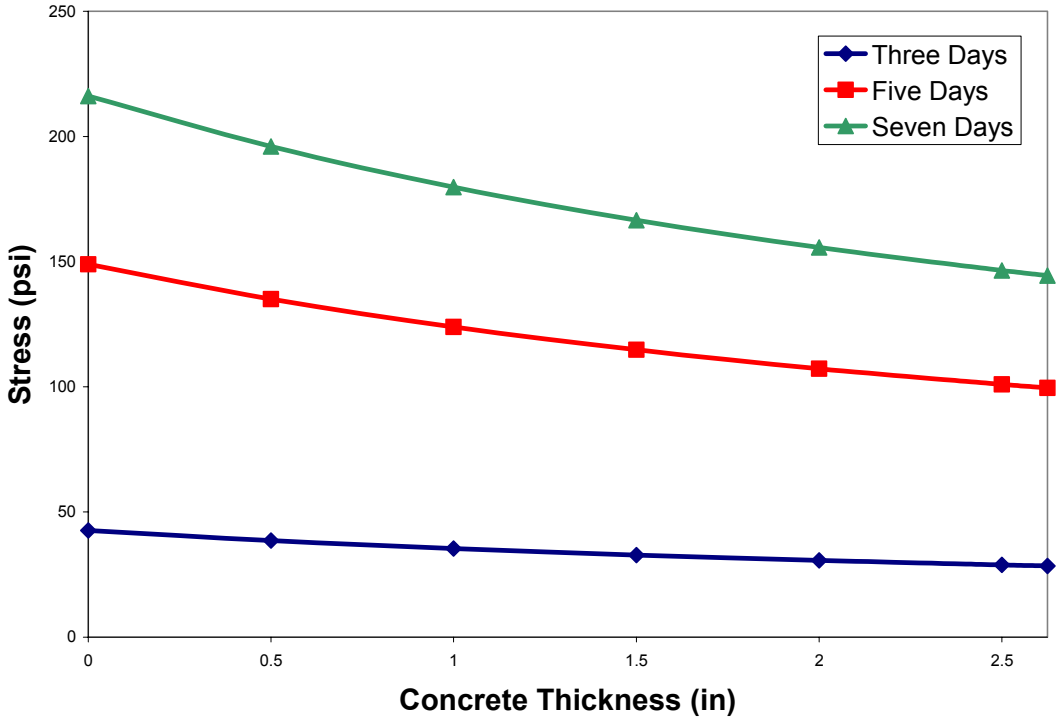

Figure 74. Residual Stress Distribution - ISL44R1 (0.375")

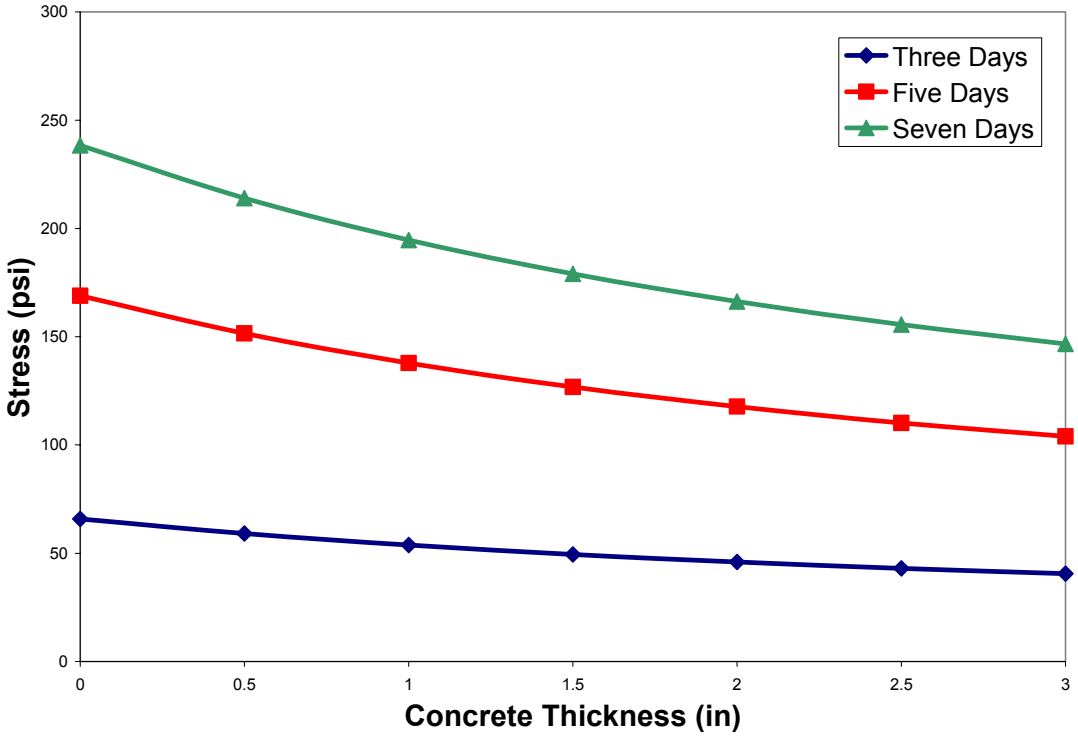

Figure 75. Residual Stress Distribution - ISL44R1 (0.5")

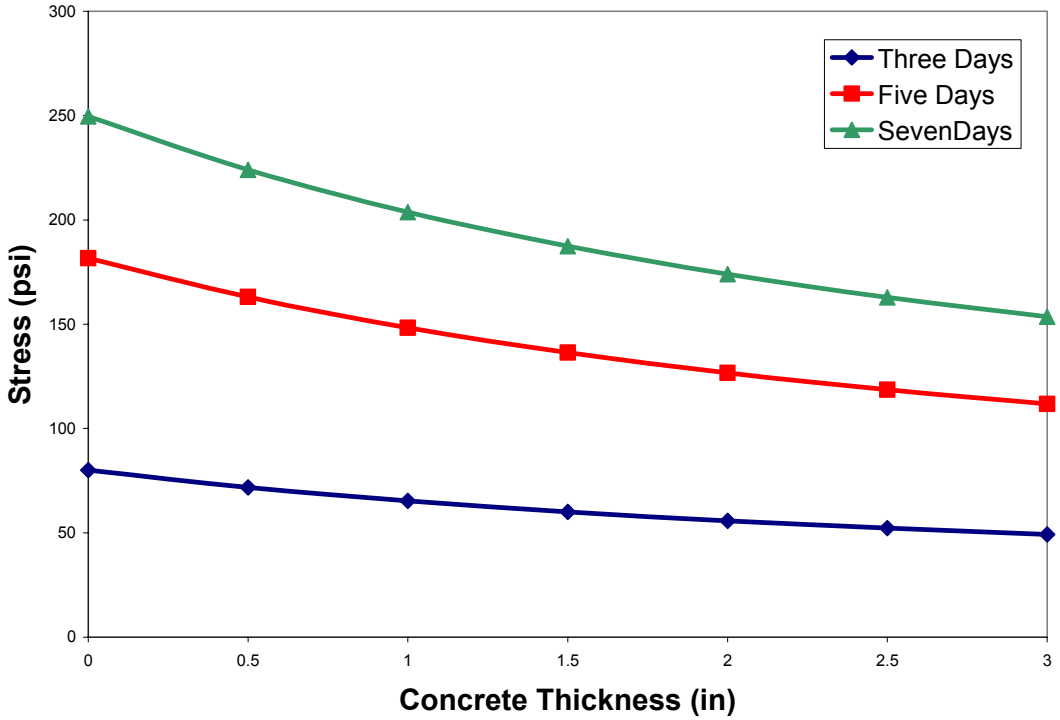

Figure 76. Residual Stress Distribution - ISL44R1 (1")

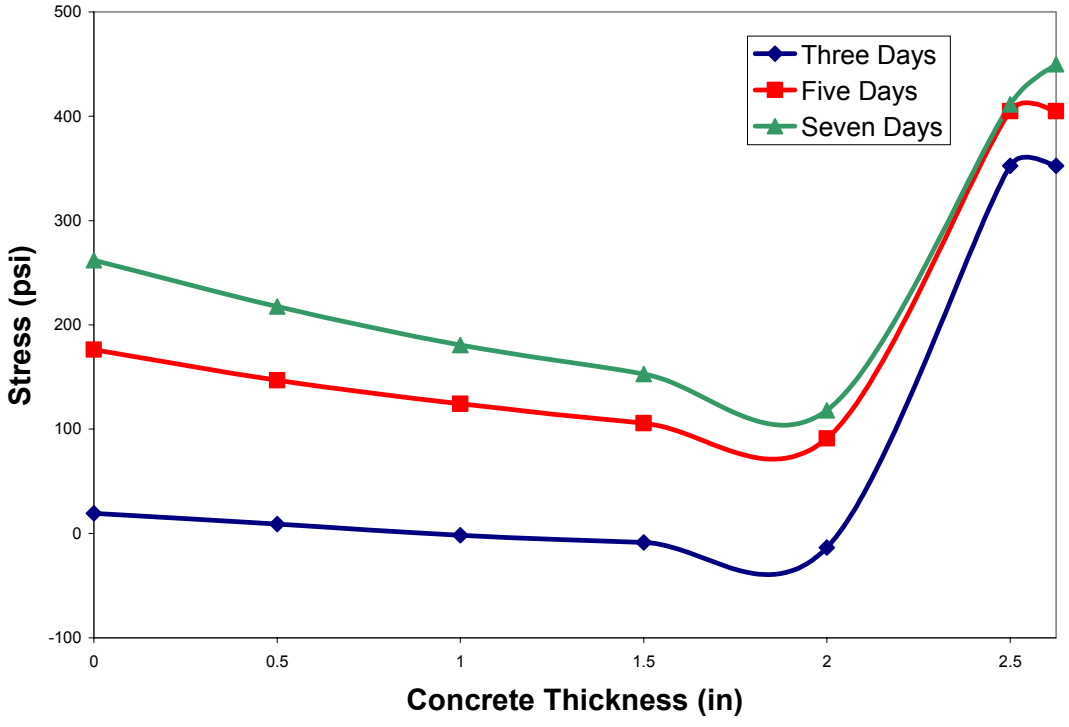

Figure 77. Combined Stress Distribution - IBL44R1 (0.375")

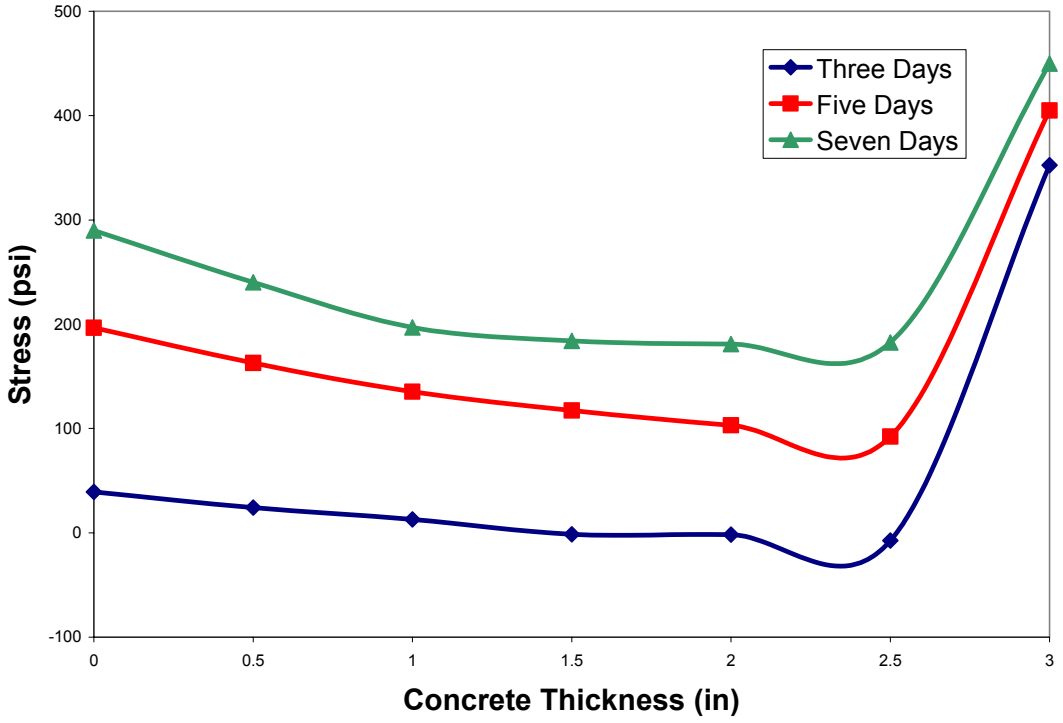

Figure 78. Combined Stress Distribution - IBL44R1 (0.5")

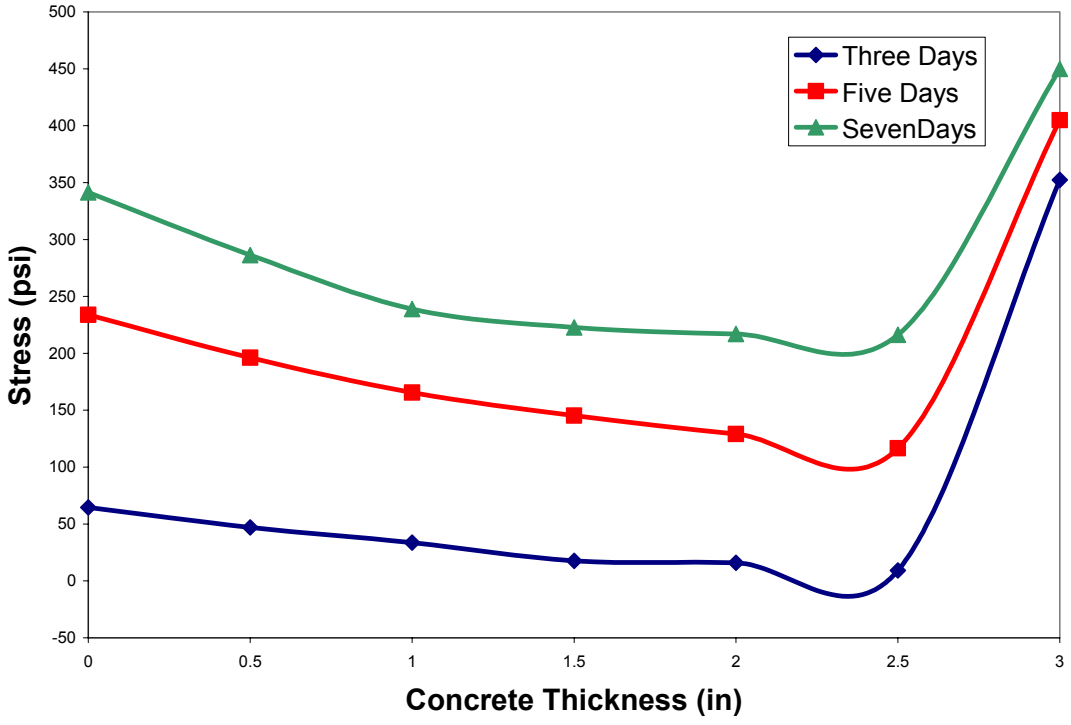

Figure 79. Combined Stress Distribution - IBL44R1 (1")

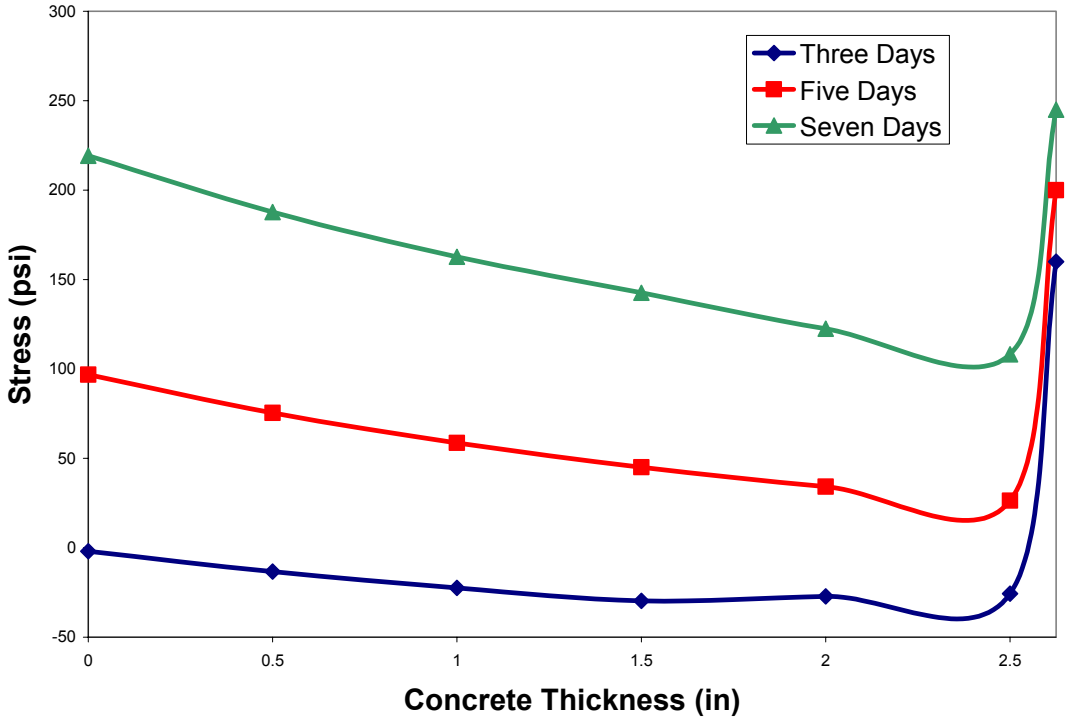

Figure 80. Combined Stress Distribution - IDL41R1 (0.5")

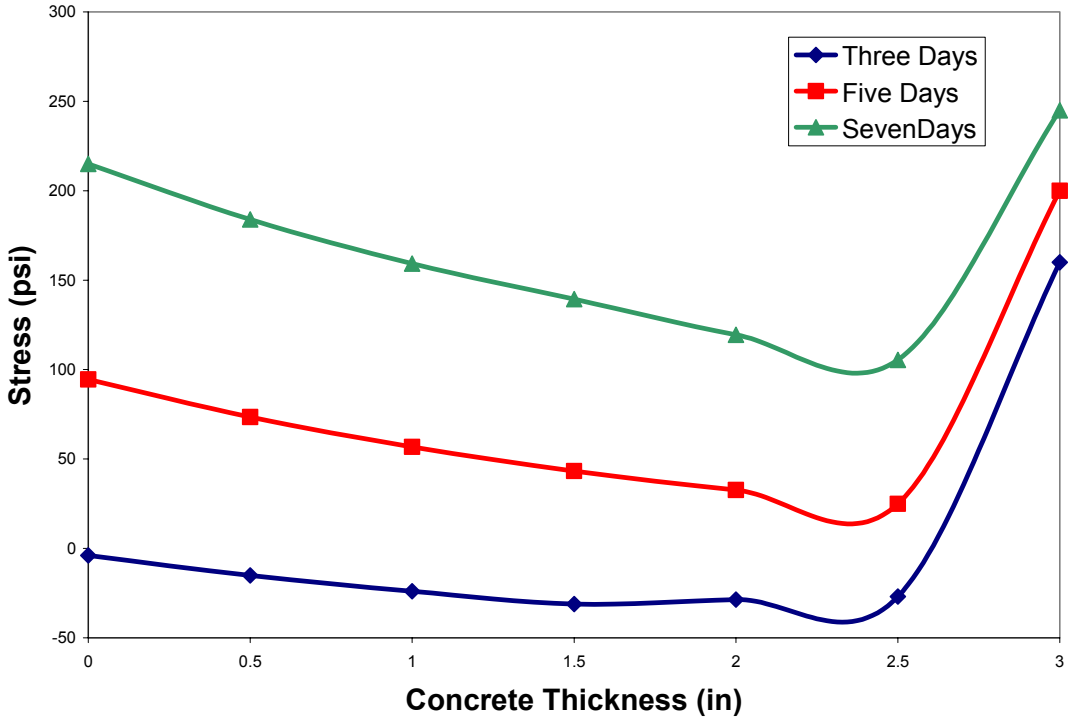

Figure 81. Combined Stress Distribution - IDL41R1 (1")

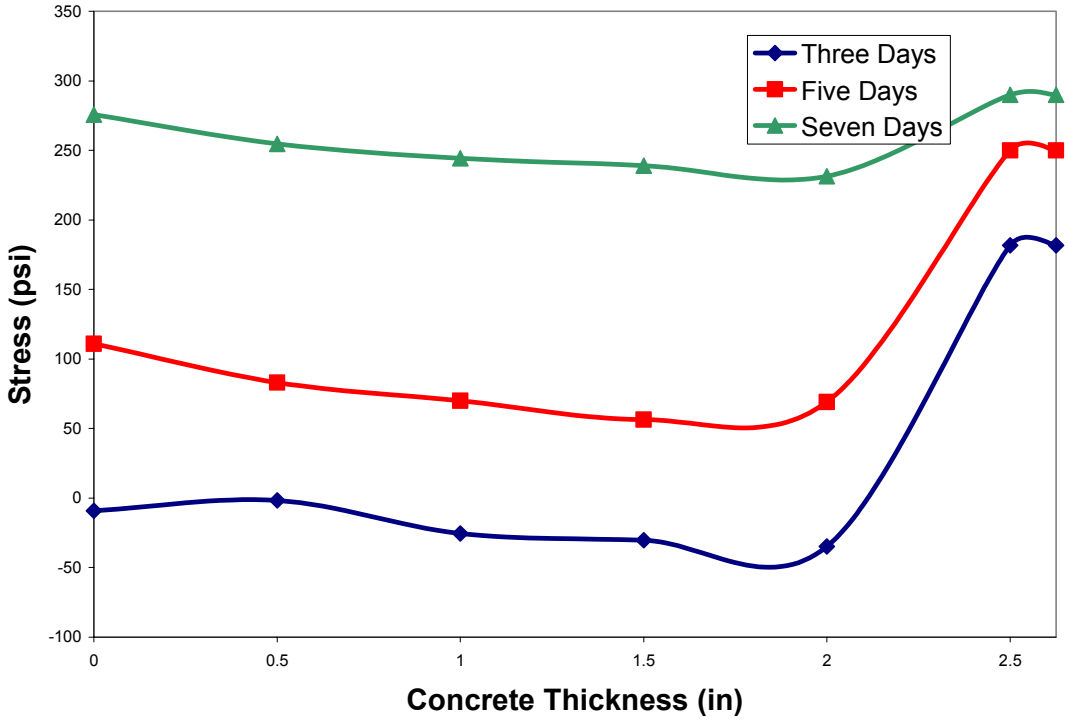

Figure 82. Combined Stress Distribution - IDL44R1 (0.375")

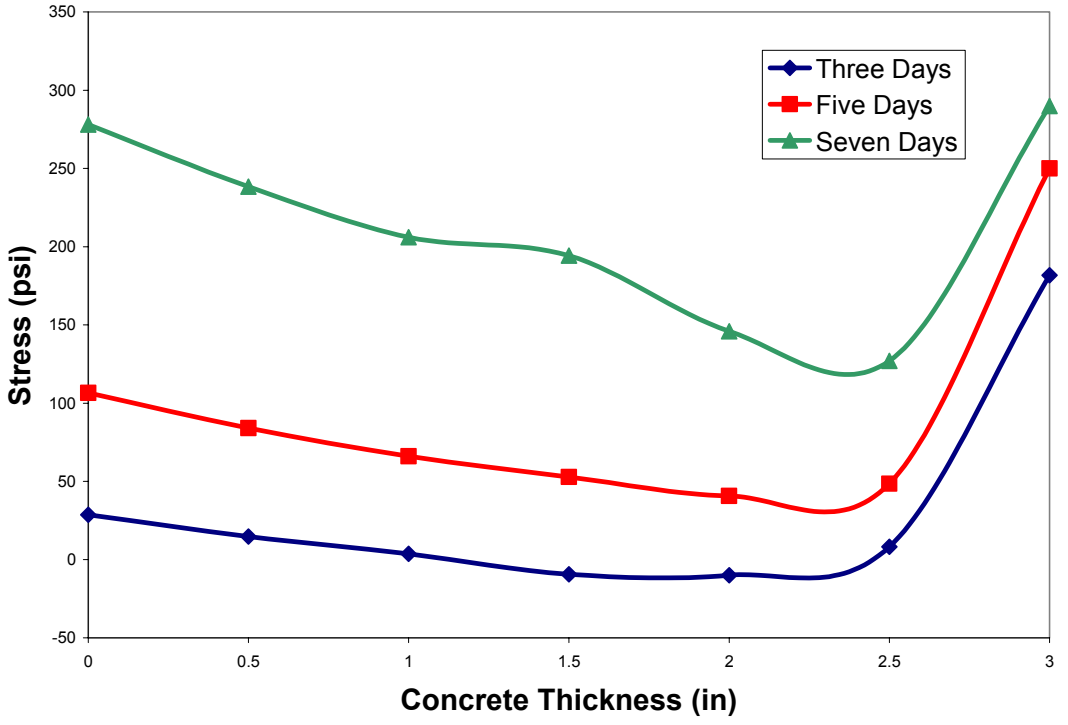

Figure 83. Combined Stress Distributions – IDL44R1 (0.5")

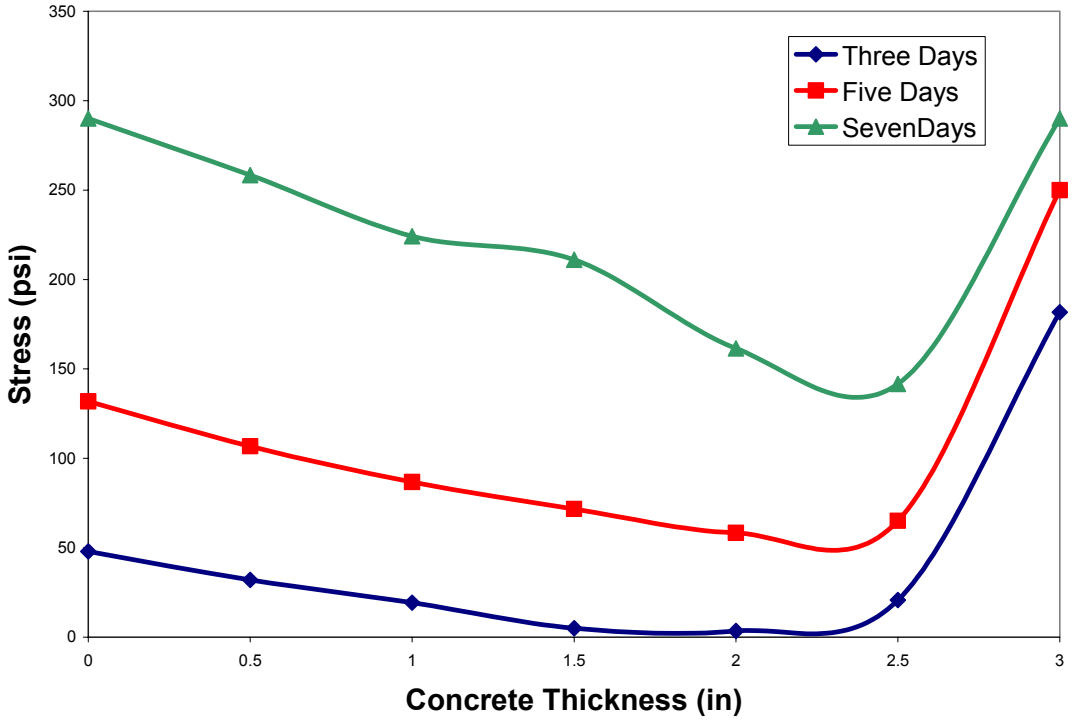

Figure 84. Combined Stress Distribution - IDL44R1 (1")

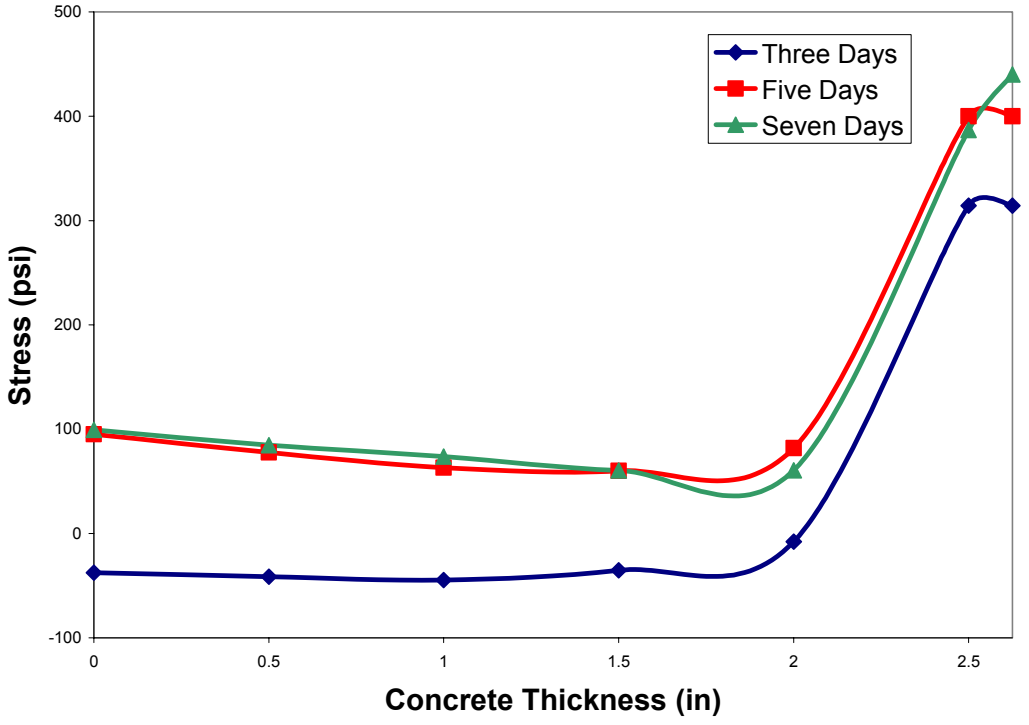

Figure 85. Combined Stress Distribution - IKL44R1 (0.375")

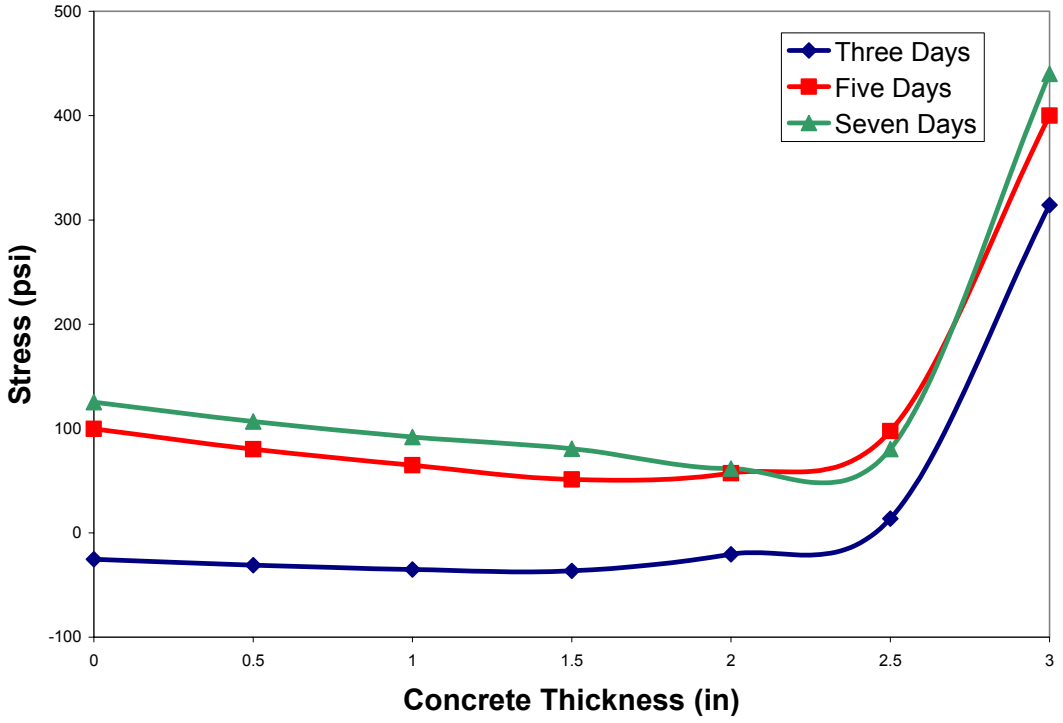

Figure 86. Combined Stress Distribution - IKL44R1 (0.5")

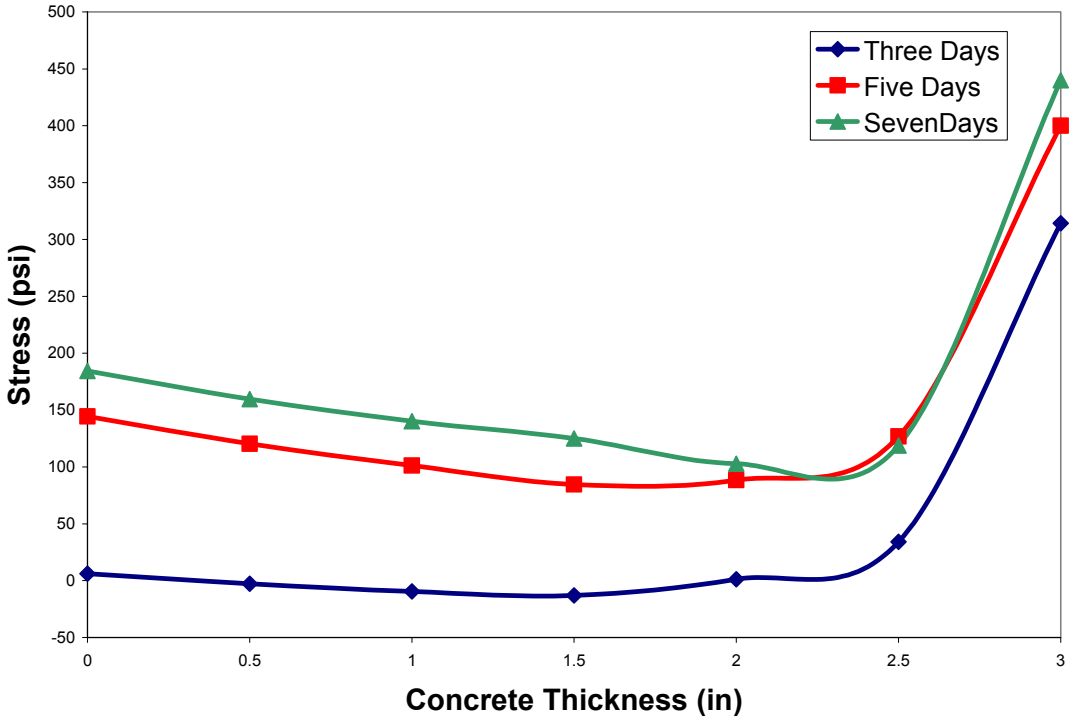

Figure 87. Combined Stress Distribution - IKL44R1 (1")

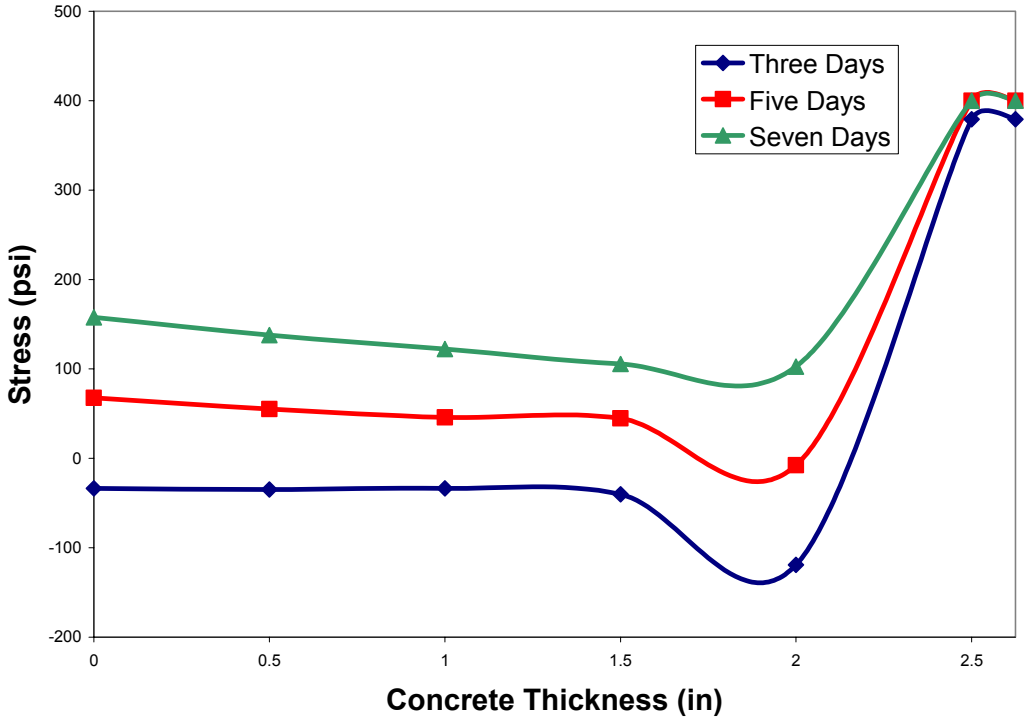

Figure 88. Combined Stress Distribution - ISL44R1 (0.375")

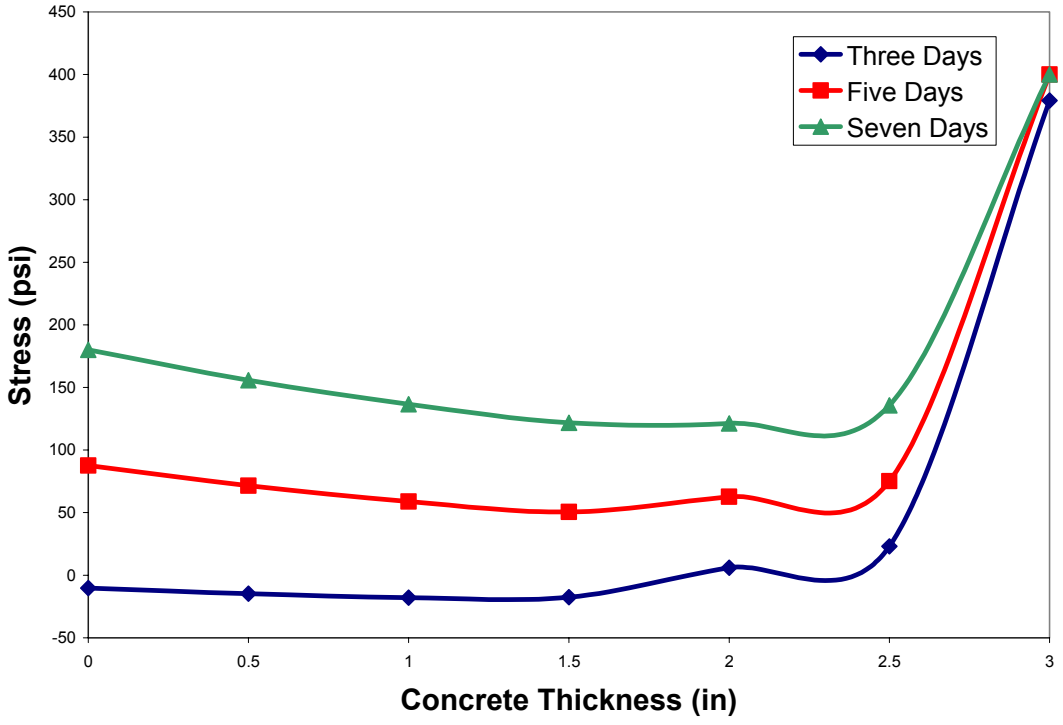

Figure 89. Combined Stress Distribution - ISL44R1 (0.5")

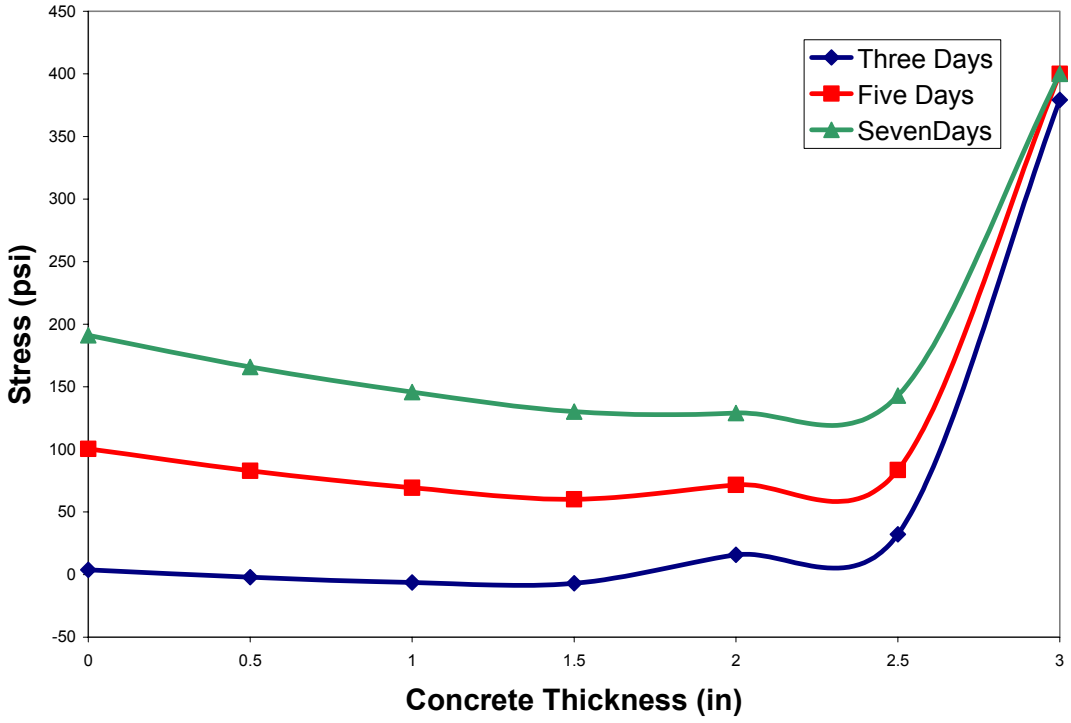

Figure 90. Combined Stress Distribution - ISL44R1 (1")

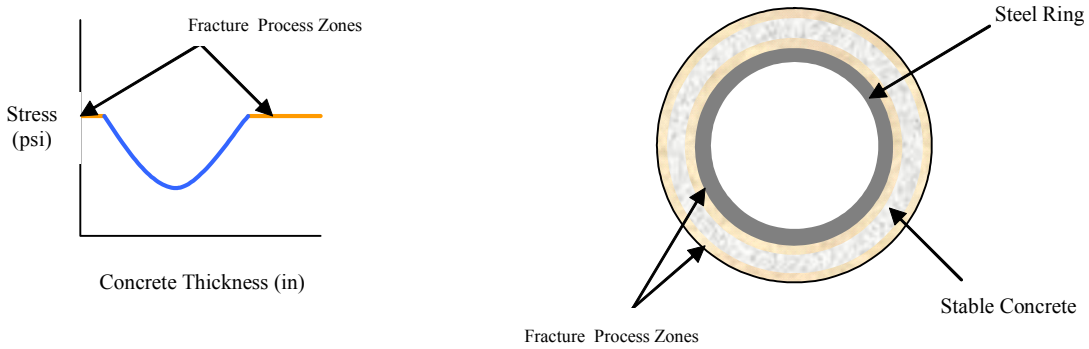

Figure 91. Development of microcracking zones in the concrete ring leading to failure

7. INTERNAL RELATIVE HUMIDITY MEASUREMENT

7.1 Introduction

There are many methods available to quantify indirectly shrinkage or shrinkage potential by examining the state of internal moisture in concrete. Among these are weight loss measurements, impedance spectroscopy (as well as electrical resistance or conductivity) measurements, microwave measurements, magnetic resonance imaging (MRI), and internal relative humidity (RH) measurements. One advantage of using internal RH to examine the state of moisture in concrete is that RH has a fundamental relationship with shrinkage stress development.

As concrete dries (either from external drying or internal moisture consumption from hydration) the largest pores empty first, followed by progressively smaller pores. Once pores have been emptied to a pore diameter of about 50 nm [1], a meniscus begins to form on the surface of the pore fluid. As drying continues, the curvature of the meniscus will become smaller. As the curvature decreases, a pressure differential develops between the vapor and liquid phases. This is demonstrated in the Laplace Equation as

$$p'' - p' = \frac{2\sigma}{r}, \qquad 7.1$$

where *p"* is the vapor pressure, *p'* is the hydrostatic pressure exerted by the liquid water, σ is the surface tension of water, and *r* is the radius of the meniscus [2]. The Laplace Equation relates a pressure differential between the liquid and vapor phases in the capillary pore structure to the surface tension of water and the average radius of meniscus curvature. Figure 92 shows a model illustration of how the pressure differential can cause a collapse of the capillary pores (and thus bulk shrinkage).

The pressure difference between the vapor and liquid water can be related to the internal relative humidity (the partial vapor pressure) by equating the Laplace Equation with the Kelvin Equation. The Kelvin Equation can be displayed as

$$\frac{2\sigma}{r} = \frac{\ln(RH)RT}{v}, \qquad 7.2$$

where σ and r are as defined previously, RH is the internal relative humidity, R is the universal gas constant, v is the molar volume of water, and T is the temperature in Kelvins [2]. The combined Kelvin-Laplace Equation is

$$p'' - p' = \frac{\ln(RH)RT}{v}, \qquad 7.3$$

where all of the terms are as previously defined. This equation allows direct association between the internal RH and the stresses that cause shrinkage. Figure 93 depicts how the pressure differential can induce bulk shrinkage in hardened cement paste.

Methods to measure the internal RH in concrete have been available for many years. Some early relative humidity probes were developed in the 1930's, and RH measurements in concrete were being conducted by 1940 [3]. Early probes were mechanical, resistive, or capacitive. Capacitive probes remain a popular instrument for measuring the internal RH in concrete, as they are relatively inexpensive and are easy to operate. Technological advances coupled with a greater focus on the mechanisms controlling capacitive RH sensors have led to a steady increase in accuracy and long-term stability of these instruments.

Our review of recent literature reveals an increasing number of research projects incorporating internal RH measurements in concrete. Researchers have warned of potential problems that may be encountered when measuring internal RH in concrete. Loukili *et al*. [5], Andrade *et al*. [6], and Parrott [7] all used RH probes to measure the internal relative humidity in concrete. Loukili used a probe to measure autogenous RH change of a sealed specimen. A

single probe was inserted into a port within a sealed, hardened concrete specimen, and was not removed through the duration of the test. The experiments by Andrade and Parrot required the removal of the instrument between measurements, a procedure that exposed a serious limitation of capacitive probes. Andrade reported that after placing the probe in a new measurement hole, it could take more than 24 hours for the measurement to stabilize at RH >90%. Parrot also acknowledged the slow response of capacitive probes at high RH. The slow response can be attributed to two sources. First, the capacitive sensor is slow to stabilize at high RH. Second, it may take a significant amount of time for the vapor pressure in the measurement hole to equilibrate with the vapor pressure in the concrete. This problem may be even more severe in high-performance concrete (HPC) where the denser microstructure slows the diffusion of moisture to the surface of the concrete in the measurement cavity [8]. Another event that can lead to erroneous RH measurements in the field occurs when the temperature of the air inside the measurement cavity is different than the temperature within the concrete. This can be a problem if measurement ports protrude from an exterior surface and are not properly insulated. For example, a difference in temperature of 1° C between the sensor and the concrete material can yield an error of approximately 6% RH [9].

The problems associated with the long stabilization time of the probes can be averted if the probes remain in the measurement hole throughout the experiment, but this requires using more probes or sensors or reducing the number of measurement ports. The stabilization time can also be reduced if the volume of air around the probe is reduced, i.e. a smaller sensor. A system which uses small embeddable sensors that can be inserted into fresh concrete offers the advantage of drastically reducing the time to equilibrate the air in the measurement cavity. The high evaporation rate of the fresh concrete would quickly equilibrate the measurement cavity

before setting occurs. Any temperature differential between sensor and concrete can also be avoided by using a small, embeddable sensor.

Since concrete dries faster on the outer surface as compared to the center of the specimen, a drying stress gradient is created. To simplify, this means that there is a higher level of tension on the drying face of the material than the average stress across the cross-section would indicate. This can induce cracking at early ages, even at average stress levels, which are lower than the material tensile strength. The importance of the drying gradient relative to the state of internal stress in concrete has been discussed elsewhere [10]. The purpose of this portion of the IDOT research project was to develop a measurement system for monitoring the internal RH in concrete and to develop a model, which utilizes internal RH data to quantify the stress distribution in drying concrete. This research furthers our understanding of early-age cracking in concrete pavements and structures and allows better interpretation of the other early-age experiments involved in this project. In particular, the stress development in the concrete ring test (see Chapter 3) is highly dependent on the drying stress gradient.

7.2 Experimental Procedures

7.2.1 The Measurement System

To accurately measure the internal RH in concrete and to characterize the drying gradient, a measurement system was developed which avoids many of the problems described in the introduction. The system uses a relatively small, commercially available sensor. The small size of the Sensirion [11] sensor reduces the required cavity volume, allowing measurement of internal RH at an exact location or depth. A small cavity volume also lowers the time to equilibration. The sensors are inexpensive and an advanced data collection system allows the

automated measurement of many sensors. There is no need to switch the sensors from one measurement location to the next. Finally, the system incorporates a sensor capable of embedment, allowing data collection to begin at the time of casting. The sensor is shown in Figure 94.

The small (~6mm x 20mm), capacitive sensor can be encased in a Gore-Tex sleeve or a small tube with a Gore-Tex cap making it capable of being embedded in concrete. The Gore-Tex allows vapor transmission while preventing the penetration of liquid moisture and ions that could invoke erroneous measurements. The packaged sensor, prepared for embedding in concrete, is shown in Figure 95. For the purpose of measuring the drying gradient, a special concrete mold was used (Figure 96) that allowed positioning of the sensors at precise depths from the drying surface.

Data is transmitted digitally from the sensors to a small microcomputer, and then collected by a datalogger or personal computer through a serial connection. UIUC has developed software to control the data collection hardware and the sensors allowing measurements to be taken from every sensor at prescribed intervals. The system is extensible, and our current system is designed to accommodate simultaneous monitoring of up to 40 sensors.

The new system overcomes many drawbacks of alternative approaches. As discussed, a major disadvantage of capacitive sensors is that the capacitance in sensor lead wires may make calibration of capacitive sensors difficult, and may negatively affect the measurement accuracy. The capacitive sensor utilized in the new measurement system does not suffer from this limitation. The analog signal is converted to a digital output on the sensor itself.

The accuracy of the sensors is reported by the manufacturer to be ±2% RH between 10% and 90% RH, and range up to ±4% at 100% RH. The drift is 1% RH per year. Linearity is excellent and hysteresis is negligible. Additional performance specifications are available [11].

Advantages of the embeddable internal RH measurement system include:

- Digital signal avoids negative effects of lead-wire capacitance
- Small size means there is a small cavity of air to equilibrate before accurate results are obtained
- Embeddable packaging allows measurements to be initiated at casting
- Cost-efficient for throw-away embedment applications
- Computerized data-acquisition
- Temperature measured on same printed circuit board as RH
- Factory calibration
- Low drift- no recalibration necessary
- Adaptable software developed at UIUC allows multiple sensors to be measured with relatively inexpensive data collection hardware

7.2.2 Test Procedure

Internal RH sensors were embedded in concrete prisms using small plastic tubes with Gore-Tex caps. The tubes were embedded using a special concrete form (Figure 96) that yielded a 3" x 3" x 13" (76 mm x 76 mm x 330 mm) prism. The tubes were positioned such that measurements were being taken at depths of 0.25" (7.35 mm), 0.5" (12.7 mm), 0.75" (19.05 mm), 1" (25.4 mm), and 1.5" (38.1 mm) from the drying surfaces. The prisms were cast and immediately the surface was sealed using plastic wrap. At an age of 23 hours (to correspond with the uniaxial test), the specimens were demolded. The top and bottom surfaces were sealed to prevent drying using an adhesive-backed aluminum tape. The two symmetric sides were allowed to dry. RH and temperature measurements commenced immediately upon casting, and were taken at each sensor location every 3 minutes. Each test lasted a total of 8 days (7 days

drying time). Throughout the duration of the test, the prism was kept in a climate-controlled chamber maintained at 23° C and 50% RH.

7.3 Results and Discussion

A traditional way to show internal RH data is to plot internal RH versus time, as shown in Figure 97. However, to better evaluate the changing moisture gradient with time, the change in internal RH (relative to the maximum RH prior to demolding) was plotted versus depth from the drying surface for an age of 3, 5, and 7 days. These plots can be seen in Figure 98 through Figure 104. The figures are labeled with the mixture design codes defined in Chapter 1. The surfaces of the drying specimens are assumed to equilibrate with the ambient RH immediately after demolding at an age of 1 day. Since the average maximum internal RH is 95% and the ambient RH is 50%, the change in RH at the outer surfaces is 45%.

The changes in RH were applied to Equation 7.3 to determine the pressure differential between the vapor and liquid water at various depths from the drying surface. This pressure differential can be thought of as negative pressure within the pore fluid. Mackenzie [12] first introduced a relationship which allows a hydrostatic pressure across a cylindrical pore in a solid material to be translated into an associated strain. Mackenzie's Equation is

$$\varepsilon = p[\frac{1}{3k} - \frac{1}{3k_0}], \qquad 7.4$$

where ε is the strain, p is the average hydrostatic pressure (which is equal to p''-p' from the Kelvin-Laplace Equation), k is the bulk modulus of the porous solid, and k_0 is the bulk modulus of the solid skeleton of the material. This equation is only perfectly true for a saturated solid containing spherical holes, and is an approximate for partially saturated cement paste. Bentz *et*

al. [13] modified Equation 7.4 to include a saturation factor, which produced reasonable results for partially a partially saturated porous medium. The modified Equation is

$$\varepsilon = pS[\frac{1}{3k} - \frac{1}{3k_0}], \qquad 7.5$$

where S is the saturation factor.

To make the equation applicable to concrete, it was multiplied by the volume fraction of cement paste (which assumes the aggregates are incompressible). The final equation for linear strain in concrete caused by drying-induced capillary pressure is

$$\varepsilon = pS[\frac{1}{3k} - \frac{1}{3k_0}]\frac{v_p}{v_t}, \qquad 7.6$$

where v_p is the volume of paste and v_t is the total volume. Instead of measuring the saturation at various depths within the concrete to obtain S, the internal RH was used as an estimate of saturation. The bulk modulus of the solid material, k_0, was assumed to be 44 GPa [14], and the bulk modulus of the porous body, k, was determined using the ACI predicted elastic modulus and an assumed Poisson's ratio of 0.20.

The strain calculated from the internal RH measurements in Equation 7.6 cannot be directly associated to a stress through Hooke's Law. This is because Equation 7.6 solves for the drying shrinkage strain *potential*. However, for a free shrinkage specimen of any substantial length (or any restrained sample), the ends of the specimen are forced to remain planar. So, the strain that has an associated stress is actually the strain required to bring the specimen back to a planar state after creep relaxation has been accounted for. This concept of strain superposition is illustrated in Figure 105. The strain components may be summed to equal the total measured free shrinkage strain as

$$\varepsilon_T = \varepsilon_{sh} + \varepsilon_{cr} + \varepsilon_{el}, \qquad 7.7$$

where ε_T is the total, measured free shrinkage strain, ε_{sh} is the calculated free shrinkage strain from Equation 7.6, ε_{cr} is the creep strain, and ε_{el} is the remaining strain required for strain compatibility (to bring the section back to a planar state). This strain, ε_{el}, has an associated stress through Hooke's Law. The creep strain, ε_{cr}, is some portion of ε_{el} and can be expressed as

$$\varepsilon_{cr} = x\varepsilon_{el}, \tag{7.8}$$

where x is some value between 0 and 1. Equations 7.7 and 7.8 can be combined and rearranged to solve for the stress at any location across the cross-section of a free shrinkage specimen as

$$\sigma = (1-x)(\varepsilon_T - \varepsilon_{sh})E_{concrete}, \tag{7.9}$$

where σ is the stress, ε_T is the measured free shrinkage, ε_{sh} is the potential shrinkage from Equation 7.6, and $E_{concrete}$ is the ACI predicted elastic modulus of concrete.

The only unknown variables in Equation 7.9 are σ and the value of x at any particular point across the cross-section. To solve for x, the stress gradient was plotted and the area beneath the curve was calculated. The value for x was determined by forcing the area under the stress gradient curve to equal zero. For equilibrium, the cumulative stress across the cross-section of a free shrinkage specimen should be zero. Figure 106 through Figure 108 show the free shrinkage stress distribution for a variety of IDOT mixes at an age of 3, 5, and 7 days. Notice that the outside of the specimens are in tension and the center in compression. In order for the areas beneath the stress gradient curve to approach zero at 3, 5, and 7 days, the variable x was allowed to vary with time and moisture as

$$x = \left(\frac{RH}{100}\right)^2 (C)(1 + t(0.10)), \tag{7.11}$$

where RH is the internal relative humidity, C is an empirical constant (0.7 for free shrinkage), and t is the number of days since an age of 3 days. Although it is an empirical fit, both the variance with moisture and time are defendable. Drying creep ensures that creep is not constant

with internal moisture. Since it is the process of drying rather than the state of being dry which induces drying creep [16], it is logical that concrete with a higher internal relative humidity would experience higher creep. The creep multiplier x is also allowed to vary with time as stress increases due to restrained drying. Figure 109 shows that the specific creep increases with stress. That is, the amount of creep relative to a given stress increases with higher stress-strength ratio. The *(1 + t(0.10))* component of Equation 7.11 is derived from the relationship in Figure 109. Figure 110 shows the creep strain profile for a free-shrinkage drying specimen with a cross-section of 3" (77.2 mm).

In the case of a restrained concrete specimen, the creep can be divided into two components as

$$\varepsilon_{cr} = x\varepsilon_{el-dry} + \varepsilon_{cr-avg}, \qquad 7.12$$

where ε_{cr} is the total creep strain, $x(\varepsilon_{el\text{-}dry})$ is the creep strain associated with the drying gradient, and $\varepsilon_{cr\text{-}avg}$ is the average creep induced by the complete restraint of the specimen.

In the case of a fully restrained concrete specimen (such as the uniaxial test), the total measured strain, ε_T, is zero. Therefore, for the fully restrained case, Equations 7.7 and 7.12 can be combined and rearranged to yield

$$\sigma = [(1-x)(-\varepsilon_{sh}) - \varepsilon_{cr-avg} E_{concrete}], \qquad 7.13$$

where all the variables are as defined previously. The areas beneath the stress profile for the restrained material should not sum to zero, but rather the average stress across the cross section. This value can be determined through the uniaxial test. The variable x (the creep multiplier) is again defined by Equation 7.11, but in the restrained case, the creep induced from the drying stress gradient is lower than in the free shrinkage case. As a result, the constant C from Equation 7.11 is 0.4 for the restrained case. It is not clear why the drying stress gradient induces less creep

in the restrained case compared to the free case, but it may have to do with the difference in the magnitude of the stresses in each case. Figure 111 through Figure 113 show the restrained stress development in symmetrically drying concrete specimens with a width of 3" (77.2 mm).

In Figure 113, a dashed line extends up to a very high stress level on the drying surface. These extensions could be drawn on nearly every free shrinkage or restrained shrinkage stress profile, indicating extremely high tensile stresses at the surface of the specimens. Since these stresses are consistently much greater than the strength of the material, it is unlikely that they are ever truly approached. It is much more likely that within this zone where the stresses surpass the strength there is extensive microcracking. Wittmann also suggests that there is a zone of high tension on the surface of drying concrete that exceeds the tensile strength of the material, thus inducing cracking [10]. This zone would still have some stress-carrying capacity, which is represented by the measured tensile strength of the material in this model (as determined through split cylinder tests). This is the flat portion of the stress gradient curves near either drying face. The model suggests these fictitious stresses (and thus microcracking) occur immediately after drying initiates in both the free and restrained shrinkage specimens. This proposition is supported by Hossain *et al*. [15], who found that acoustic emissions testing indicates shrinkage-induced microcracking can occur within an age of 1 day. The model also indicates that as drying continues the stresses in the free shrinkage specimens are relaxed while the stresses in the restrained specimens continue to increase. The microcracking zone gradually increases in the restrained case as the material ages and continues to dry. This is as expected.

Results from the uniaxial device in Chapter 5 indicate that restrained concrete specimens exposed to drying conditions on average fail at a stress/strength ratio of about 0.83. A reasonable explanation for the reduction in strength may be the stress gradient induced in drying specimens. Figure 114 shows the stress gradients in the restrained concrete specimens at the

time of failure. In general, the materials with the lowest gradient failed at the latest age. Figure 115 plots the failure age versus the differential stress range across the specimen cross-section, illustrating the relationship between gradient severity and failure age. If the gradients are examined at the same time, the trends between gradient severity and failure age of the material hold true.

7.4 Conclusions

Internal RH measurements provide useful information regarding the stress development in restrained concrete exposed to drying conditions. The data suggests that there is little variation between the IDOT mixes tested. In addition, shrinkage-induced microcracking occurs at an early age. As drying continues in restrained concrete, the zone of microcracking progresses inward as drying continues. In free shrinkage, the stresses are highest immediately after drying initiates, slowly relaxing over time.

Concrete often fails at stresses below the measured tensile strength. This research has shown that there may be a link between the failure age of the material and the severity of the drying stress gradient. This research reinforces the importance of limiting early age drying. The longer concrete can be cured (either wet or sealed), the better the chance that shrinkage cracking will be avoided. The drying gradient stresses could also be reduced by producing a dense concrete microstructure that limits the rate of drying. However, increased autogenous shrinkage and reduction of creep might offset any benefits gained by reducing the drying gradient.

REFERENCES

1. S.M. Mindess, J.F. Young, Concrete, Prentice Hall, Inc., Englewood Cliffs, NJ (1981).

2. R. Defay, I. Prigogine, A. Bellemans, D.H. Everett, Surface Tension and Adsorption, John Wiley and Sons, Inc., NY (1966).

3. R.R. Gause, J. Tucker, Jr., Method for Determining the Moisture Condition in Hardened Concrete, J. of Res., Nat Bureau Standards 25 (1940) 403-416.

4. P.S. Anderson, Mechanism for the Behavior of Hydroactive Materials Used in Humidity Sensors, J of Atmospheric and Oceanic Tech 12 (1995) 662-667.

5. A. Loukili, A. Khelidj, P. Richard, Hydration Kinetics, Change of Relative Humidity, and Autogenous Shrinkage of Ultra-High-Strength Concrete, Cem Conc Res 29 (1999) 577-584.

6. C. Andrade, J. Sarría, C. Alonso, Relative Humidity in the Interior of Concrete Exposed to Natural and Artificial Weathering, Cem Conc Res 29 (1999) 1249-1259.

7. L.J. Parrott, Moisture Profiles in Drying Concrete, Adv In Cem Res 1 (1988) 164-170.

8. G. Hedenblad, Measurement of Moisture in High Performance Concrete, Utilization of High-Strength/High-Performance Concrete, Proceedings 2 Sandefjord, Norge (1999).

9. B. Persson, Chemical Shrinkage and Internal Relative Humidity Tests, in: A. Bentur (Ed.), Early Age Cracking in Cementitious Systems, RILEM (2002) 257-274.

10. F.H. Wittmann, Creep and Shrinkage Mechanisms, Chapter 6 in Creep and Shrinkage in Concrete Structure, Ed. Bazant and Wittmann, John Wiley & Sons, Ltd. (1982).

11. Sensirion, Preliminary Specifications for SHT1x/SHT7x Humidity and Temperature Sensmitter, Zurich, Switzerland (2002).

12. J.K. Mackenzie, The Elastic Constants of a Solid Containing Spherical Holes, Proc Phys Soc B 683 (1950) 2-11.

13. D.P. Bentz, E.J. Garboczi, D.A. Quenard, Modelling Drying Shrinkage in Reconstructed Porous Materials: Application to Porous Vycor Glass, Modelling Simul Mater Sci Eng, 6 (1998) 211-236.

14. L.F. Nielsen, A research note on sorption, pore size distribution, and shrinkage of porous materials, Building Materials Laboratory, The Technical University of Denmark, Lyngby, Denmark (1991) TR 245/91.

15. A.B. Hossain, B. Pease, J. Weiss, Quantifying Early-Age Stress Development and Cracking in Low *W/C* Concrete Using The Restrained Ring Test With Acoustic Emission, Submitted for publication to Transp Res Rec, March (2003).

16. A.M. Neville, Properties of Concrete, 4th Ed., John Wiley & Sons, Inc., NY (1996).

17. S. Mindess, Fracture Process Zone Detection, Chapter 5 in Fracture Mechanics Test Methods for Concrete, RILEM Report 5, Ed. S.P. Shah, A. Carpinteri, Chapman and Hall, NY (1991) 231-262.

18. H. Horii, T. Ichinomiya, Observation of Fracture Process Zone by Laser Speckle Technique and Governing Mechanism in Fracture of Concrete, Int J of Fracture 51 (1991) 19-29.

19. H. Mihashi, N. Nomura, Microcracking and Tension-Softening Properties of Concrete, Cem & Conc Comp 14 (1992) 91-103.

20. F. Ansari, Mechanism of Microcrack Formation in Concrete, ACI Mat J 86 (1989) 459-464.

FIGURES

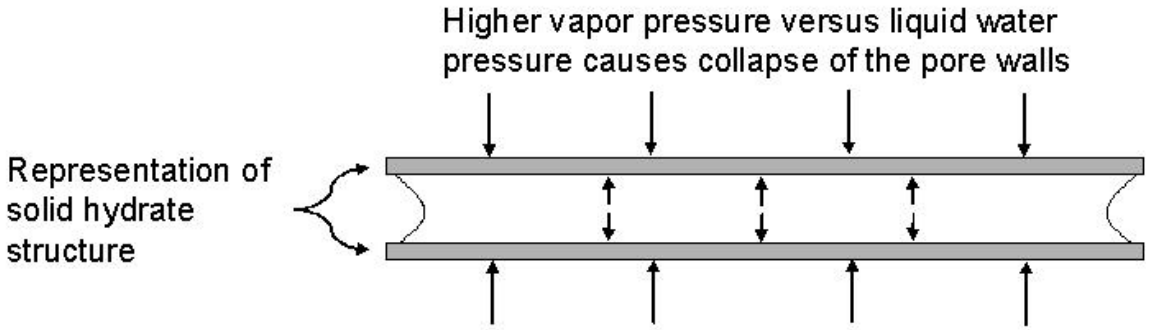

Figure 92. Model illustration of pressure differential caused by curved menisci

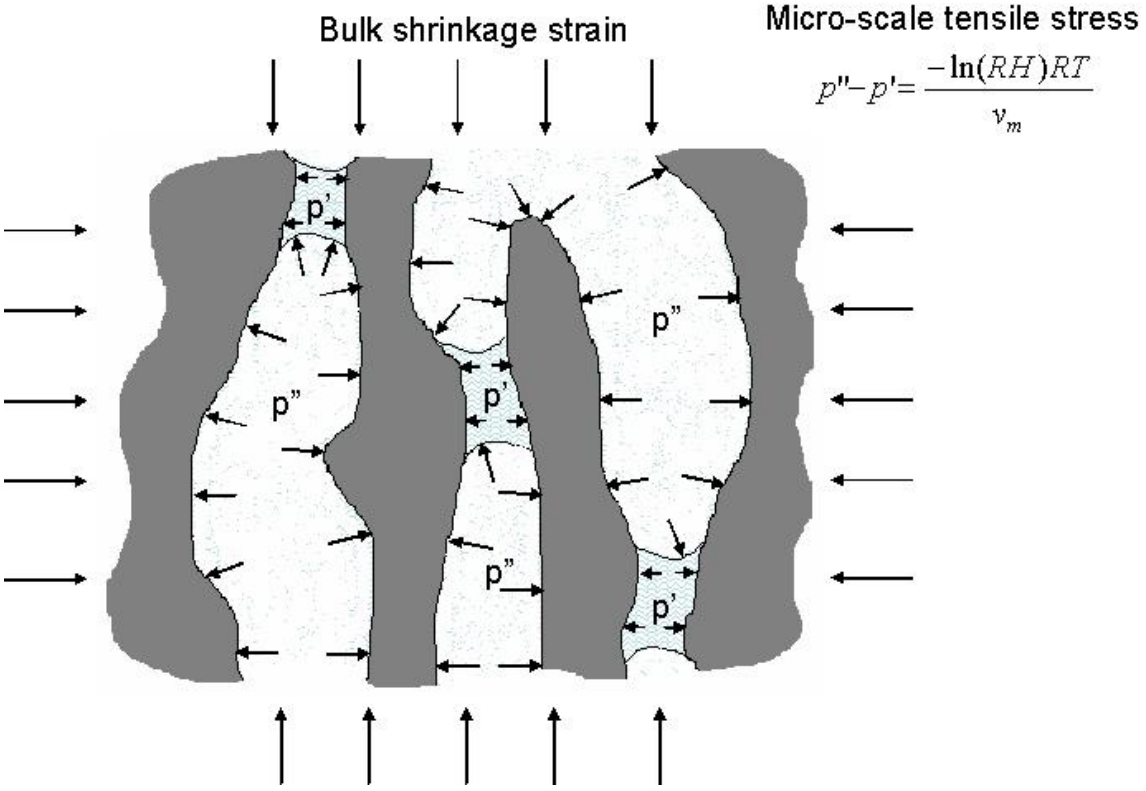

Figure 93. Illustration of how differential pressures cause bulk shrinkage in cement paste

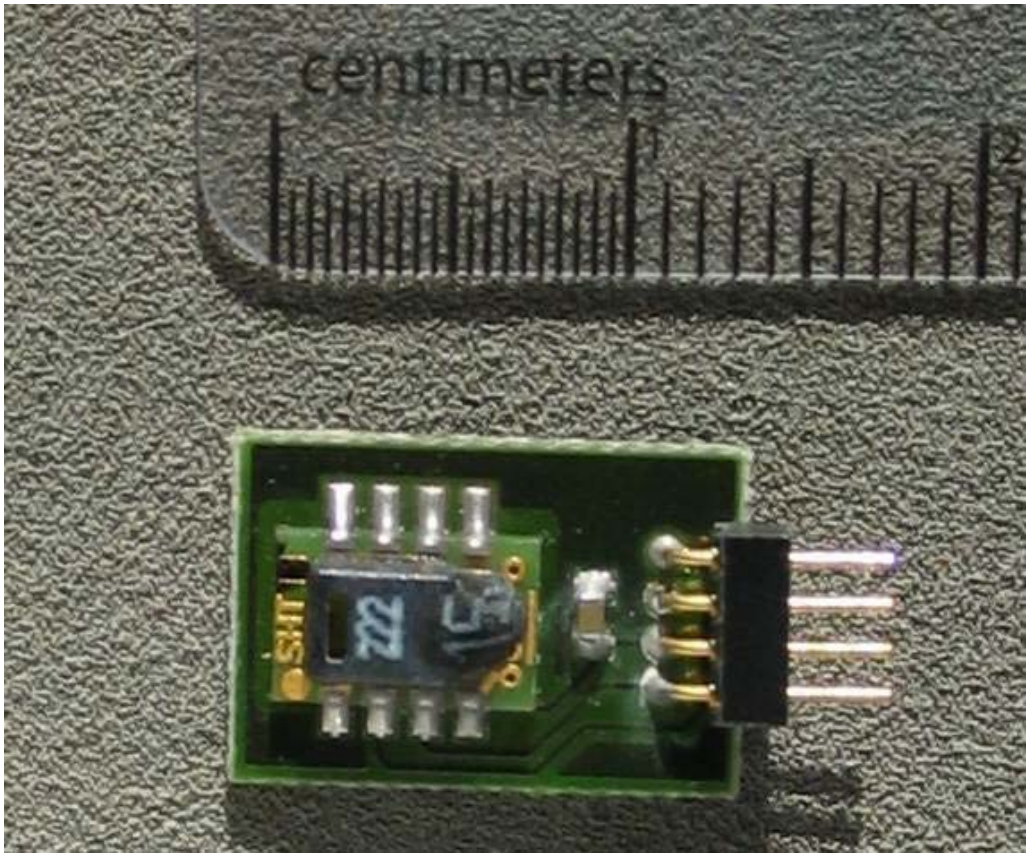

Figure 94. Digital, embeddable RH sensor (shown without embedment packaging)

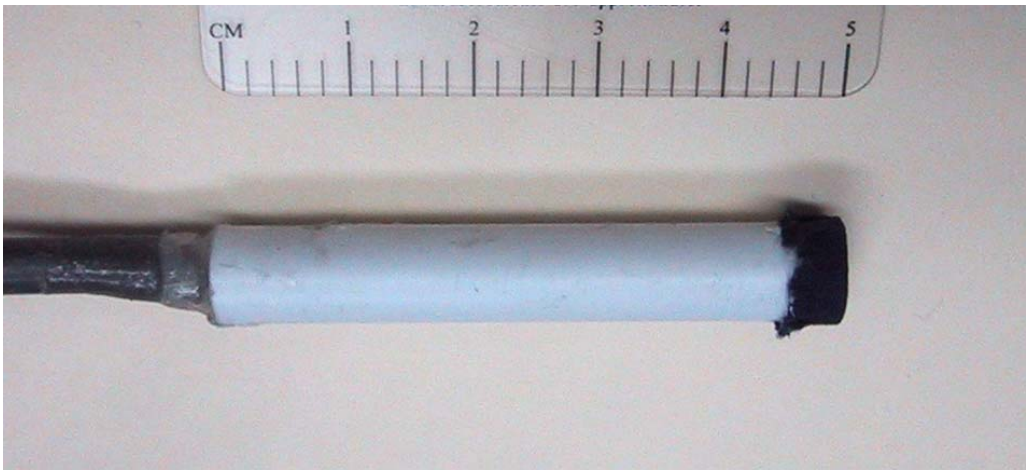

Figure 95. Packaged RH sensor ready for embedment in concrete

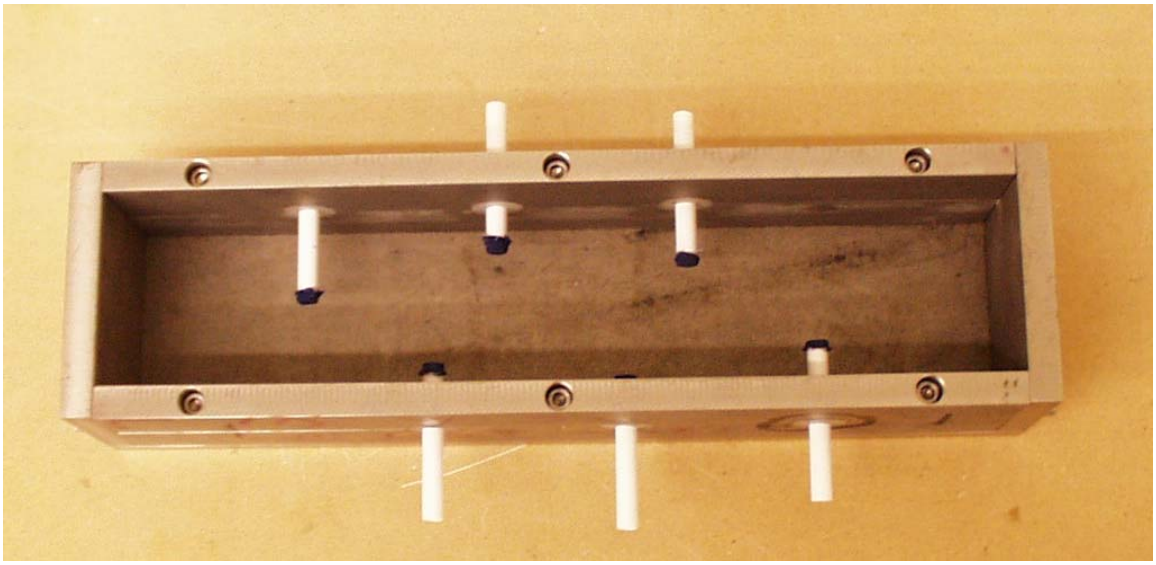

Figure 96. Mold for casting concrete prism with embedded RH sensors at various depths

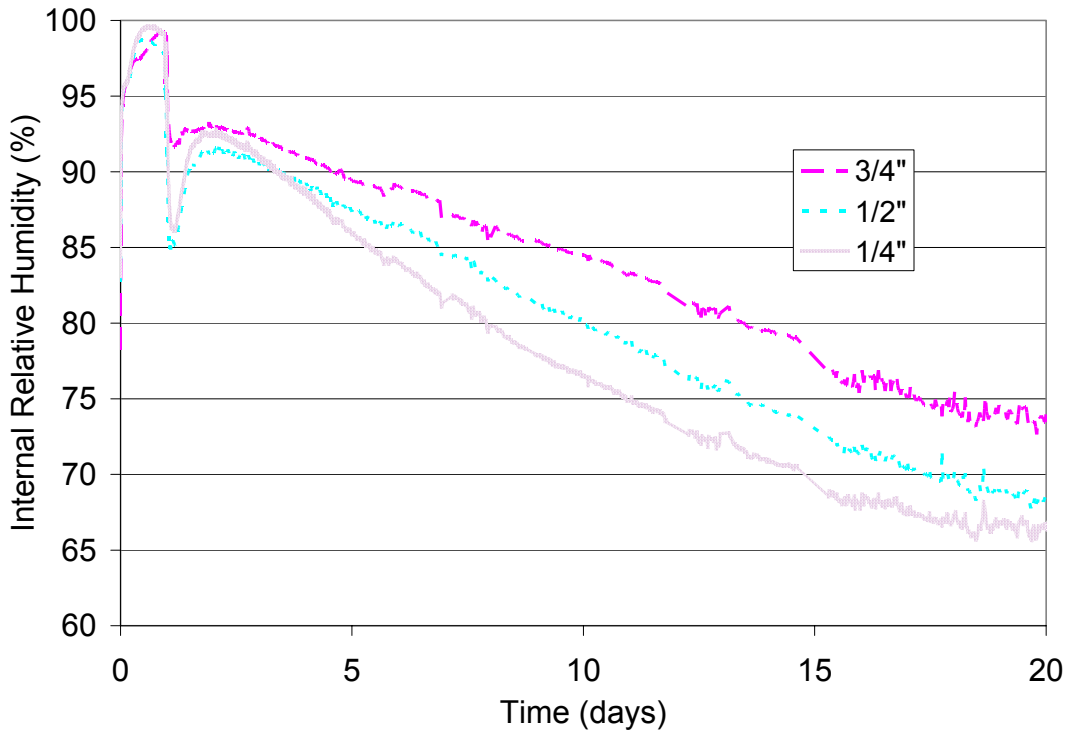

Figure 97. Internal RH at 3 depths from drying surface (drying from 1 day)

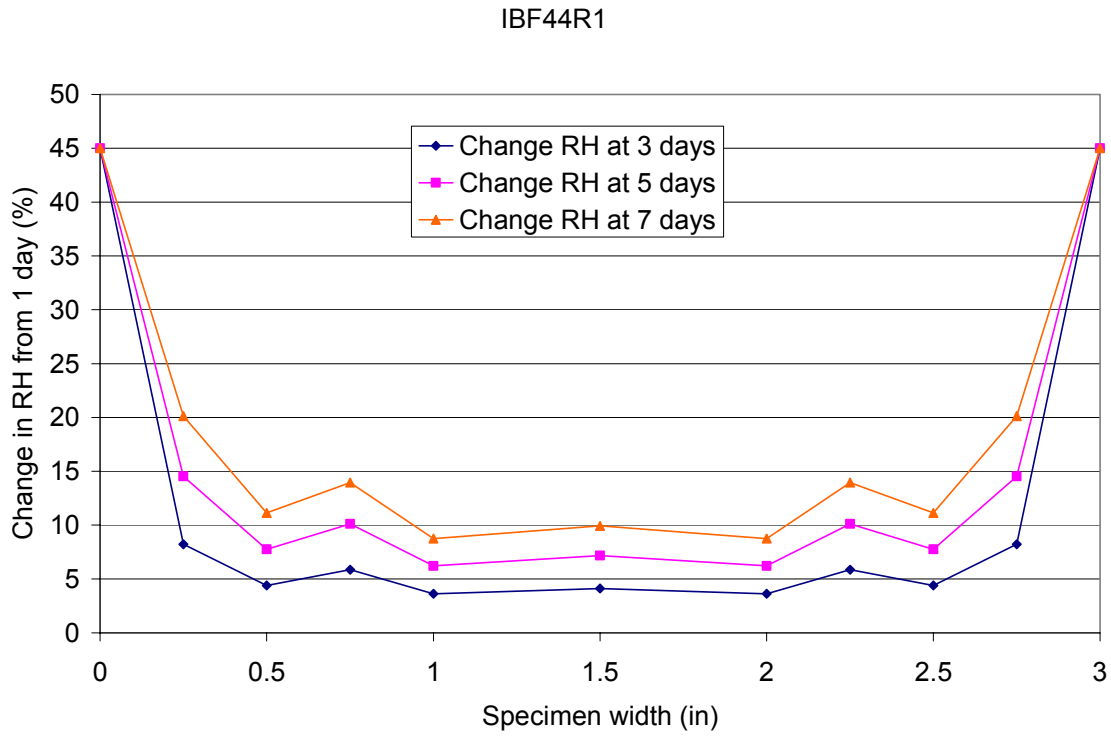

Figure 98. Drying profile for symmetrically drying 3" cross-section (IBF44R1)

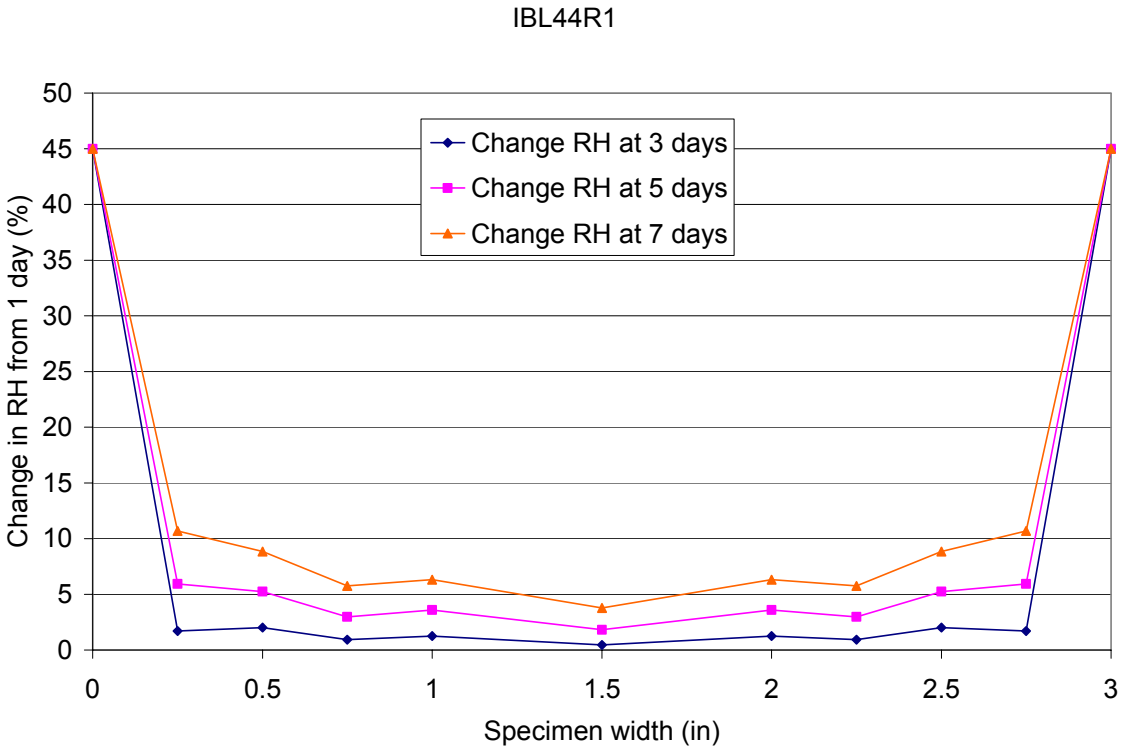

Figure 99. Drying profile for symmetrically drying 3" cross-section (IBL44R1)

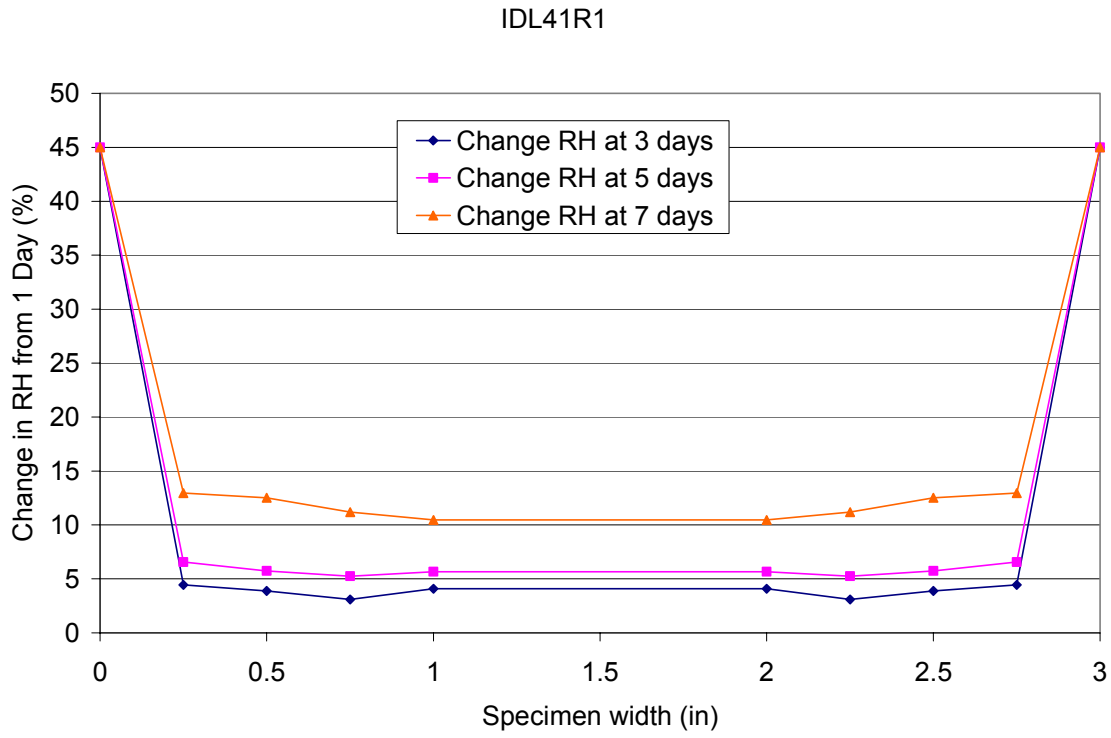

Figure 100. Drying profile for symmetrically drying 3" cross-section (IDL41R1)

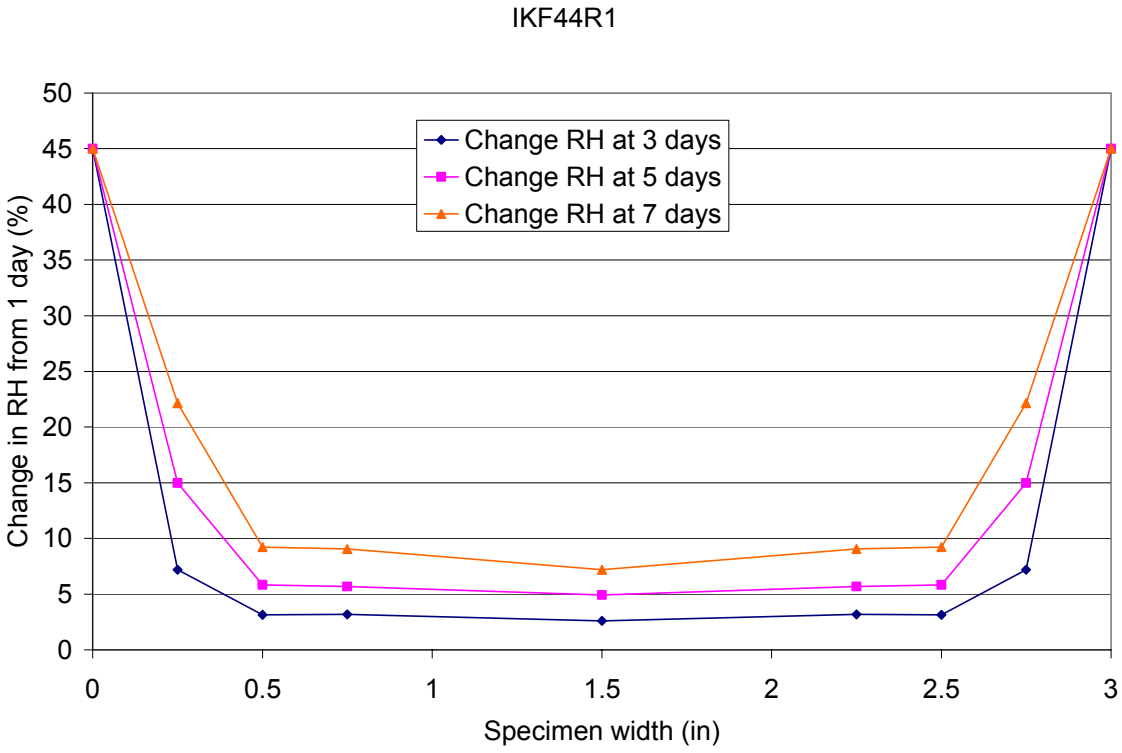

Figure 101. Drying profile for symmetrically drying 3" cross-section (IKF44R1)

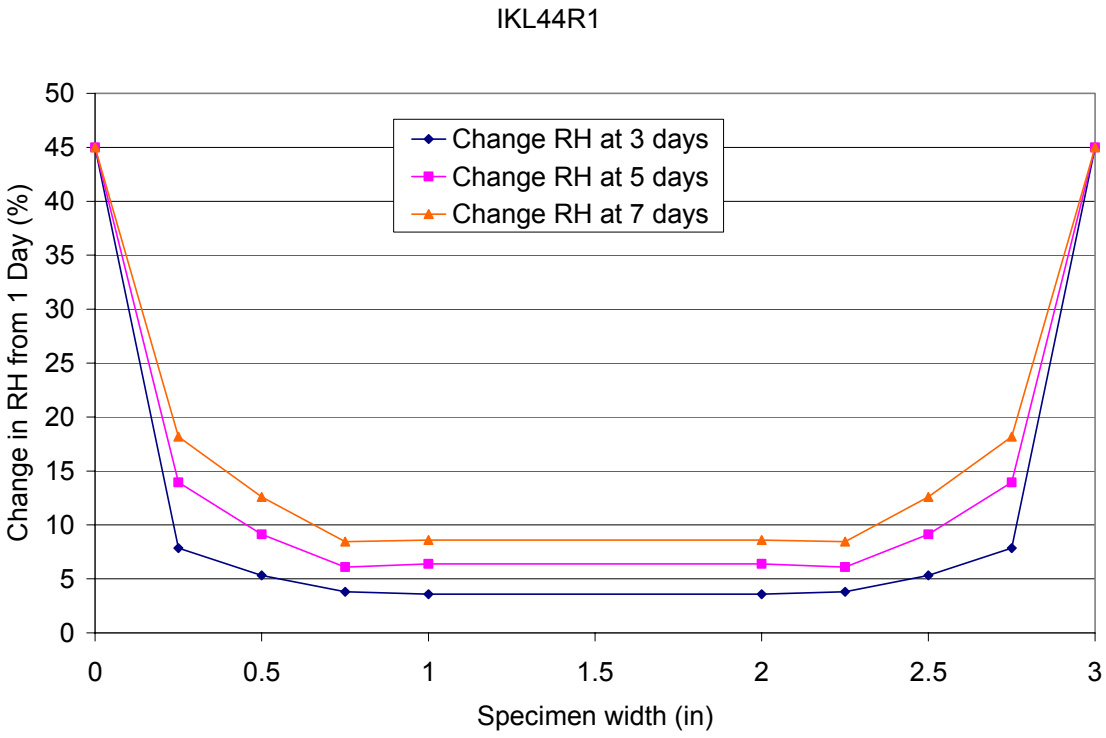

Figure 102. Drying profile for symmetrically drying 3" cross-section (IKL44R1)

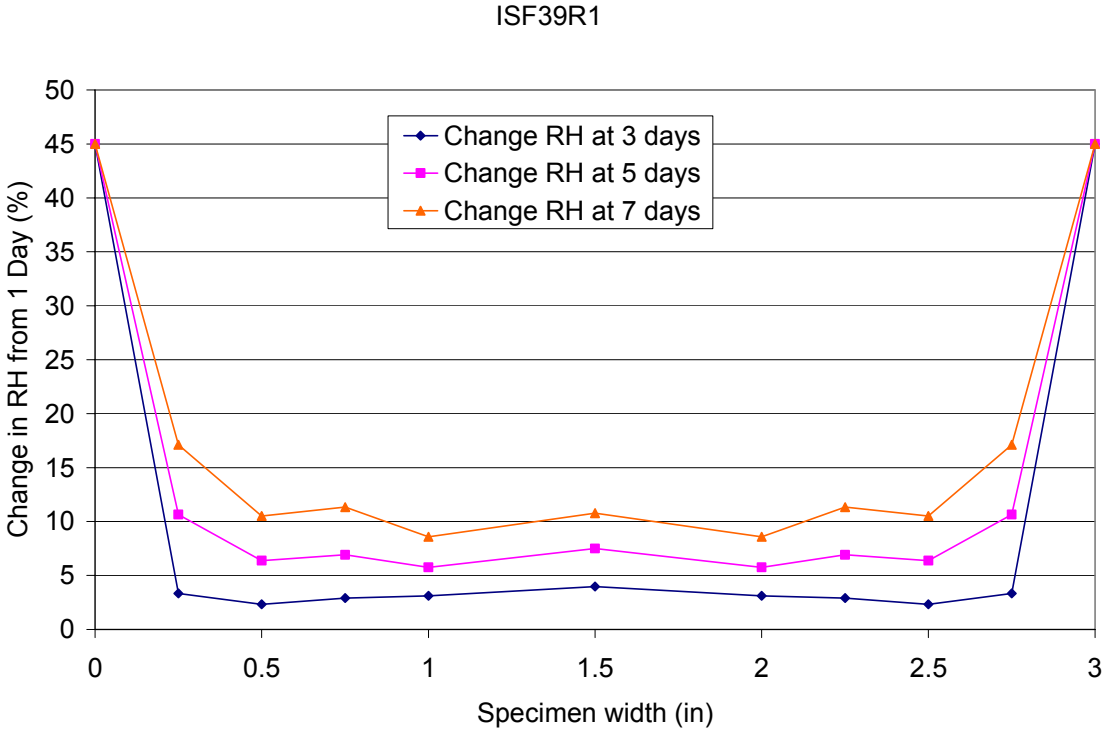

Figure 103. Drying profile for symmetrically drying 3" cross-section (ISF39R1)

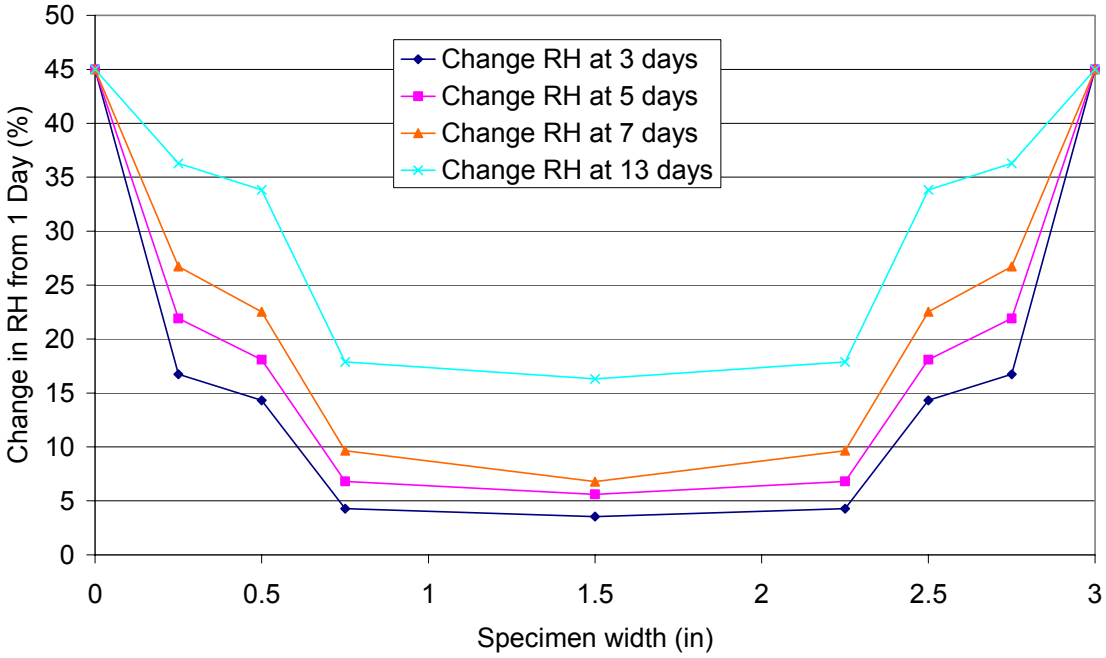

Figure 104. Drying profile for symmetrically drying 3" cross-section (ISL44R1)

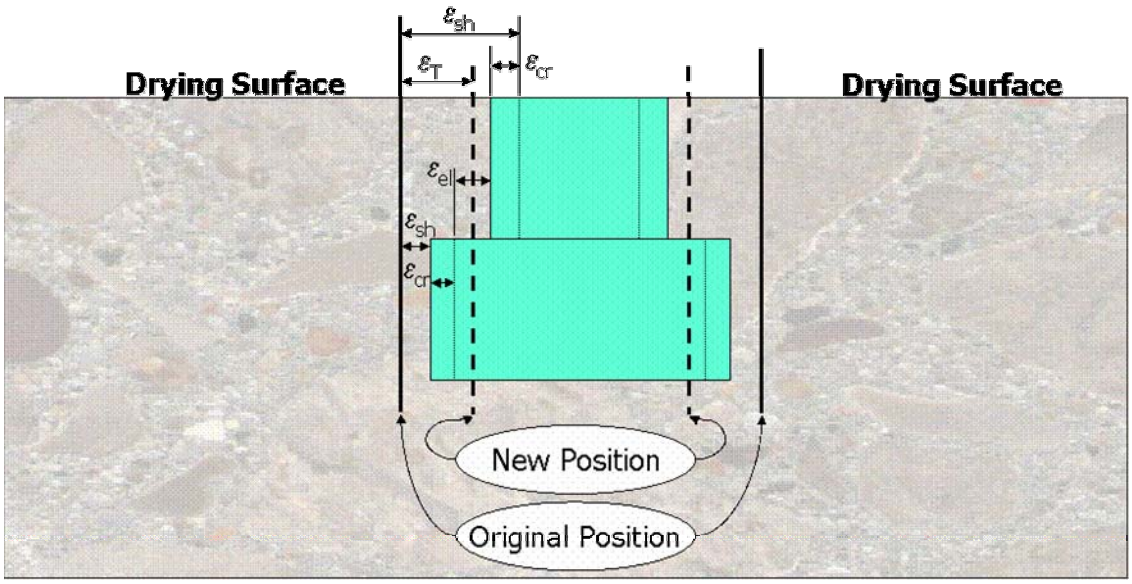

Figure 105. Graphic illustration of strain components in concrete free shrinkage

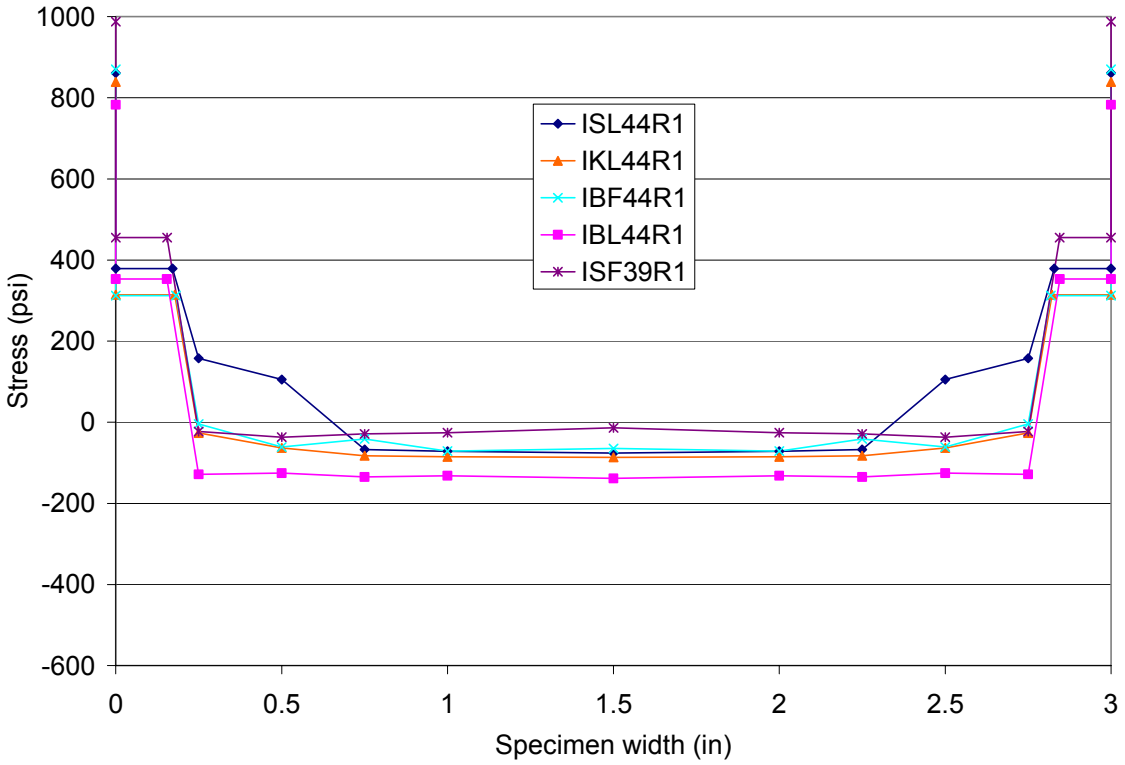

Figure 106. Stress profile in free shrinkage prism exposed to symmetric drying (3 days)

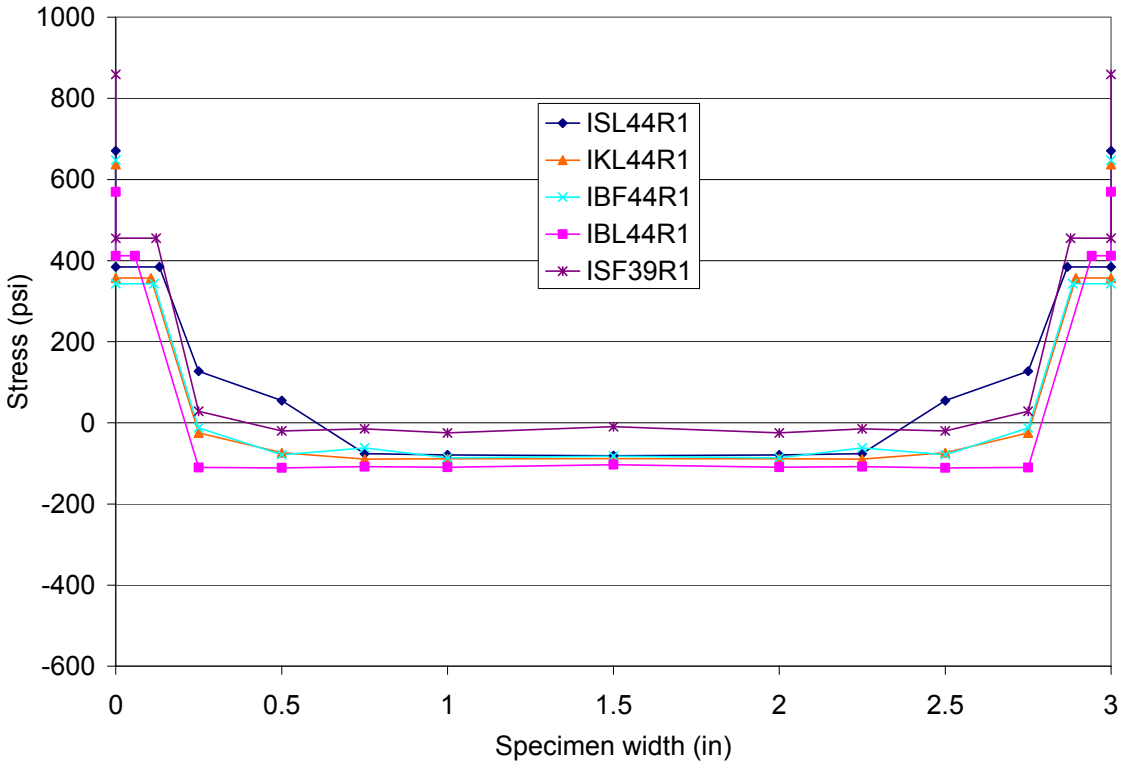

Figure 107. Stress profile in free shrinkage prism exposed to symmetric drying (5 days)

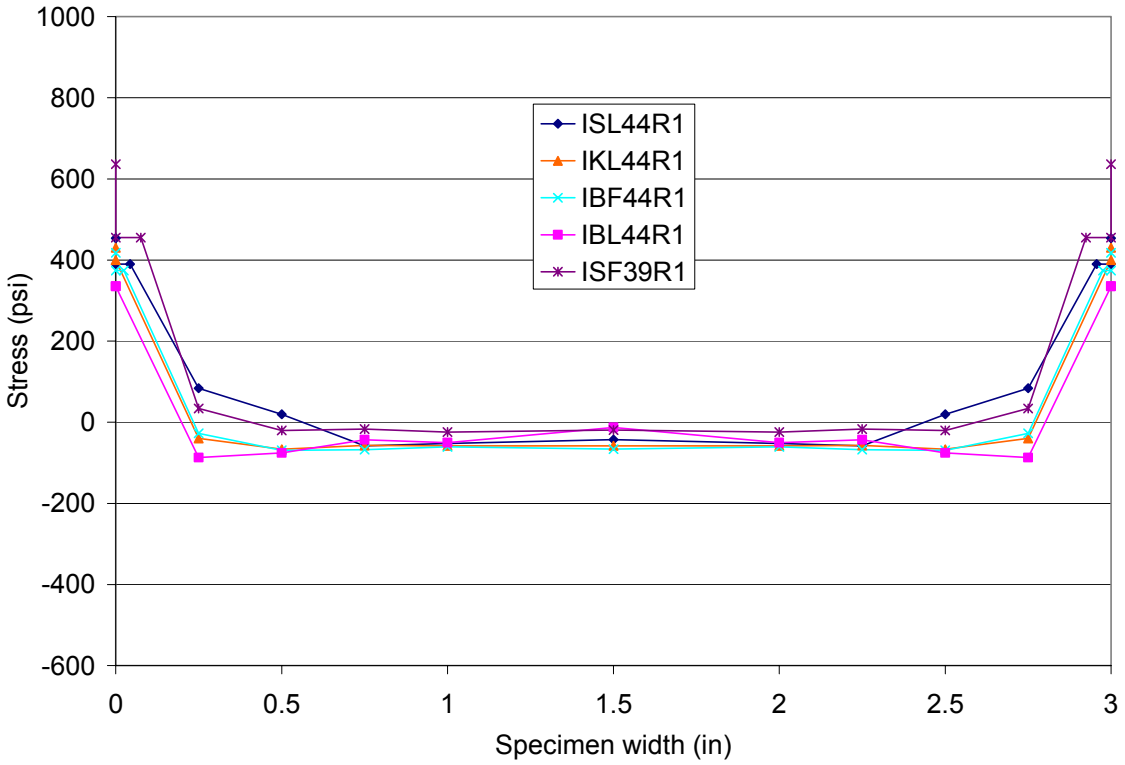

Figure 108. Drying stress profile in free shrinkage prism (7 days)

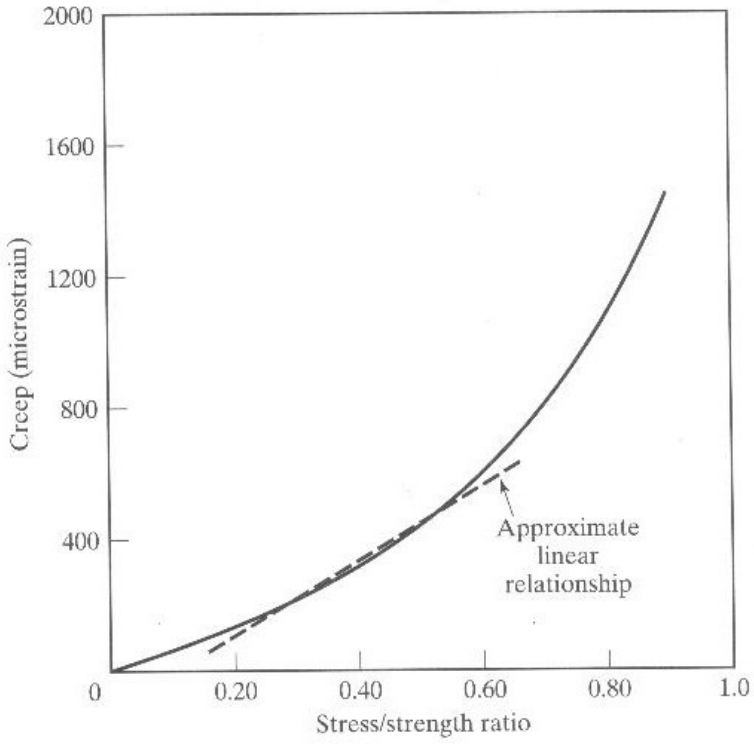

Figure 109. Change in specific creep with stress in concrete, from Mindess and Young [1]

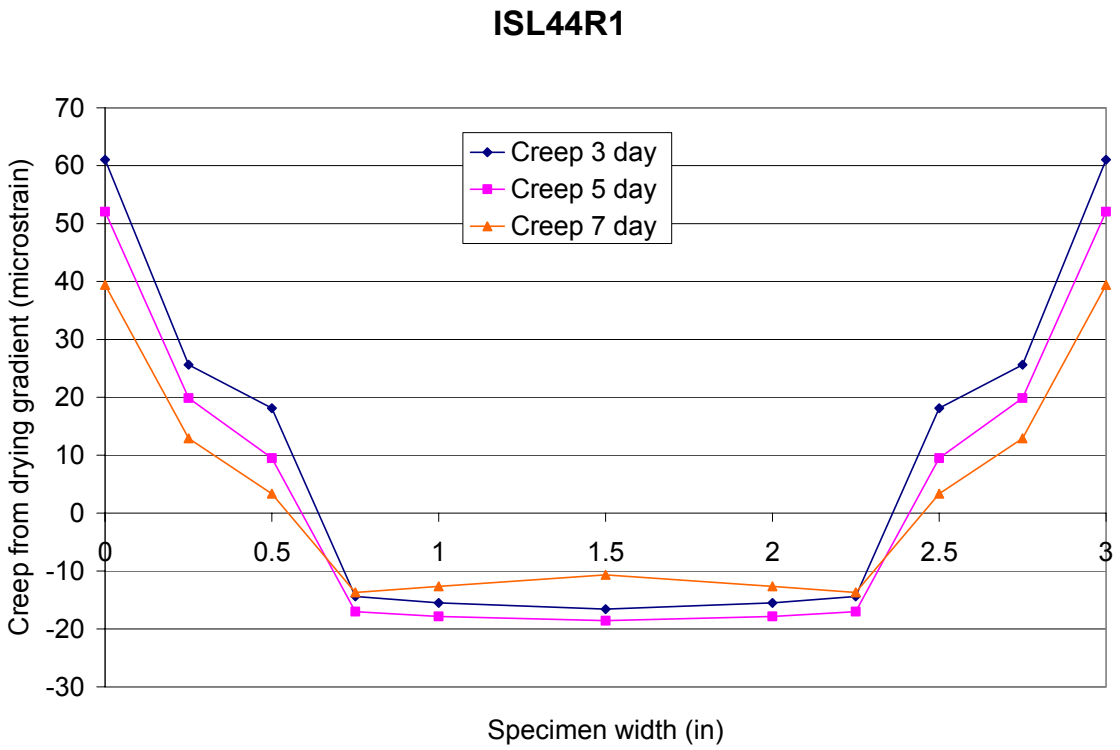

Figure 110. Creep strain due to drying stress gradient, calculated from Eq. 7.11

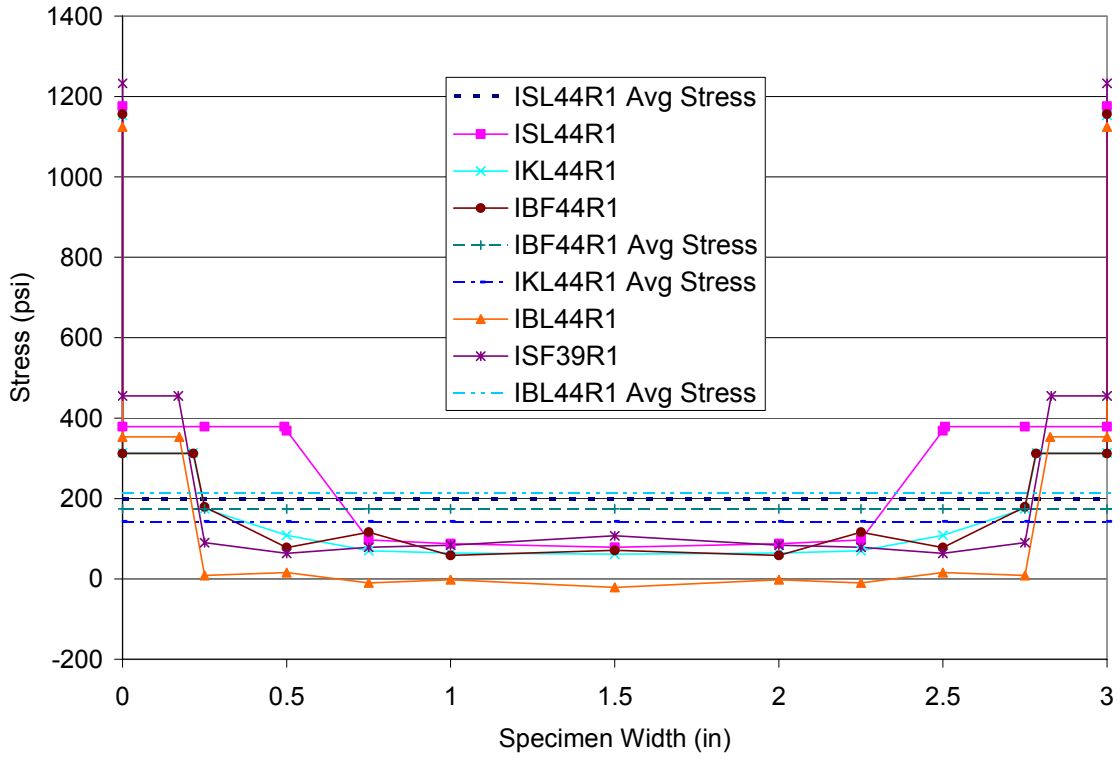

Figure 111. Drying stress profile in restrained concrete specimen (age: 3 days)

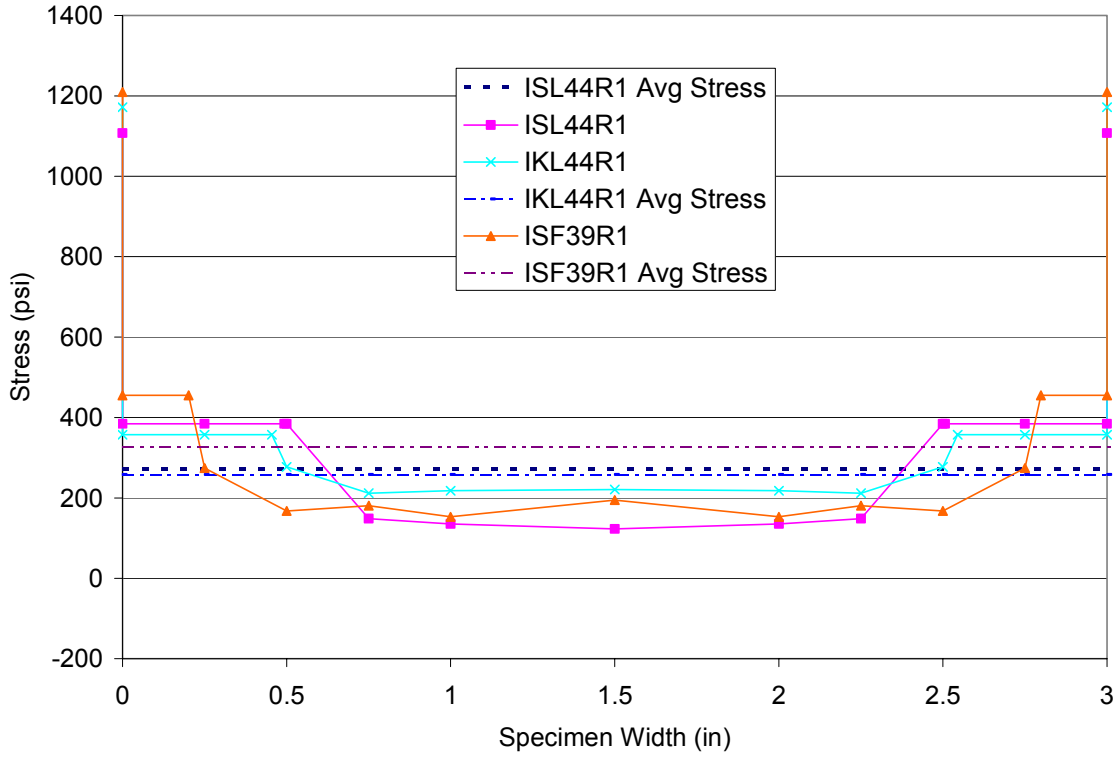

Figure 112. Drying stress profile in restrained concrete specimen (age: 5 days)

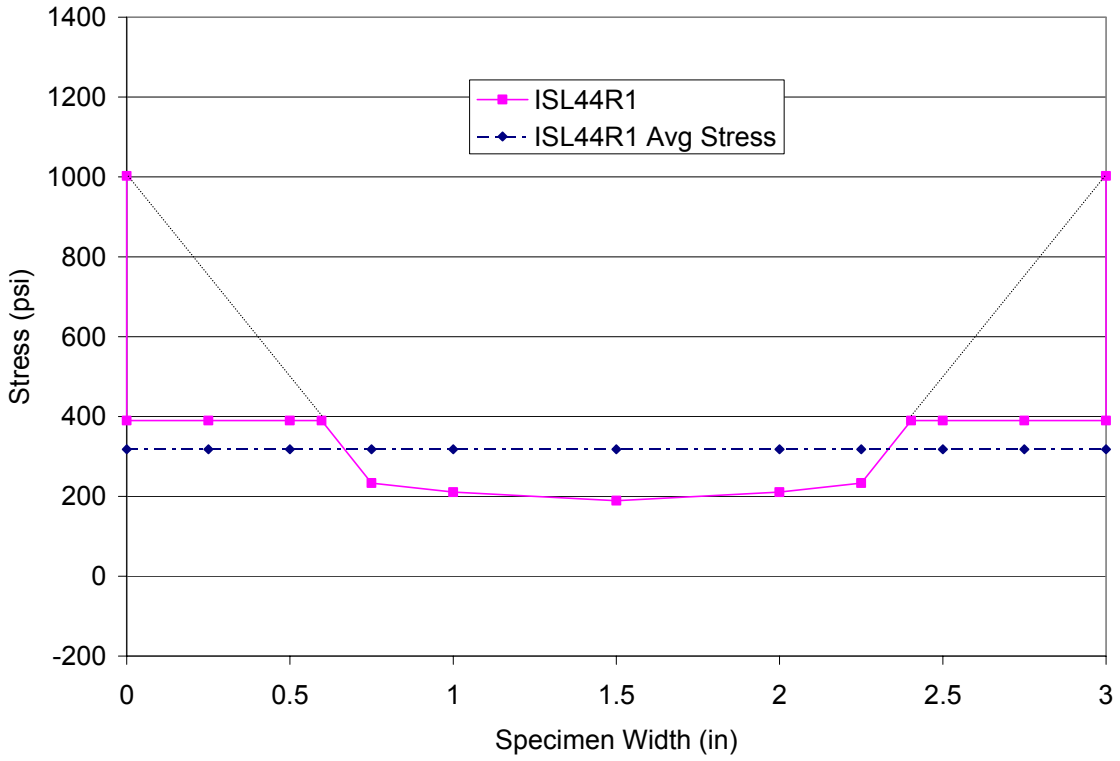

Figure 113. Drying stress profile in restrained concrete specimen (age: 7 days)

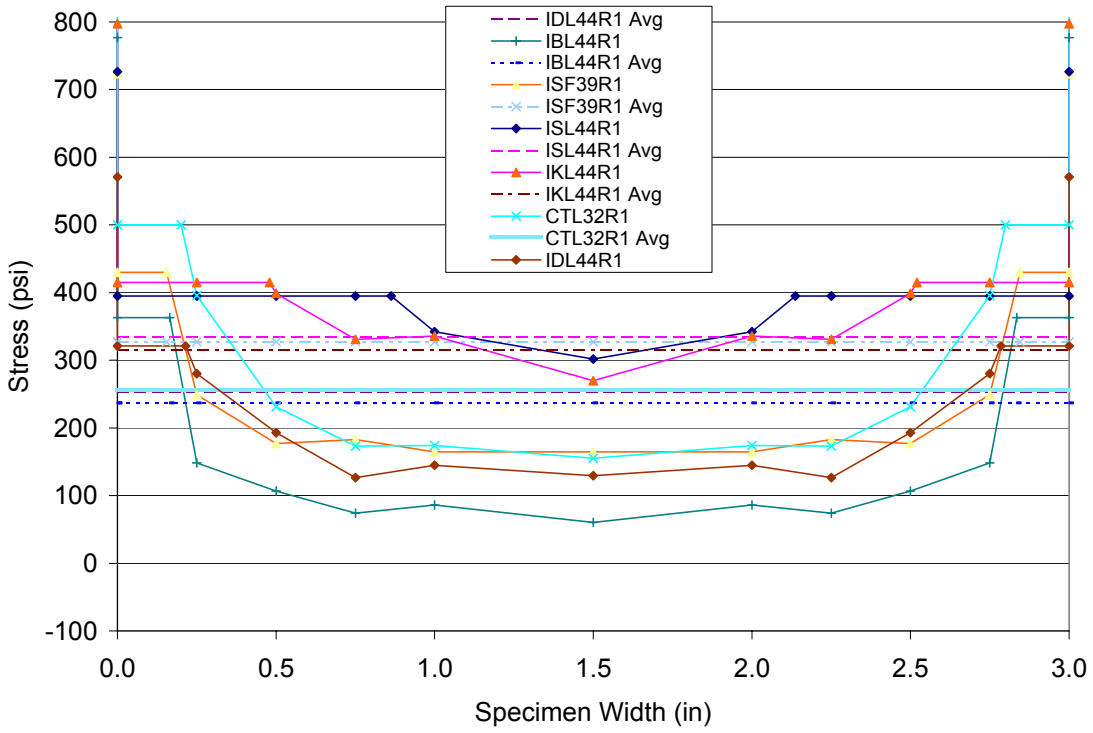

Figure 114. Drying stress gradients at time of failure

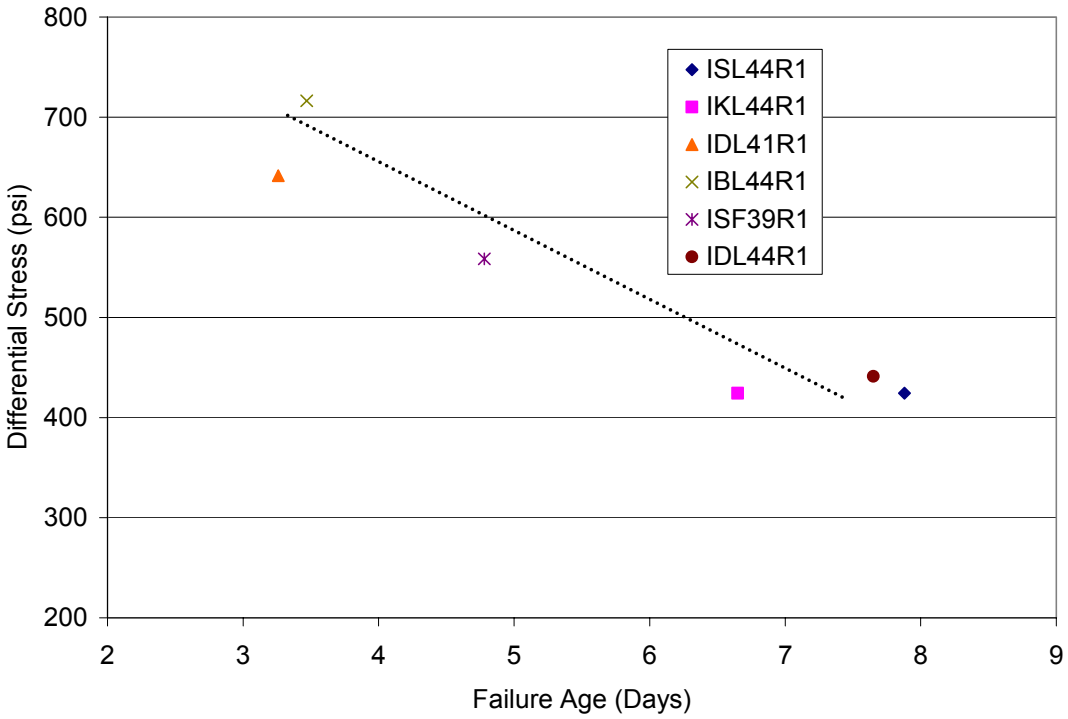

Figure 115. Differential stress over cross-section vs. failure age

8. LABORATORY STUDY CONCLUSIONS

High Performance Concrete (HPC) offers compelling advantages for transportation structures such as bridge decks and substructures. HPC can have unique behavior and mixture characteristics that cause problems such as early age cracking. The IDOT approach to designing HPC mixtures has resulted in materials that do not differ much in material behavior from conventional OPC mixtures. IDOT mixtures tested did not have low *w/c* or high amounts of silica fume. Therefore, autogenous shrinkage was not very high and did not play a significant role in early age stress development and cracking. The heat generated during hydration was the same for IDOT HPC and conventional mixtures, indicating that there was no increased risk of thermal stress development in comparison to OPC mixtures. By adding relatively small amounts of silica fume or metakaolin, the additional heat sometimes associated with HPC materials was not observed. The cementitious material source and *w/c* ratio had the greatest impact on material behavior in this study.

Cracking of HPC is dependent on the combined effects of volumetric changes and response of the material to stress. Stress develops due to volumetric changes such as drying shrinkage and autogenous shrinkage when the material is restrained. Creep acts as a relaxation mechanism to reduce the stress developed by shrinkage. When the stress reaches a critical level, cracking occurs, but the stress level that causes cracking is usually lower than the measured tensile strength. The stress that develops is not uniform over the cross section due to the drying gradient. Stress reaches much higher levels at the concrete surface where drying originates. A correlation was observed between the failure age of concrete in the restrained uniaxial test to the severity of the differential stress from the drying gradient. Average shrinkage stress levels were approximately 80% of the concrete tensile strength at the time of failure. Concrete specimens in

direct tension often fail below their measured split tensile strength. Part of the difference may be attributed to this indirect method for tensile strength measurement.

Early age tensile strength plays a critical role in the long-term durability of concrete structures. Shrinkage stresses that develop at early age will cause cracking much sooner if sufficient strength has not been achieved. High strength is usually associated with low creep, which is detrimental to crack resistance. The importance of wet curing for as long as possible is reinforced here as well. Not only does wet curing delay the start of drying shrinkage, but also the strength of the material continues to develop, which further reduces the risk of cracking. Concrete will continue to gain strength over time, so if shrinkage stress development is prevented during the very early age when the concrete is one or two days old, the risk for cracking is greatly diminished.

To successfully evaluate the potential performance of a concrete mixture for use in an IDOT bridge deck, an analysis tool was developed for the concrete ring test. The average stress of the drying concrete ring was compared to the measured steel ring strain, and a graph was devised for comparing the stress development in any concrete ring using a steel ring thickness of 3/8", ½", or 1". This criteria will allow IDOT to set a material performance benchmark by testing a material that is known to have acceptable performance, and then comparing all future materials with the benchmark.

III. FIELD PROJECTS AND INSTRUMENTATION

1. INTRODUCTION

In an effort to increase the lifespan of concrete bridges, many state DOTs are turning to high-performance concrete (HPC) for their bridge deck material. High-performance concrete often exhibits a reduction in permeability and an increase in strength relative to ordinary portland cement concrete (OPC). However, the risk of early-age cracking in HPC relative to OPC is unclear.

Several state DOTs have begun implementing HPC in real structures in an effort to evaluate their performance. The Virginia Department of Transportation (VDOT) has recently constructed bridge decks using HPC with partial replacement of cement by ground granulated blast furnace slag, and a water to cementitious ratio (*w/c*m) of 0.40 and 0.38 [1]. The New York State DOT (NYSDOT) has used an HPC mixture that uses a 6% replacement of cement by silica fume and 20% replacement by fly ash, and a *w/c*m ratio of 0.40 [2]. The mixture was developed to meet permeability requirements as well as strength requirements. By 1998, NYSDOT had constructed over 80 bridge decks using this mixture. No cracking was exhibited on approximately 49% of the decks, which was considered an improvement over decks constructed with OPC. It was also recognized that in the HPC decks that exhibited cracking, the cracks occurred within 14 days of initial concrete placement. This observation reinforces the importance of stress development in HPC at an early age.

The Nebraska Department of Roads (NDOR) has used an HPC mixture that incorporates a 10% addition of fly ash and a *w/c*m ratio of 0.34 [3]. Like the NYSDOT, NDOR developed the HPC mixt design based on permeability requirements in addition to strength. The Texas

Department of Transportation (TxDOT) has recently used a variety of low-permeability HPC mixtures that incorporate 28-32% replacement of cement by fly ash, and *w/c*m ratios ranging from 0.31 to 0.43 [4]. Some shrinkage cracks were observed in the HPC decks that were typical of cracks seen in OPC decks. The New Hampshire Department of Transportation (NHDOT) has also investigated HPC bridge decks [5]. A mixture incorporating a 7.5% replacement of cement with silica fume and a *w/c* ratio of 0.38 was used in a bridge deck cast in 1996. The mixture also contained an added corrosion inhibitor.

Not only has there been an increase recently in HPC, but there has also been an increase in interest in structural monitoring of bridge decks in general. One of the first instrumentations of an HPC bridge deck in North America occurred in 1992 [6]. The bridge deck was instrumented with thermocouples to measure temperature and vibrating-wire extensometers to measure strain. Measurements were taken for a period of one year after casting. In a similar study at the Cincinnati Infrastructure Institute [7], a concrete bridge deck was also instrumented with extensometers and thermocouples.

The following chapters in this report describe the instrumentation of concrete bridge decks utilizing OPC and various HPC mixtures. The bridges were instrumented by UIUC and IDOT in an effort to better understand the development of stresses in concrete bridge decks utilizing varying materials and structural components.

References

1. C. Ozyildirim, HPC Bridge Decks in Virginia, Concrete International, February (1999), 59-62.

2. S. Alampalli, F. Owens, Increasing Durability of Decks Using Class HP Concrete, Concrete International, July (2000), 33-35.

3. M.W. Beacham, HPC Bridge Deck in Nebraska, Concrete International, February (1999), 66-68.

4. M.L. Ralls, Texas HPC Bridge Decks, Concrete International, February (1999), 63-65.

5. C.M. Waszczuk, M.L. Juliano, Application of HPC in a New Hampshire Bridge, Concrete International, February (1999), 61-62.

6. M. Lachemi, A-P. Bois, B. Miao, M. Lessard, P-C. Aitcin, First Year Monitoring of the First Air-Entrained High-Performance Bridge in North America, ACI Structural Journal 93 (1996), 379-386.

7. M.S. Lenett, V.J. Hunt, A.J. Helmicki, A.E. Aktan, Instrumentation, Testing, and Monitoring of a Newly Constructed Reinforced Concrete Deck-on-Steel Girder Bridge-Phase III, Report # UC-CII 01/1 (2001).

2. EXPERIMENTAL PROCEDURES

2.1 Instrumentation Equipment

The concrete bridge decks were instrumented with strain gages and thermocouples. This section will detail the instrumentation and data collection used in the field research. In addition to the strain and temperature instrumentation, relative humidity sensors were used in the field study to a limited degree, but this measurement system is addressed separately in a later chapter.

2.1.1 Strain gages

The strain gages were an embedment type gage produced by Vishay Micro-Measurements Group. The sensor consists of a 4 inch 350 ohm (Ω) foil strain gage (nickel-chromium alloy on polymide backing) covered in a proprietary polymer concrete casing so that it can be embedded in concrete. Figure 116 shows the embedment strain gage. The surface of the gage has a honeycomb pattern that helps it adequately bond to concrete. The gage is waterproof, and is designed to be placed in fresh concrete. The gages have 22 AWG copper lead wires pre-attached.

The embedment strain gages were connected to 22 AWG lead wires ranging between 10 to 130 feet, depending on their location to be cast in the bridge deck. The gages were connected in a three-wire quarter bridge circuit using bridge completion modules provided by Campbell Scientific.

2.1.2 Thermocouples

The thermocouple wire used in the bridge deck instrumentation was a Type T 20 gage wire produced by Omega. These thermocouples consist of copper and constantan wires, and are functional between -250 to 250° C. The ends of the solid thermocouple wires were twisted and then soldered to ensure an adequate electrical connection.

2.1.3 Data Collection

Both the strain data and the temperature data was recorded using Campbell Scientific Data acquisition hardware and software. Leadwires from the strain gages were routed through either an AM416 or an AM16-32 multiplexer, using a separate completion module for each gage on the multiplexer, or using a single completion module for all the gages positioned between the multiplexer and the datalogger. The datalogger used was a Campbell Scientific CR10X, shown in Figure 117. The thermocouple wires were routed through an AM25T multiplexer, which has an internal RTD (resistance temperature detector) to measure the cold junction temperature required to compute the temperature at the soldered end of the thermocouple. The multiplexer was controlled by the CR10X datalogger. The CR10X datalogger stored the measured strain and temperature data to memory until it was collected via download from a cellular modem. A cellular antenna wired to the CR10X allowed for this remote data collection. The system was powered by a 12 V battery for which the charge was maintained using a solar panel shown in Figure 118. The antenna, cellular modem, and the solar panel were purchased from Campbell Scientific. All of the data acquisition hardware was sealed in a waterproof fiberglass enclosure. Additional specifications of the Campbell Scientific equipment can be obtained in the user manuals. In addition to the strain and temperature instrumentation, relative humidity sensors were used in the field study.

2.1.4 Accuracy and Sources of Potential Error

The accuracy of the temperature measurements is controlled primarily by the AM25T multiplexer rather than the thermocouple. The advertised accuracy of the AM25T is ± 0.2° C between operating temperatures of -25 to 50° C. The accuracy of the strain gages is more difficult to approximate. The gages have an advertised resistance deviation of 0.8%. There is an additional source of potential error caused by the leadwire resistance. The leadwire lengths used on all bridges instrumented ranged from 10 to 130 feet. For the leadwire used, the resistance associated with those lengths ranges from 0.5 to 4.5 mΩ. Any loss in sensitivity in the strain measurement caused by leadwire resistance was minimized by using a 3-wire connection. Compared to a 2-wire hookup, the 3-wire hookup reduces the sensitivity loss caused by leadwire resistance by 50%. The remaining error associated with leadwire resistance can be calculated as

$$1 + \frac{R_L}{R_g},$$

where R_L is the resistance in the leadwires and R_g is the gage resistance. Using this equation, the maximum loss in sensitivity caused by the resistance in the 130 ft lead wire is less than 1%.

A potential source of error in the strain gages is the self-temperature compensation. The mV/V output of the strain gages themselves varies with the temperature of the gage. The gages are designed to output a temperature dependent voltage that completely negates any actual strain increase in the surrounding concrete due to thermal dilation. The gages correct for 10.3 με/C°, which a rough approximation for the coefficient of thermal expansion for concrete. This was a problem, however, since one of the main interests in instrumenting the bridge decks was to monitor the concrete thermal strains. A correction factor of 10.3 με/C° was applied to the measured data in order to "back-out" the self-temperature compensation of the strain gages.

2.2 Sensor Validation

Concrete embedment gages manufactured by Vishay Micromeasurements Group were used extensively to monitor strains in the concrete bridge decks. Due to this widespread application of the gages, a series of tests were performed to validate their accuracy. These tests included cyclic loading to analyze the potential for hysteresis and measurements of concrete shrinkage in the laboratory.

For the cyclic testing, an embedment gage was epoxied to an aluminum bar (1" by 12" x ¼" thick) as shown in Figure 119. The bar was then gripped on each end and loaded cyclically in tensile force of 500 lbs. The load was cycled 5 times. Figure 120 shows the strain reading output from the embedment gage at each load cycle. There appears to be very little if any hysteresis caused by the cyclic loading. The results of the cyclic loading are shown in another manner in Figure 121, which plots the strain output versus time. Again, there is little measurable hysteresis.

Since the embedment gages will be used to measure strains in hardened concrete, it was also decided to compare the results of the strains measured from an embedded gage to strains measured in another manner. Since shrinkage strains of 3" x 3" x 11" concrete prisms are routinely measured in the lab using a length change comparator, embedment gages were cast into three prisms. The embedment gages prepared in concrete prisms are shown in Figure 122. Figure 123 shows agreement between strains from the comparator and those measured by the embedded gage.

The cyclic stability and general agreement between the embedment gage measurements and other accepted strain measurements indicates that the embedment gage measurements in the field should be reliable.

2.3 Instrumentation Procedures and Project Descriptions

UIUC researchers were involved with the instrumentation and analysis of six bridge decks from summer 2000 until summer 2003. The bridge projects consisted of US-51 in IDOT District 5 (Macon, IL), Duncan Rd over I-72 in IDOT District 5 (Champaign, IL), the I-55 bridge over Lake Springfield in IDOT District 6 (Springfield, IL), the I-70 bridge over Big Creek in IDOT District 5 (Clark Co.), and the US-51 bridge over the Kaskaskia River in IDOT District 7 (Vandalia, IL). A summary of the structural design aspects of each bridge is shown in Table 4. The focus of this analysis will be on two bridges, Duncan Rd over I-72 and I-70 over Big Creek because of the overall quality of data and the finite element models that were developed. Other bridges will be discussed and data presented in Appendix B.

2.3.1 Duncan Rd / I-72

The Duncan Rd project consisted of a two lane bridge deck for northbound and southbound traffic. UIUC provided the data collection equipment and performed the instrumentation for this deck with assistance from IDOT personnel. The deck was instrumented at five locations corresponding to the zero, maximum positive and maximum negative moment regions in the deck as shown in Figure 124. Locations A and B each have four embedment strain gages and five thermocouples. One embedment gage was used to measure transverse strain at these positions. Locations C, D, and E each have three strain gages and five thermocouples. Two free shrinkage beams were constructed and each contained one strain gage and two thermocouples. The 350-ohm strain gages were manufactured by Measurement Group, Inc. and had an active gage length of 4 inches. Type T thermocouple wire (22 AWG) with Teflon insulation was used. Figure 125 shows a longitudinal cross section displaying the individual

gage orientation. Figure 126 shows the data collection equipment during installation and Figure 127 shows the finished installation with the solar panel and cellular antenna.

The instrumentation work was performed in the week of September 17, 2001 and the deck was placed on September 20, 2001. The concrete mixture is shown in Chapter 4, Table 4-1. The material was a conventional deck mixture used by IDOT that contained fly ash and had a 0.44 *w/c* ratio. The concrete was pumped during placement followed by finishing of the deck with a paving machine. Following placement, a curing compound was applied to the concrete surface.

2.3.2 I-70 / Big Creek

The Big Creek project consisted of a two-lane bridge deck for westbound traffic on Interstate 70 near Marshall, IL. UIUC provided the data collection equipment and performed the instrumentation for this deck with assistance from IDOT personnel. The deck was instrumented at three locations based on the predicted maximum and minimum stress points in the deck as shown in Figure 128. It was decided based on previous experience that the locations corresponding to the zero, maximum positive, and maximum negative moment regions in the deck were not as critical. Locations each have four embedment strain gages and five thermocouples. One embedment gage was used to measure transverse strain at these positions. Two free shrinkage beams were constructed and each contained three strain gages and four thermocouples. Three additional thermocouples were installed in the parapet on top of the deck. The 350-ohm strain gages were manufactured by Measurement Group, Inc. and had an active gage length of 4 inches. Type T thermocouple wire (22 AWG) with Teflon insulation was used. Figure 129 shows a longitudinal cross section displaying the individual gage orientation. Figure 130 shows the data collection equipment during installation and Figure 131 through Figure 135

show the sensors installed at various locations. In Figure 136, the data collection system and the free shrinkage beams are shown. Figure 137 through Figure 139 are of the concrete placement operation. The procedures described are typical of all the bridge deck installations that were performed.

The instrumentation work was performed on August 21, 2001 and the deck was placed on August 27, 2001 starting at 6:30 am. The concrete mixture is shown in Chapter 4, Table 1. The material was an HPC deck mixture with optimized aggregate gradation. The concrete was pumped during placement followed by finishing of the deck with a paving machine. Following placement, wet cotton mats were applied to the concrete surface as seen in Figure 139.

TABLES

Table 4. Structural Configuration of IDOT Bridges

Bridge	Total Length (ft)	# of Spans	Span Length	Beam Type	Beam Spacing
US 51/Macon NB	80	1	80	54" concrete girder	7'-3"
US 51/Macon SB	80	1	80	54" concrete bulb tee	7'-3"
I-72/Duncan Rd.	222	4	41/68	33" steel WF beam	6'-6"
I-55/Lake Springfield	723	5	121/158	54" steel plate girder	8'
I-70/Big Creek	272	4	67/68	42" concrete bulb tee	7'-9"
US 51/Kaskaskia	429	4	84/108	40" steel plate girder	7'-6"

FIGURES

Figure 116. Micro-Measurements embedment strain gage

Figure 117. CR10X datalogger produced by Campbell Scientific

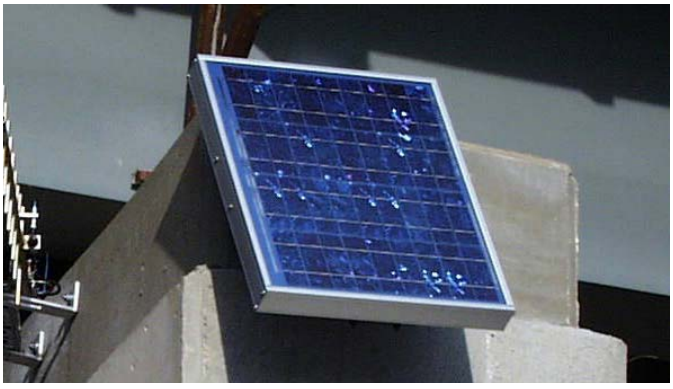

Figure 118. Solar panel for charging 12V battery powering data acquisition system

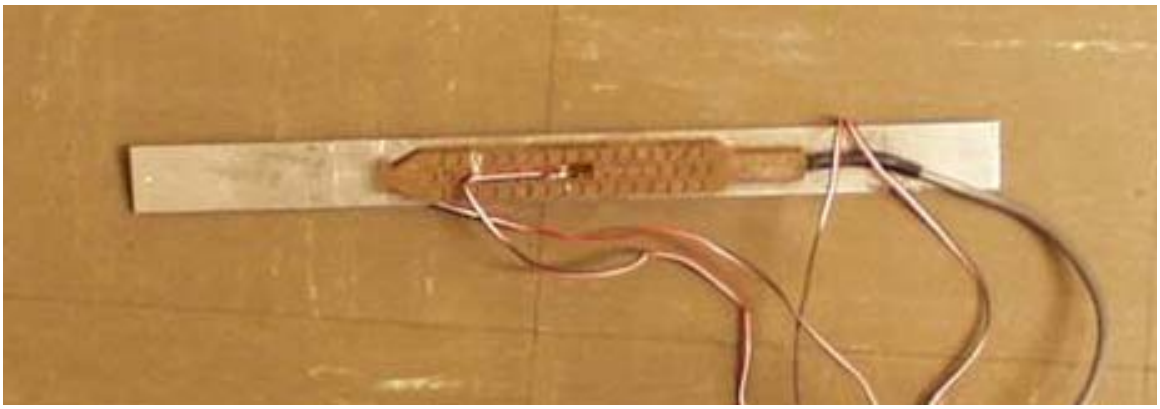

Figure 119. Embedment gage epoxied to an aluminum bar for cyclic loading

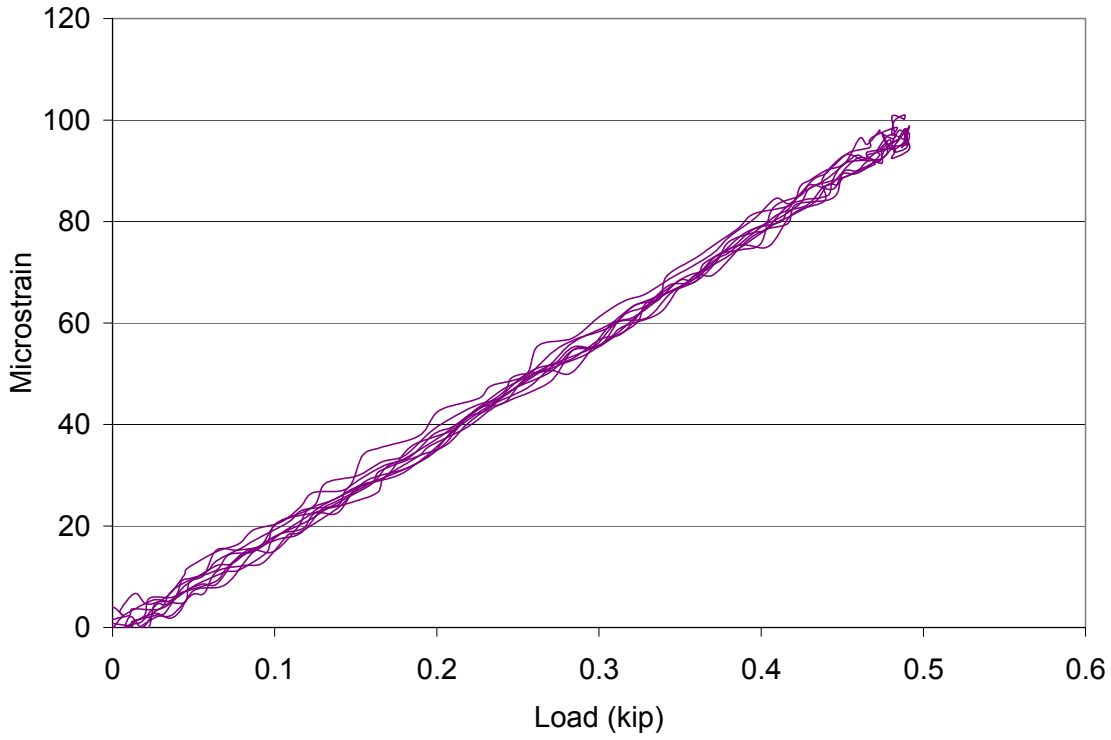

Figure 120. Cyclic loading of aluminum bar with attached embedment gage

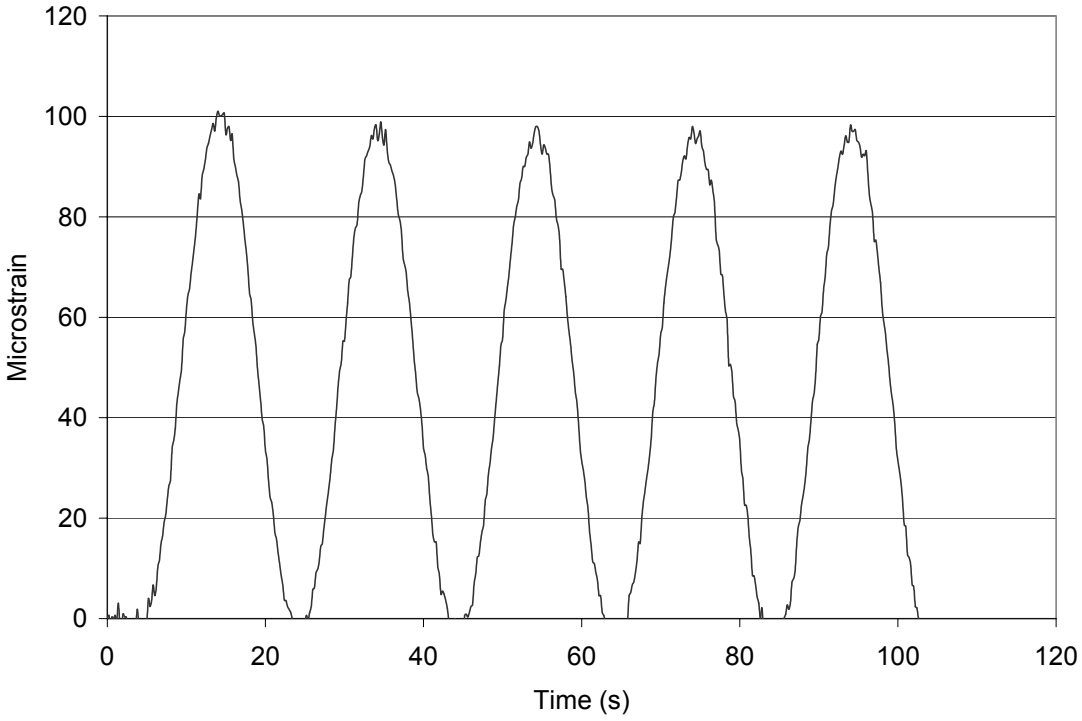

Figure 121. Cyclic loading of aluminum bar with attached embedment gage

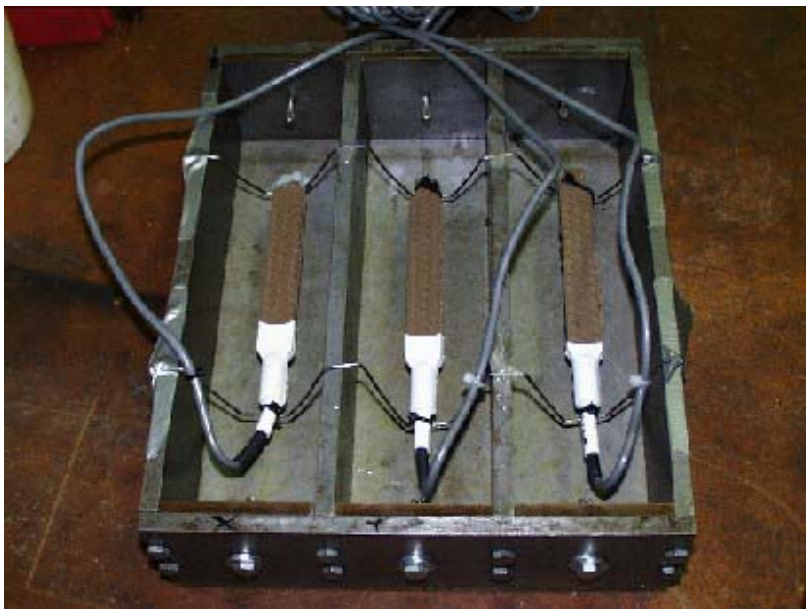

Figure 122. Embedment gages were cast in 3" x 3" x 11" concrete prisms

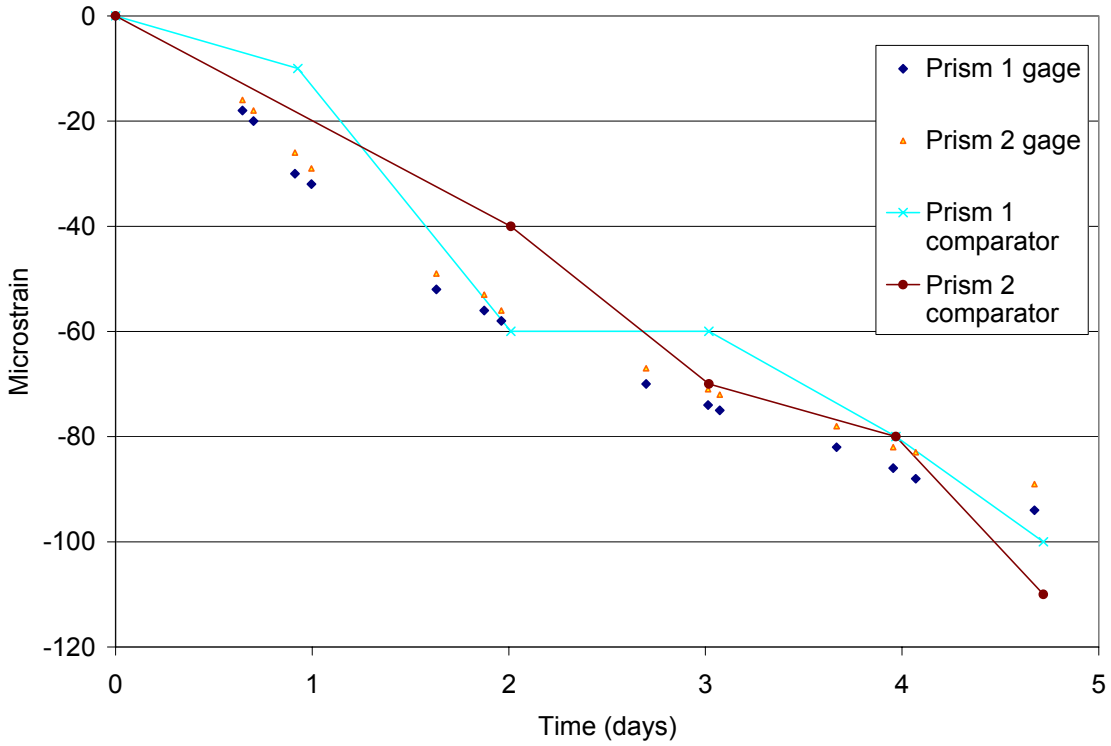

Figure 123. Comparison between embedment gage and comparator measured strains

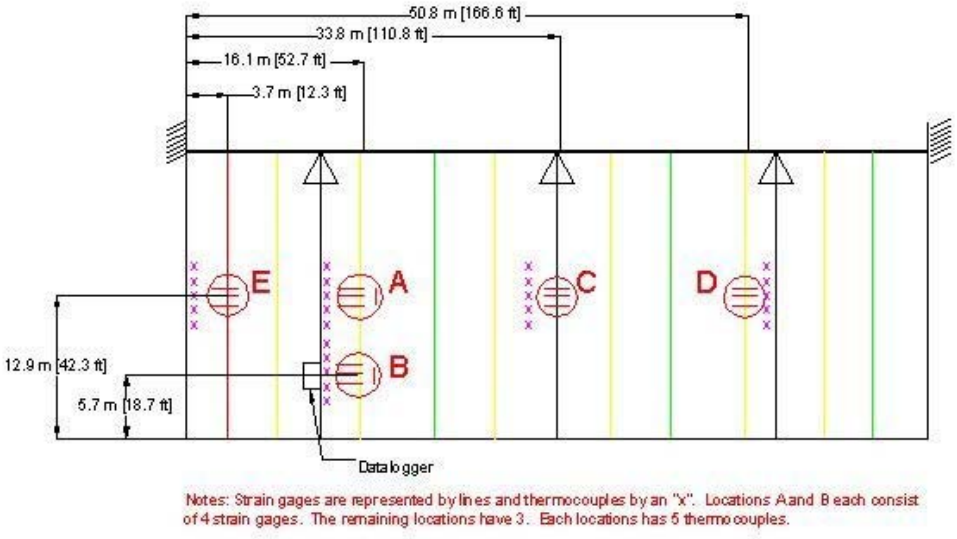

Figure 124. Sensor location map for Duncan Rd

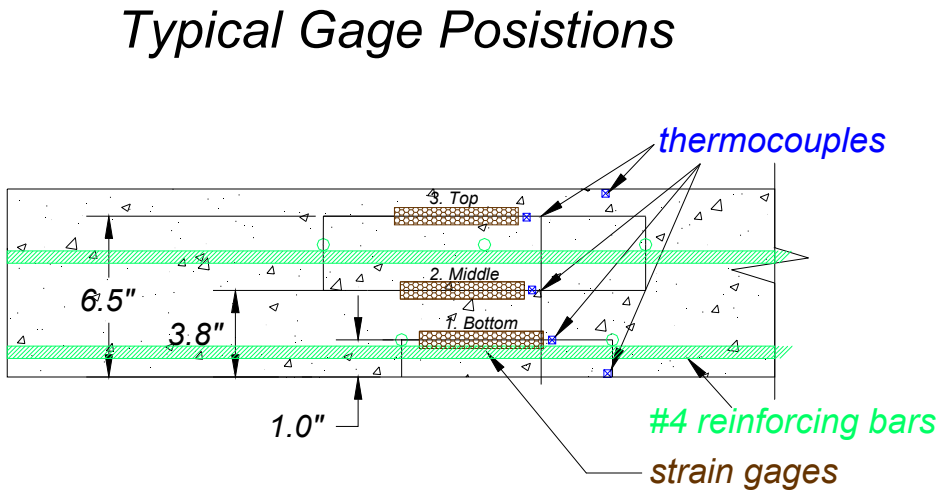

Figure 125. Sensor positions for Duncan Rd

Figure 126. Data collection equipment during installation on pier at Duncan Rd

Figure 127. Complete installation with solar panel and cellular antenna

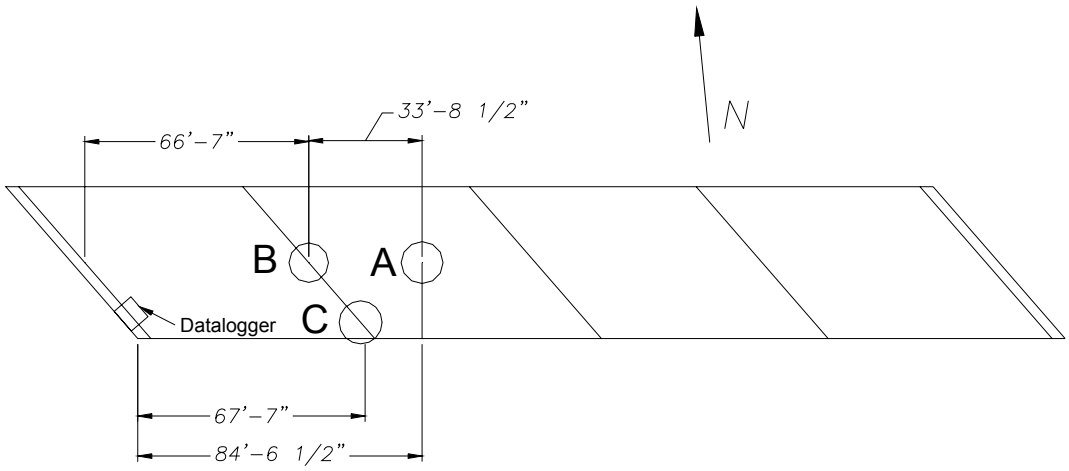

Figure 128. Big Creek sensor location map

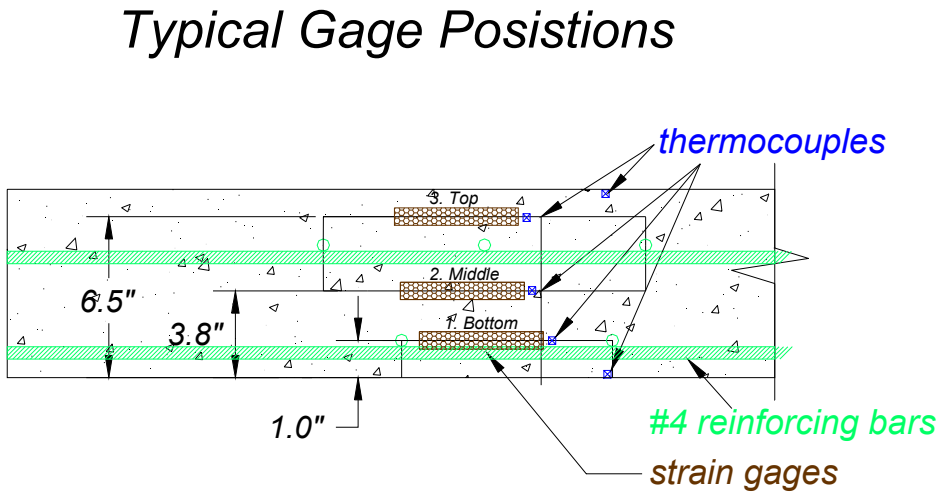

Figure 129. Big creek sensor positions

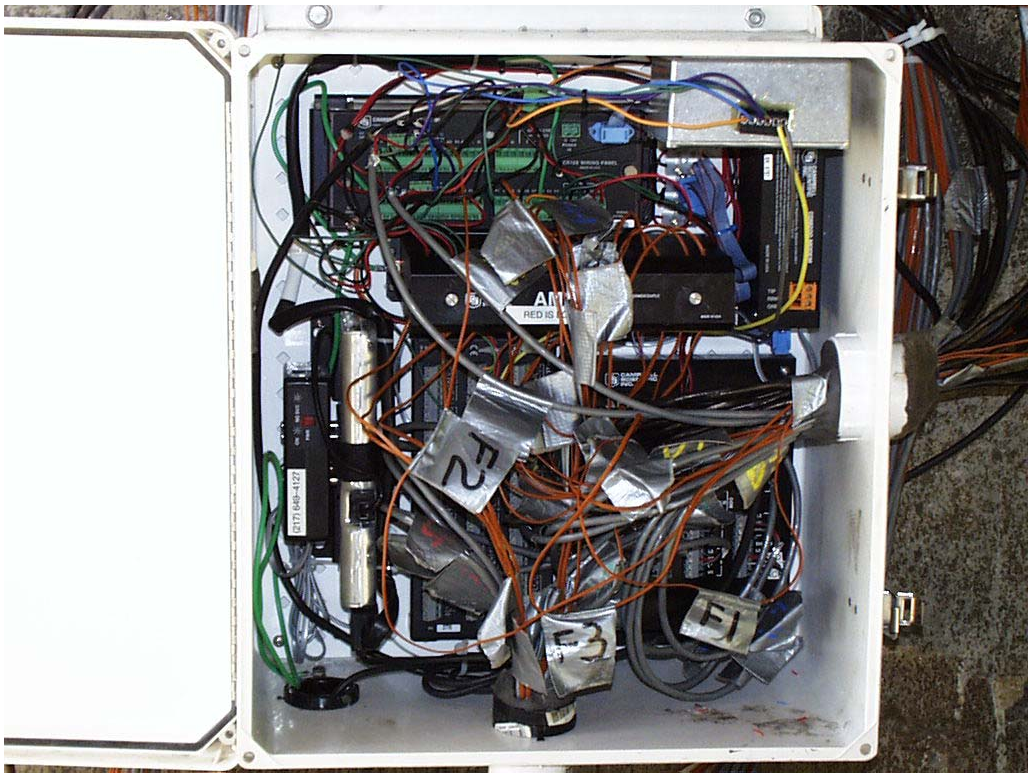

Figure 130. Data collection system during installation

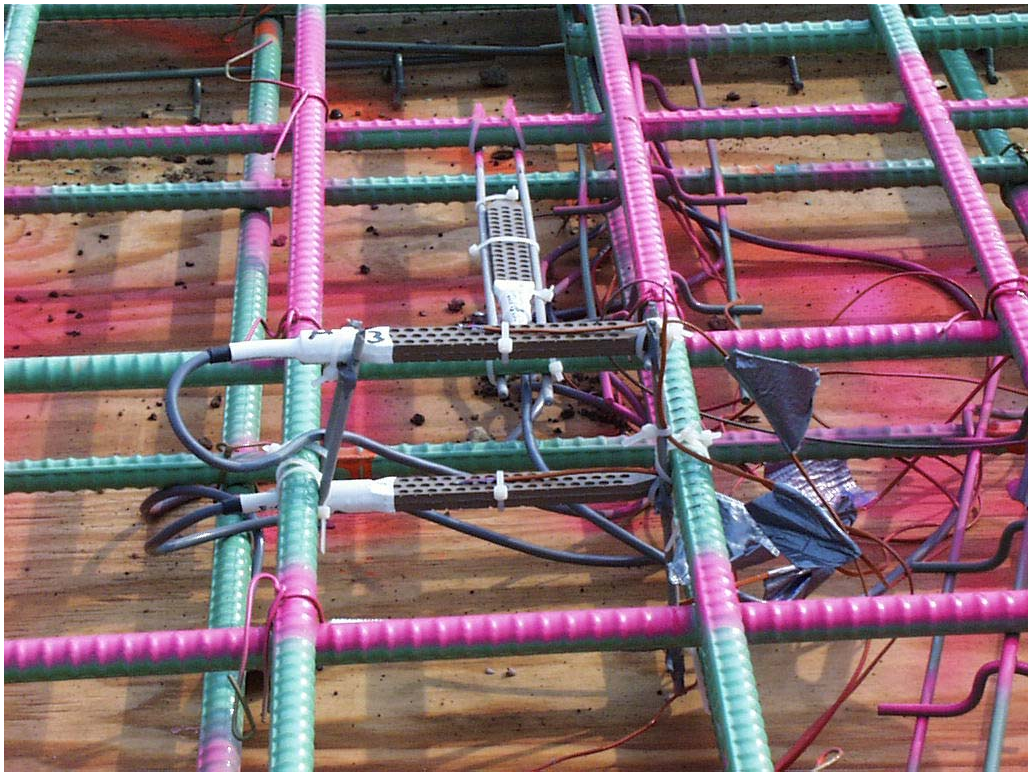

Figure 131. Sensors installed at location A

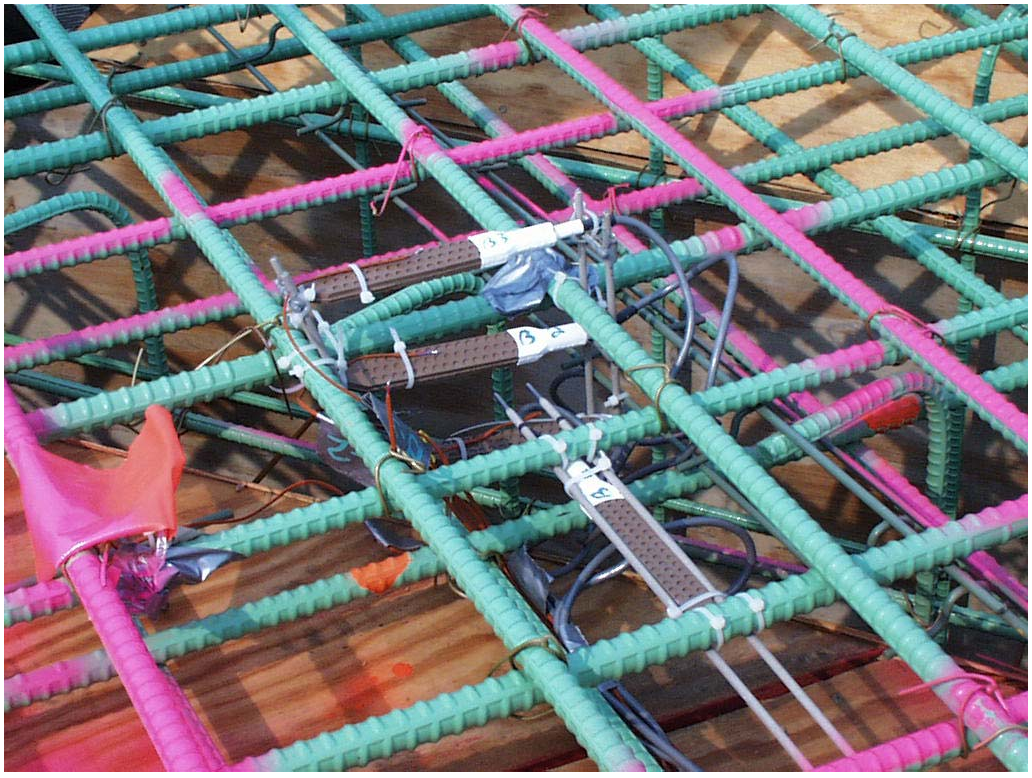

Figure 132. Sensors installed at location B

Figure 133. Sensors installed at location C

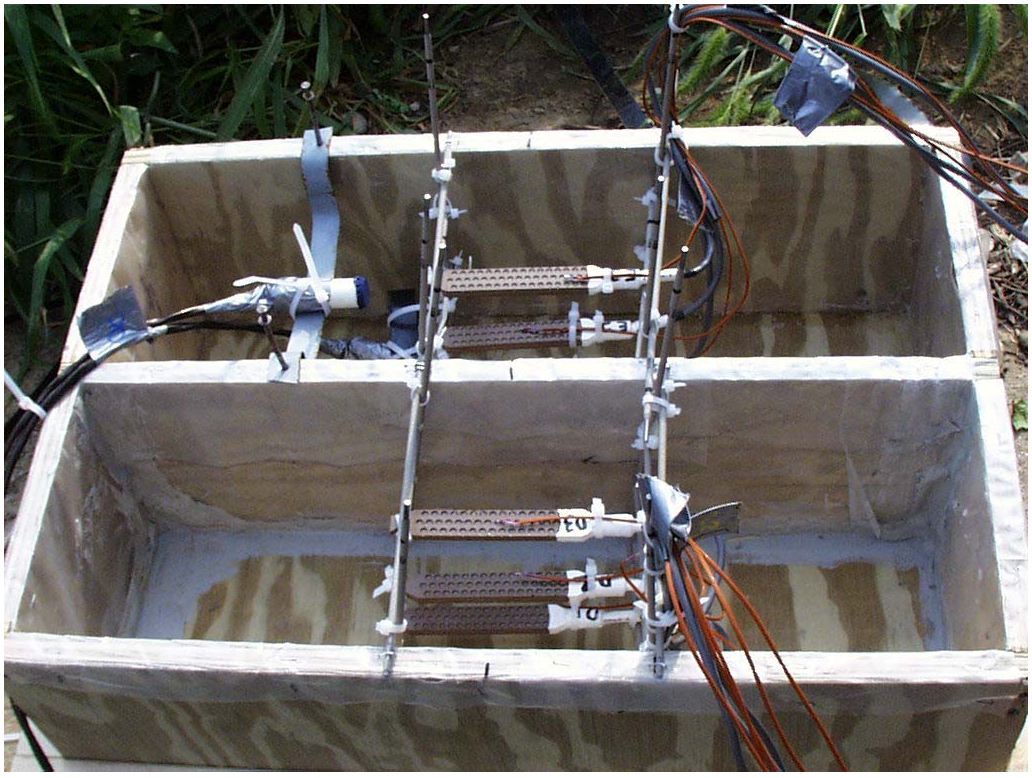

Figure 134. Sensors installed in free shrinkage beams

Figure 135. Sensors installed in parapet wall

Figure 136. Data collection system and free shrinkage beams

Figure 137. Concrete pumping operation

Figure 138. Placing and finishing concrete

Figure 139. Applying wet cotton mats for curing

3. RESULTS OF BRIDGE INSTRUMENTATION

3.1 Duncan Rd/I-72

3.1.1 Temperature Measurements

The strain gage and thermocouple data span a period of seven months. Interruptions in data collection occurred due to unexpected disconnection of cellular service in February, 2002. The cellular modem equipment used for transmission of data must be used with an analog cellular provider. This was discovered after the network switched to digital service and our service was terminated. During this time, the data were collected manually. Air temperature was measured at the project location. Temperature data for the first week after placement are shown in Figure 144. Internal concrete temperatures followed the measured air temperature with a slight lag. This is expected as the concrete conducts heat slowly and adjusts to ambient conditions. Measured temperatures reached almost 50°C (122°F) during hydration, but the temperature gradient through the thickness of the deck was only 10°C. The temperature data after one month are shown in Figure 145 and the complete temperature history is shown in Figure 146. The maximum temperature gradient in the deck during daily temperature cycles usually occurred during the late morning/early-afternoon heating of the top of the deck on sunny days. The gradient often reached 9-10°C, but did not exceed 11°C. On days that the sun was obscured by clouds, the temperature gradient was less than 1°C. The typical distribution of temperature through the thickness of the deck is shown in Figure 147 for a case where heating occurs from solar radiation. The heating curve shows that the top two to three inches of the deck are most affected by heating. A model was developed to describe heat transfer in the bridge deck and is described further in Chapter 4.

3.1.2 Strain Measurements

The general trends of the strain data correspond to both daily cycles of temperature and weekly temperature variation. The data are shown in Figure 148 through Figure 150. Strain measurements were corrected for thermal output as discussed in Chapter 2. Several strain sensors did not survive the concrete placement. Measured strains reflect the amount of displacement in the bridge and should not be confused with the strain associated with stress. The two additional factors that control stress in the bridge deck are the level of structural restraint and the creep capacity of the material. The level of restraint is less for temperature deformation than it is for shrinkage. The beams supporting the bridge are changing with temperature along with the deck, although the coefficient of thermal dilation is not the same, the restraint will not be significant. However, shrinkage of the concrete deck is highly restrained by the steel beams. The strain measurements reflect only temperature changes in the deck, but a finite element model in Chapter 4 was combined with shrinkage and creep models in Chapter 5 of the laboratory section to understand the stress that develops in the bridge deck.

3.2 I-70/Big Creek

3.2.1 Temperature Measurements

The strain gage and thermocouple data span a period of eleven months. Air temperature was measured at the project location. Temperature data for the first week after placement are shown in Figure 151 through Figure 154. Internal concrete temperatures followed the measured air temperature with a slight lag. This is expected as the concrete conducts heat slowly and adjusts to ambient conditions. Measured temperatures reached almost 60°C (140°F) during hydration, but the temperature gradient through the thickness of the deck was only 10°C. Hydration temperatures were the highest over the pier location. The deck was placed

monolithically with the diaphragm and thus had a greater mass of concrete leading to higher heat evolution. Temperature measurements in the parapet are shown in Figure 155. The maximum parapet temperature during hydration was 54°C and the temperature gradient between the top and bottom of the parapet was about 6°C. The free shrinkage beams developed lower heat, as was expected due to their smaller size compared to the deck. The complete temperature history is shown in Figure 156. The maximum temperature gradient in the deck during daily temperature cycles usually occurred during the late morning/early-afternoon heating of the top of the deck on sunny days. The gradient often reached 9-10°C, but did not exceed 10.5°C. A model was developed to describe heat transfer in this bridge deck and is described further in Chapter 4.

3.2.2 Strain Measurements

The general trends of the strain data correspond to both daily cycles of temperature and weekly temperature variation. The data are shown in Figure 157 through Figure 168. Strain measurements were corrected for thermal output as discussed in Chapter 2. Most of the strain sensors survived concrete placement for this bridge. Magnitudes of the transverse strain sensors are similar to longitudinal sensors. No significant differences were noticed between locations in the deck. The strain varies with temperature at each location, and bending deflections are seen during morning heating and evening cooling cycles. These warping deflections are also seen in the free shrinkage beams at locations D and E as shown in Figure 160 and Figure 161. Warping in the free shrinkage beams is well behaved during heating and cooling, where the top strain elongates as it heat and there is almost a linear relation to depth. In the bridge deck however, the warping strain is not always evenly spaced. This indicates a higher level of restraint against bending in the deck is changing the strain distribution. This is expected since the bridge girders

are not heated directly by solar radiation and do not have the same tendency to warp. It should be noted that measured strains reflect the amount of displacement in the bridge and should not be confused with the strain associated with stress. The two additional factors that control stress in the bridge deck are the level of structural restraint and the creep capacity of the material. The level of restraint is less for temperature deformation than it is for shrinkage. The beams supporting the bridge are changing with temperature along with the deck, although the coefficient of thermal dilation is not the same, the restraint will not be significant. The only restraint to temperature deformation is from the pier. However, shrinkage of the concrete deck is highly restrained by the steel beams. The strain measurements reflect only temperature changes in the deck, but a finite element model in Chapter 4 was combined with shrinkage and creep models in Chapter 5 of the laboratory section to understand the stress that develops in this bridge deck.

3.2.3 Internal Relative Humidity Measurements

In addition to the embeddable strain gages and thermocouples already being implemented in the bridge deck field experimentation, internal relative humidity sensors were installed. The internal RH measurement system used in the field research was a preliminary system developed at UIUC prior to the system used in the laboratory research. The system consisted of a G-Cap2 capacitive RH sensor manufactured by General Eastern enclosed in a 1/2" PVC tube. The end of the tube was covered in Gore-Tex to allow moisture vapor transmission while blocking liquid water and solid particles. Figure 140 shows the internal RH sensors ready to be cast in the concrete bridge deck on I-70 near Marshall, IL (Big Creek). The data was collected every 10 minutes by the same Campbell Scientific datalogger that recorded the temperature and strain data.

The RH sensors appeared to function properly for a couple of weeks after the bridge deck was cast before going out of range. It is unclear at this time why the sensors went out of range, but it may be due to eventual water infiltration. The end of the PVC tube that had the lead wire exit (opposite from the end covered in Gore-Tex) was plugged with Duck-Seal, which is a sealing putty. It is possible that this seal developed leaks over time and the sensor became exposed to liquid moisture and dissolved salts from the pore solution.

Before the RH sensors went out of range, the internal RH gradient was measured in the concrete bridge deck. The data for a six day period is shown in Figure 141. The most interesting observation to make from the data is that the internal RH varies synchronously with the internal temperature. This is opposite from intuition. Relative humidity is defined as the partial vapor pressure (the actual amount of moisture in the air) relative to the saturation vapor pressure at a given temperature. In an open environment, when the temperature goes down the saturation vapor pressure goes down, which means the RH goes up with constant partial vapor pressure. This means that normally there is an inverse relationship between RH and temperature.

The observation that RH varies synchronously with temperature means that in partially saturated concrete where capillary menisci are present, capillary tension decreases as temperature increases. In other words, there is a relaxation of shrinkage stresses as the temperature is increased, allowing an additional expansion of the material (see Figure 142). Furthermore, this indicates a dependence of the coefficient of thermal dilation (CTD) on the state of moisture in concrete. The highest increase in the CTD occurs in concrete that has an internal RH of about 50%, which is the lowest internal RH before capillary menisci become unstable. Figure 143 illustrates the dependence of the CTD on the state of internal moisture [1].

Practically, this means that in concrete that is exposed to drying on the top surface (i.e. has an internal RH gradient) there will be a thermal stress gradient induced. Different layers

throughout the depth of the material will have different coefficients of thermal dilation. This could potentially exacerbate the thermal cracking potential of drying concrete.

REFERENCES

1. N.G. Zoldners, Thermal Properties of Concrete Under Sustained Elevated Temperatures, ACI SP 25-1 (1971), 1-31.

FIGURES

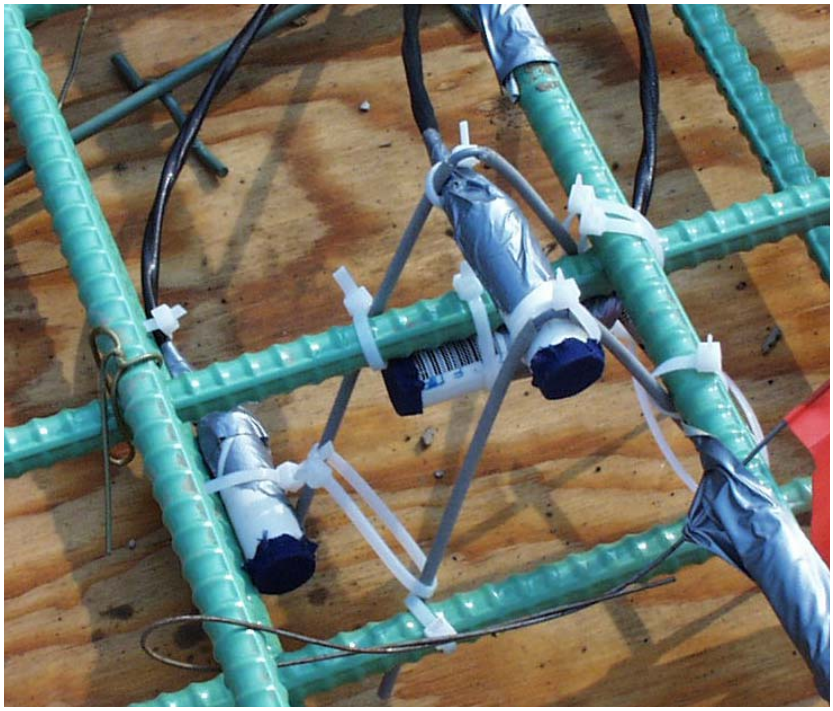

Figure 140. Internal RH sensors mounted for casting in concrete bridge deck

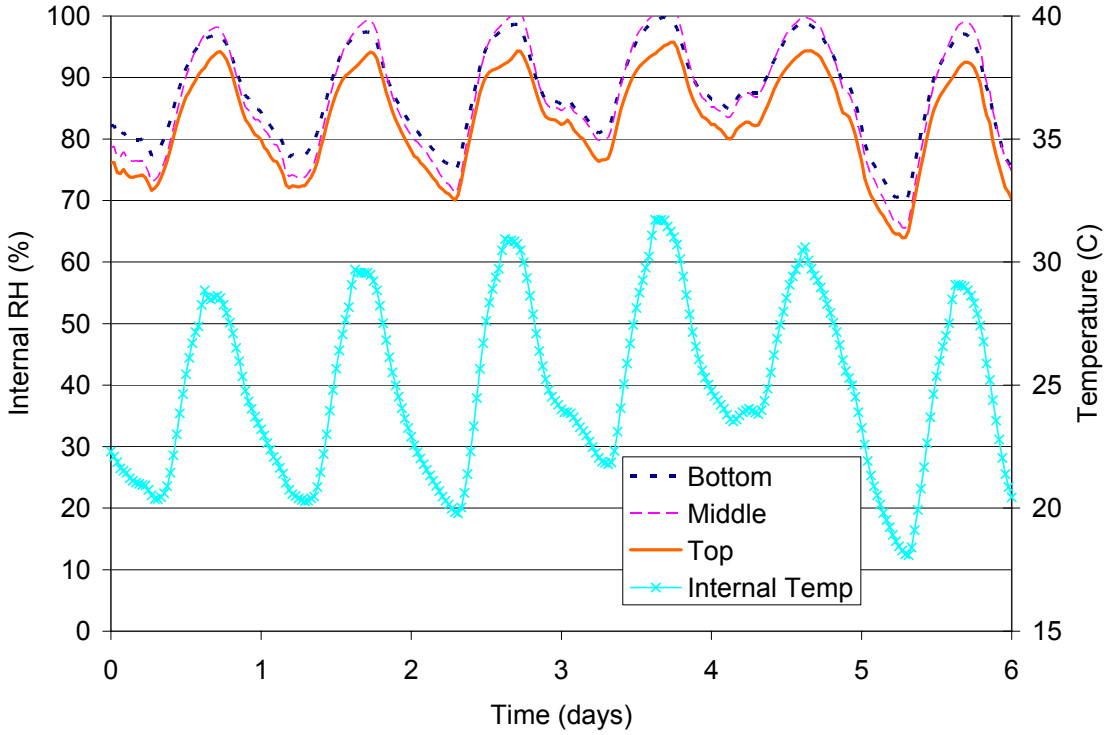

Figure 141. Internal RH and temperature cycles in concrete bridge deck

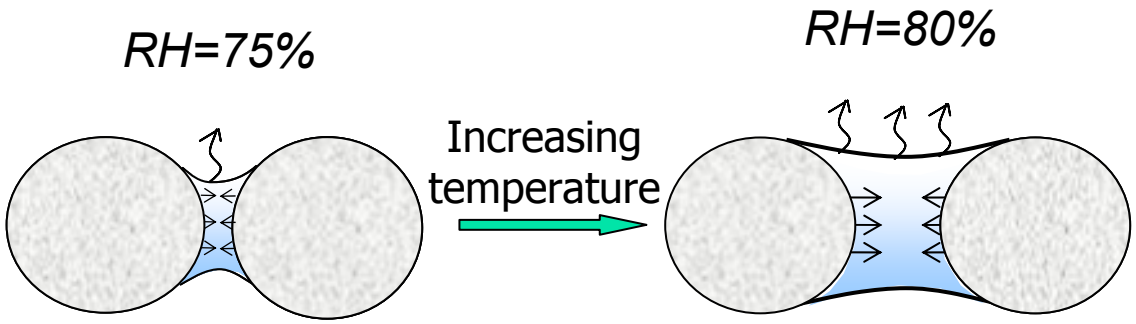

Figure 142. Effect of increasing temperature on capillary shrinkage pressure

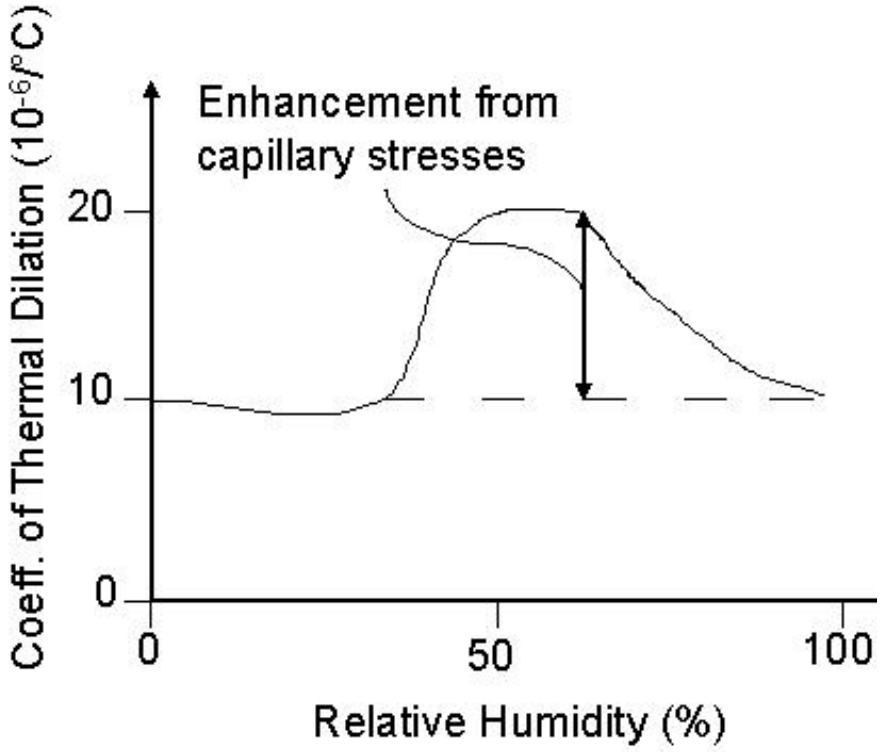

Figure 143. Dependence of CTD on state of internal moisture [1]

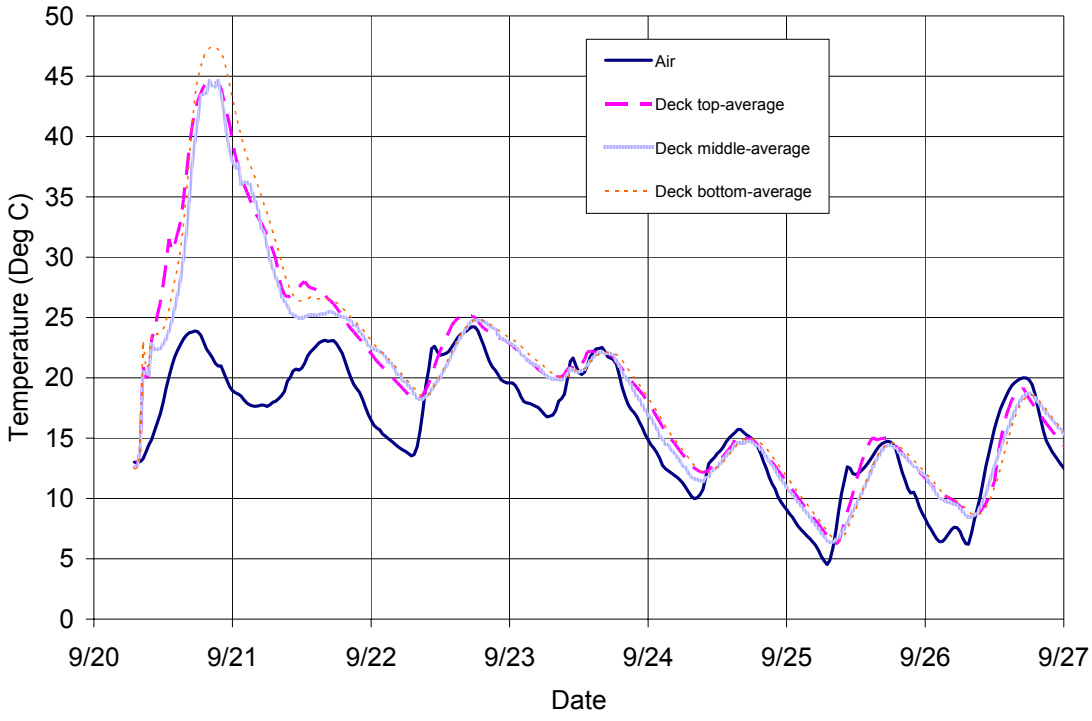

Figure 144. Measured temperatures after 1 week, Duncan Rd

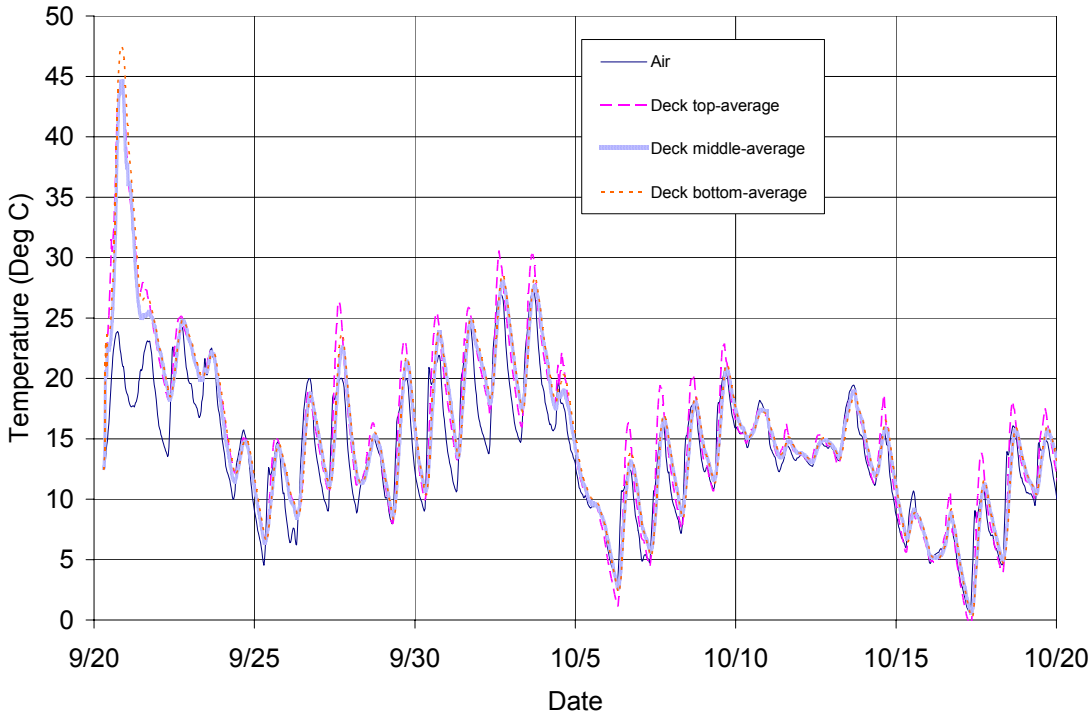

Figure 145. Measured temperatures after 1 month, Duncan Rd

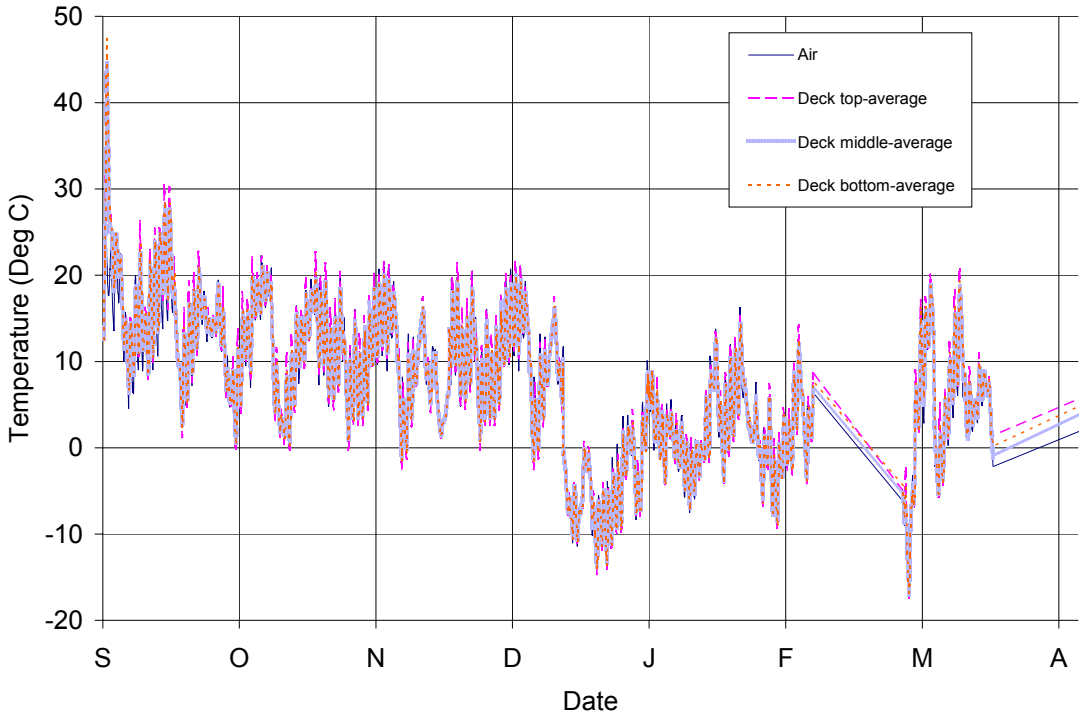

Figure 146. Measured temperatures after 6 months, Duncan Rd

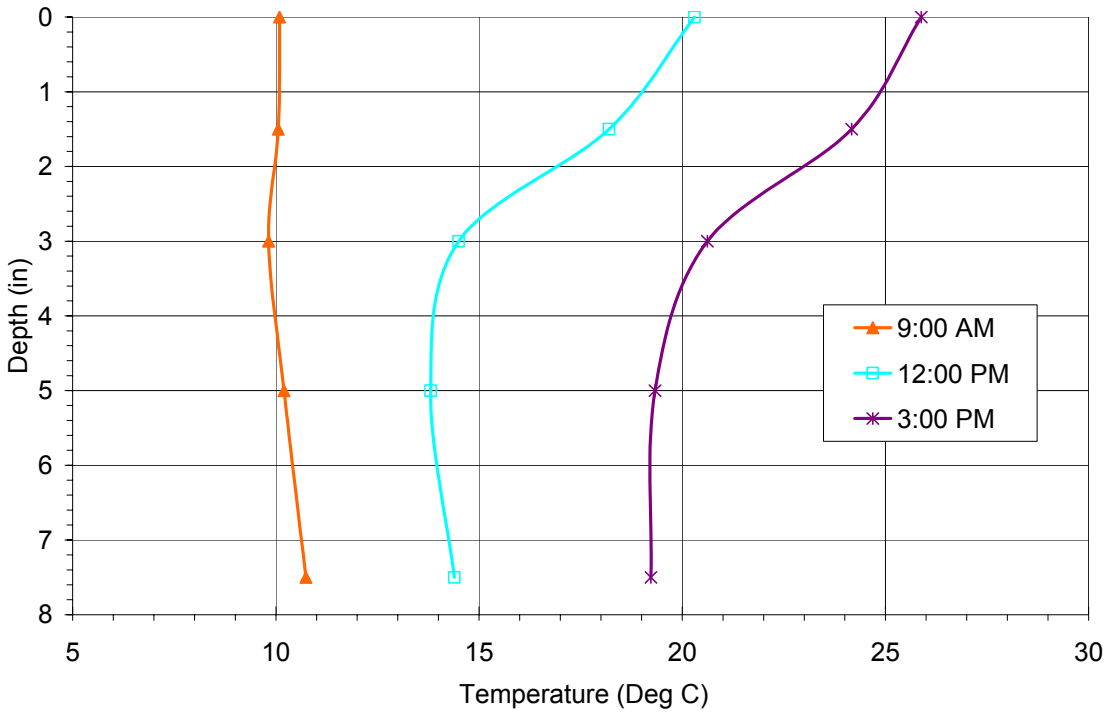

Figure 147. Temperature gradient in the deck during early afternoon heating

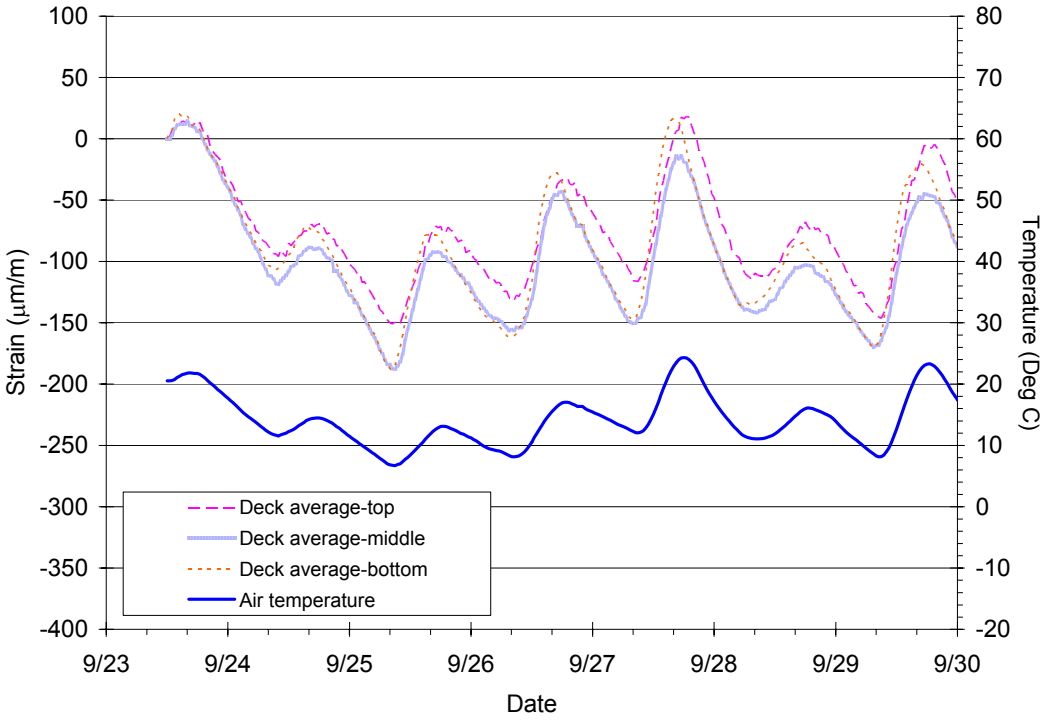

Figure 148. Measured strain after 1 week, Duncan Rd

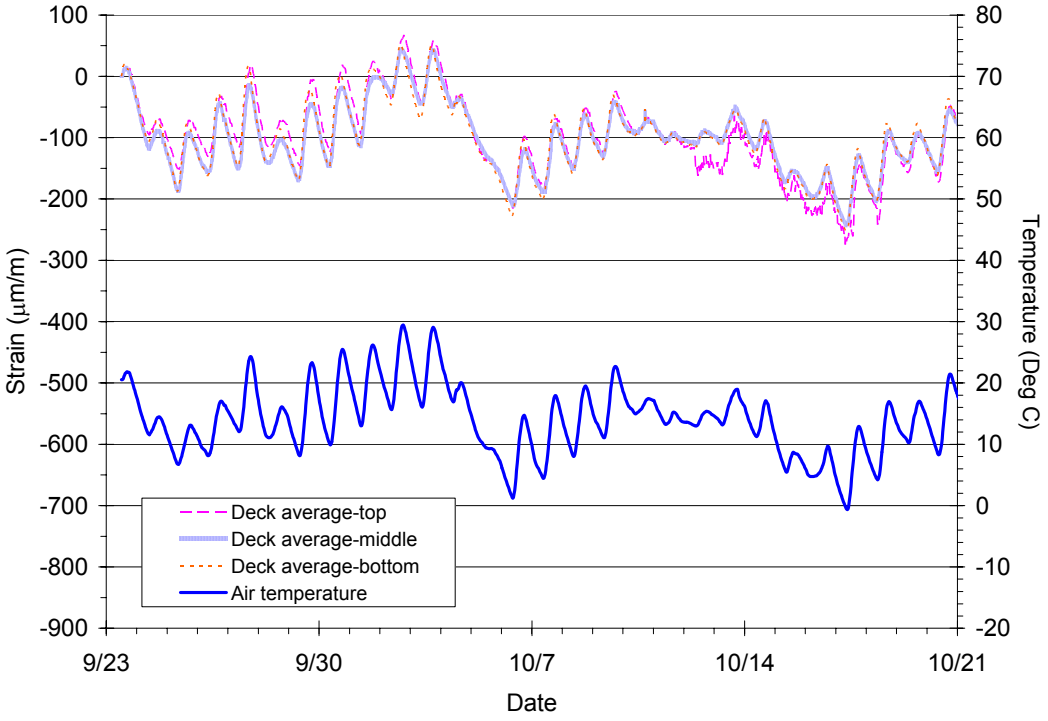

Figure 149. Measured strains after 1 month, Duncan Rd

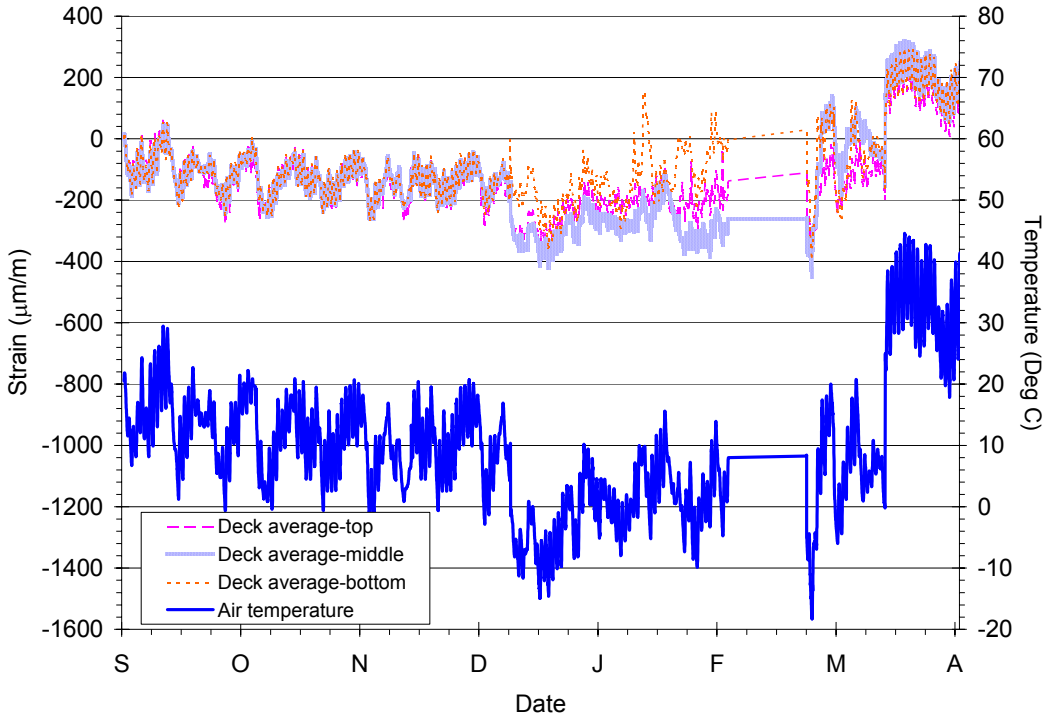

Figure 150. Measured strains after 6 months, Duncan Rd

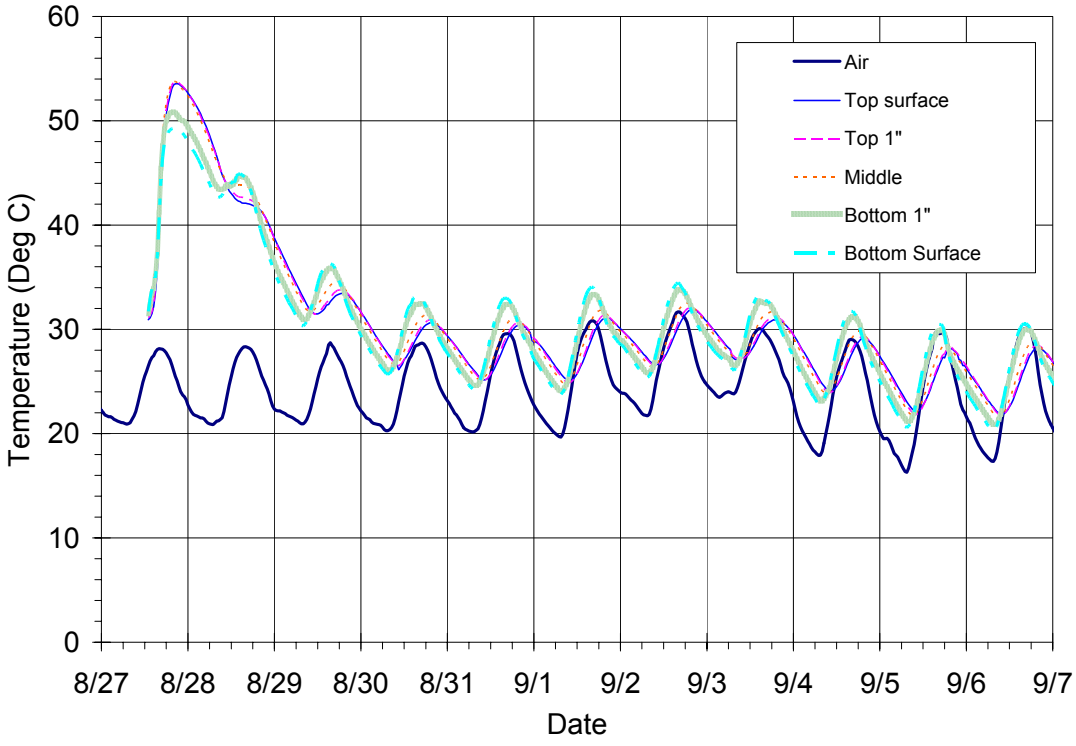

Figure 151. Temperature measurements at location A, midspan, center of deck, Big Creek

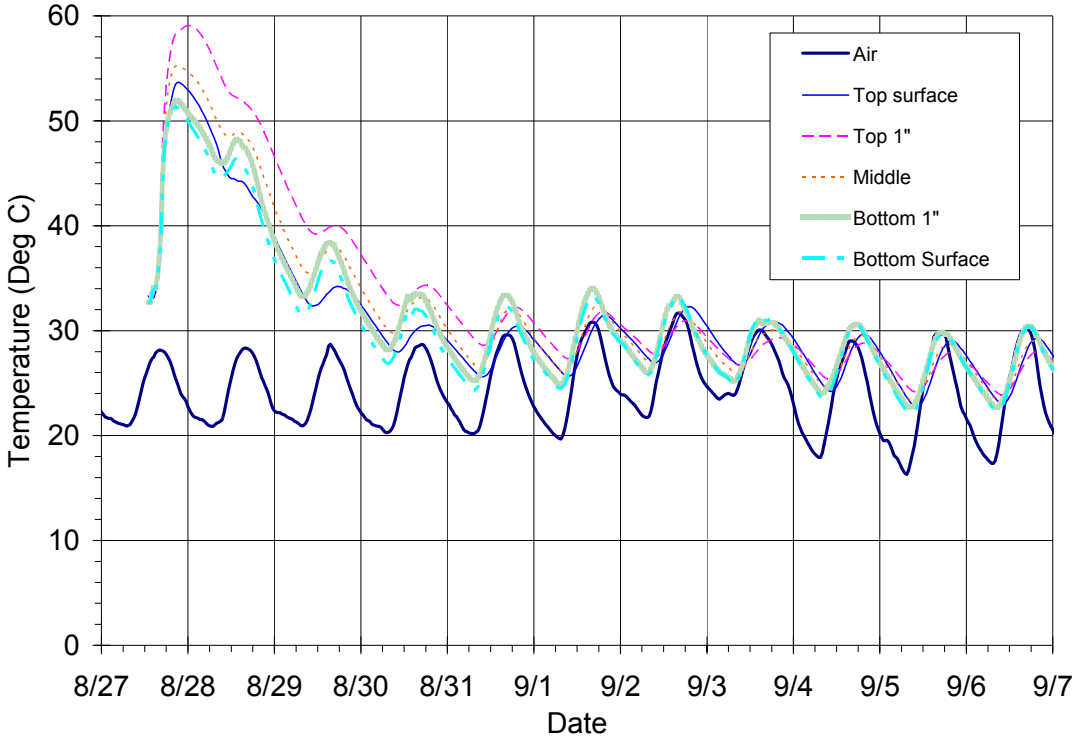

Figure 152. Temperature measurements at location B, over pier, center of deck, Big Creek

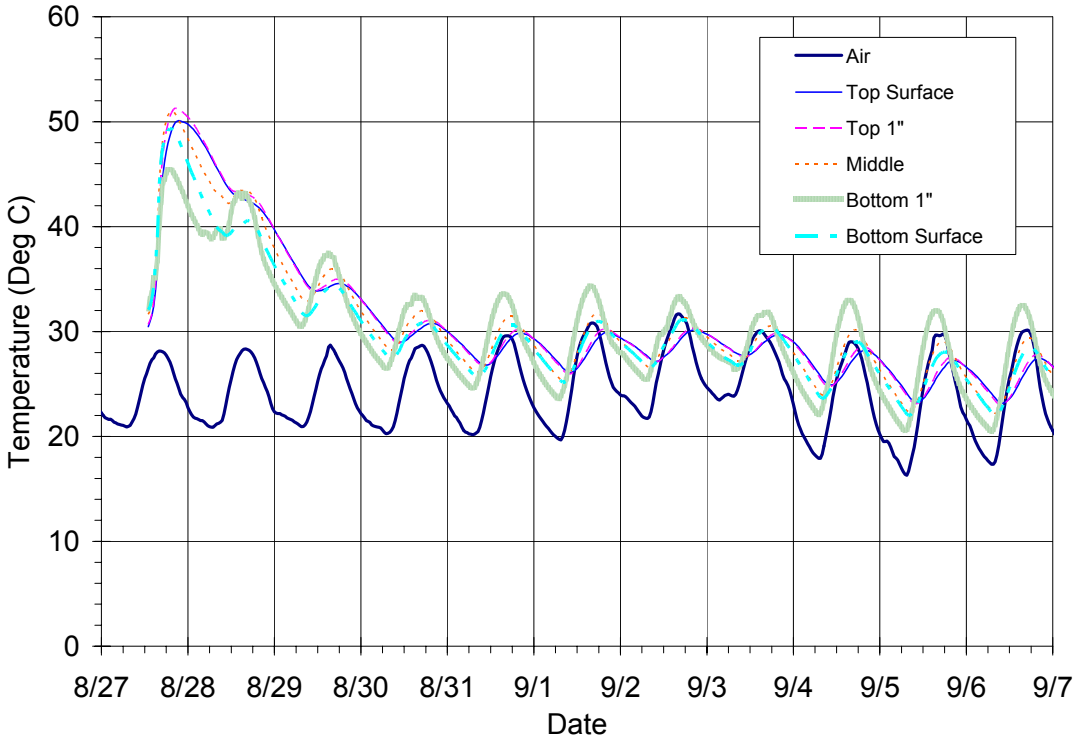

Figure 153. Temperature measurements at location C, over pier, edge of deck, Big Creek

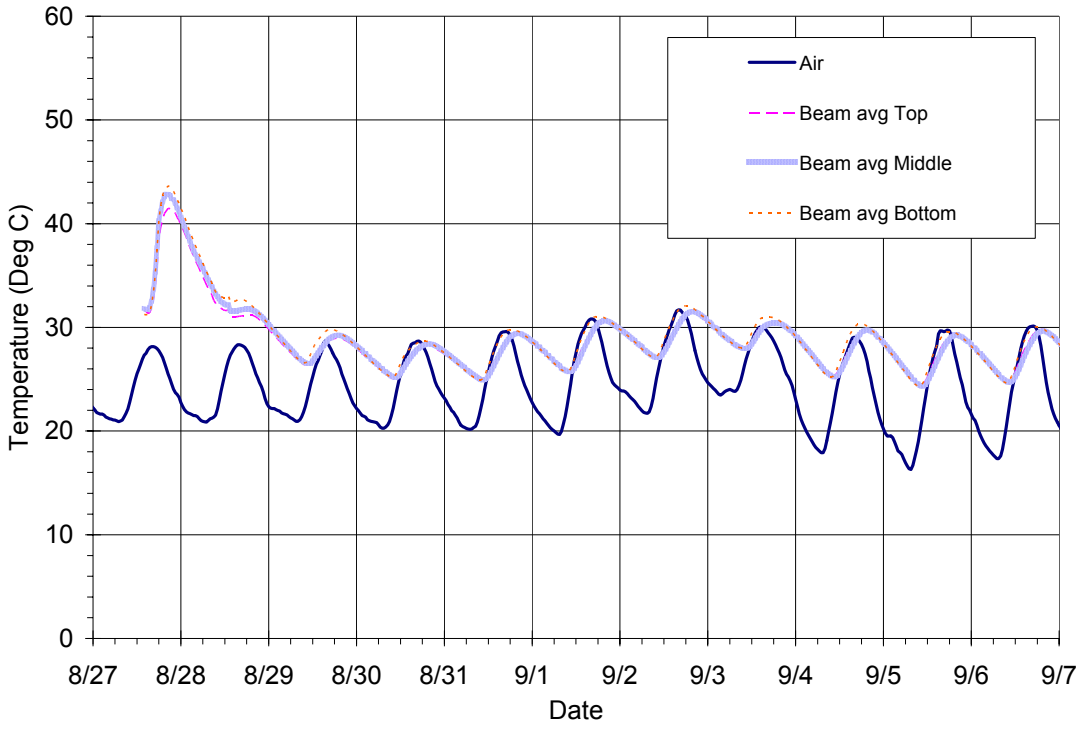

Figure 154. Temperature measurements in free shrinkage beams, Big Creek

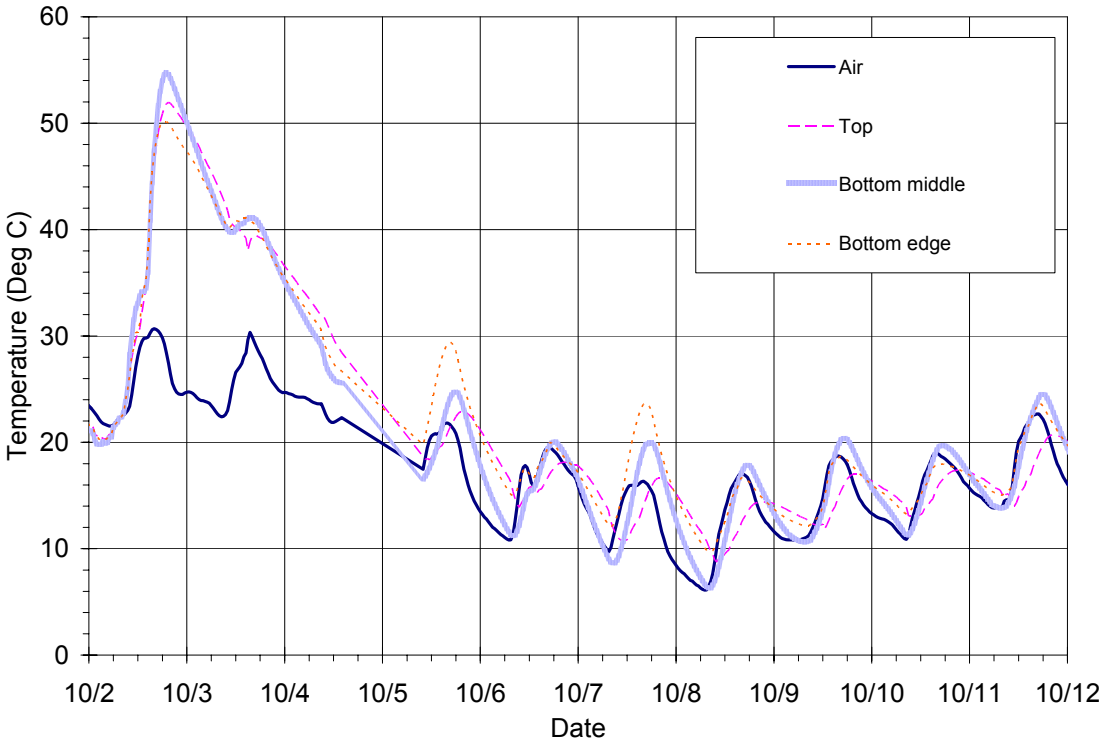

Figure 155. Temperature measurements in parapet wall after 1 week, Big Creek

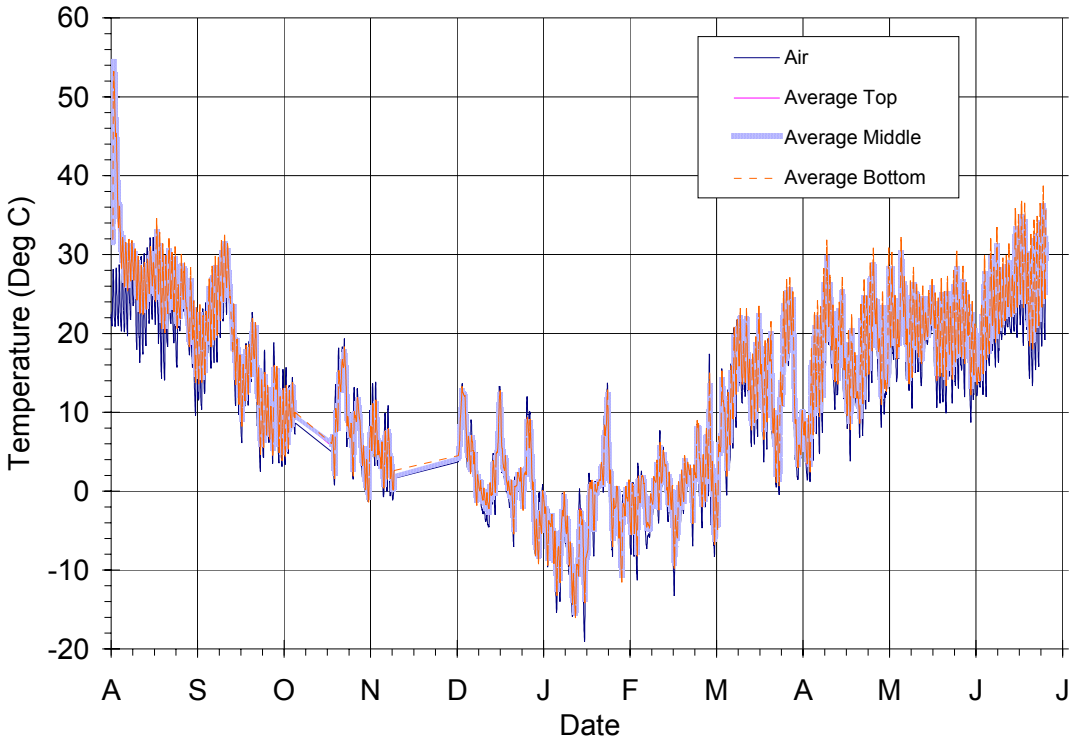

Figure 156. Average temperature history for Big Creek bridge deck for one year, Big Creek

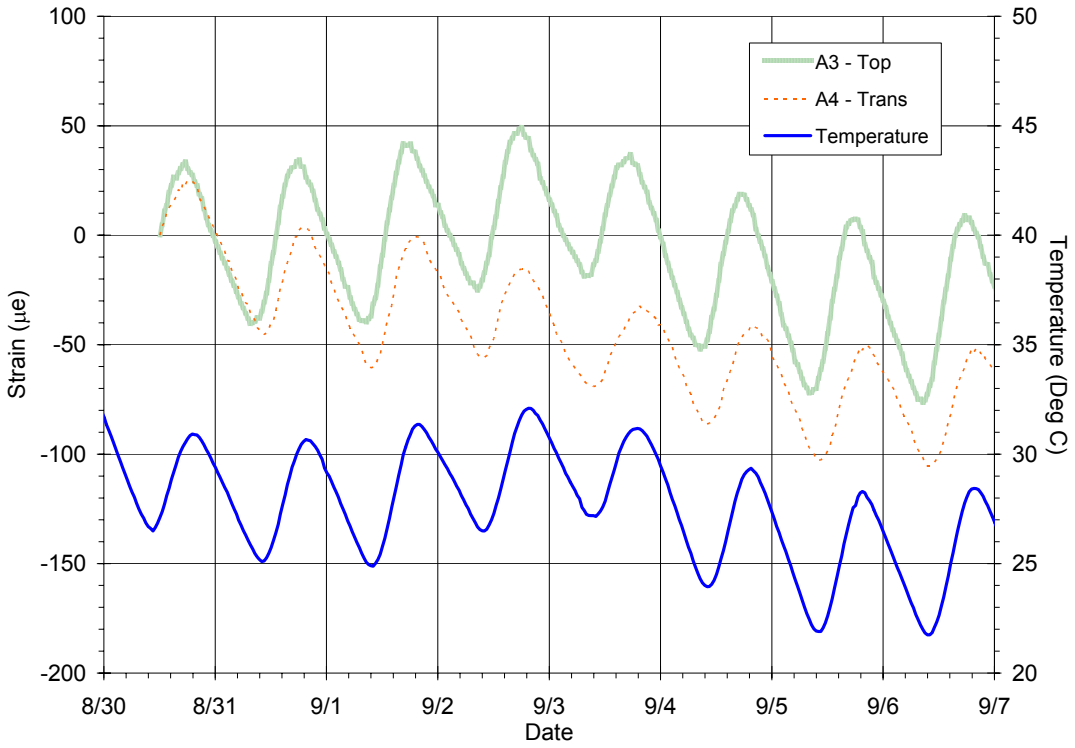

Figure 157. Strain measurements at location A, midspan, center of deck, Big Creek

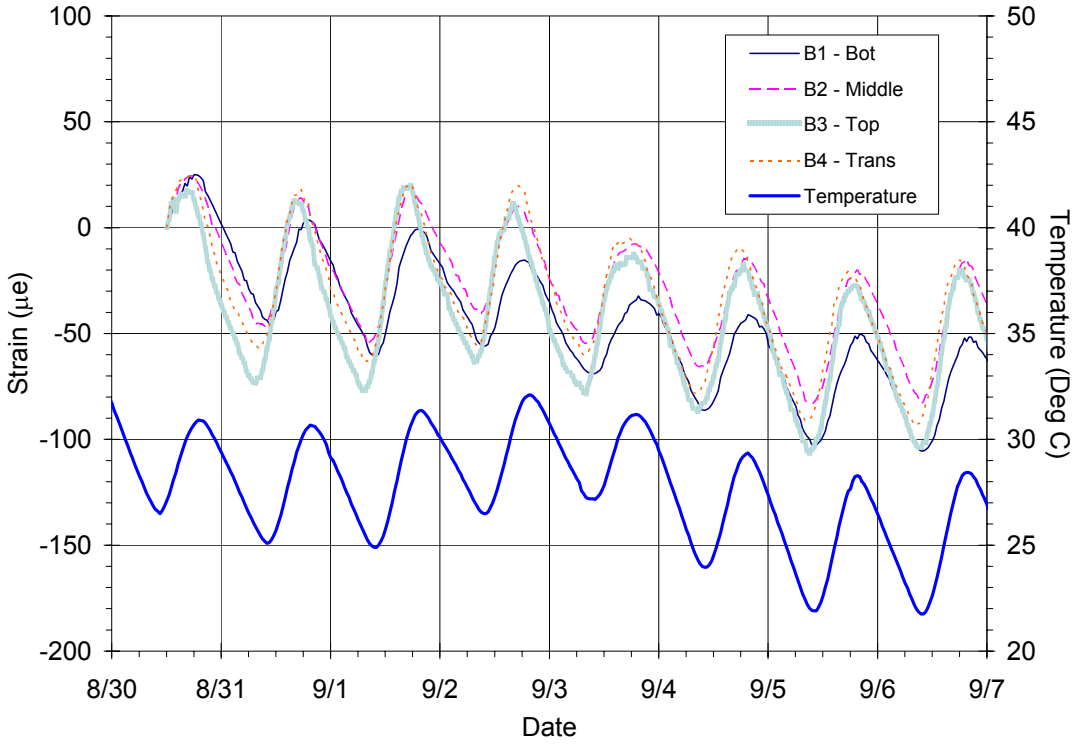

Figure 158. Strain measurements at location B, over pier, center of deck, Big Creek

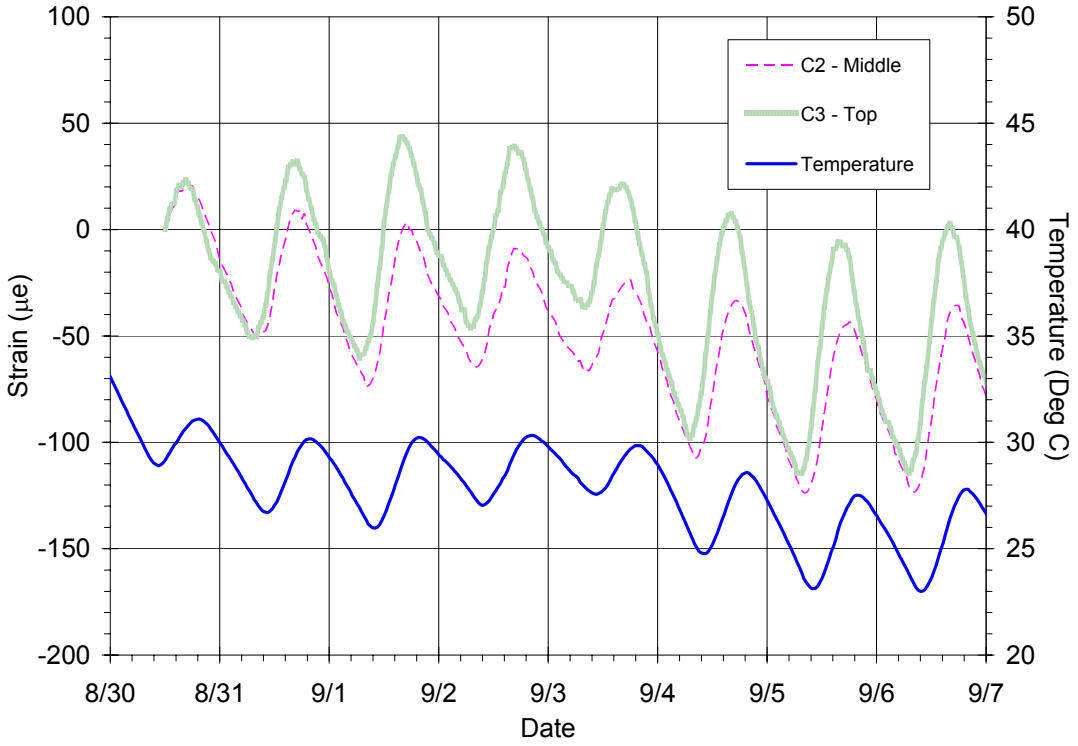

Figure 159. Strain measurements at location B, over pier, edge of deck, Big Creek

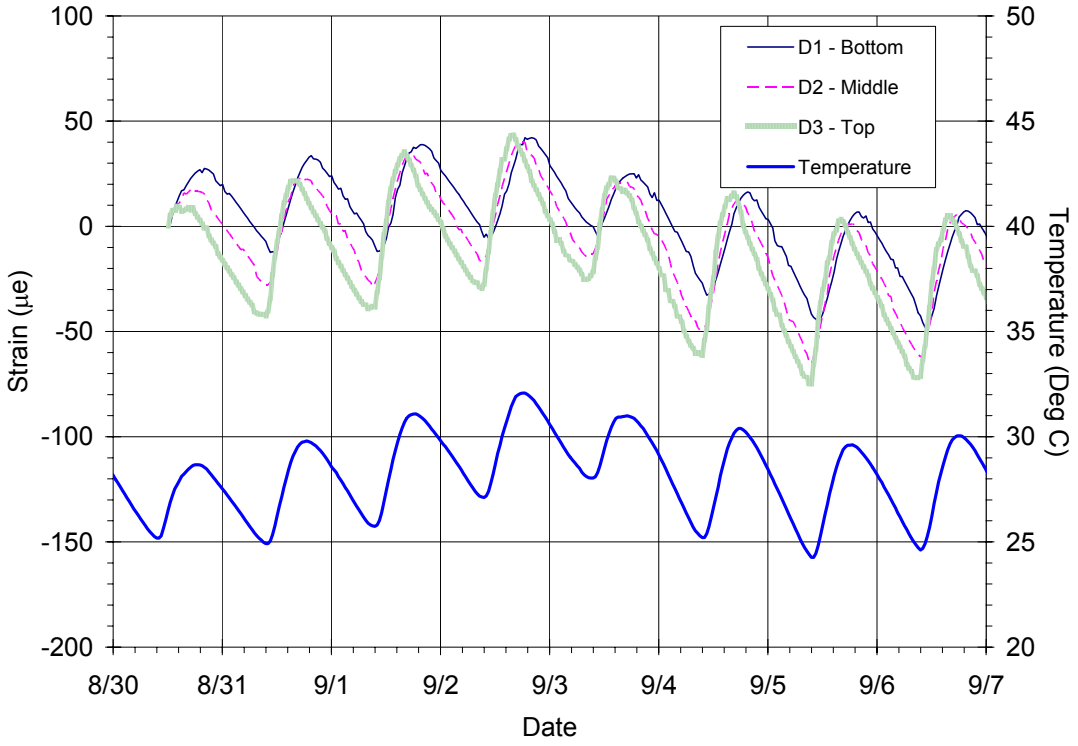

Figure 160. Strain measurements at location D, free shrinkage beam 1, Big Creek

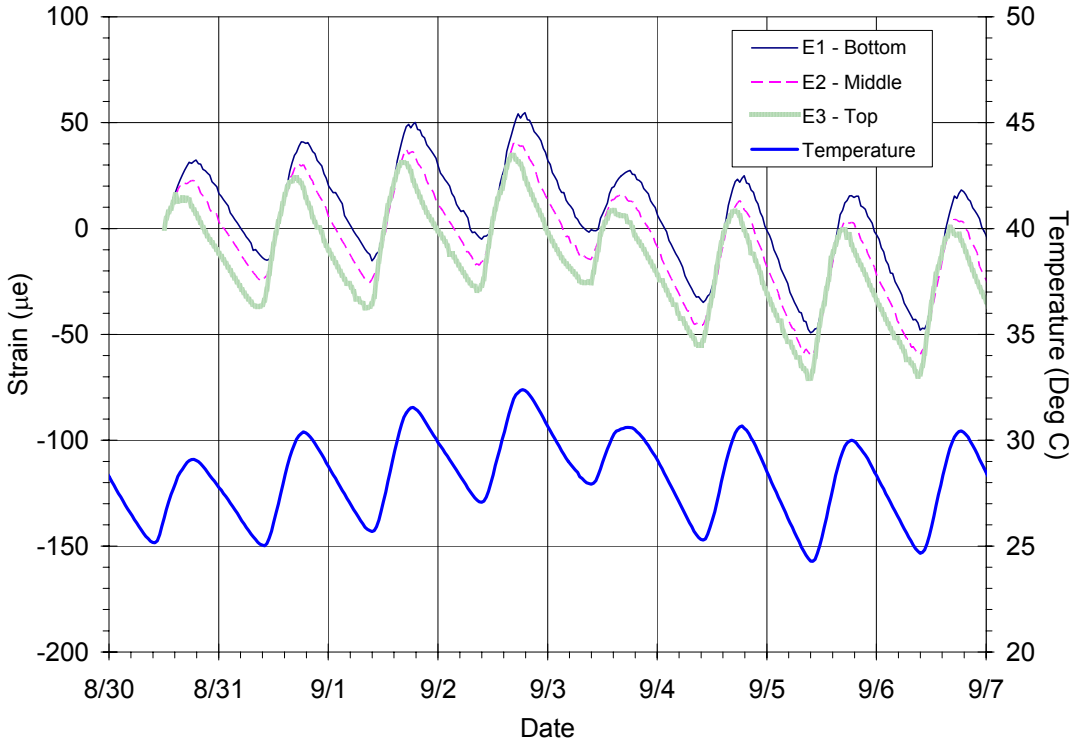

Figure 161. Strain measurements for location E, free shrinkage beam 2, Big Creek

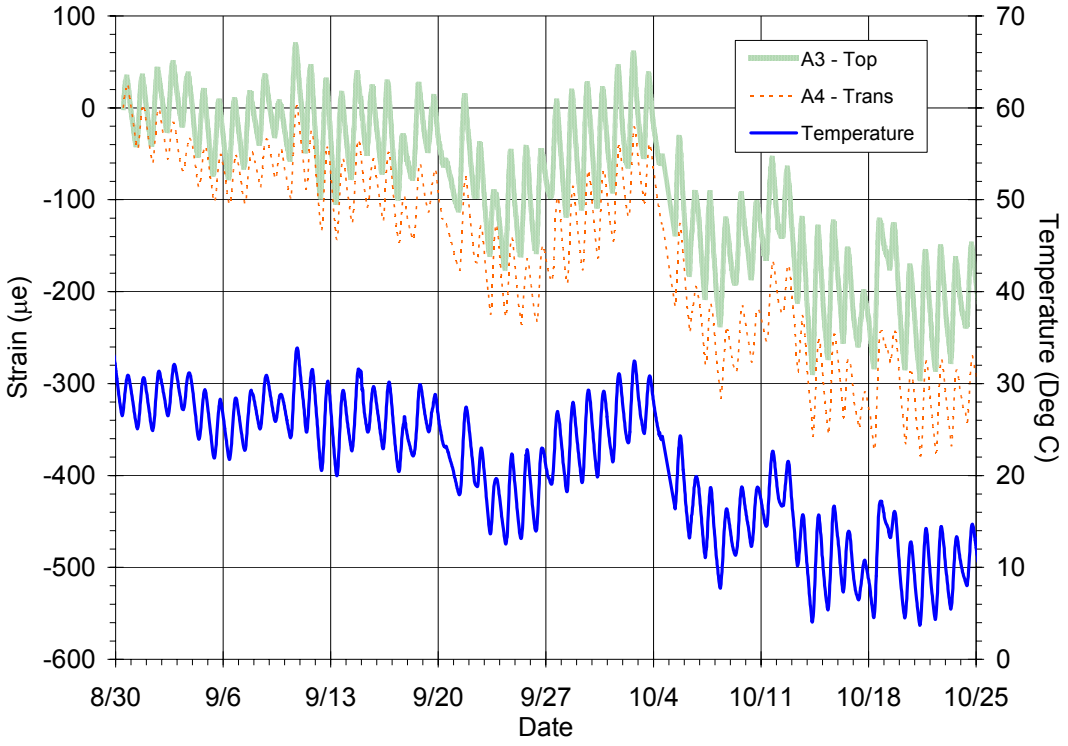

Figure 162. Strain measurements at location A, midspan, center of deck, Big Creek

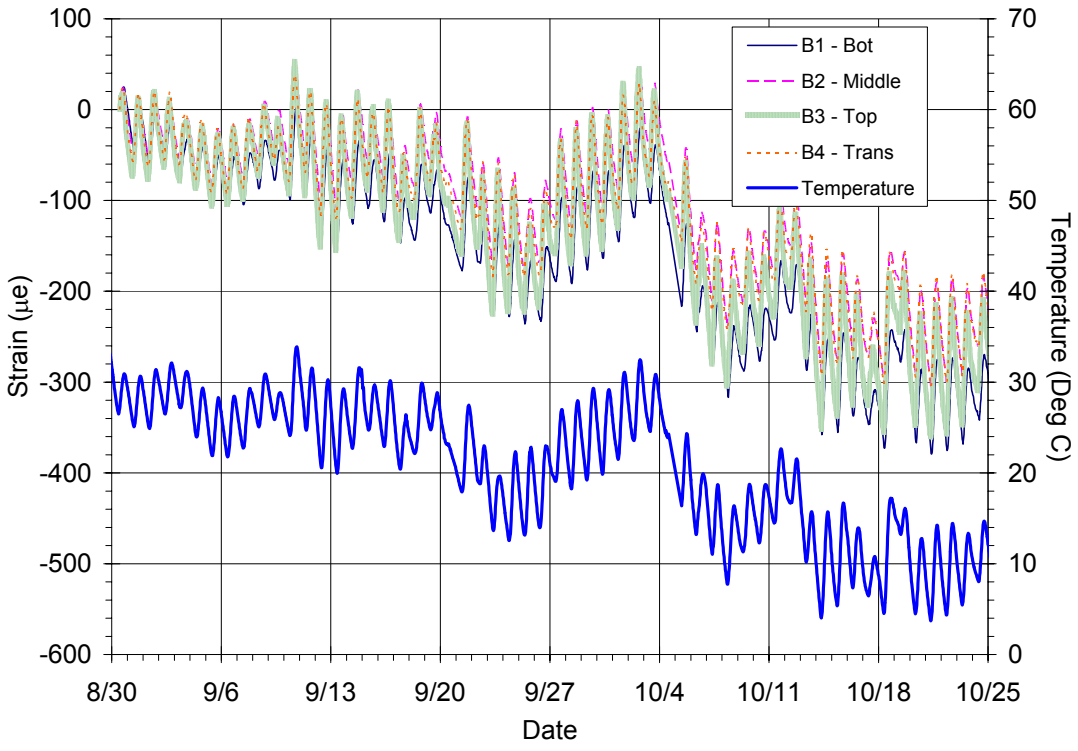

Figure 163. Strain measurements at location B, over pier, center of deck, Big Creek

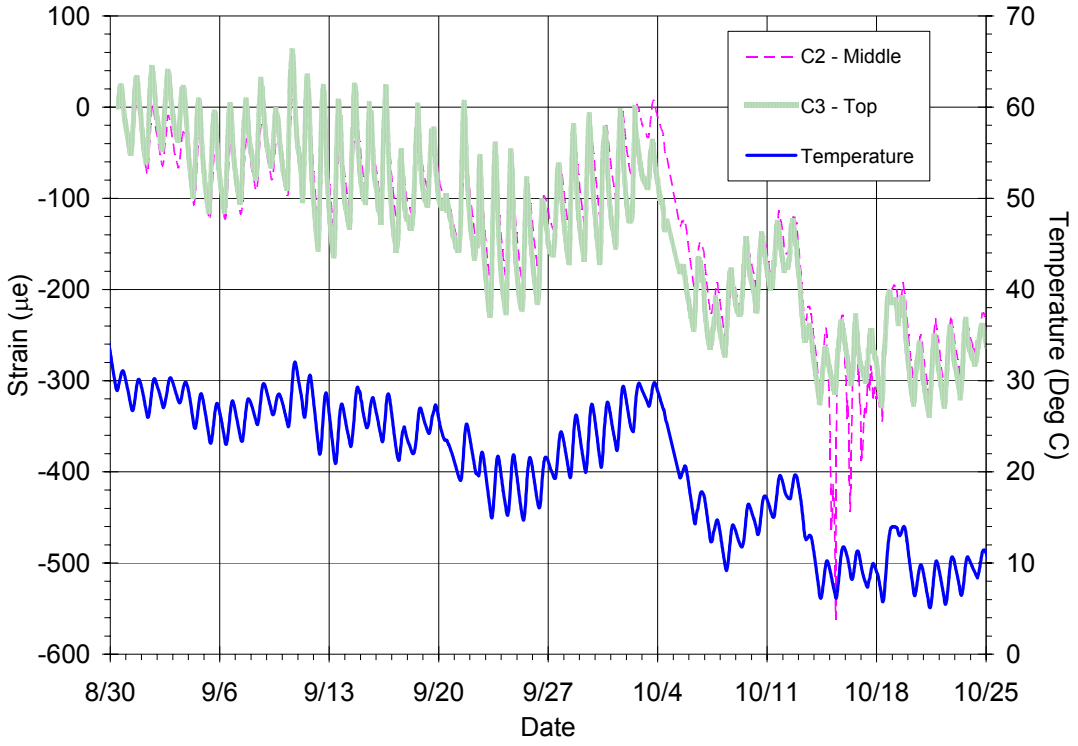

Figure 164. Strain measurements at location C, over pier, edge of deck, Big Creek

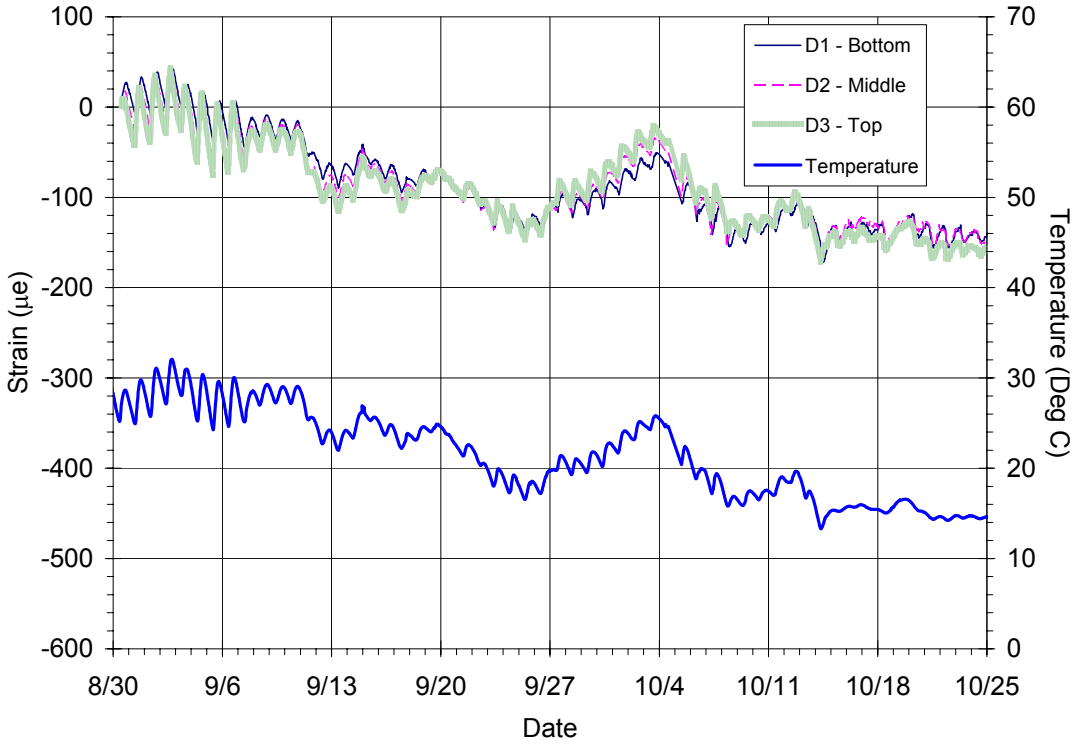

Figure 165. Strain measurements at location D, free shrinkage beam 1, Big Creek

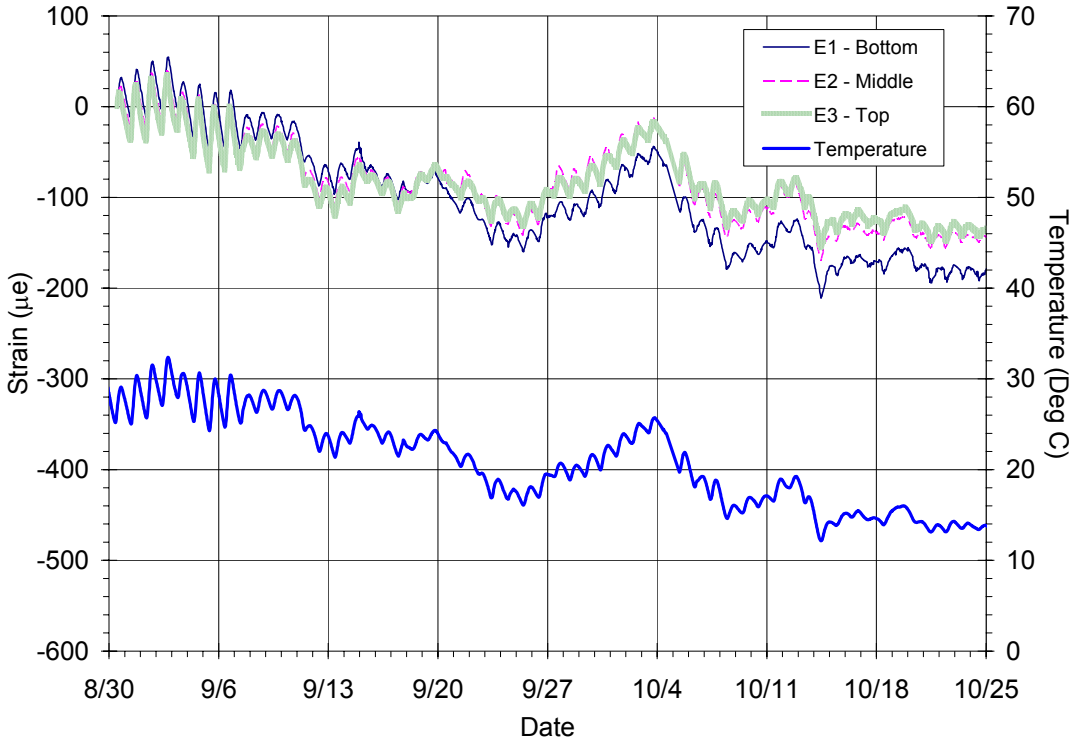

Figure 166. Strain measurements at location E, free shrinkage beam 2, Big Creek

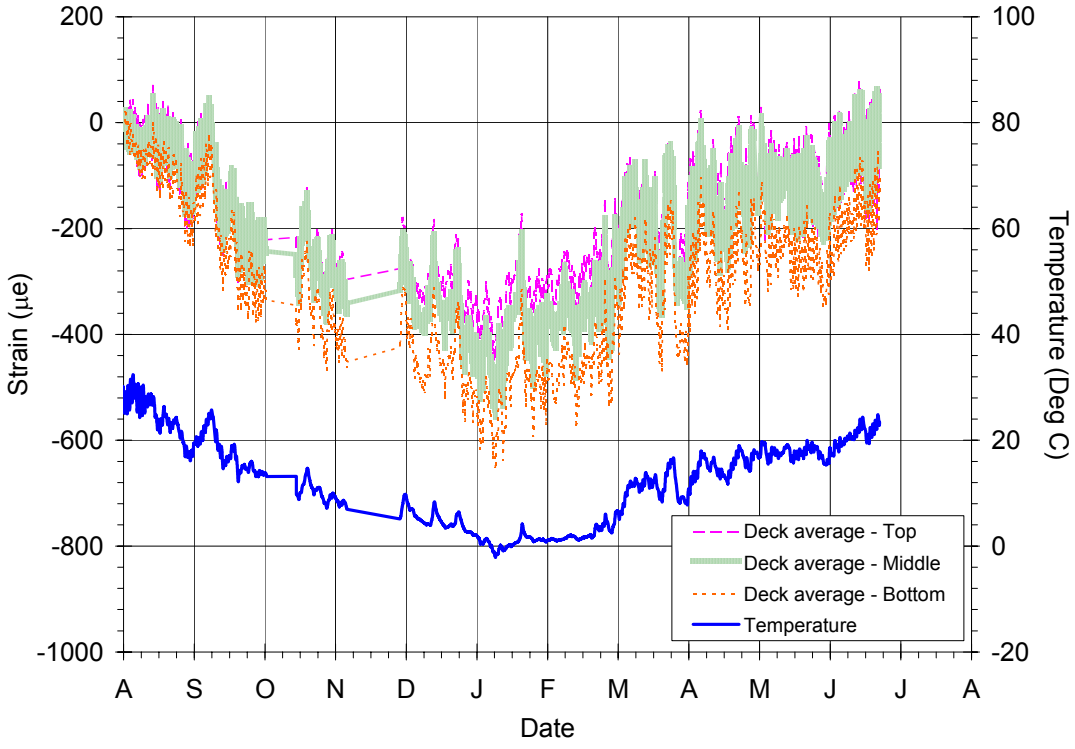

Figure 167. Average long term strain measurements of the bridge deck, Big Creek

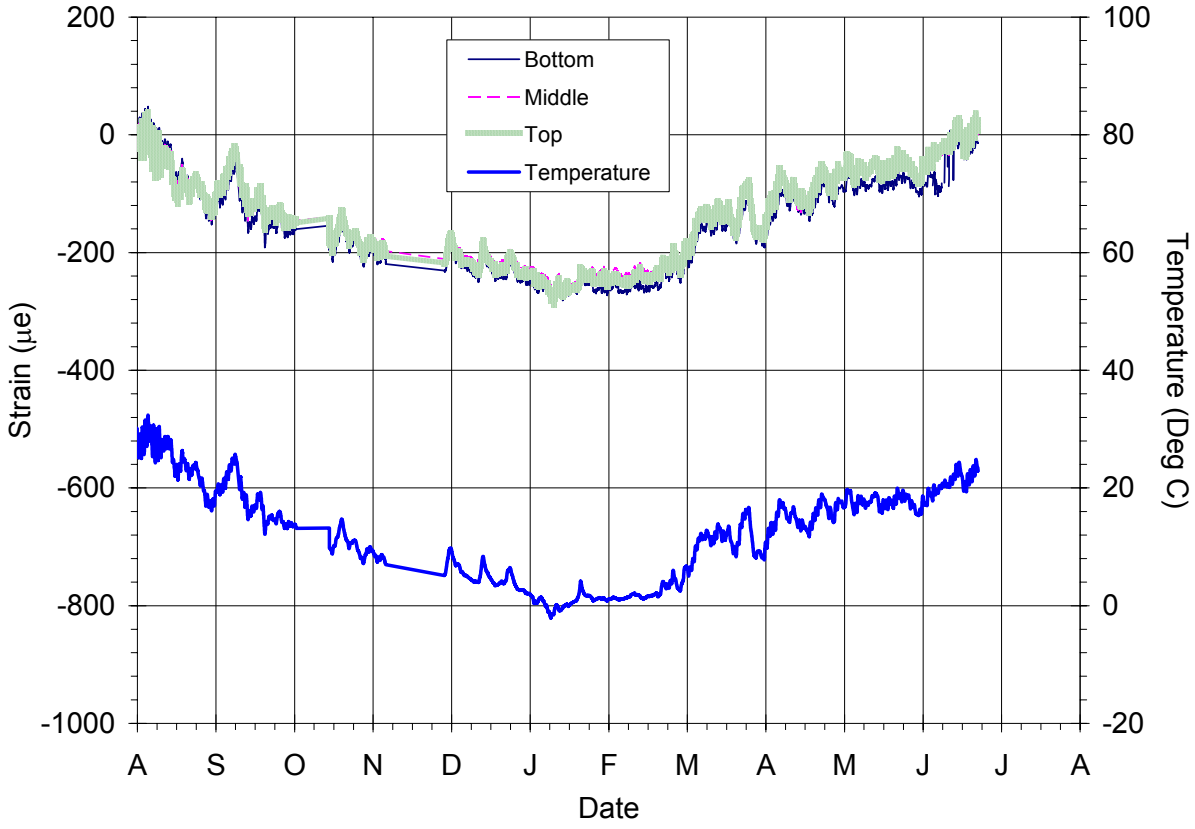

Figure 168. Average long term strain measurements of free shrinkage beams, Big Creek

4. FINITE ELEMENT MODELING AND ANALYSIS FOR BRIDGE DECKS

The bridge deck analysis can be divided into two parts, thermal analysis, and structural analysis. In field work, the temperature gradient of bridge deck was measured directly from the thermo-couple system. However, for the structural analysis under the thermal loading, temperature gradient data of bridge girders are also required. This temperature gradient can be computed by a thermal analysis using the measured temperature data of the bridge deck and atmosphere.

Two IDOT bridges, Duncan Rd/I-72 and Big Creek/I-70 bridge, were considered for the finite element analysis. There are two major differences, the plan view and girder system, between the bridges. Duncan Rd bridge has a rectangular plan view and steel girder system where as the Big Creek bridge has skewed-edge-rectangular plan view and concrete girder system.

Figure 169 shows the outline of the bridge deck analysis. Not only the thermal loading but also the shrinkage and creep were considered in the structural analysis. ABAQUS was used for the finite element modeling and structural analysis.

4.1 Thermal analysis for bridge girder

The thermal analysis of the bridge girder can be treated as a two-dimensional problem because heat transfer along the longitudinal direction is very small compare to the other directions. Heat conduction, convection, and radiation are the main components in the heat transfer mechanism. Heat radiation from the environment to the bridge girders was ignored because the other two components (conduction, convection) govern the heat transfer since the girders are covered by the bridge deck.

4.1.1 Finite element modeling

There are two different types of bridge girders, steel and concrete. The thermal properties and the geometries of the girders are quite different and they affect to the thermal analysis result. The thermal properties of the bridge girders are shown in Table 5.

A computer program code was developed for the thermal analysis using MATLAB. This code can be used for 2-dimensional transient conduction/convection problems. Triangular elements, which can capture the linear varying temperature inside the element, were used for both bridge girders. The inner elements consider only conduction whereas the outside elements also consider convection and temperature boundary conditions. Figure 170 shows the finite element mesh of two bridge girders for the thermal analysis.

4.1.2 Load and boundary conditions

The temperatures were measured at three to five locations on the bridge deck. The measured temperature gradient through the deck thickness at different locations was similar but not identical. So, a representative temperature at location (A) for both bridges shown in Figure 124 and Figure 128 was used for the entire bridge deck area for thermal and structural analysis.

The top surface of the bridge girder has contact area with the bottom surface of the bridge deck. Therefore, the temperature measured on the bottom surface of bridge decks can be used as the temperature boundary condition for the top surface of the bridge girder. The other surfaces exposed to atmosphere were dealt with convectional boundary conditions with ambient temperature.

The initial temperature of the girders was assumed to be equal to the ambient temperature. This assumption might not lead to the exact temperature gradient at early times of the analysis. However, after several hours, the temperature gradient in the girders could be

converged according to the temperature assigned as boundary conditions. The time duration of the analysis was 84 days for the Duncan Rd bridge and 56 days for the Big Creek bridge.

4.1.3 Analysis and result

Figure 171 shows the temperature gradient variation for a one-day-cycle. The number below each figure represents the time of the day. As shown in this figure, no temperature variation occurs across the steel section perpendicular to either the flange or web. This is due to the high conductivity of the steel. In direction parallel to the flange and web, small temperature differences can be found across the section. In the case of the concrete girder, the temperature distribution is more complicated than that of the steel girder, and it exhibits full two-dimensional behavior. At time 0:00, the temperature inside the concrete girder is higher than that of the surface concrete. As time goes to 6:00, the ambient temperature decreased, so the temperature outer concrete also decreased. However, at this moment, the temperature of inner concrete remains higher than that of the outer concrete due to the high heat capacity and low conductivity of the material.

Figure 172 shows the temperature sampling locations in the girders. These locations are identical to the temperature sampling points for the structural analysis. Figure 173 shows the temperature variations with time at these locations. The temperature variations in both steel and concrete girders show a phase difference among the sampling locations due to the thermal conductivity and the boundary conditions. The steel girder shows smaller temperature differences among the sampling locations than the concrete girder due to the high conductivity of steel. The temperature gradient of the girders obtained from the thermal analysis was used for the structural analysis as input data.

4.2 Structural analysis for bridge deck and girder system.

4.2.1 Finite element modeling

Two basic concepts of the bridge deck modeling for structural analysis are simplicity and efficiency. There might be several ways to model the bridge deck and girder system for the structural analysis. However, several conditions should be satisfied for a proper analysis. First, bridge decks are restrained by the bridge girders so the higher stresses are expected in the deck above the girders. This fact says that the contact area between bridge deck and girder is important and needs a refined model for a good analysis. Second, the thermal loading should be assigned properly to the deck and girders. The thermal loadings in ABAQUS can be assigned only by node base and not by element. So the bridge deck and upper flange of the girder should have independent nodes for the different temperature assignment.

The model in Figure 174, which consists of shell elements and multiple constraints (MPC), satisfies these two conditions. Thus it was chosen for our bridge deck and girder model. The MPC in ABAQUS acts like a rigid beam connection between two nodes so that both nodes move together. This feature fulfills our requirements, i.e. independent nodes were used for the bridge deck and upper flange of the girder but they behave as if they have common nodes.

The cross-section of the steel girder has a simple I shape so the exact geometry of the steel girder was modeled. In the case of the concrete girder, the cross-section is more complicated than that of a steel girder. Therefore, the cross-section of the concrete girder was converted to a simple geometry whose depth and the moment of inertia about the major axis has the same value of the original cross-section of the girder. Figure 175 shows an example of this conversion of the concrete girder. Even in this conversion, the girder can provide the same flexural stiffness about major axis and the same area of the original upper flange. The base line

of this conversion is that the main interest of this study is the deck behavior rather than the girder behavior.

The thickness of the steel girder is thin enough so that the girder flange and web can share common nodes without much error in geometry. Moreover, the temperatures through the thickness of the flange and web are almost identical because of the high conductivity of steel. Therefore 1-point-temperature use of each node in the flange and web is enough to simulate the real temperature gradient. So the steel girder was modeled so that the flange and web have common nodes.

In the case of the concrete girder, the thickness of the flange and web is much thicker than those of steel girder. Moreover, the temperature is not identical through the flange or web thickness. Therefore, more than one point of temperature assignment is required at each node in the concrete flange and web. So the elements for each flange and web were placed at the center plane of their own geometry and connected to each other using MPC. With this scheme, the geometric error in the concrete girder can be reduced and more than one point temperature can be assigned at the nodes.

Five temperature points through the bridge deck depth were assigned. Each vertical location of temperature point in the bridge decks was matched to the actual location of the thermocouple used for measuring the temperature change.

Figure 176 shows the finite element mesh of the bridge deck and girder system. The number of the degrees of freedom in both models is about 60,000. The finite element models were implemented based on the model in Figure 174 using ABAQUS. More refined meshes were used around the girder and pier lines to capture the rapid variation of stress usually expected in a similar structural system.

4.2.2 Load and boundary conditions

The temperature gradients of the bridge deck and girders were applied to the finite element model as thermal loadings. The temperature gradient in the bridge deck measured in the field was used for the analysis. In the case of the bridge girder, the temperature gradient computed in the thermal analysis was used. The temperature in the girders was not measured. One and three temperature points were used for the steel and concrete girder respectively.

The reference (initial) temperatures are required to calculate the thermal expansion or contraction. Before the age of 3 days, the temperature changes are very dramatic and not stable. So the temperatures in the concrete deck at the age of 3 days were selected for the reference temperatures. The periods of the analysis are from the age of 3 to 84 days for the Duncan Rd bridge and 3 to 56 days for the Big Creek bridge. The time step for the analysis was 2 hours.

Shrinkage and creep information should be also considered in structural analysis. The shrinkage and creep in concrete girders are ignored. The shrinkage information was modeled using Bazant's B3 model in Chapter 5. As mentioned in this chapter, the results indicate that 50% of the shrinkage strain is relaxed by creep with the fully restrained boundary condition. It is assumed that the girders and reinforcement can restrain the deck concrete in bridge so that the concrete can obtain the fully restrained boundary condition. Based on this assumption, 50% of the shrinkage strain was relaxed by creep in this model.

Two different levels of shrinkage, 100% and 20% of the shrinkage measured in laboratory, were applied in the analysis to identify the shrinkage effect on the behavior of the bridge deck.

ABAQUS does not provide a simple way to deal with the shrinkage and creep effects in static analysis. So shrinkage and creep were implemented using an equivalent temperature [1]. Generally, the equivalent temperature cannot capture a change in strain due to the different

numbers of degree of freedom between strain and temperatures, i.e. strain is a tensor which has three independent components, but temperature is a scalar which has only one component. However, in some special cases such as our configuration, when the three strain components have the same values, it is possible to emulate the shrinkage and creep effects using the equivalent temperature.

Figure 177 shows the schematic of the equivalent temperature for the shrinkage and creep. The equivalent temperature (Te) was defined as summation of the measured temperature (Tt), shrinkage equivalent temperature (Tsh) and creep equivalent temperature (Tcr). The shrinkage creep equivalent temperature was defined as the strain value divided by the thermal expansion coefficient.

The bridges were placed on the x-z plan. All supports on the piers and abutment, except one node, were assigned with 2-directional roller support, which has free translation in x and z direction and fixed translation in y direction. The three rotational components are all free in this roller boundary condition. One node was assigned with pin support for the stability of the analysis.

4.2.3 Material properties

All materials were assumed to be linear elastic material for simplicity and based on the fact that concrete behaves as a linear material before cracking. Due to this assumption, this model cannot capture the nonlinear behavior of concrete after the crack initiation. However, the main idea of this modeling is to predict the potential cracking zone on bridge decks under thermal and shrinkage loading.

Table 6 shows the mechanical properties of concrete and steel in the bridge girders. ABAQUS does not provide a simple way to implement the varying material properties in static analysis. A fixed elastic modulus of concrete at age of 28 days was used. Therefore the interpretation of the stress evaluated with this fixed modulus is required for the concrete at the age before 28 days.

One thing we need to remember is that the evolution of elastic modulus of concrete is much faster than that of strength. It could be said that the difference between the elastic modulus at age of 7 and 28 days is not very large. So stress changes between 7 and 28 days are slightly exaggerated and stresses between the age of 3 and 7 days are more exaggerated than in real material. Nevertheless, this modeling approach is a conservative way to evaluate the stress at early age.

4.3 Analysis and Results

Figure 178 shows the deformation shapes of the bridges at an age of 56 days. The deformation shape of both bridges was magnified by a factor of 1000. As expected, the temperature gradient and shrinkage caused not only longitudinal bending but also warping in the transverse direction of the bridge deck. The bending and warping behavior would be more pronounced without girders under the decks. In other words, the girders restrain the bending and warping behavior so high stresses are expected in the middle of the bridge decks.

The transverse stress in the bridge deck is much smaller than the longitudinal stress. Therefore, the transverse stress will not be discussed in this chapter and the terms ‘stress’ and ‘strain’ mentioned in this chapter represent the longitudinal values. The stress we are concerned with in the concrete deck is tensile stress so the term ‘stress’ without a description represents tensile stress. Positive sign convention was used for tension in all figures and graphs.

4.3.1 Strain comparison with field data.

Figure 179 and Figure 180 compare the computed strains from the analysis and the measured strains in the deck. The computed strains were not matched to the measured strains but they follow the measured strains nearly in phase and have similar magnitude. This means the analysis agrees well with the measured field behavior.

There might be several reasons for the offset between the analysis and field data. One reason could be the initial conditions. The temperatures at age of 3 days were used as the reference temperature for the analysis. The reference temperatures are very important in the analysis, but the exact reference temperature cannot be determined. Another reason could be the visco-elastic behavior of the early age concrete that could relax. Besides these reasons, many factors can affect the initial conditions of the analysis.

The fact that stress is basically a function of strain provides us a good way to overcome the uncertainty of initial conditions at early ages. We have measured strain data in the field and if the calibration procedure were adopted to match the strains at early ages then a reasonable stress variation could be obtained. Therefore, the reference temperatures were calibrated so that the early age strains from the analysis and the measured field strains approximately matched each other and then the stresses were recalculated based on the calibrated reference temperatures. Figure 181 shows the strain comparison of the two bridges after the calibration procedure.

4.3.2 Stress development on the bridge decks

Figure 182 shows the longitudinal stress development of the two bridge decks based on the calibrated reference temperatures. The stresses in this figure are only for one location and cannot be used to judge the behavior of the entire bridge deck. However, we can judge the general behavior with this figure.

The stresses in both bridge decks fluctuated with 1-day-cycles and gradually increased with age. This behavior well represents the temperature changes and the shrinkage. The Duncan Rd bridge deck shows much less stress development compared to the Big Creek bridge deck, i.e. less than 200 psi was developed in the Duncan Rd bridge deck by the age of 30 days but more that 350 psi was developed in Big Creek bridge deck by the same age. A similar amount of stress difference between the two bridges was generally observed in other locations.

Figure 183 shows the stress distribution of the Duncan Rd bridge deck. 200 psi of tensile stress was used for the threshold in this figure. The shaded area in the plan view of the bridge deck represents the elements that experienced a stress higher than the threshold by the given ages. For example, the shaded area of the plan view in Figure 183(a) labeled as 35 represents the elements that experienced more that 200psi of longitudinal stress at top the surface by the age of 35 days.

There are some differences in stress development between the top and bottom surface. On top surface, the high stress area starts from the girder line and spreads out to the entire bridge deck area. Once the area on the girder lines reached a certain stress level, another high stress region around the outer pier lines occurred and spread to the area around the center pier line. On the bottom surface, the high stress area initiates from the area near the outer pier lines and spreads out toward the center pier line. Up to an age of 35 days, the girder line area does not show high tensile stress.

Both top and bottom surfaces shows a common behavior in stress development, i.e. the high stress area initiates from inside of the bridge deck and spreads to the outside of the bridge deck. It could be said that this behavior is as expected in a usual bridge deck and girder system. The inside of the deck is more restrained by girders. Stress develops due to this restrain because thermal and shrinking strains are the only load conditions in the system.

Figure 184 shows the stress distribution of the Big Creek bridge deck. The stress develops very similarly to the Duncan Rd bridge. High stress initiates from inside of the deck and spread to the outside of the bridge deck. However, the level of the stress was much different. A threshold of 400psi was used for presentation purposes, i.e. the Big Creek bridge deck shows much higher tensile stress than Duncan Rd bridge deck so the stress distribution cannot be shown properly with the same stress threshold value (200psi) as the Duncan Rd. bridge.

4.3.3 Location of highest stresses in bridge decks

Figure 185 shows the stress distribution of the Duncan Rd bridge deck at an age of 84 days. In this figure, similar to Figure 184, the shaded region represents the elements exceed threshold stress specified under each plan view at an age of 84 days. With this figure, the highest stress region can be identified, i.e., the area around the girder lines on the top surface and the outer pier lines on bottom surface shows the highest stress.

Figure 186 shows the stress distribution of the Big Creek bridge deck. Stress develops similarly to the Duncan Rd bridge deck but the location of the higher stress region is different, i.e. the area around the outer pier lines on the top surface and the girder lines on bottom surface shows the highest stress. This is reversed from the higher stress location of the Duncan Rd bridge deck.

The common locations of higher stress region in both bridges decks are the area around the girder lines and outer pier lines. However, the stress level is much higher than that of the Duncan Rd bridge deck even at an earlier age (56 days). The similar stress distribution patterns can be observed in 500 psi threshold in Big Creek bridge deck (Figure 186) and 300 psi threshold in Duncan Rd bridge deck (Figure 185).

4.3.4 Restraint and stress development

The analysis used similar material properties for both of the bridge decks. So the differences in the stress level and the location of stress initiation are related to the structural aspect of the bridge.

There are several structural differences between the bridges. The Duncan Rd bridge has a rectangular plan view and steel girders whose thermal and mechanical properties are different to that of concrete. It has 4 continuous spans (3 piers and 2 abutments) and the 2 spans contacted to the abutments have about half the length of the other 2 spans. The Big Creek bridge has a skewed-edge-rectangular plan view and concrete girders. It also has 4 continuous spans but each span has nearly the same length.

All of these properties can affect the result of the structural analysis, but the major factor for the analysis seems to be the flexural stiffness of the girders.

A simple index, which can represent the flexure stiffness in bridge system, was defined as below to compare the degree of restraint of the bridge systems.

$$SI = N \times I \times E$$

where,

N = number of the girders

I = moment of the inertia in major axis

E = elastic modulus

With this index, the ratio of the restraint in the Big Creek bridge to that in the Duncan Rd bridge can be obtained as below.

SI of Big Creek bridge / SI of Duncan Rd bridge = 1.37

This ratio says that the degree of restraint in the Big Creek bridge is much higher than that of the Duncan Rd bridge. A higher degree of restraint leads to greater stress in the bridge deck.

4.3.5 Role of daily and seasonal temperature cycles on stress distribution

The temperature change including daily fluctuation in the bridge system does not result in greater stress than the shrinkage because the temperature change affects the whole movement of the bridge system including the girders. The bridge is restrained from temperature deformation only by the piers and abutments. However, the shrinkage of the deck is restrained by the girders, which do not experience shrinkage. This restraint causes a stress development in the concrete deck over time. This stress development is related to the cracking behavior.

The magnitudes of the volume change due to the temperature and shrinkage are different. Strain due to the temperature change up to an age of 2 months was about 150 με for both bridges but the shrinkage (plus creep) during this period was about 225 με. Therefore, shrinkage is a more dominant factor than temperature at relatively early ages (about 2 months).

4.3.6 Stress distribution for case with low shrinkage concrete

To simulate the low shrinkage effect for the same bridge geometries, 20% of the shrinkage (plus creep) data measured in laboratory was used. This may represent a lower shrinkage mixture such as concrete utilizing shrinkage reducing admixtures (SRAs).

Figure 187 and Figure 188 shows the stress distribution of the bridge decks. Both bridge decks shows very low tensile stress development. The top surface of the Duncan Rd bridge deck shows no region where the longitudinal tensile stress exceeds 50 psi during the analysis period. The other surfaces of the bridges decks show very small regions where the stress exceeds 200 psi during the analysis period. This level of should not cause crack initiation.

The location of the higher stress region for the lower shrinkage material was different than the normal shrinkage concrete. With normal concrete, the higher stress region was on the outer pier lines. But the low shrinkage concrete shows higher stress region at the abutment and center pier line.

Using only 20% of normal shrinkage (plus creep) represents about 11 ^{o}C of equivalent shrinkage plus creep temperature during the period. This equivalent temperature change is relatively small compared to the temperature change (about 15 ^{o}C) during the same period. So the location and pattern of higher stress region seem to be governed by temperature variation rather than shrinkage.

Figure 189 shows the maximum stress at the location over the pier and the top of a girder in the Big Creek bridge deck with different degree of the shrinkage effect. According to this figure, if the shrinkage strain was reduced by 15%, stress did not exceed 500 psi in the deck. A 40% reduction in shrinkage reduced the maximum stress to below 400 psi. Assuming that a high quality bridge deck will have sufficient long-term durability even if some cracking is allowed, then reducing shrinkage by 15-40% will produce a durable high quality bridge deck.

4.4 Summary

A systematic procedure was developed for the stress analysis of a bridge deck undergoing temperature and shrinkage variations over a long period. High stress in the bridge deck develops on the girder lines and piers. The high stress development initiates from the inside of the bridge deck and spreads to the outside of the decks. The higher restraint due to the girders in the bridge system cause higher stress in the deck. Lower shrinkage material reduces high stress development and changes the location of the higher stress regions on the bridge deck.

REFERENCES

1. Shin, Hak-Chul Early age behavior of bonded concrete overlays due to shrinkage and thermal changes, Ph.D. thesis, University of Illinois at Urbana-Champaign, 2000

TABLES

Table 5. Thermal properties of the bridge girders

Thermal Properties	Steel Girder (Duncan Rd bridge)	Concrete Girder (Big Creek bridge)
Conductivity (W/ m °C)	120	1.4
Convectivity (W/m^2 °C)	8	8
Specific heat (J/kg °C)	460	1000
Density (kg/m^3)	7800	2500

Table 6. Mechanical properties of the bridge girders

Mechanical Properties	Steel Girder (Duncan Rd bridge)	Concrete Girder (Big Creek bridge)
Elastic Modulus (ksi)	27500	4415
Poisson Ratio	0.25	0.20
Expansion Coefficient (με/°C)	12	10
Moment of Inertia (in^4)	7450	90950
Corss-section area (in^2)	42	443

Table 7. Mechanical properties of the bridge decks

Mechanical Properties	Duncan Rd bridge	Big Creek bridge
Elastic Modulus (ksi)	3372	3274
Poisson Ratio	0.20	0.20
Expansion Coefficient (με/°C)	10	10

FIGURES

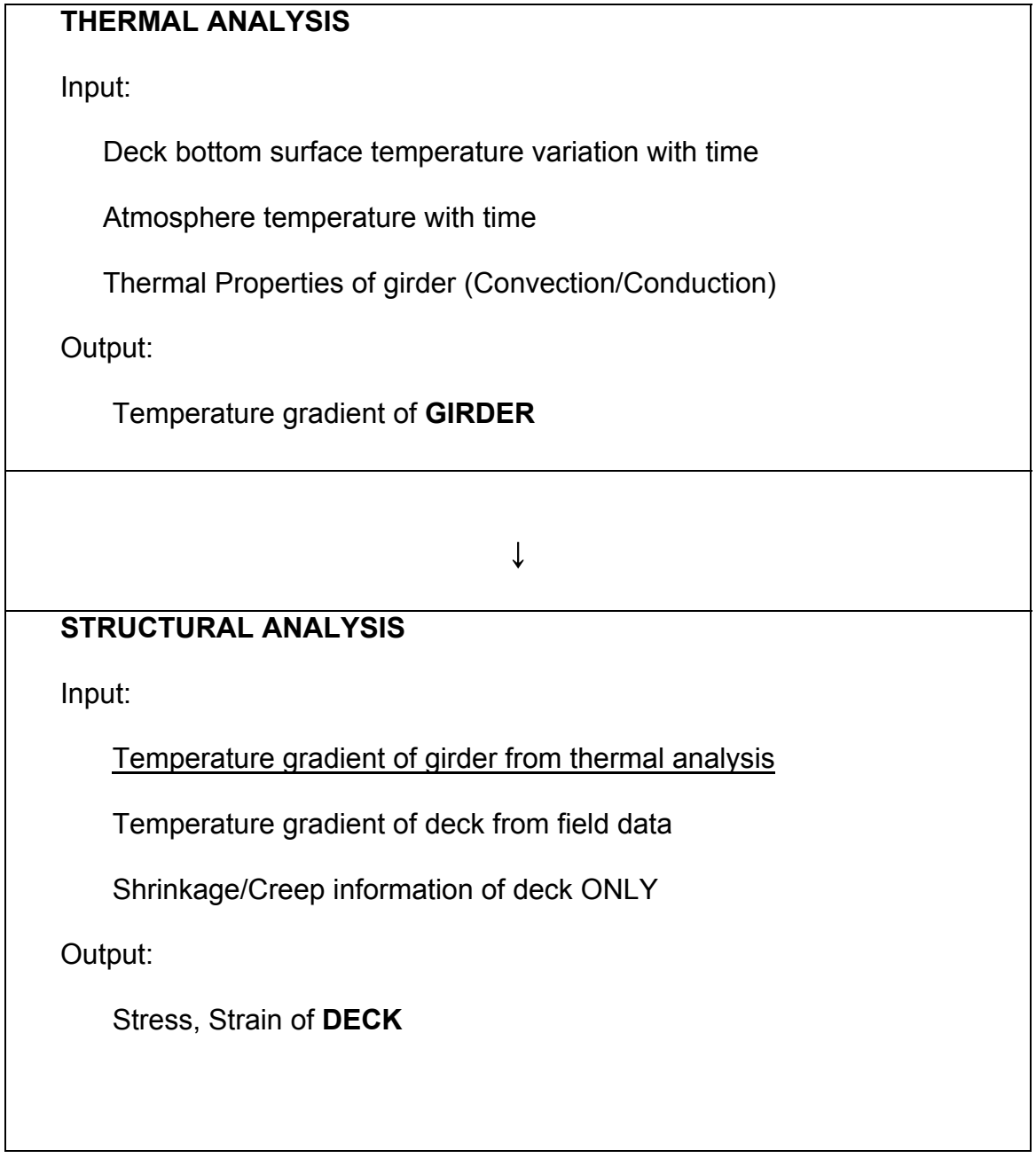

Figure 169. Two phases of bridge deck analysis

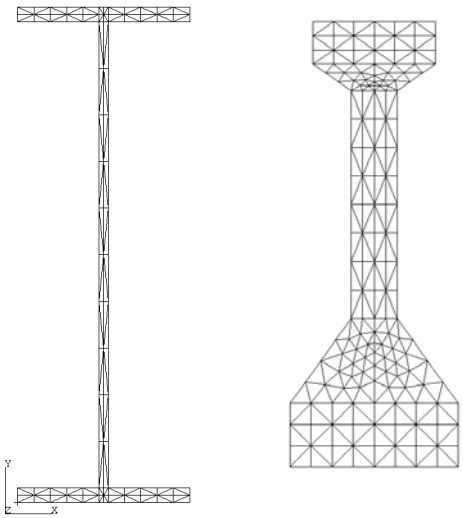

Figure 170. Finite element meshes for thermal analysis (a) Steel girder (b) concrete girder

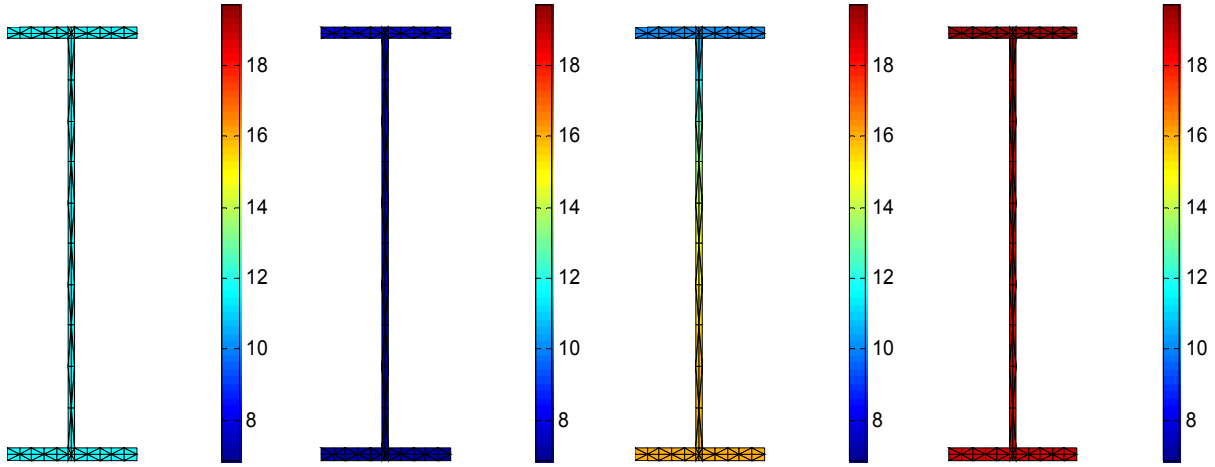

0:00 6:00 12:00 18:00

(a) Steel girder (11/07/2001)

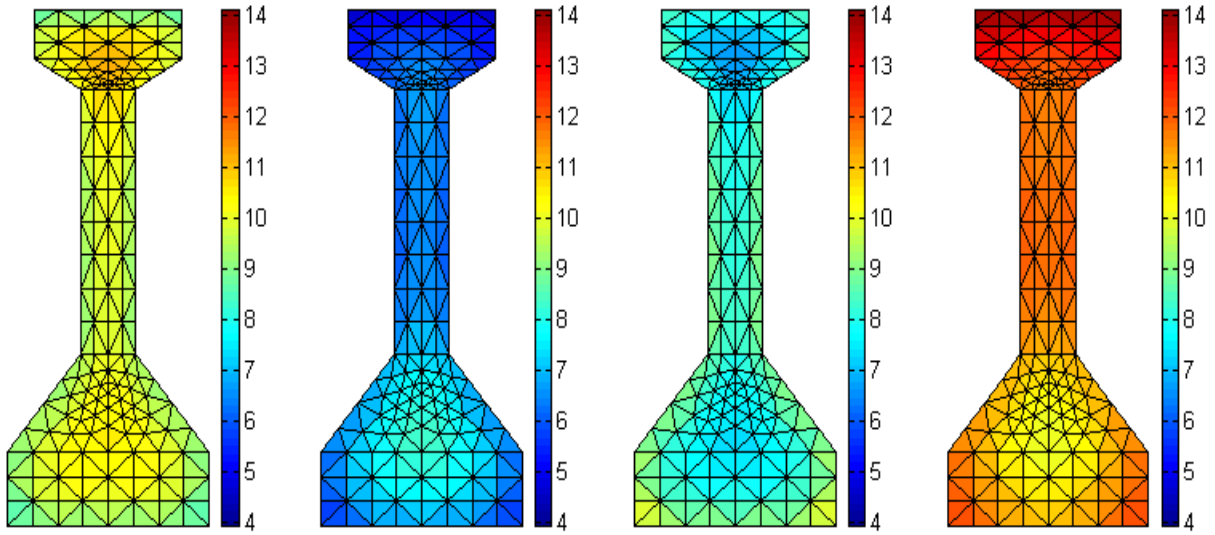

0:00 6:00 12:00 18:00

(b) Concrete girder (10/21/2002)

Figure 171. Variation of temperature gradient in one-day cycle

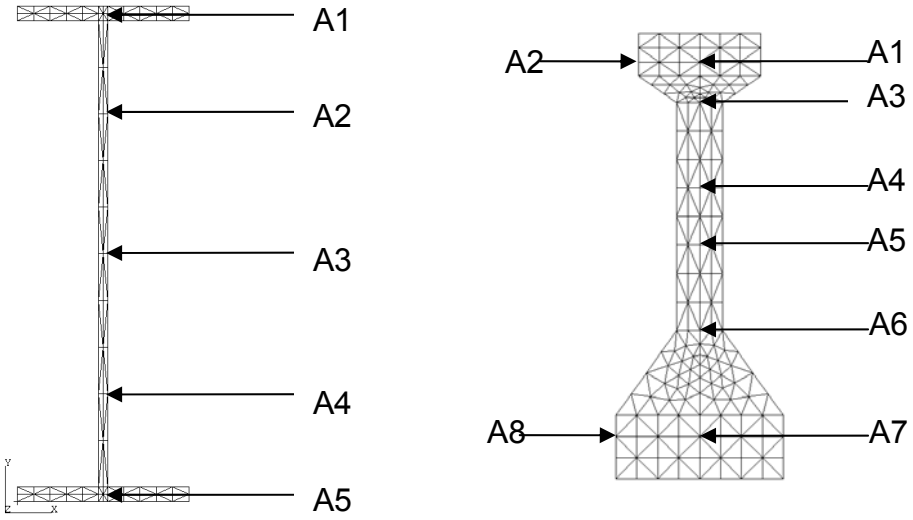

(a) Steel girder (b) concrete girder

Figure 172. Temperature sampling points for the structural analysis

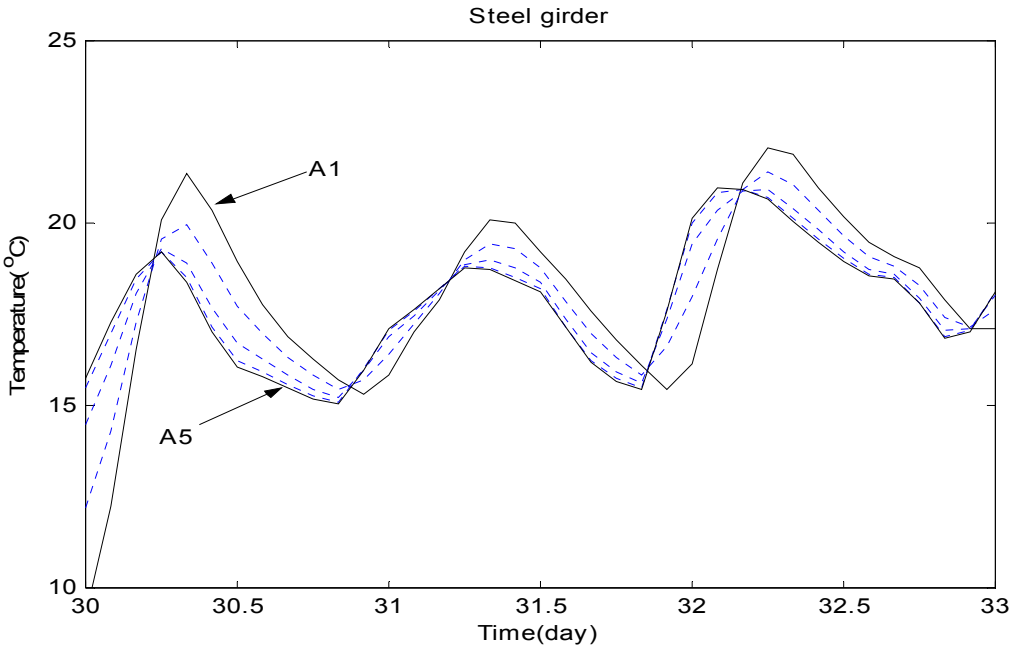

(a) Steel girder

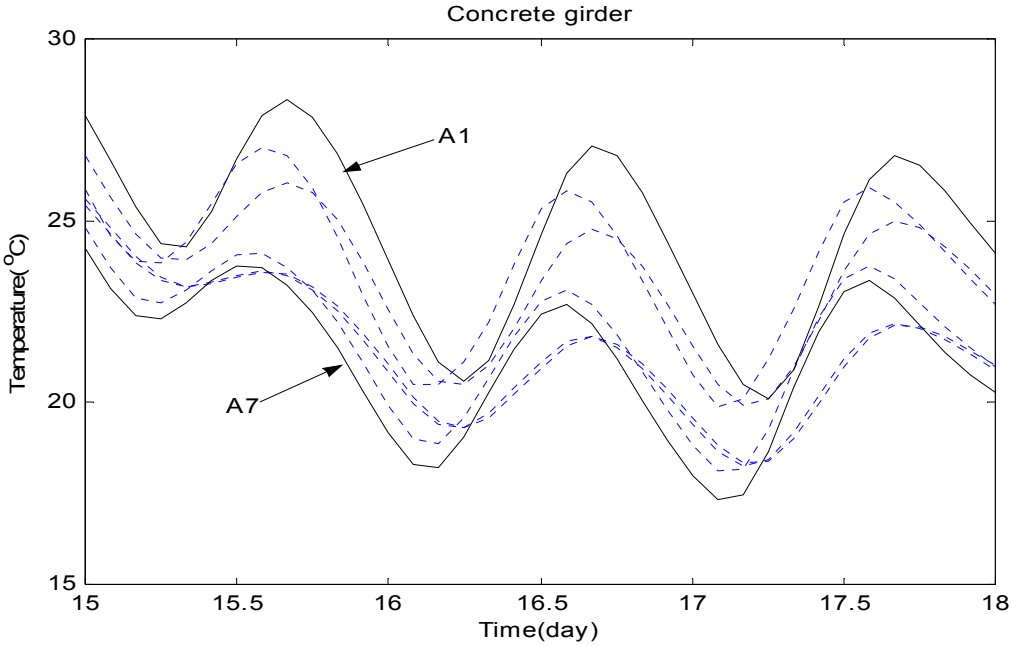

(b) Concrete girder

Figure 173. Temperature variations at the sampling points

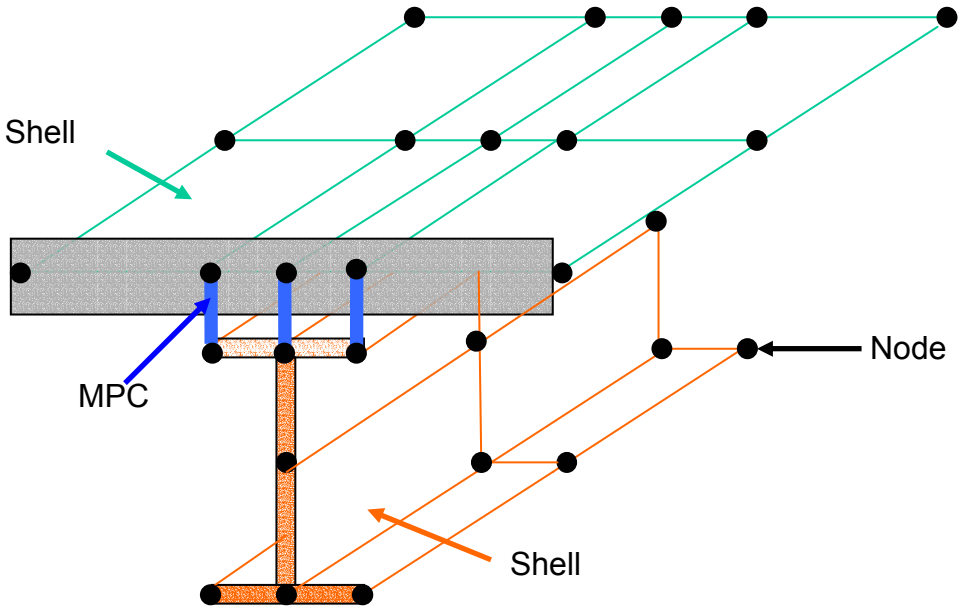

Figure 174. Finite element modeling for bridge deck and girder system

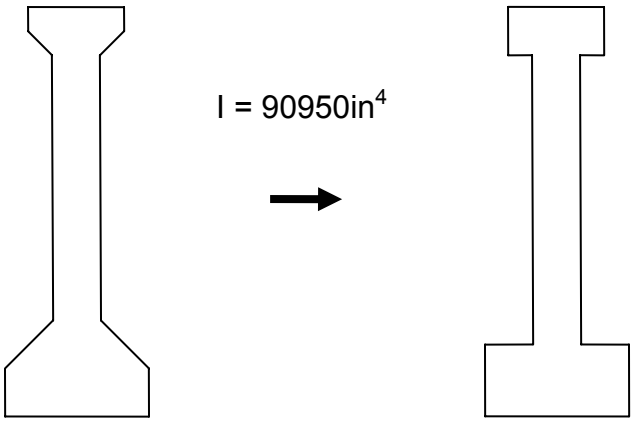

Original concrete girder section Equivalent section

Figure 175. Equivalent geometric conversion of concrete girder

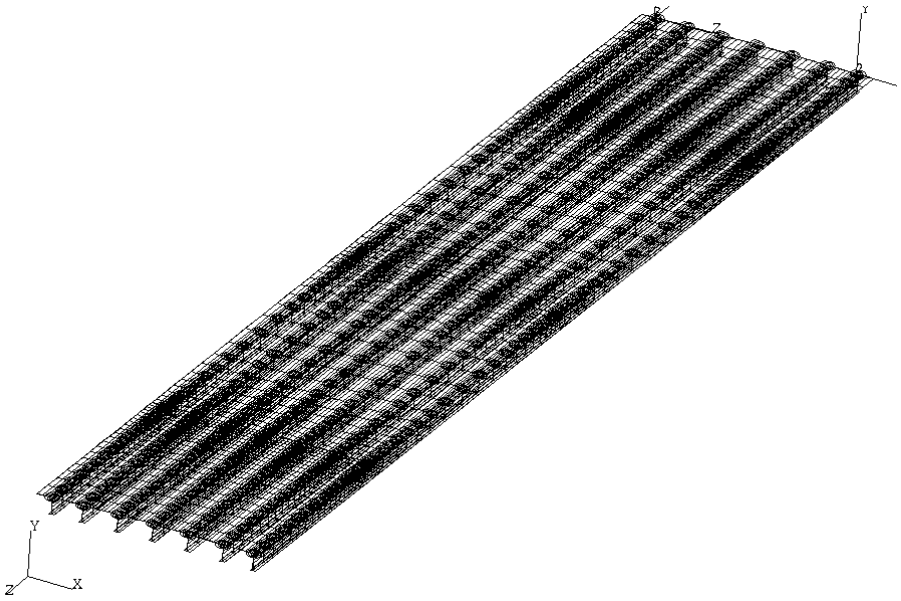

Duncan Rd Bridge

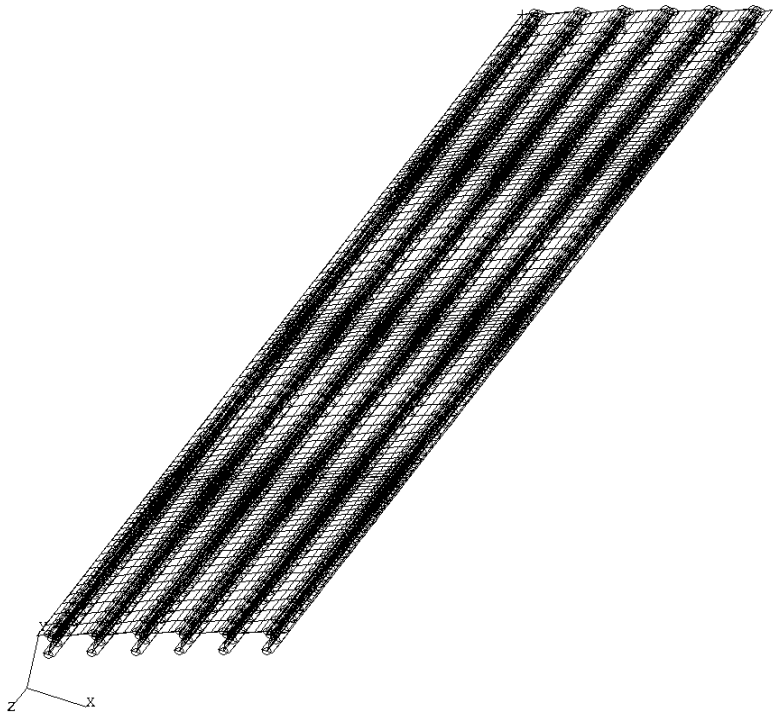

(B) Big Creek Bridge

Figure 176. Finite element meshes

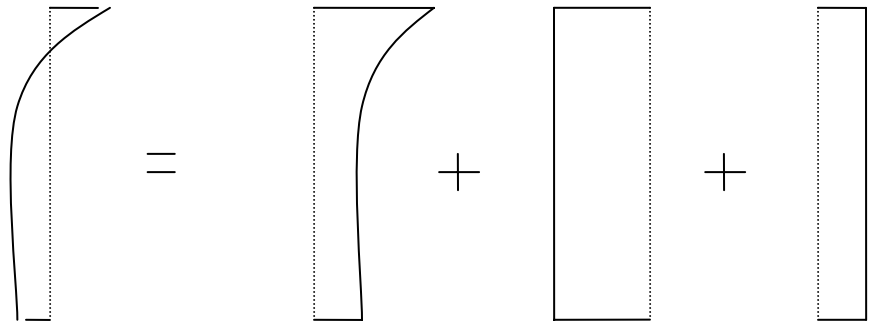

Te Tt Tsh Tcr

Figure 177. Schematics of equivalent temperature for the shrinkage and creep

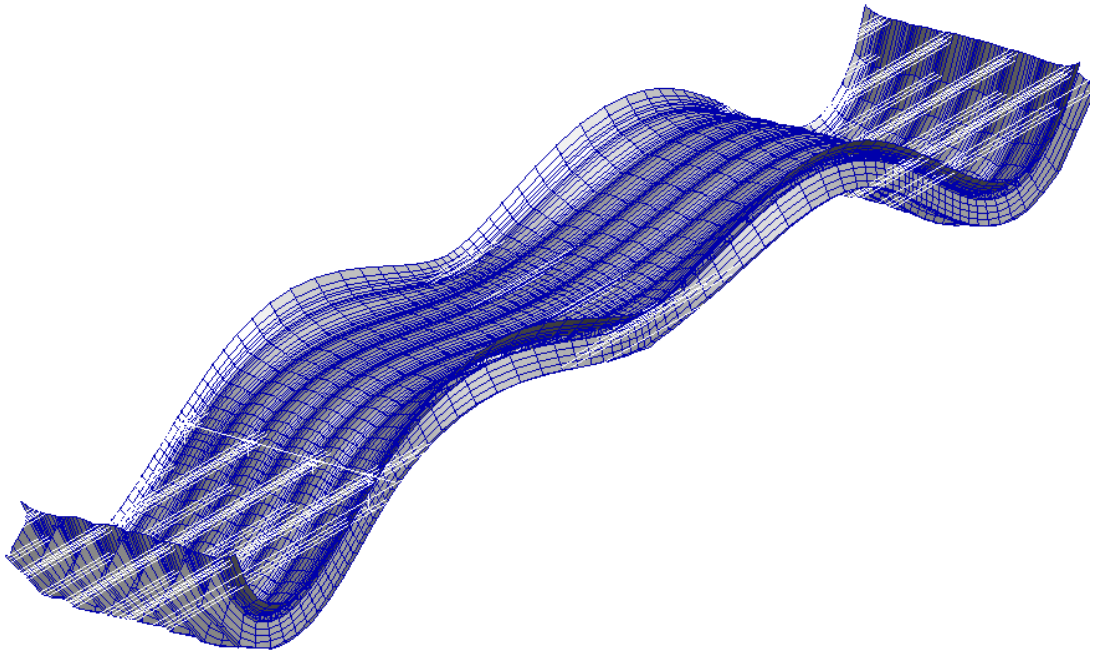

(a) Duncan Rd Bridge

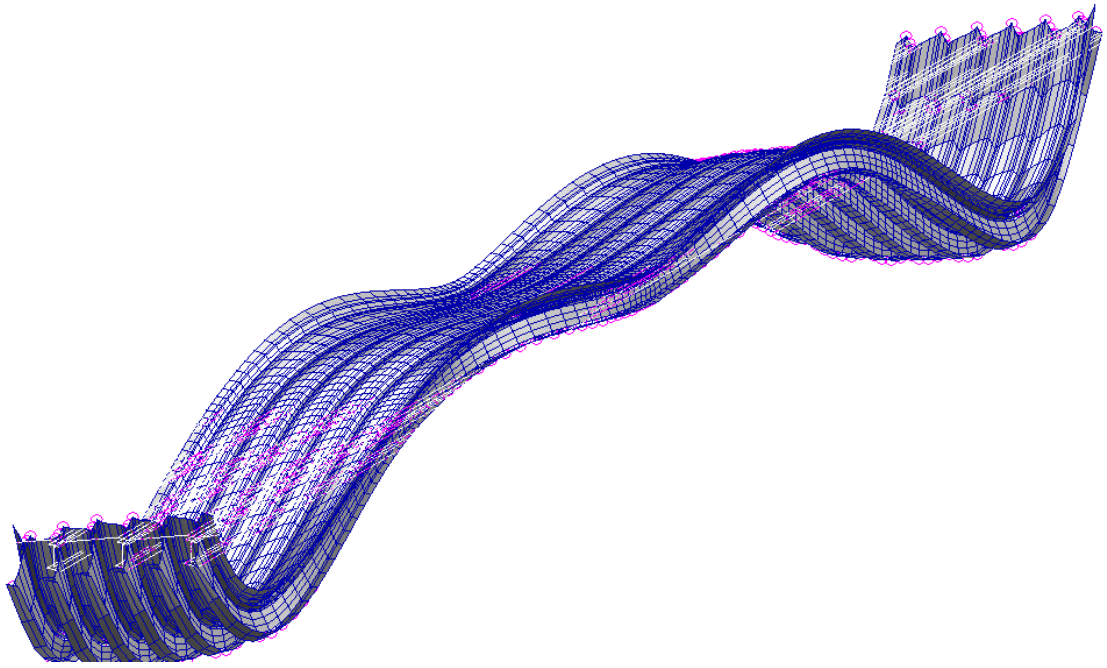

(b) Big Creek Bridge

Figure 178. Deformation of bridges due to the thermal and shrinkage loading

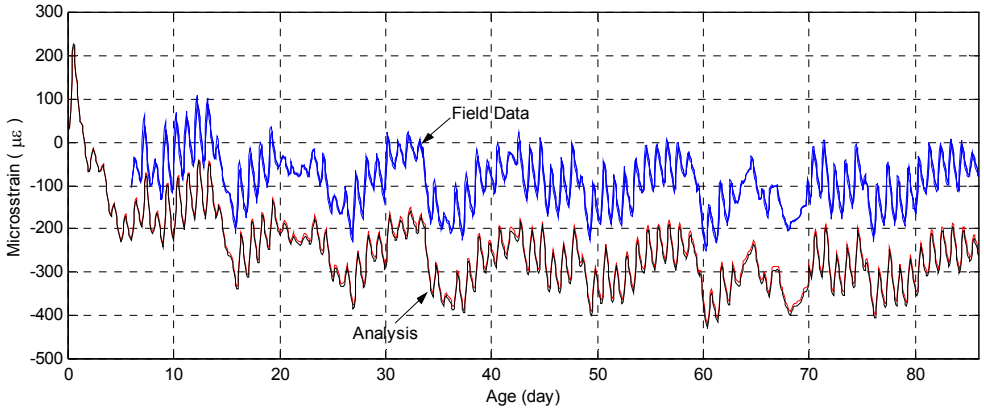

(a) Location A

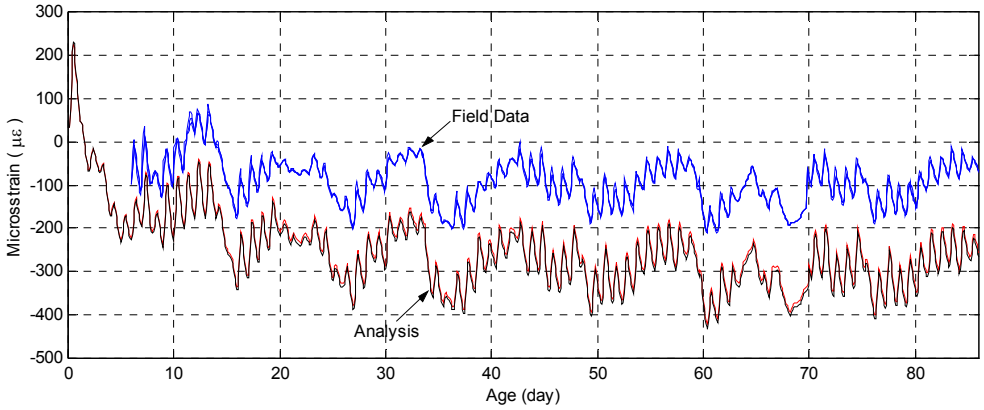

(b) Location B

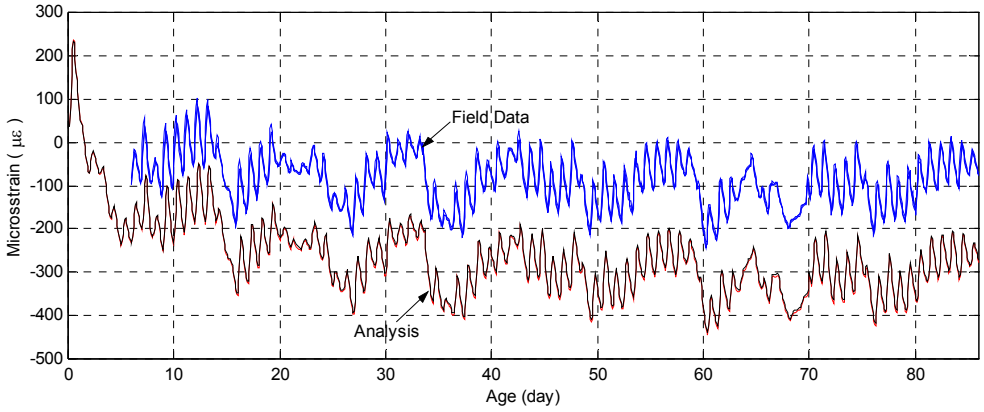

(c) Location C

Figure 179. Comparison of model strains with field data for Duncan Rd Bridge

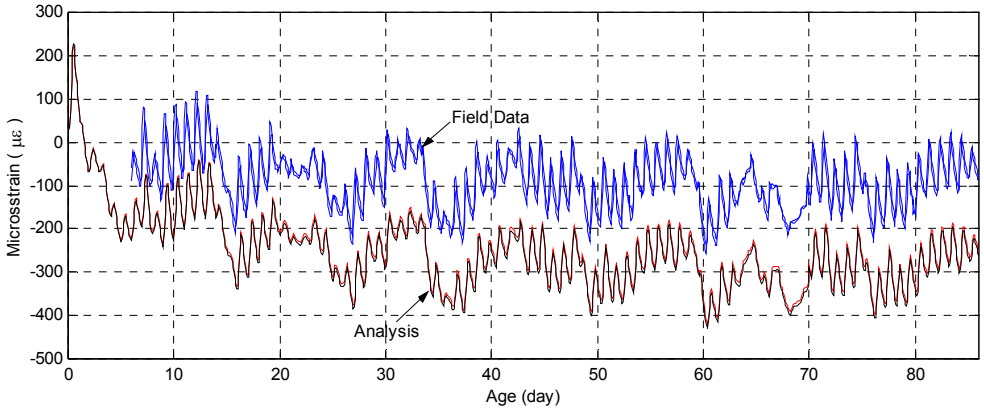

(d) Location D

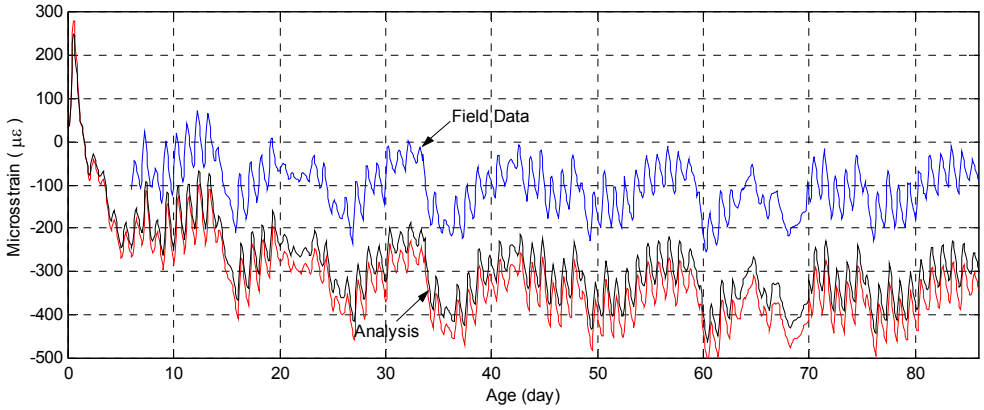

(e) Location E

Figure 179(cont.) Comparison of model strains with field data for Duncan Rd Bridge

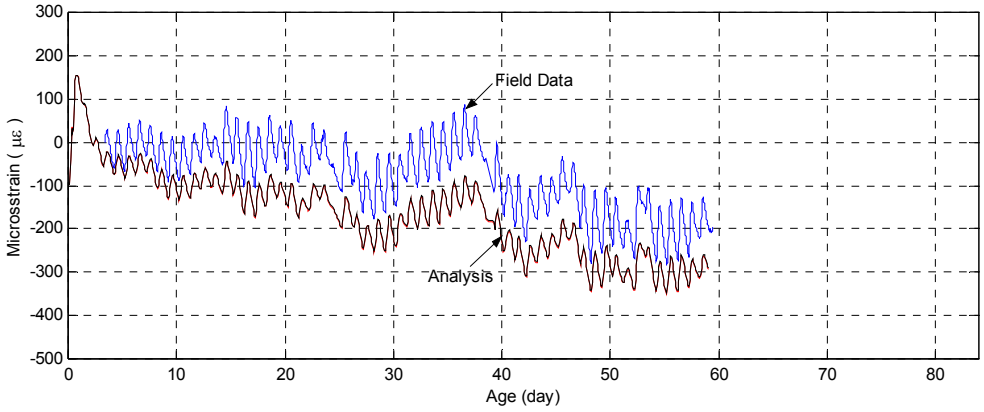

(a) Location A

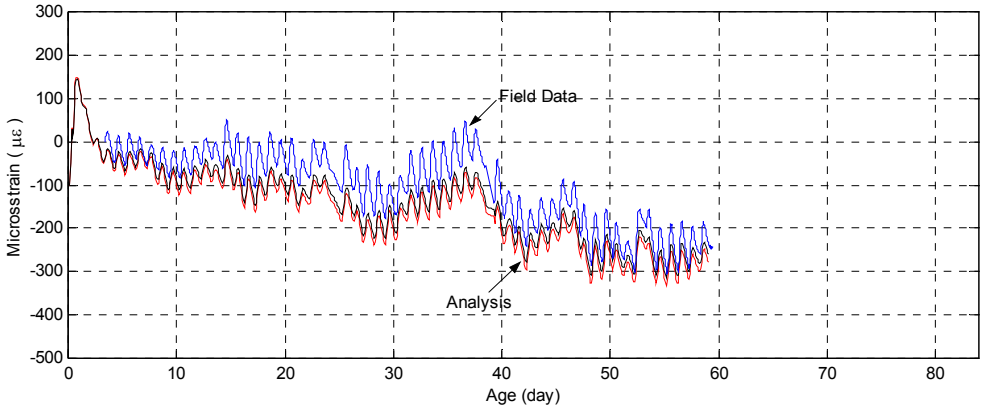

(b) Location B

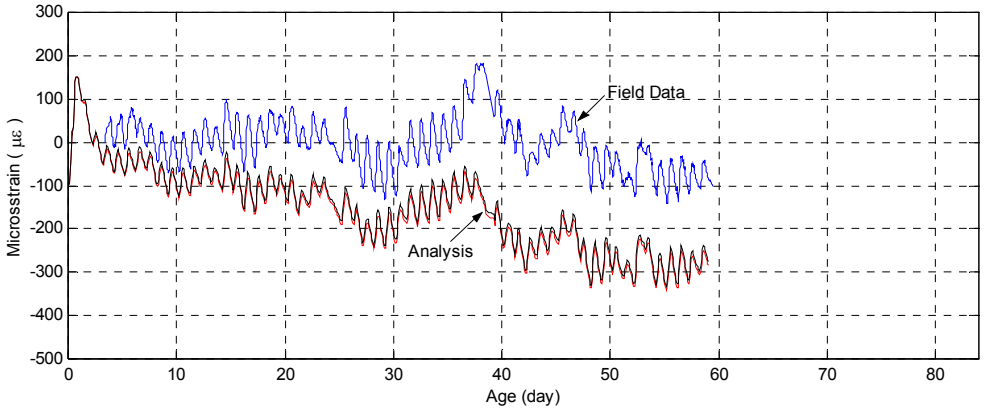

(c) Location C

Figure 180. Comparison of model strains with field data for Big Creek Bridge

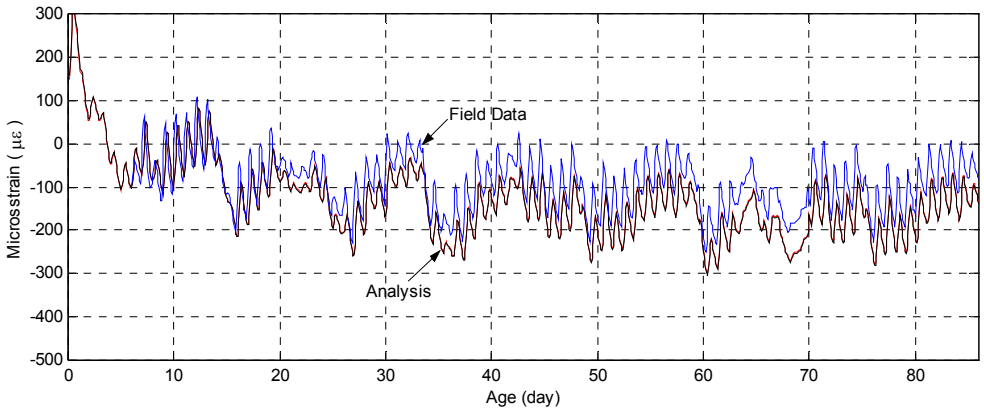

(a) DUNCAN, location A

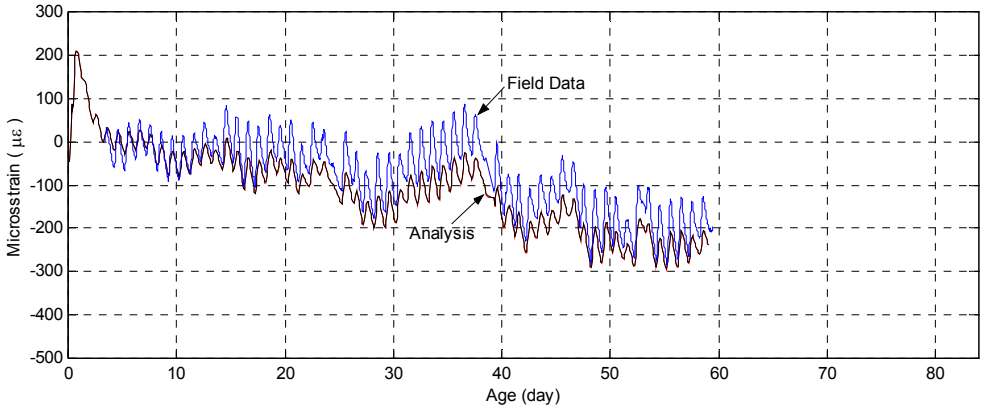

(b) BIG CREEK, Location A

Figure 181. Strain comparison after calibration procedure

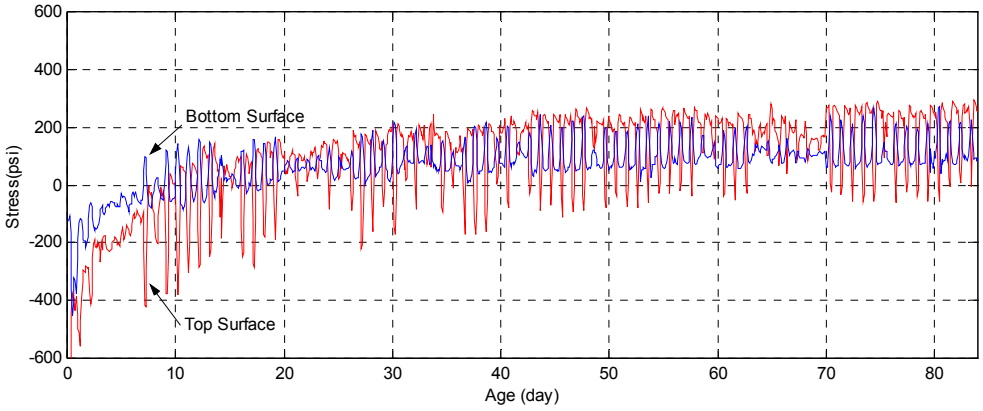

(a) Duncan Rd bridge, Location A

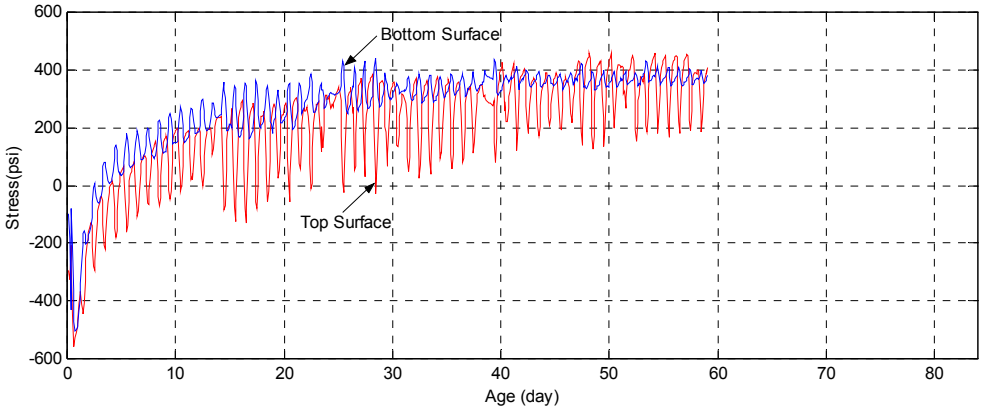

(b) Big Creek bridge, Location A

Figure 182. Longitudinal stress development in bridge decks

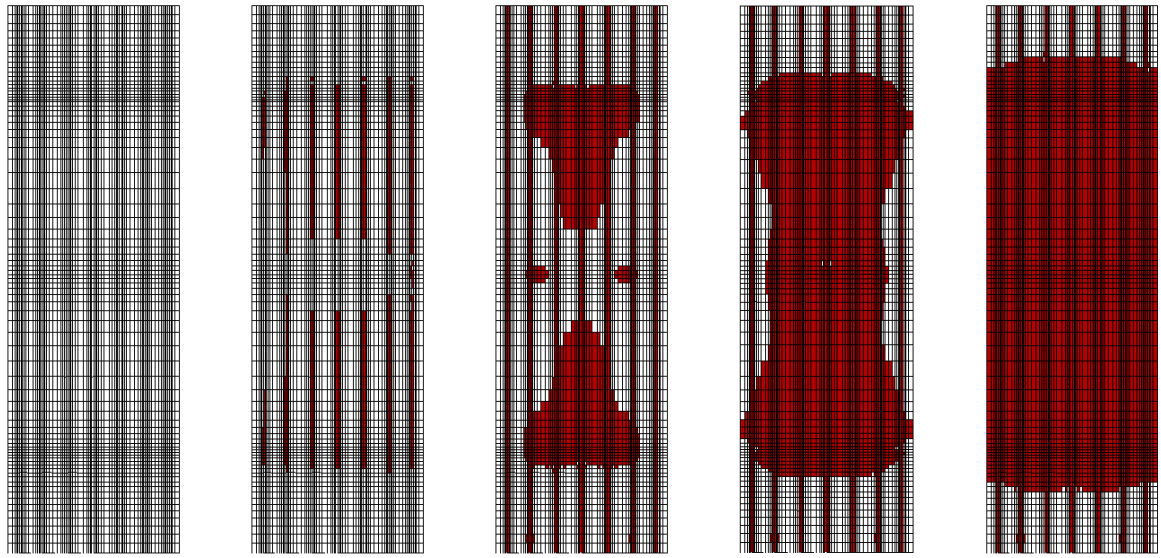

28 30 35 70 84 days

(a) Top surface (200psi threshold)

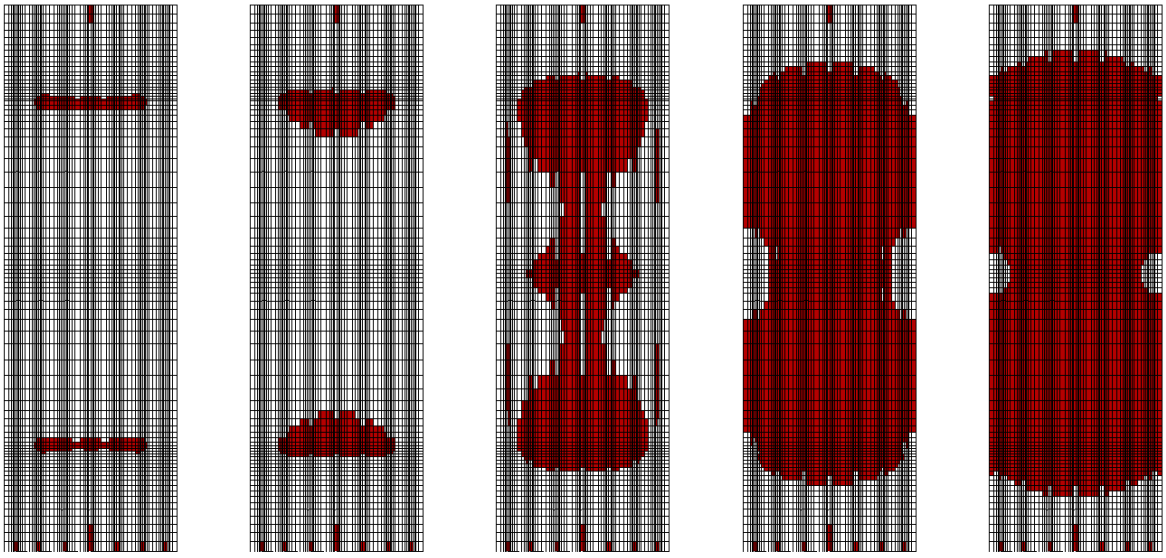

28 30 35 70 84 days

(b) Bottom Surface (200psi threshold)

Figure 183. Longitudinal stress distributions of Duncan Rd bridge deck

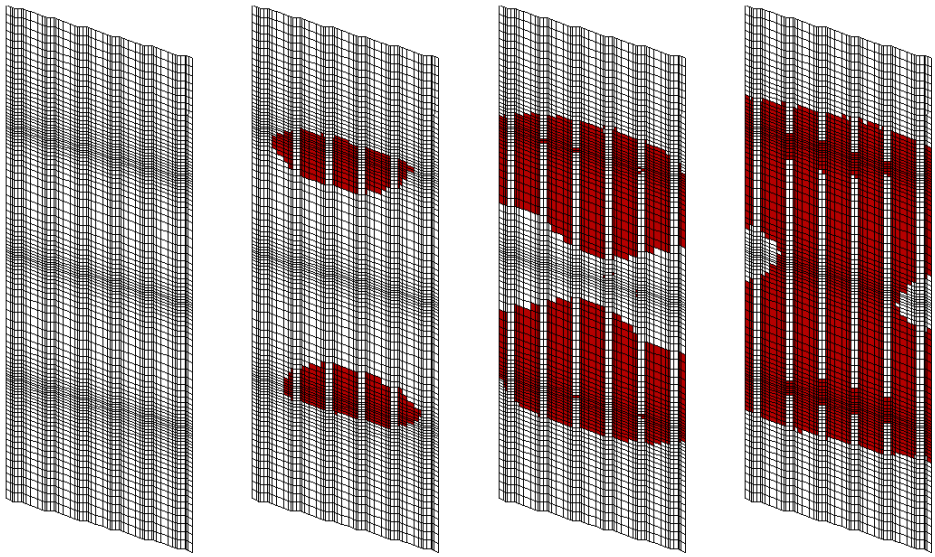

21 28 42 56 days

(a) Top surface (400psi threshold)

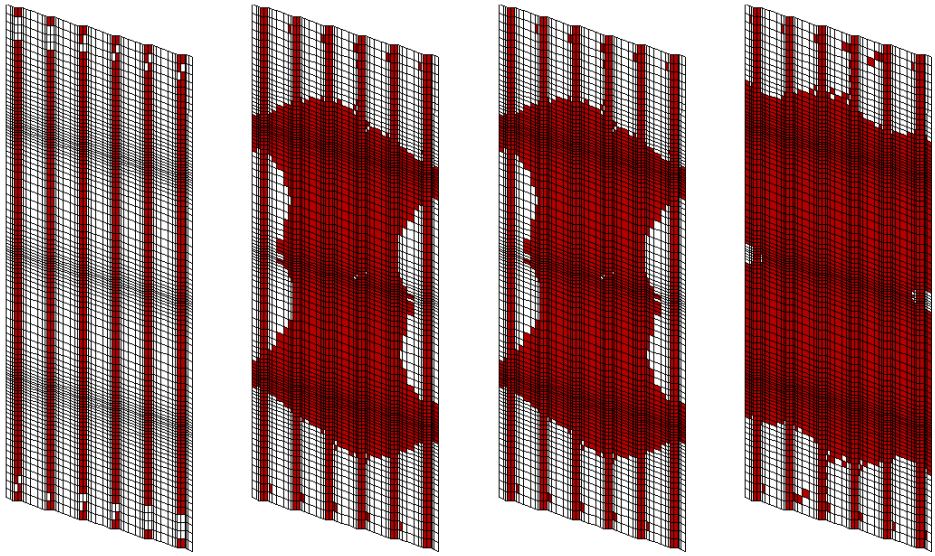

21 28 42 56 days

(b) Bottom Surface (400psi threshold)

Figure 184. Longitudinal stress distributions of Big Creek bridge deck

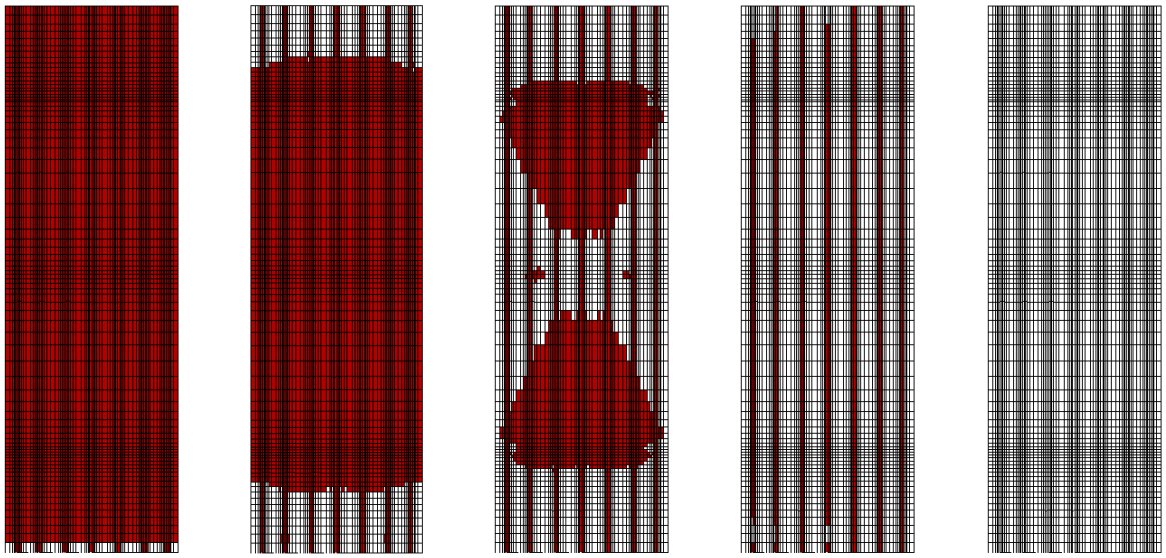

150 200 210 250 300 psi

(a) Top surface (84 day age)

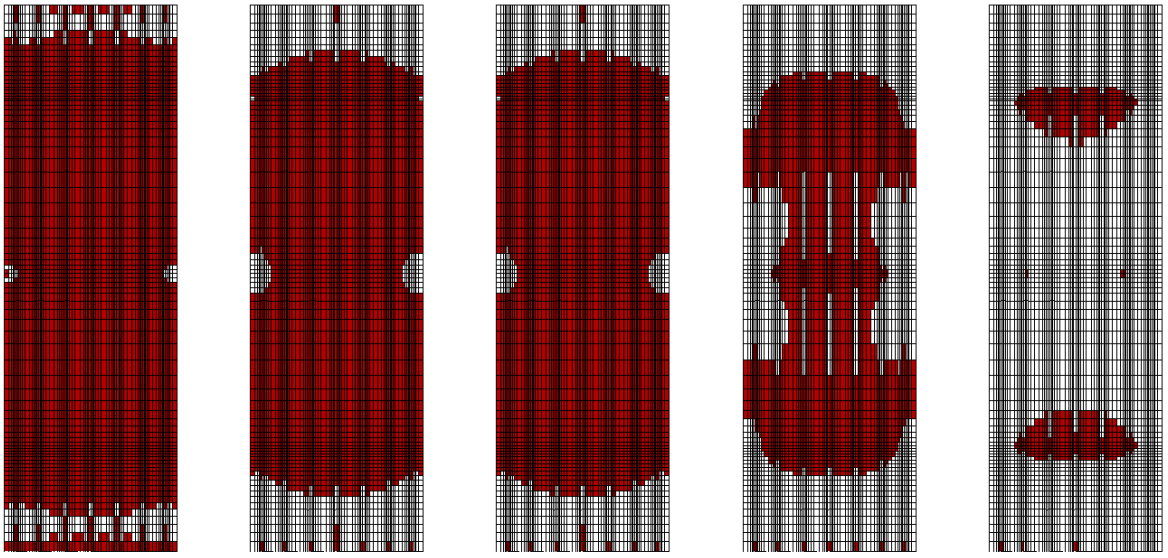

150 200 210 250 300 psi

(b) Bottom Surface (84 day age)

Figure 185. Longitudinal stress distributions of Duncan Rd Bridge deck

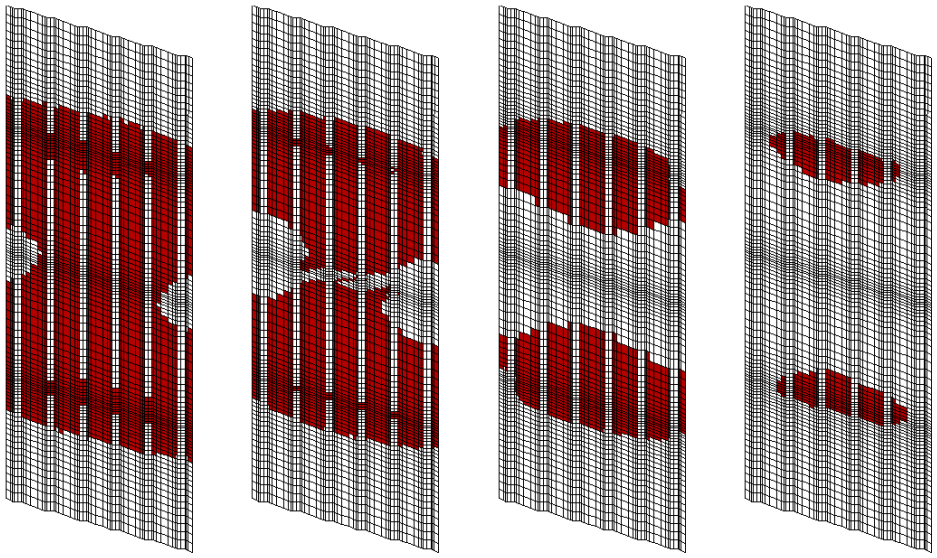

400 425 450 500 psi

(a) Top surface (56 day age)

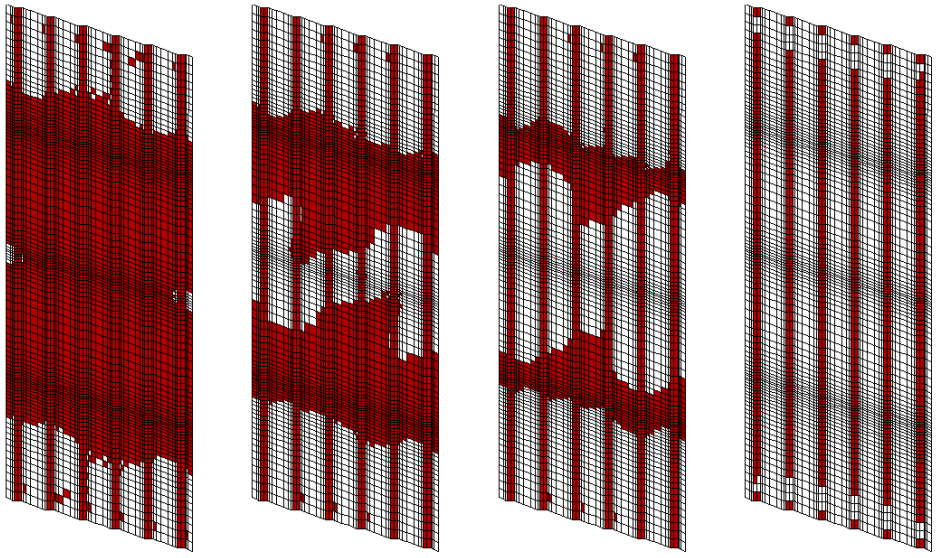

400 425 450 500 psi

(b) Bottom Surface (56 day age)

Figure 186. Longitudinal stress distributions of Big Creek bridge deck

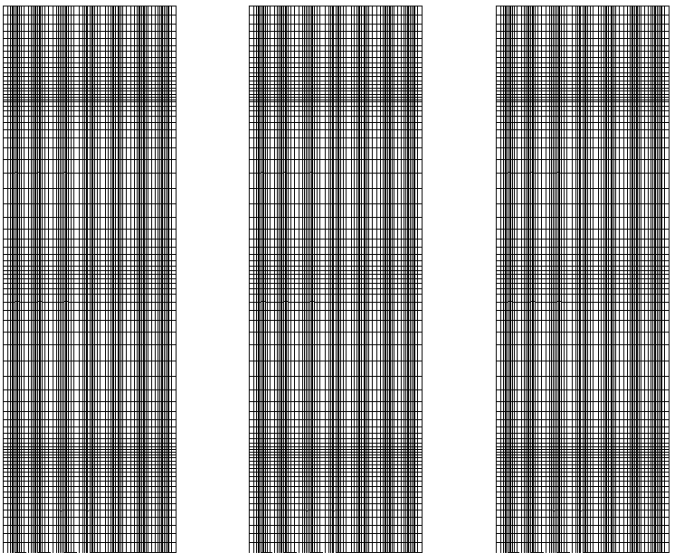

50 100 200 psi

(a) Top surface (84 day age)

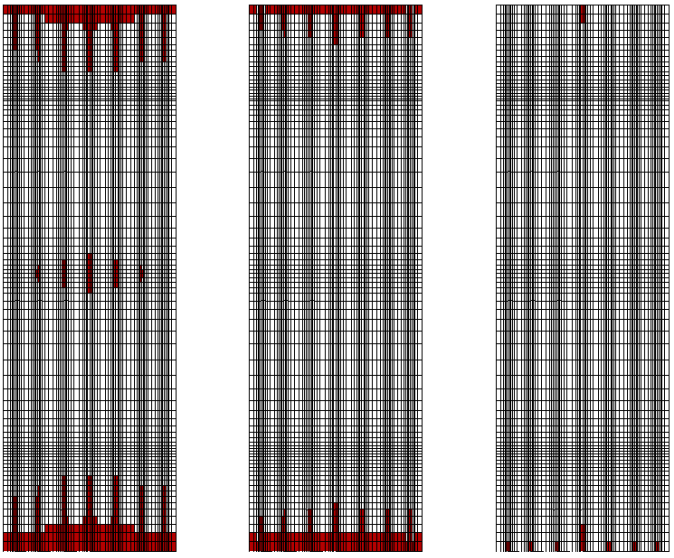

50 100 200 psi

(b) Bottom Surface (84 day age)

Figure 187. Longitudinal stress distributions of Duncan Rd Bridge deck, LOW shrinkage

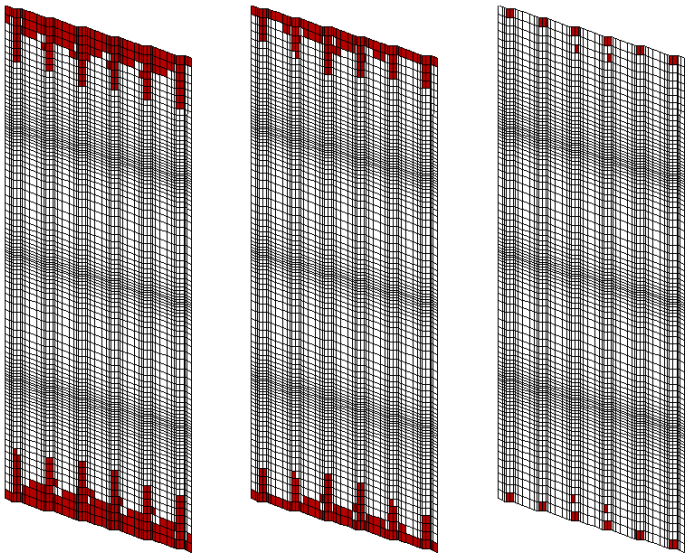

50 100 200 psi

(a) Top surface (56 day age)

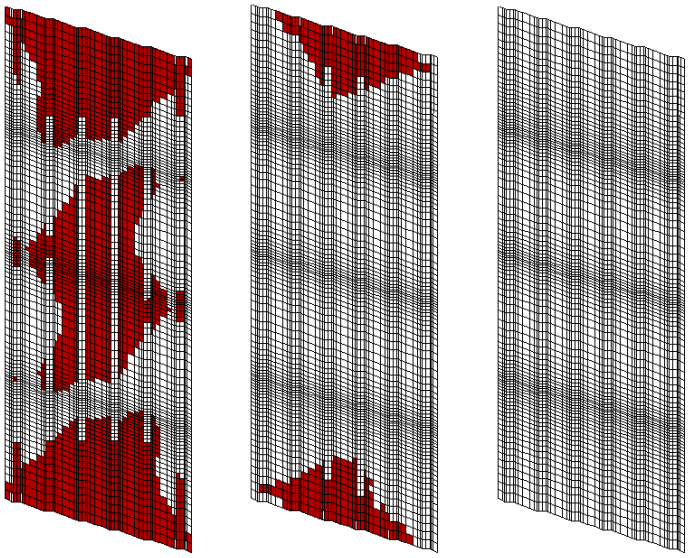

50 100 200 psi

(b) Bottom Surface (56 day age)

Figure 188. Longitudinal stress distributions of Big Creek bridge deck, LOW shrinkage

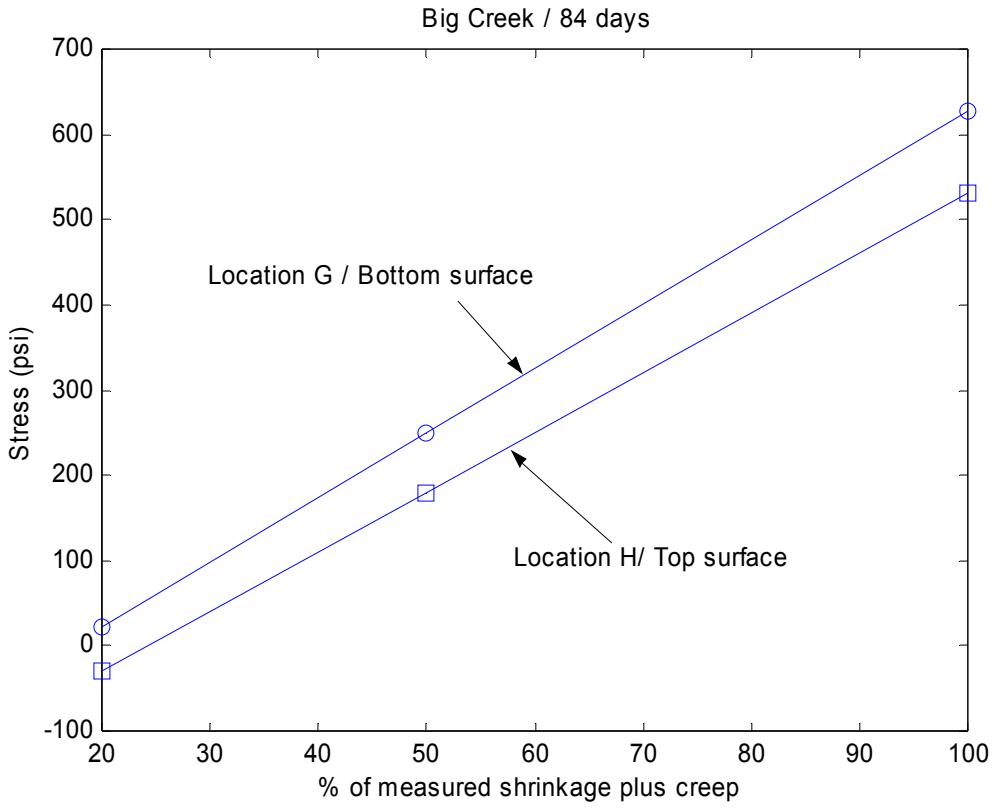

Figure 189. Maximum bridge deck stress vs. drying shrinkage

5. CONCLUSIONS OF FIELD STUDY

UIUC researchers participated in the instrumentation and analysis of six bridge decks from July 2000 to July 2003. High performance concrete was used in five out of the six bridges. The objective of the study was to assess the performance of IDOT high performance concrete mixtures in practice and evaluate the risk for cracking when compared to conventional concrete mixtures. Sensors were installed in six bridge decks to measure strain and temperature. Relative humidity sensors were also used in two of the bridges. The data were used to validate a finite element model for two of the bridge decks. From the observations of strain and temperature behavior in the measured data, and the understanding of stress development from the finite element model, several important conclusions were drawn about the performance of IDOT bridges.

Internal concrete temperatures followed the measured air temperature, but lagged behind since the concrete conducts heat slowly and adjusts to ambient conditions. Measured temperatures reached 50-60°C (140°F) during hydration, but the temperature gradient through the thickness of the deck was only about 10°C. The maximum temperature gradient in the deck during daily temperature cycles usually occurred during the late morning/early-afternoon heating of the top of the deck on sunny days. The gradient often reached 9-10°C. From these field measurements of temperature, the model was used to calculate stress in the deck. The model results show that the stress that develops due to daily temperature cycles and long-term temperature changes are relatively small when compared to the drying shrinkage stress. Long-term temperature changes will experience some relaxation by creep.

The general trends of the strain data correspond to both daily cycles of temperature and weekly temperature variation. Magnitudes of the transverse strain sensors were similar to longitudinal sensors and significant differences were not observed between locations in the deck.

The strain varies with temperature at each location, and bending deflections are seen during morning heating and evening cooling cycles. It should be noted that measured strains reflect the amount of displacement in the bridge and should not be confused with the strain associated with stress. The two additional factors that control stress in the bridge deck are the level of structural restraint and the creep of the material. The level of restraint is less for temperature deformation than it is for shrinkage. The beams supporting the bridge are changing with temperature along with the deck, although the coefficient of thermal dilation is not the same, the restraint will not be significant. The only restraint to temperature deformation is from the pier. However, shrinkage of the concrete deck is highly restrained by the steel beams. The strain measurements reflect only temperature changes in the deck, but a finite element model was integrated with shrinkage and creep models for the HPC materials to understand the stress that develops in each bridge deck. High stress in the bridge deck developed on the girder lines and piers when drying shrinkage was incorporated into the finite element model. The high stress initiated from the inside of the bridge deck and spread to the outside of the decks. The model was used to compare the level of structural restraint between the two bridges. It was determined that the bridge with a higher degree of stiffness in the girder system also developed higher stress. Lower shrinkage material reduces stress development and changes the stress distribution of the bridge deck. According to Figure 189, if the simulated shrinkage strain was reduced by 15%, stress did not exceed 500 psi in the deck. A 40% reduction in shrinkage reduced the maximum stress to below 400 psi. Assuming that a concrete will have sufficient long-term durability even if some cracking is allowed, then reducing shrinkage by 15-40% will produce a durable, high quality bridge deck.

IV. SUMMARY AND CONCLUSIONS

The overall purpose of this project was to analyze all conditions that cause cracking in IDOT concrete bridge decks. Crack formation in concrete bridge decks is dependent on two major issues: concrete material properties such as shrinkage, creep, and strength, and the contribution of the overall bridge structure, which is restraint. For concrete to crack under low external loads, two conditions must be present. The concrete must have some self-induced volume change and this volume change must be resisted by the structure. If concrete were stronger, had lower shrinkage, or higher creep relaxation, the probability of cracking would be significantly reduced. Likewise, if the restraint provided by the structure were reduced cracking would also be reduced. The first section of this report, the Laboratory Study, examines the material properties that affect concrete cracking. The second section of this report, the Field Study, investigates the role of structural restraint in concrete cracking. The different bridge structures and concrete bridge deck materials were examined extensively in this project, and their relationship to concrete bridge deck cracking was established.

Specific questions that arose during the initial establishment of this project can be addressed with the results of this study. A primary finding of the study, that HPC mixtures used by IDOT are not significantly different from OPC, is relevant for this discussion. IDOT HPC proportioning strategies resulted in many of the benefits of HPC, such as low permeability, but without the drawbacks of some HPC materials. It is common to find HPC materials with very low *w/c* ratios around 0.30 and high additions of silica fume. These factors will significantly increase autogenous shrinkage and heat evolution and could potentially cause cracking. By maintaining a relatively normal *w/*c ratio and limiting the use

of silica fume to around 5%, autogenous shrinkage was not significantly high and heat evolution was similar to OPC. The problems associated with HPC were avoided with IDOT's approach, which can be considered an "optimized" view of HPC. Good curing techniques were also a part of this strategy and are essential to avoiding early age cracking. Curing for fourteen days versus seven seems to be costly for construction time, so the disadvantages seem to outweigh the benefits here. Seven days of continuous wet curing should be sufficient to produce high quality concrete. It is recommended that curing blankets be allowed to dry before removal to avoid temperature shock to young concrete. This can be a source of early age cracking due to the rapid cooling effect of evaporation, which occurs when the wet concrete surface is exposed to air.

The maximum concrete temperature in IDOT HPC materials, provided that IDOT continue to use similar HPC strategies, should not be different from OPC limits. The heat development measured for HPC materials was not significantly greater than OPC, so problems should not be expected from temperature rise. Similarly, the maximum gradients allowable in the deck should be unchanged for HPC. The effect of ambient temperature change on the deck is highly dependent on the bridge structural restraint, but again, IDOT HPC mixtures will not add to the cracking problem. Slightly higher strength will be beneficial to resist early stress from temperature change and shrinkage. The most severe temperature gradients were observed consistently during late morning-early afternoon heating of the deck, and not due to cold weather fronts causing rapid cooling. This is due to the absorption of solar radiation of concrete causing faster heating and then the slower heat transfer during the cooling period. Therefore, a "night pour" strategy would not necessarily give any benefit to reduction of early age cracking.

Steel fibers can be advantageous to reduce the effect of cracking. Although the HPC strategies used by IDOT are not expected to cause an increase in cracking, fibers act mainly to distribute stresses more evenly and this will reduce crack width significantly. Since concrete permeability is dependent on crack width, steel fibers will help to achieve durable concrete.

The laboratory test data from this study and the results in the literature allow the conclusion that, for low addition rates of around 5%, silica fume and metakaolin do not differ much in performance. At higher addition rates, some differences may be apparent, possibly due to the smaller particle size of silica fume.

The strategies used by IDOT to formulate HPC have succeeded in producing a material with beneficial properties such as low permeability, but without the drawbacks of high heat development and high autogenous shrinkage. The practical use of the material also includes the structural restraint of the bridge, and should be considered as well. The ultimate goal of achieving a bridge deck that does not crack is a two-part problem of material and structural importance.

Appendix A – Materials Characterization

Table 8. Laboratory aggregate gradation

	Sieve Size	*Weight Retained (lb)*	*Amount Retained (%)*	*Cumulative Amount Retained (%)*	*Cumulative Amount Passing (%)*
Coarse aggregate (crushed limestone) AC = 1.54%, typical MC = -1.4%	3/4"	3.5	9%	9%	91%
	1/2"	19.1	47%	55%	45%
	3/8"	9.5	23%	79%	21%
	#4	7.6	19%	97%	3%
	pan	1.1	3%	100%	0%
	Total	40.8	100%		
	Sieve Size	*Weight Retained (lb)*	*Amount Retained (%)*	*Cumulative Amount Retained (%)*	*Cumulative Amount Passing (%)*
Fine aggregate (natural torpedo sand) AC = 2.24%, typical MC = -2.0%	#4	0.02	2%	2%	98%
	#8	0.10	9%	11%	89%
	#16	0.14	12%	23%	77%
	#30	0.19	17%	40%	60%
	#50	0.49	44%	84%	16%
	#100	0.15	13%	97%	3%
	#200	0.02	2%	99%	1%
	pan	0.01	1%	100%	0%
	Total	1.1	100%		

Table 9. Field fine aggregate gradations

Kaskaskia	Sieve Size	Weight Retained (lb)	Amount Retained (%)	Cumulative Amount Retained (%)	Cumulative Amount Passing (%)
	0.25	0.1	2%	2%	98%
	0.125	0.5	10%	12%	88%
	0.0625	0.72	15%	27%	73%
	0.033	0.84	17%	44%	56%
Fine aggregate	0.02	1.66	34%	78%	22%
	0.01	0.96	20%	98%	2%
	0.005	0.06	1%	99%	1%
	0.001	0.04	1%	100%	0%
	Total	4.88	100%		
Lake Springfield	Sieve Size	Weight Retained (lb)	Amount Retained (%)	Cumulative Amount Retained (%)	Cumulative Amount Passing (%)
	0.25	0.12	2%	2%	98%
	0.125	0.58	11%	14%	86%
	0.0625	0.84	16%	30%	70%
	0.033	0.92	18%	48%	52%
Fine aggregate	0.02	1.92	37%	85%	15%
	0.01	0.68	13%	98%	2%
	0.005	0.06	1%	100%	0%
	0.001	0.02	0%	100%	0%
	Total	5.14	100%		
Big Creek	Sieve Size	Weight Retained (lb)	Amount Retained (%)	Cumulative Amount Retained (%)	Cumulative Amount Passing (%)
	0.25	0	0%	0%	100%
	0.125	0.72	15%	15%	85%
	0.0625	1.06	22%	37%	63%
	0.033	1.5	31%	67%	33%
Fine aggregate	0.02	1.3	27%	94%	6%
	0.01	0.26	5%	100%	0%
	0.005	0.02	0%	100%	0%
	0.001	0	0%	100%	0%
	Total	4.86	100%		

Table 10. Field coarse aggregate gradations

Kaskaskia - SCA	Sieve Size	Weight Retained (lb)	Amount Retained (%)	Cumulative Amount Retained (%)	Cumulative Amount Passing (%)
Small coarse aggregate (crushed limestone)	1"	0	0%	0%	100%
	3/4"	0	0%	0%	100%
	1/2"	0	0%	0%	100%
	3/8"	1.98	3.5%	3.5%	96%
	#4	35.68	63.9%	67.5%	33%
	pan	18.16	32.5%	100.0%	0%
	Total	55.82	100%		
Kaskaskia - LCA	*Sieve Size*	*Weight Retained (lb)*	*Amount Retained (%)*	*Cumulative Amount Retained (%)*	*Cumulative Amount Passing (%)*
Large coarse aggregate (crushed limestone)	1"	0	0%	0%	100%
	3/4"	5.12	9%	9%	91%
	1/2"	29.88	50%	59%	41%
	3/8"	15.26	26%	84%	16%
	#4	6.22	10%	95%	5%
	pan	3.2	5%	100%	0%
	Total	59.68	100%		
Kaskaskia - COMBINED	*Sieve Size*	*Weight Retained (lb)*	*Amount Retained (%)*	*Cumulative Amount Retained (%)*	*Cumulative Amount Passing (%)*
Combined coarse aggregate (crushed limestone)	1	0	0%	0%	100%
	3/4	4.096	7%	7%	93%
	1/2	23.904	41%	48%	52%
	3/8	12.604	21%	69%	31%
	1/4	12.112	21%	89%	11%
	1/8	6.192	11%	100%	0%
	Total	58.908	100%		
Lake Springfield	*Sieve Size*	*Weight Retained (lb)*	*Amount Retained (%)*	*Cumulative Amount Retained (%)*	*Cumulative Amount Passing (%)*
Coarse aggregate (crushed limestone)	1	0	0%	0%	100%
	3/4	1.1	7%	7%	93%
	1/2	7.62	50%	57%	43%
	3/8	3.4	22%	80%	20%
	1/4	2.52	17%	96%	4%
	1/8	0.54	4%	100%	0%
	Total	15.18	100%		

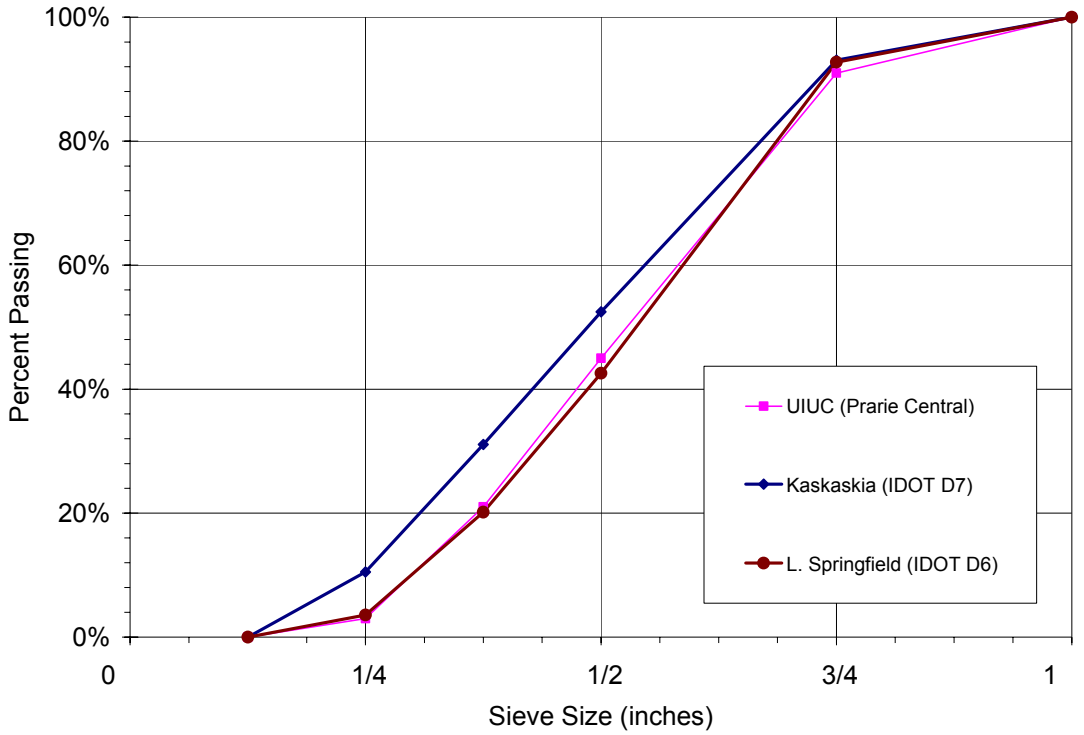

Figure 190. Coarse aggregate gradation

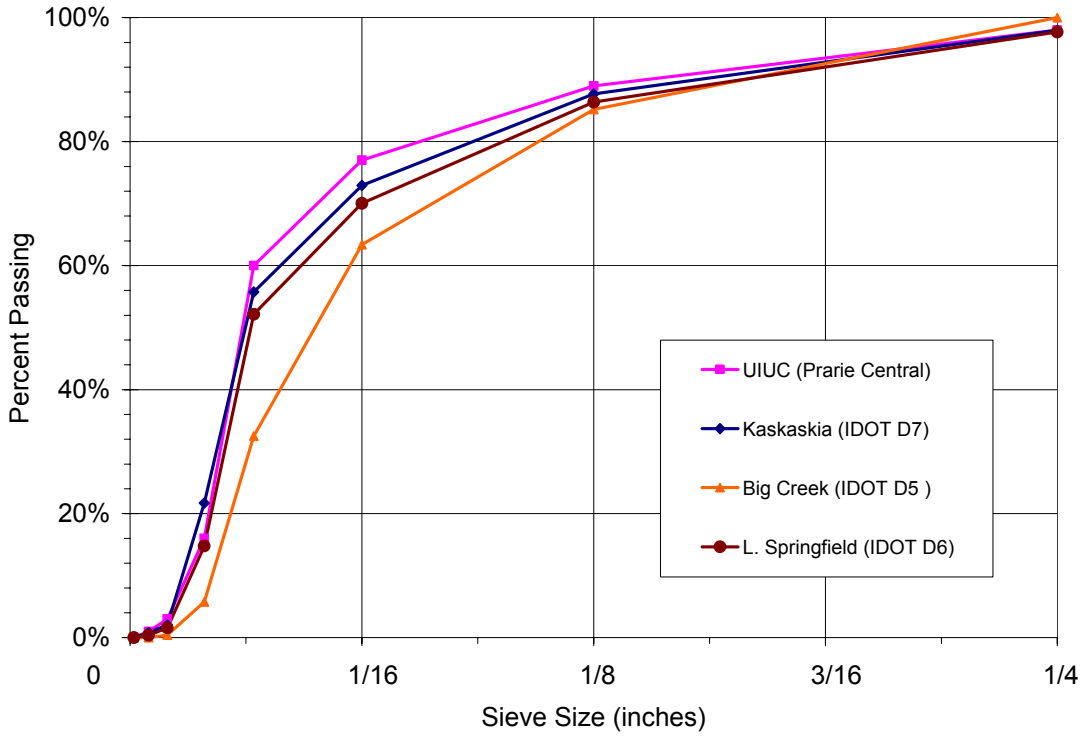

Figure 191. Fine aggregate gradation

Table 11. Chemical oxide compositions

Chemical Oxide Composition Analysis by X-ray Flouresence (XRF) on Dry Sample Basis														
	Cement						Flyash						Silica Fume	Metakaolin
(wt%)	UIUC Lab Cement, Essroc Saylor's Type I	Macon	Duncan Rd	Kaskaskia	Big Creek	L. Springfield	UIUC Class C, Mineral Sols	Macon Class C	Duncan, Class C	Duncan (rep)	Kaskaskia, Class C	L. Springfield, Class C	Grace Force 10,000d	Englehard Metamax HRM
SiO_2	22.01	21.30	18.26	19.98	19.80	19.83	32.29	33.04	36.63	36.91	32.97	32.78	94.13	50.41
Al_2O_3	4.60	4.72	4.50	4.26	5.01	4.22	17.24	15.83	20.85	19.78	17.47	17.54	0.37	46.52
Fe_2O_3	1.64	2.30	2.33	1.47	1.59	2.53	5.11	4.61	5.22	5.14	4.59	4.59	<0.01	0.27
CaO	62.59	61.83	59.01	62.85	60.68	63.29	28.59	31.84	22.64	22.48	27.72	27.82	1.14	0.13
MgO	2.45	2.66	3.28	2.46	1.72	2.44	6.24	5.59	4.06	4.13	5.42	5.33	0.36	0.06
K_2O	0.07	0.62	1.31	0.18	0.72	0.47	0.40	0.52	0.60	0.62	0.56	0.56	0.51	0.13
Na_2O	0.05	0.14	0.14	0.09	0.09	0.19	2.89	1.73	1.50	1.59	1.55	1.52	<0.1	<0.1
TiO_2	0.31	0.17	0.15	0.24	0.22	0.17	1.25	1.00	1.45	1.47	1.23	1.22	0.02	1.58
P_2O_5	0.10	0.19	0.07	0.08	0.10	0.24	1.44	1.45	1.22	1.25	1.49	1.50	0.13	0.06
MnO	<0.1	<0.1	0.04	0.09	0.05	0.09	0.01	0.03	0.03	0.03	0.02	0.02	0.03	<0.01
SO_3	4.42	5.23	4.21	3.13	3.66	2.68	0.28	0.25	1.84	2.17	2.45	2.49	0.01	0.01
Sr(ppm)	414	487	336	187	356	513	2763	2474	3111	3074	2745	2596	112	59
Ba (ppm)	207	349	19	169	215	232	6432	5740	5647	6653	6690	6491	121	177
Zr(ppm)	81	74	56	56	84	87	324	280	466	457	384	367	<50	118
LOI (1000oC)*	1.62	0.68	1.53	1.31	1.42	0.18	0.39	0.54	0.61	0.52	0.29	0.40	3.05	0.49
H2O (110oC)	0.75	0.25	0.51	0.66	0.50	0.13	0.08	0.27	0.15	0.12	0.17	0.17	0.6	0.34

* LOI: loss on ignition at 1000oC, in %.

Bogue Calculation							ASTM 618 Class C / Class F
A/F	2.81	2.06	1.94	2.90	3.15	1.67	S+A+F min 50/70%
C_3S	41.66	39.91	55.84	64.35	50.22	67.32	SO3 max 5%
C_2S	31.68	30.95	10.23	8.73	18.87	6.08	H20 max 3%
C_3A	9.41	8.63	8.00	8.81	10.57	6.91	LOI max 6%
C_4AF	4.98	6.99	7.08	4.48	4.84	7.69	

Appendix B – US-51 District 5 (Macon, IL)

The Macon project consisted of two separate bridge decks for northbound (NB) and southbound (SB) lanes. IDOT personnel provided the data collection equipment and performed the instrumentation for this deck. Each deck was instrumented with five embedment strain gages and eight thermocouples. Three strain gages and three thermocouples were located at the midpoint of each deck. Two strain gages and five thermocouples were located at the quarter point of each deck. The 350-ohm strain gages were manufactured by Measurement Group, Inc. and had an active gage length of 4 inches. Figure 192 shows a plan view of the gage positions and Figure 193 shows a longitudinal cross section displaying the individual gage orientation. The overall dimensions of the deck were approximately 80 ft by 40 ft.

The strain gages were oriented longitudinally along the deck and they were positioned so the top and bottom gages were approximately 1" from the surface and the middle gage (midpoint only) was near the center of the deck. Thermocouples were positioned at the top and bottom surfaces, center depth, and at the strain gage locations (quarter point only). In Figure 194 through Figure 197, the sensor locations are shown prior to placement of the concrete.

The SB deck was cast on October 3, 2000 followed by the NB deck on October 12, 2000. The concrete mixtures for each deck are shown in Chapter 4, Table 4-1. The difference between mixtures is that HPC-1 contains high-reactivity metakaolin (HRM) and HPC-2 contains micro-silica (MS). Superplasticizer was not used during the first two-thirds of the southbound deck during placement.

The concrete was pumped during placement followed by finishing of the deck with a paving machine. Following placement, the bridge decks were moist cured for (at least) 14 days using wet cotton mats. Prior to installation of the wet mats, evaporation from the surface was

prevented using a water fogger. Fresh concrete temperature of 80ºFwas measured two hours into placing for the southbound deck.

Data Analysis

The strain gage and thermocouple data span a period of five months from October 3, 2000 to March 9, 2001. Due to data collection system errors, temperature data are missing for the southbound deck between February 2, 2001 and March 9, 2001, and for the northbound deck from October 19, 2000 to February 6, 2001. Since concrete temperature data were crucial for assessment of behavior, the missing data were replaced with corresponding measurements from the other deck, when possible. Air temperature was not measured at the project location, so atmospheric data was collected from local weather stations at the Decatur and Springfield airports. The atmospheric data were used to confirm temperature measurements within the concrete and to assess the heat evolution during hydration.

Strain and Temperature Data

Figure 198 and Figure 199 show the measured strains and temperatures for the southbound deck at the midpoint and quarter point respectively. Figure 200 and Figure 201 show the measured strains and temperatures for the northbound deck at the midpoint and quarter point respectively. The starting point corresponds to the beginning of concrete placement. Missing temperature data was supplemented from the opposite deck when needed. The temperature measurements for both decks were discarded for the first 1.5 days due to data collection errors. The strain values measured while concrete hydrates include errors from temperature output. The strains were re-zeroed after about 1.5 days to reduce error. Since the

deck was constantly wet cured during this time period, it is expected that minimal volumetric changes occurred due to drying.

The measured strain in all cases corresponds to daily and seasonal temperature cycles. Temperature data from inside the concrete correlate well with the atmospheric data obtained from local weather stations. The atmospheric data obtained consist of both a wet bulb and a dry bulb temperature. Typically, the temperatures in the deck corresponded to the dry bulb air temperature, but during the wet curing period, it can be observed that the temperatures in the deck more closely resembled the wet bulb temperature because of evaporation from the wet surface.

The overall strain behavior of both decks follow the same trend suggesting there is not much difference between the northbound and southbound deck materials. This was confirmed in the laboratory study, where the early-age creep/shrinkage properties were very similar for the Macon MS and HRM mixtures. Final set times of the deck can be approximated based on peak curve in the temperature data. The southbound deck with HRM reached final set 18 hours after casting and the northbound deck with silica fume after 26 hours. This difference in setting time can be attributed to the colder ambient temperatures the northbound deck experienced during casting. Laboratory tests did not show a difference between HRM and silica fume materials.

It appears that the curing blankets were removed at approximately the same time for both decks producing a longer curing period for the southbound deck. The estimated date of formwork and curing blanket removal corresponds to October 26, 2000. As seen in the previous figures, it is on this date that significant changes begin to occur in the behavior of both decks. The first month of data is shown in Figure 202 through Figure 205. From these figures, the daily temperature and strain cycles can be observed more closely. The differential temperature between the top and bottom surfaces of the deck is shown for the southbound deck. The

differential temperature was not plotted for the northbound deck since the actual temperature data are not available. It can be observed that the maximum temperature differential in the first month is about 15ºF for the southbound deck.

The general trends of the data correspond to both daily cycles of temperature and weekly temperature variation. Closer examination of the daily changes in strain versus temperature reveal that the bottom strain actually has a slightly larger response than the middle strain, which could indicate that the deck is somewhat restrained at mid-depth due to the presence of reinforcing steel. In the first five days, both decks appear to have undergone some elongation with temperature.

After estimated curing blanket removal, the response of the deck changes and it is assumed that drying begins from the top surface. The top surface is now more responsive to atmospheric temperature changes. When the formwork was removed, the bottom surface was more responsive to thermal changes. During morning heating cycles the top of the deck expands and the bottom contracts producing a differential strain. Then during the evening as the deck cools, the top contracts and the bottom expands producing the reverse effect. A differential rate of drying is also possible since a higher rate of evaporation would be likely on the top of the bridge due to solar radiation and higher wind speeds. The middle gage has relatively little response to daily cycles, since it is closer to the neutral axis of bending.

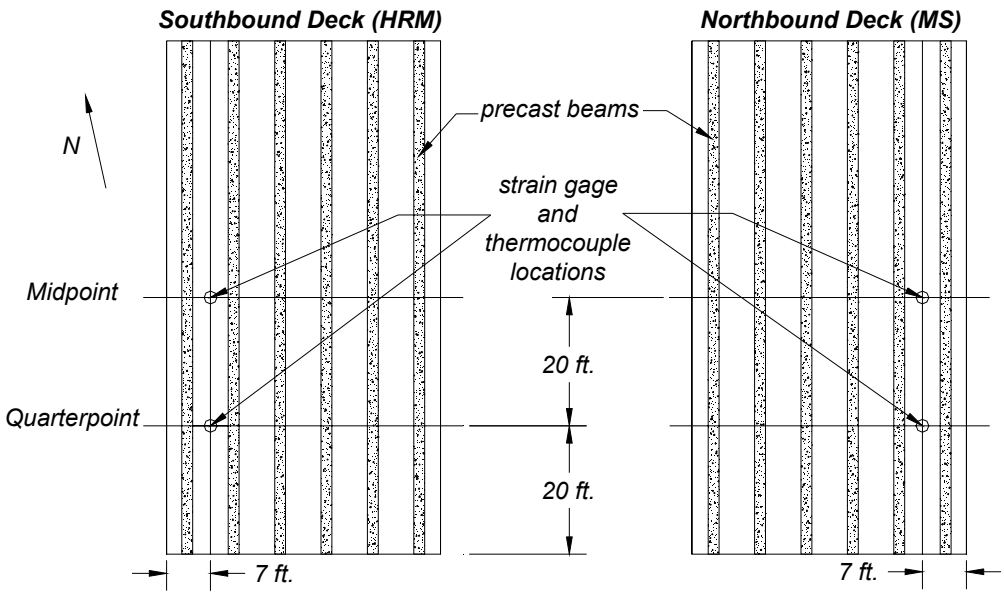

Figure 192. Sensor locations for Macon bridge

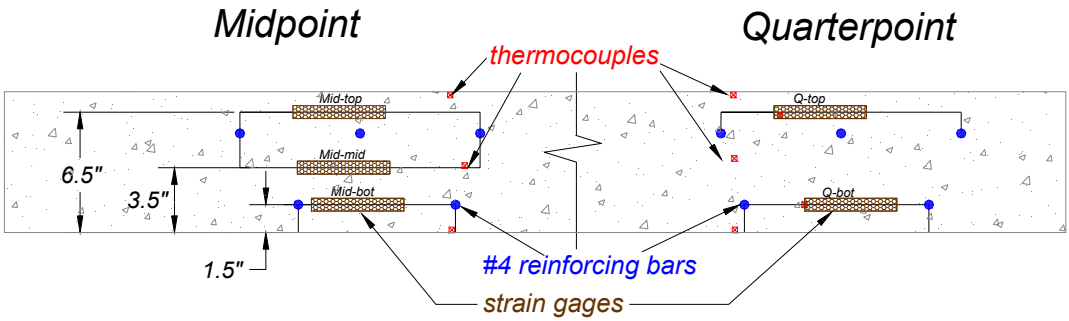

Figure 193. Sensor positions for Macon bridge decks

Figure 194. NB midpoint sensors

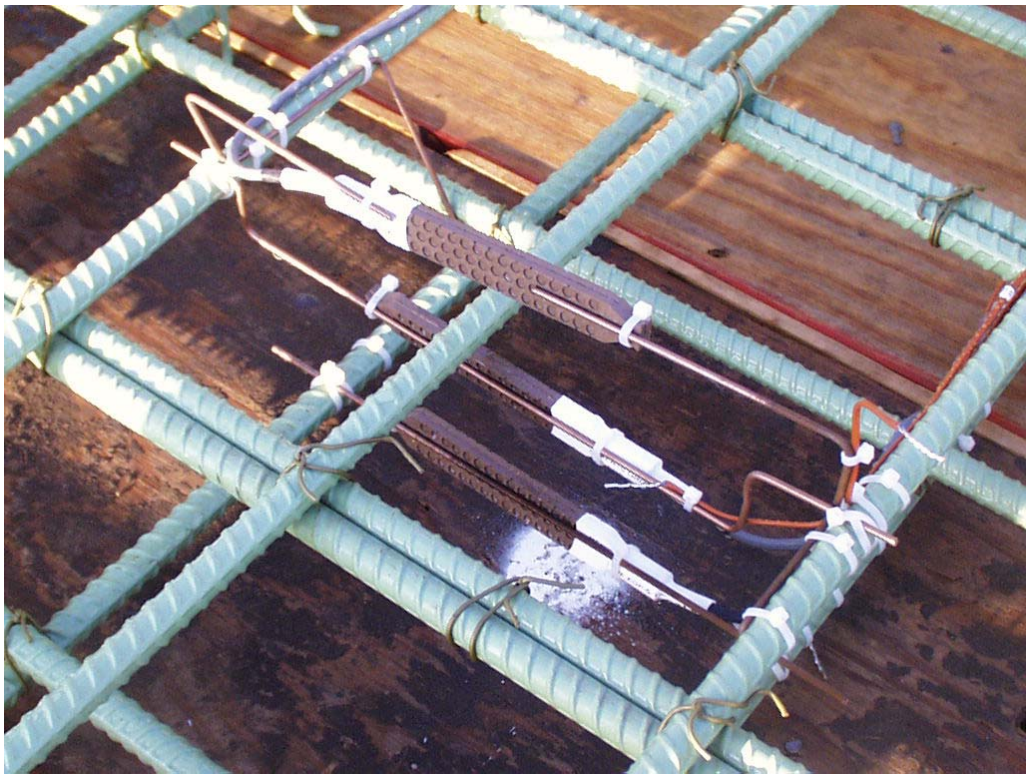

Figure 195. NB quarterpoint sensors

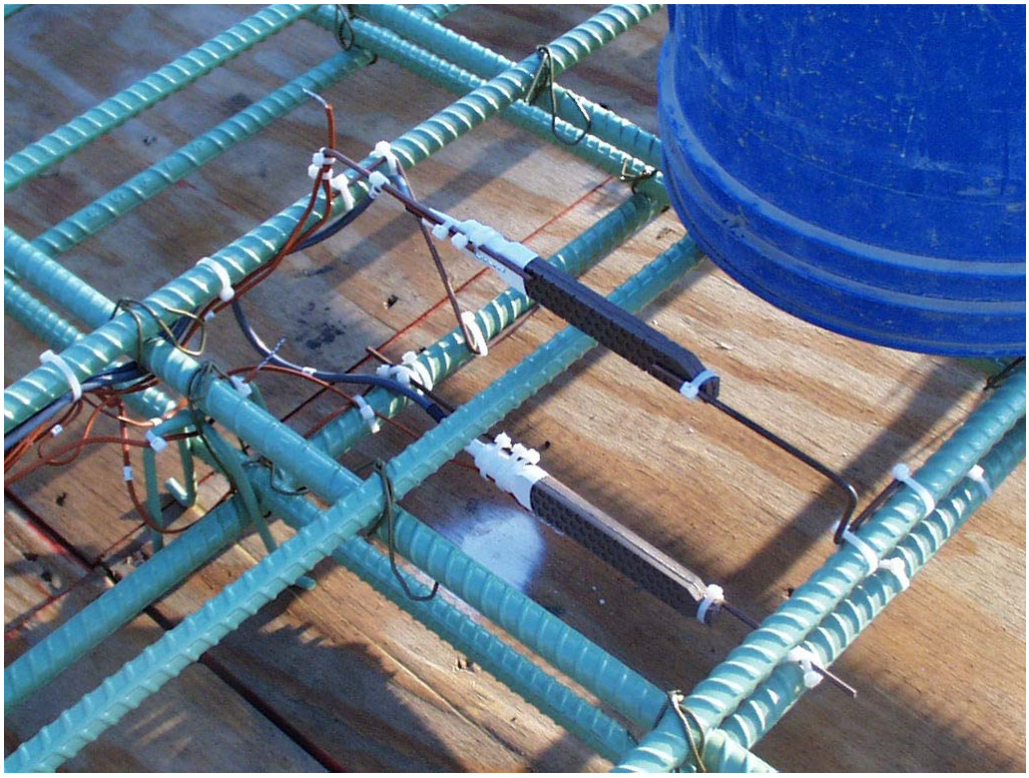

Figure 196. SB midpoint

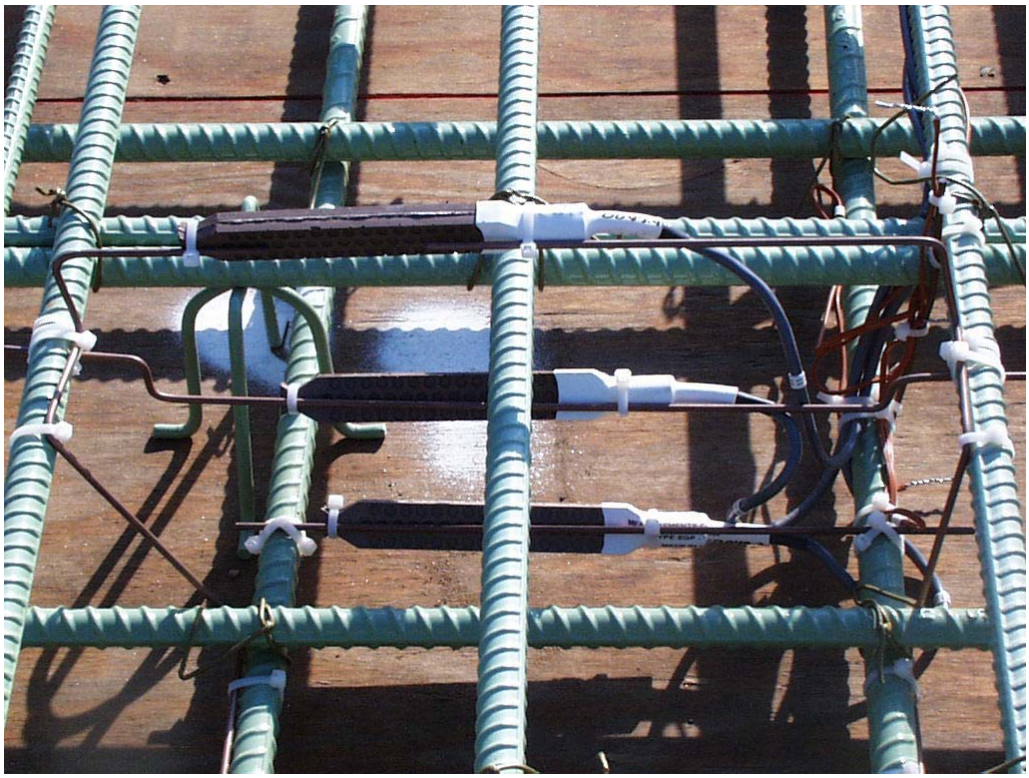

Figure 197. SB quarterpoint

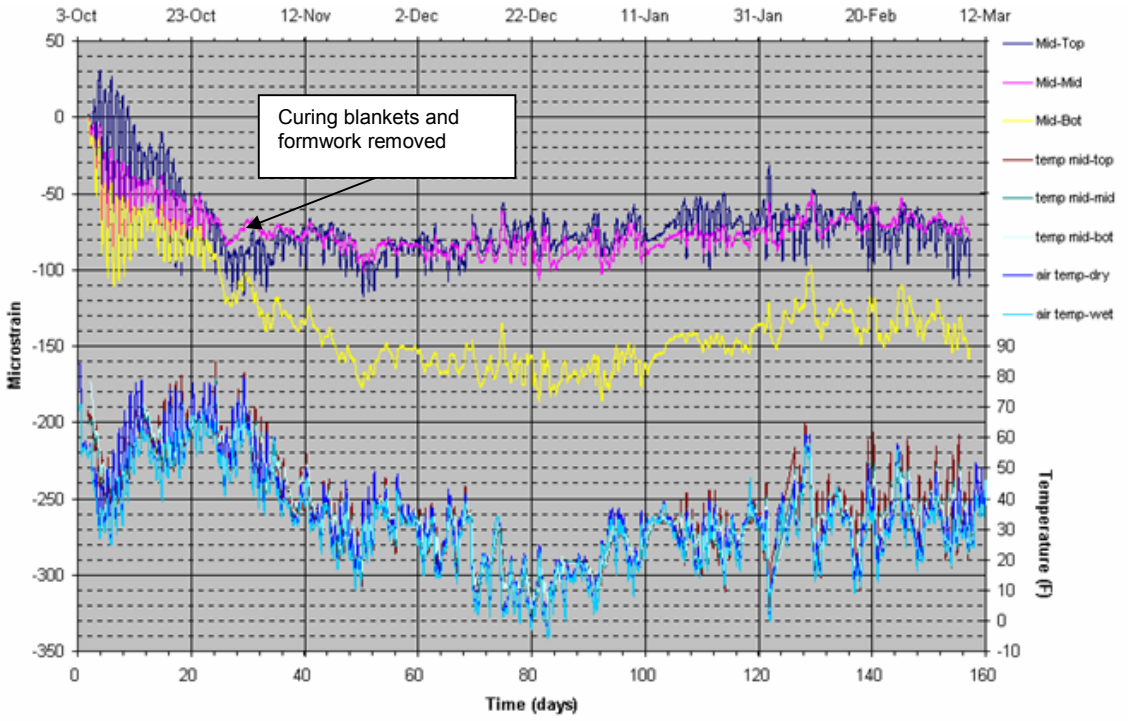

Figure 198. Macon SB Midpoint measured strains and temperatures

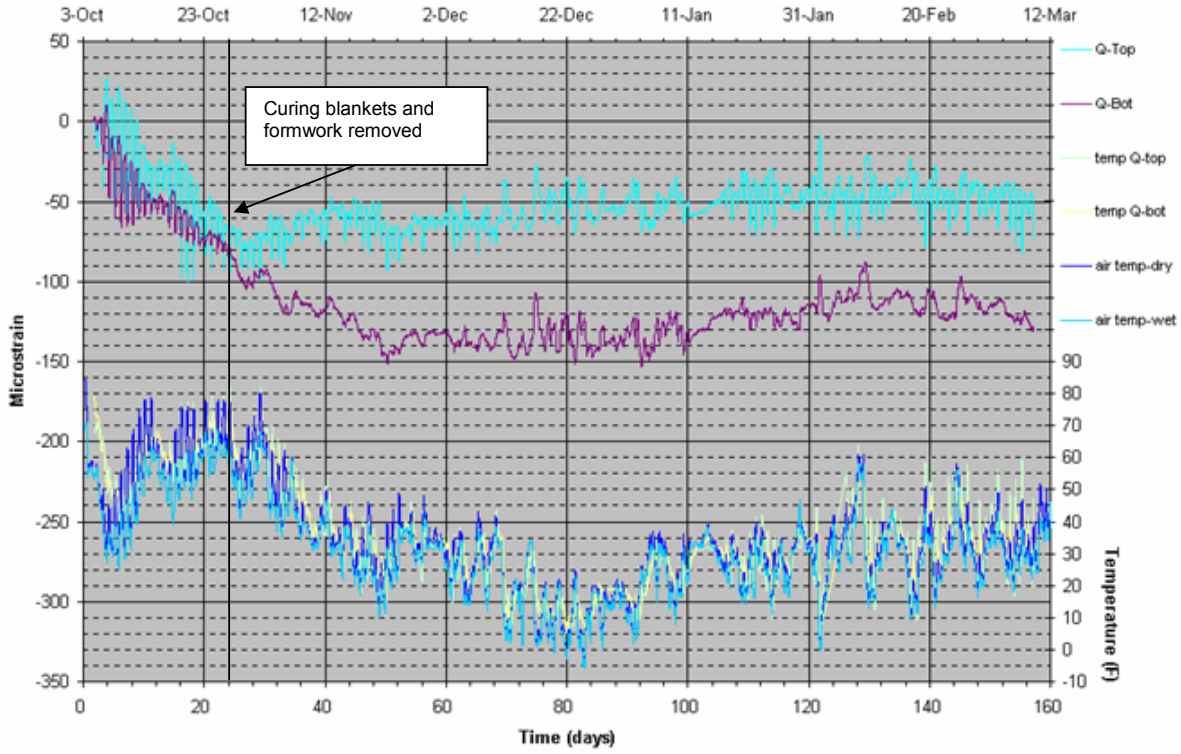

Figure 199. Macon SB Quarterpoint measured strains and temperatures

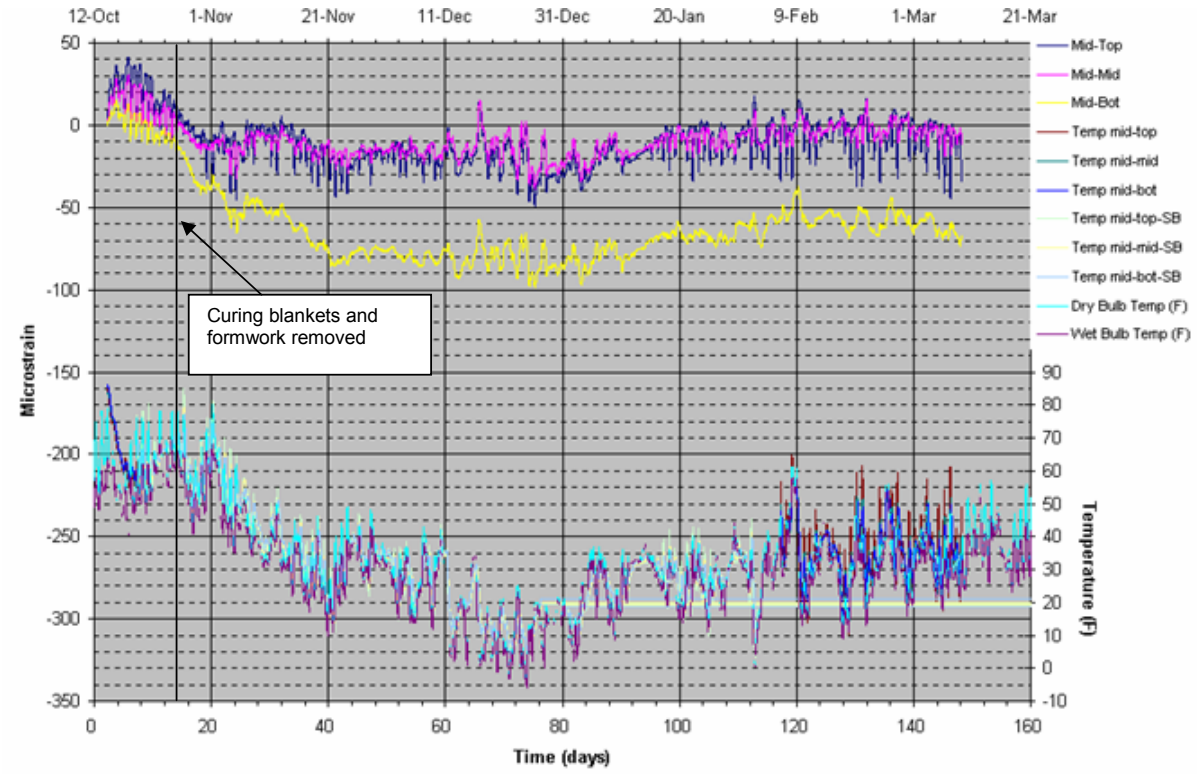

Figure 200. Macon NB Midpoint measured strains and temperatures

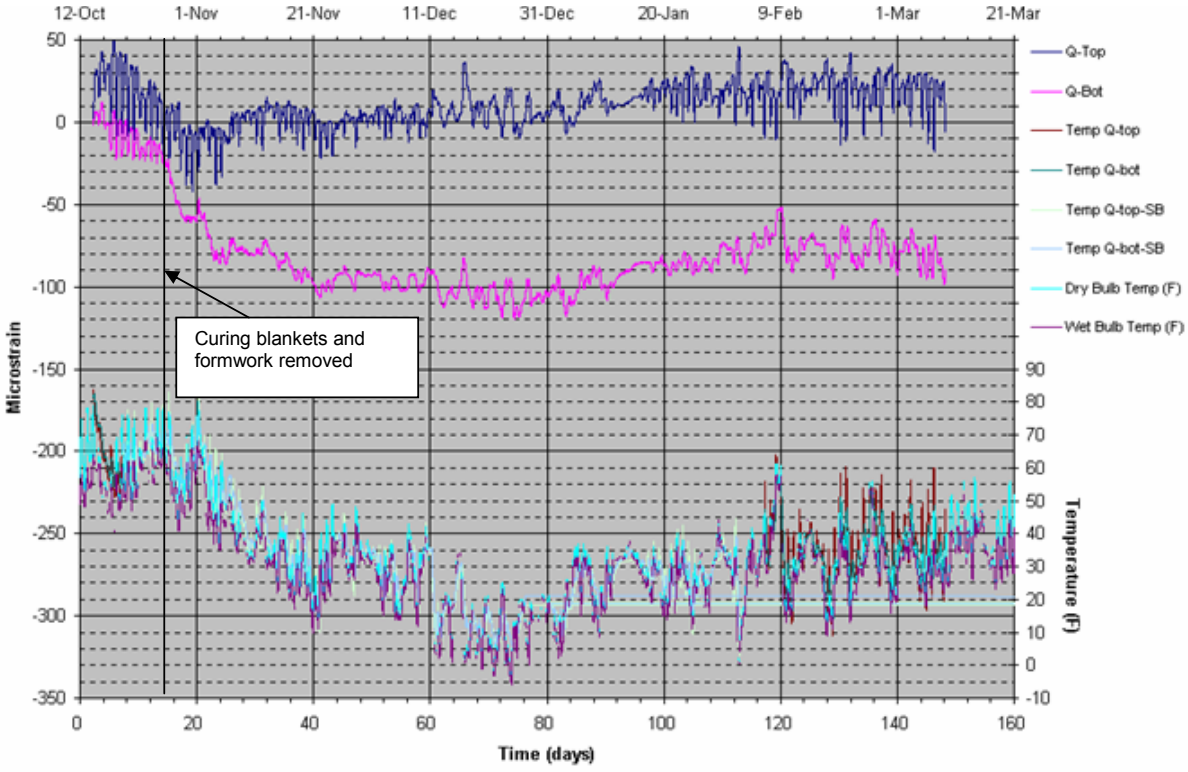

Figure 201. Macon NB Quarterpoint measured strains and temperatures

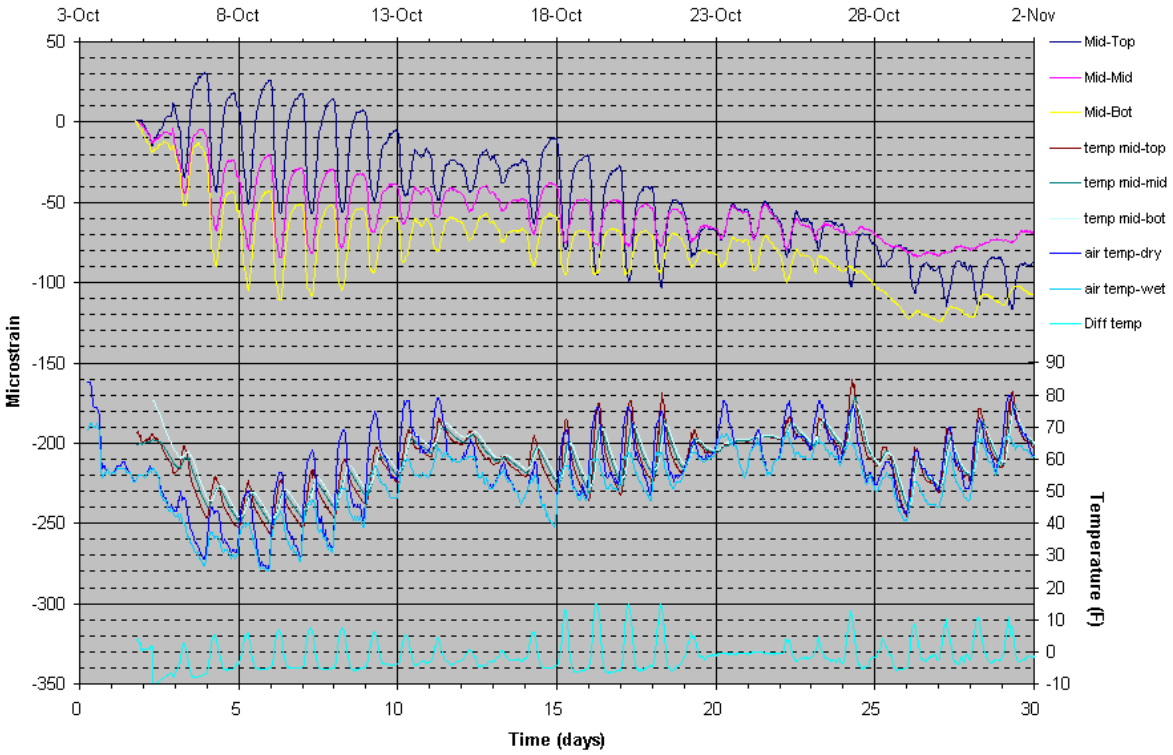

Figure 202. Macon SB Midpoint 1st month measured strains and temperatures

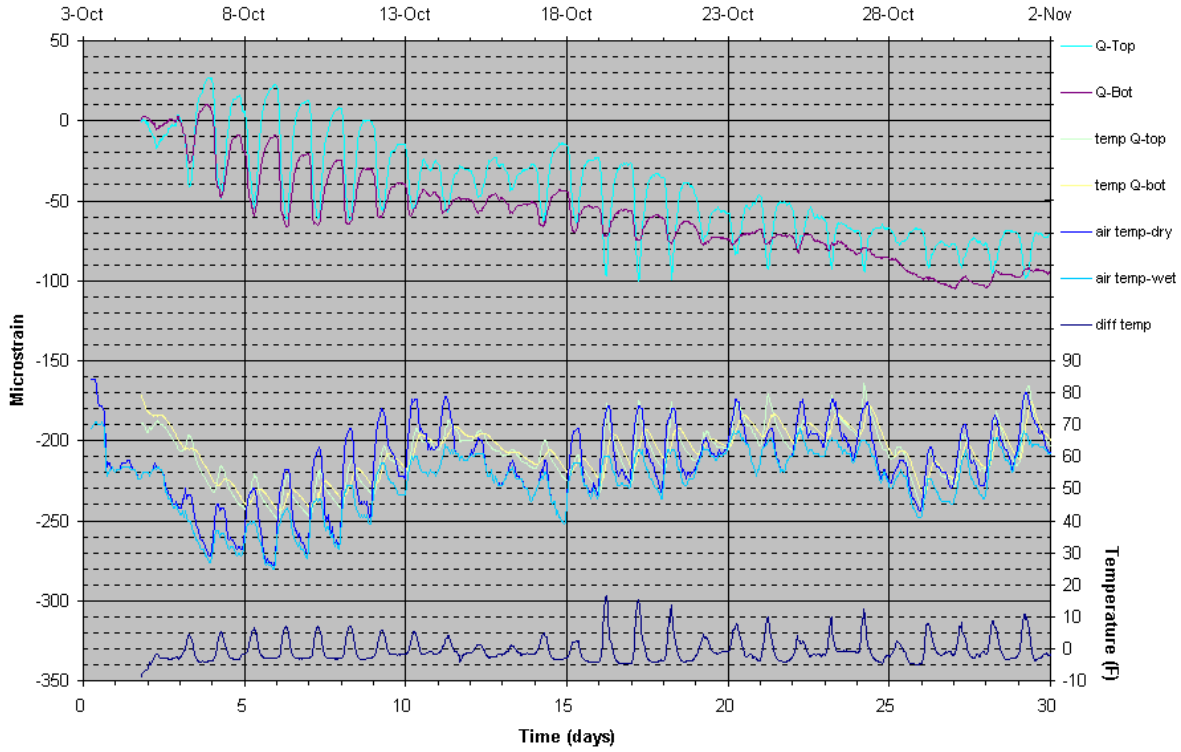

Figure 203. Macon SB Quarterpoint 1st month measured strains and temperatures

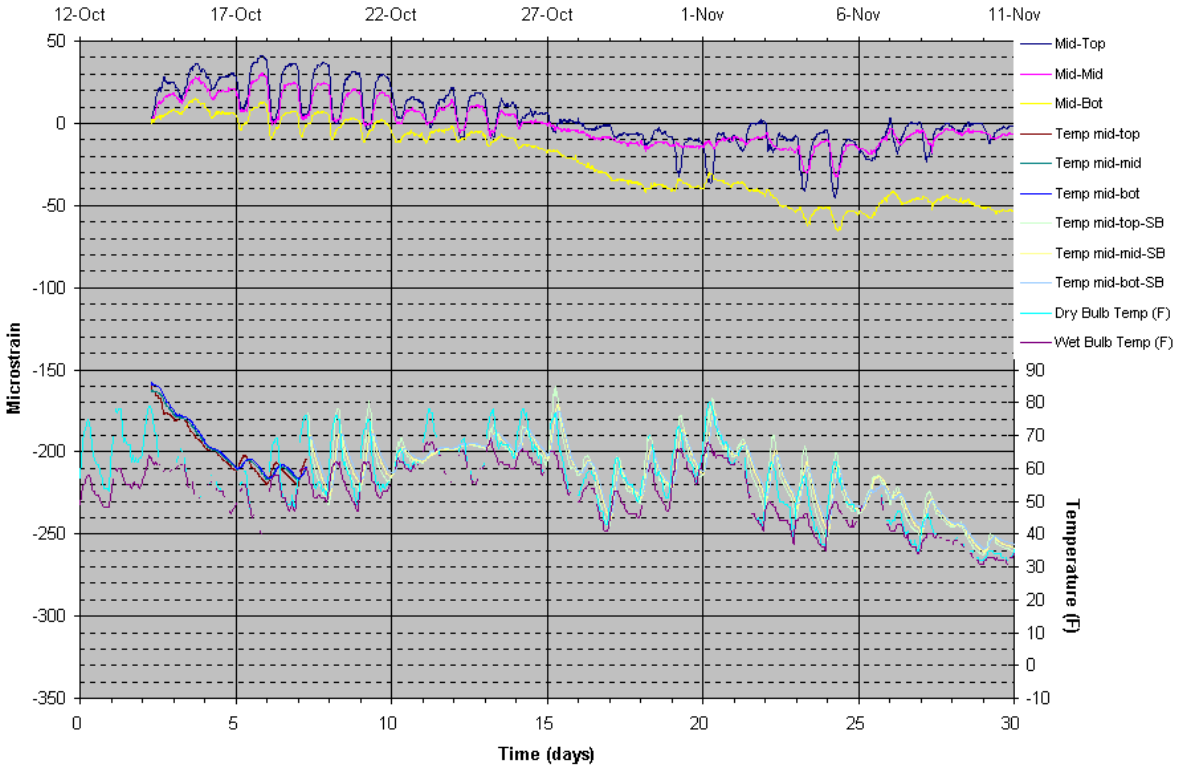

Figure 204. Macon NB Midpoint 1st month measured strains and temperatures

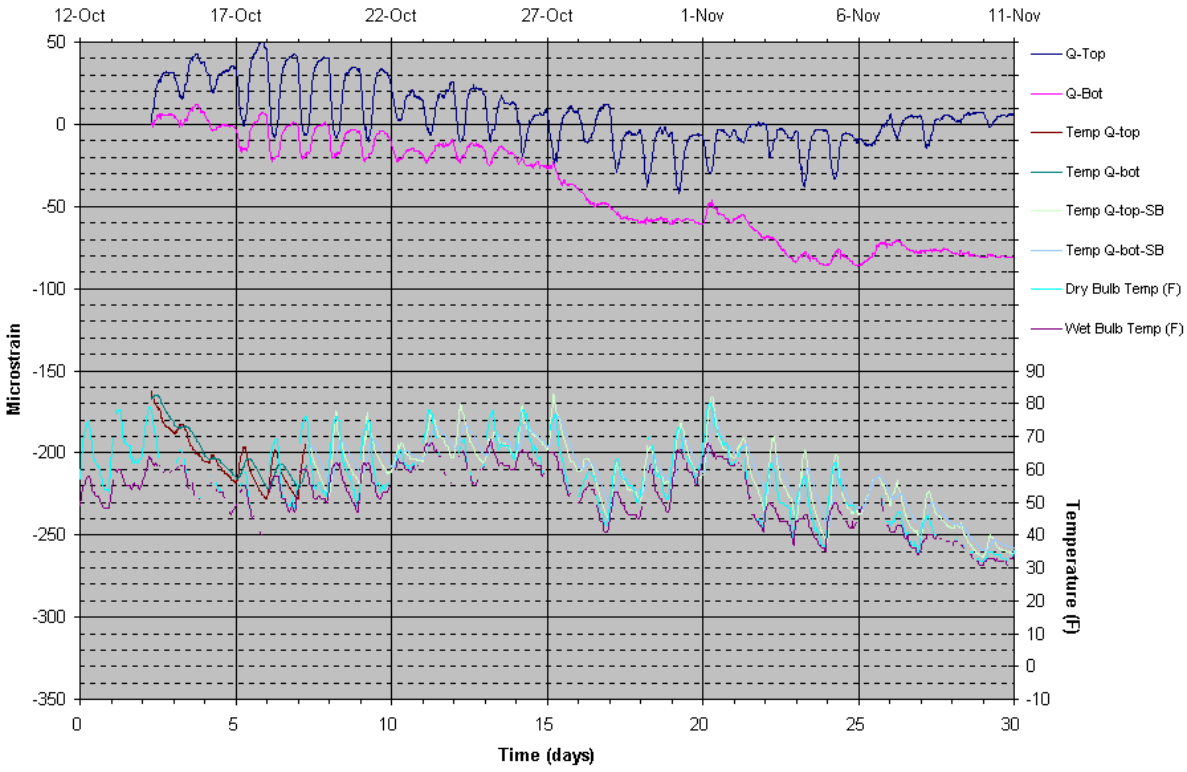

Figure 205. Macon NB Quarterpoint 1st month measured strains and temperatures

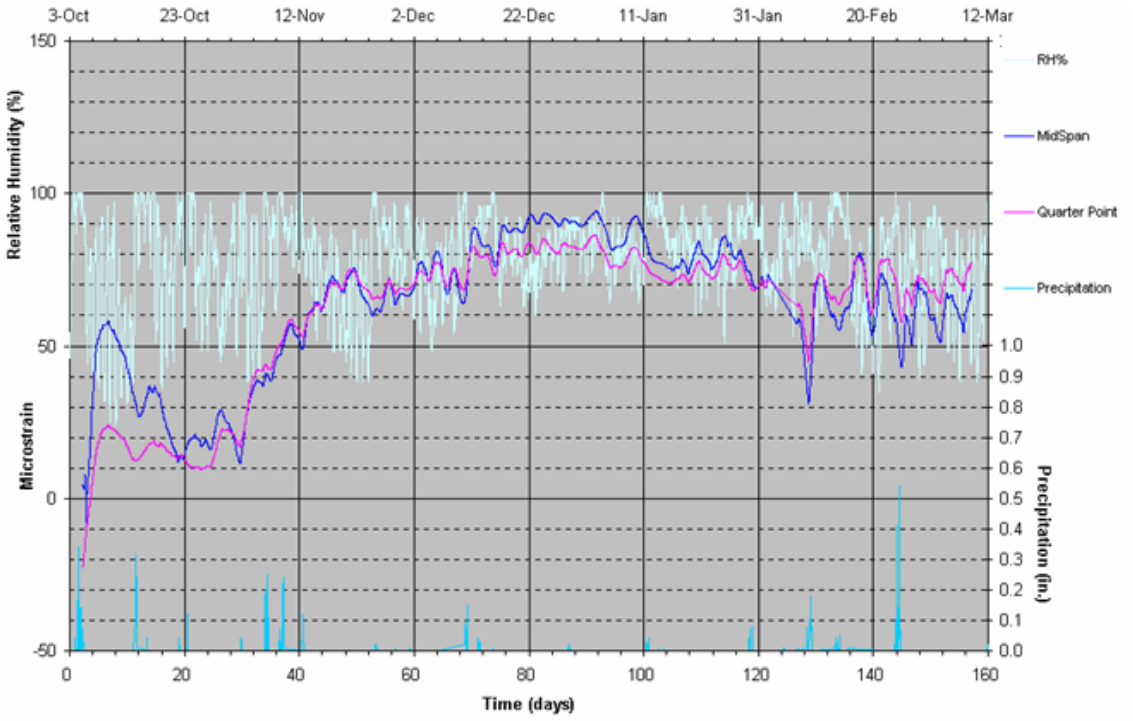

Figure 206. Macon NB differential strains

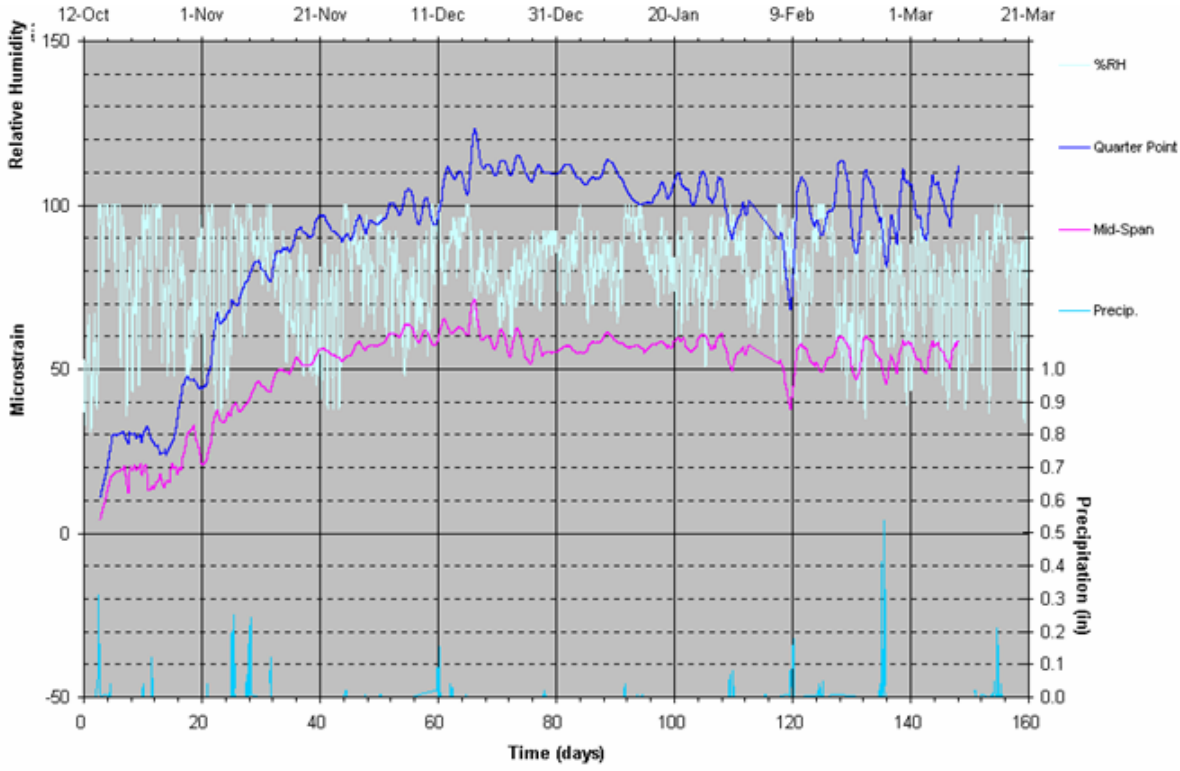

Figure 207. Macon NB Differential strains and temperatures

Appendix C – Duncan Rd / I-72 District 5 (Champaign, IL)

The Duncan Rd project consisted of a two lane bridge deck for northbound and southbound traffic. UIUC provided the data collection equipment and performed the instrumentation for this deck with assistance from IDOT personnel. The deck was instrumented at five locations corresponding to the zero, maximum positive and maximum negative moment regions in the deck as shown in Figure 124. Locations A and B each have four embedment strain gages and five thermocouples. One embedment gage was used to measure transverse strain at these positions. Locations C, D, and E each have three strain gages and five thermocouples. Two free shrinkage beams were constructed and each contained one strain gage and two thermocouples. The 350-ohm strain gages were manufactured by Measurement Group, Inc. and had an active gage length of 4 inches. Type T thermocouple wire (22 AWG) with Teflon insulation was used. Figure 125 shows a longitudinal cross section displaying the individual gage orientation. Figure 126 shows the data collection equipment during installation and Figure 127 shows the finished installation with the solar panel and cellular antenna.

The instrumentation work was performed in the week of September 17, 2001 and the deck was placed on September 20, 2001. The concrete mixture is shown in Chapter 4, Table 4-1. The material was a conventional deck mixture used by IDOT that contained fly ash and had a 0.44 *w/c* ratio. The concrete was pumped during placement followed by finishing of the deck with a paving machine. Following placement, a curing compound was applied to the concrete surface.

Temperature Data

The strain gage and thermocouple data span a period of seven months. Interruptions in data collection occurred due to unexpected disconnection of cellular service in February. The cellular modem equipment used for transmission of data must be used with an analog cellular provider. This was discovered after the network switched to digital service and our service was terminated. During this time, the data were collected manually. Air temperature was measured at the project location. Temperature data for the first week after placement are shown in Figure 144. Internal concrete temperatures followed the measured air temperature with a slight lag. This is expected as the concrete conducts heat slowly and adjusts to ambient conditions. Measured temperatures reached almost 50°C (122°F) during hydration, but the temperature gradient through the thickness of the deck was only 10°C. The temperature data after one month are shown in Figure 145 and the complete temperature history is shown in Figure 146. The maximum temperature gradient in the deck during daily temperature cycles usually occurred during the late morning/early-afternoon heating of the top of the deck on sunny days. The gradient often reached 9-10°C, but did not exceed 11°C. On days that the sun was obscured by clouds, the temperature gradient was less than 1°C. The typical distribution of temperature through the thickness of the deck is shown in Figure 147 for a case where heating occurs from solar radiation. The heating curve shows that the top two to three inches of the deck are most affected by heating. A model was developed to describe heat transfer in the bridge deck and is described further in Chapter 4.

Strain Data

The general trends of the strain data correspond to both daily cycles of temperature and weekly temperature variation. The data are shown in Figure 148 through Figure 150. Strain measurements were corrected for thermal output as discussed in Chapter 2. Several strain sensors did not survive the concrete placement. Measured strains reflect the amount of displacement in the bridge and should not be confused with the strain associated with stress. The two additional factors that control stress in the bridge deck are the level of structural restraint and the creep capacity of the material. The level of restraint is less for temperature deformation than it is for shrinkage. The beams supporting the bridge are changing with temperature along with the deck, although the coefficient of thermal dilation is not the same, the restraint will not be significant. However, shrinkage of the concrete deck is highly restrained by the steel beams. The strain measurements reflect only temperature changes in the deck, but a finite element model in Chapter 4 was combined with shrinkage and creep models in Chapter 5 of the laboratory section to understand the stress that develops in the bridge deck.

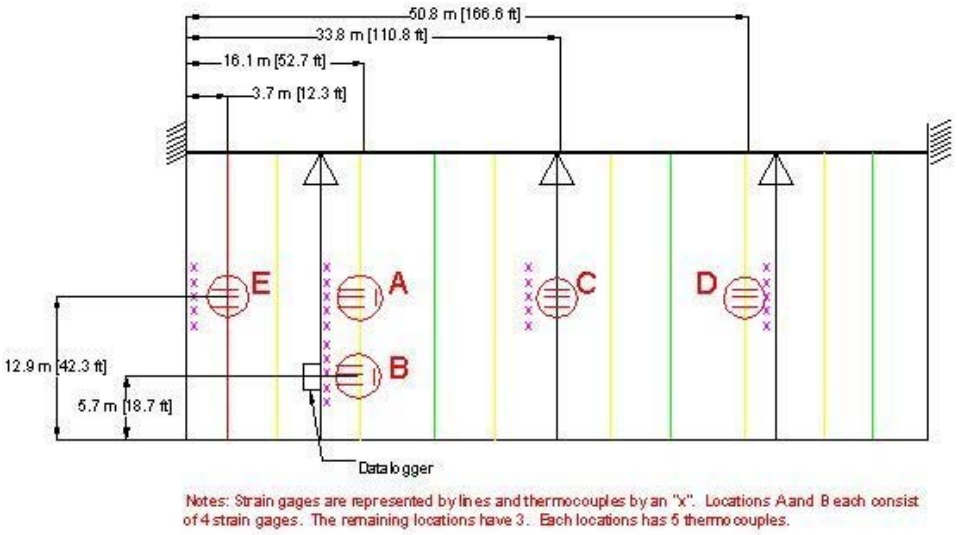

Figure 208. Sensor location map for Duncan Rd

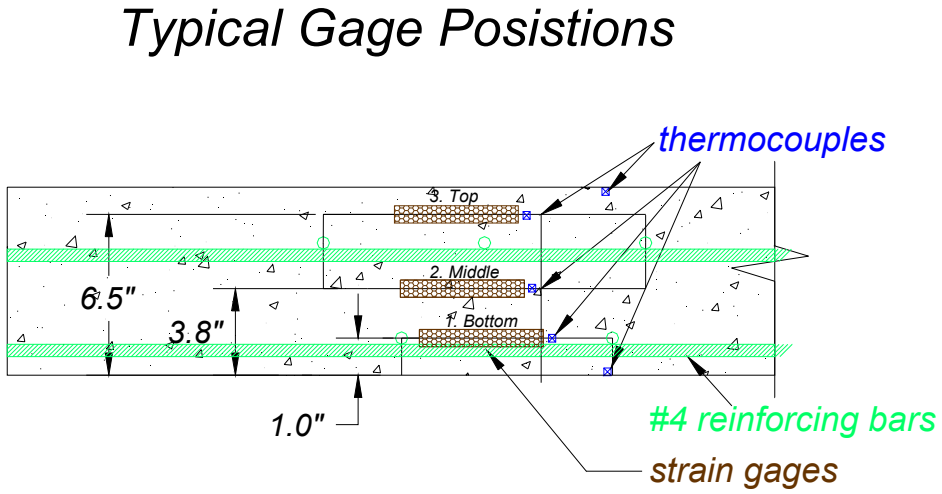

Figure 209. Sensor positions for Duncan Rd

Figure 210. Data collection equipment during installation on pier at Duncan Rd

Figure 211. Complete installation with solar panel and cellular antenna, Duncan Rd.

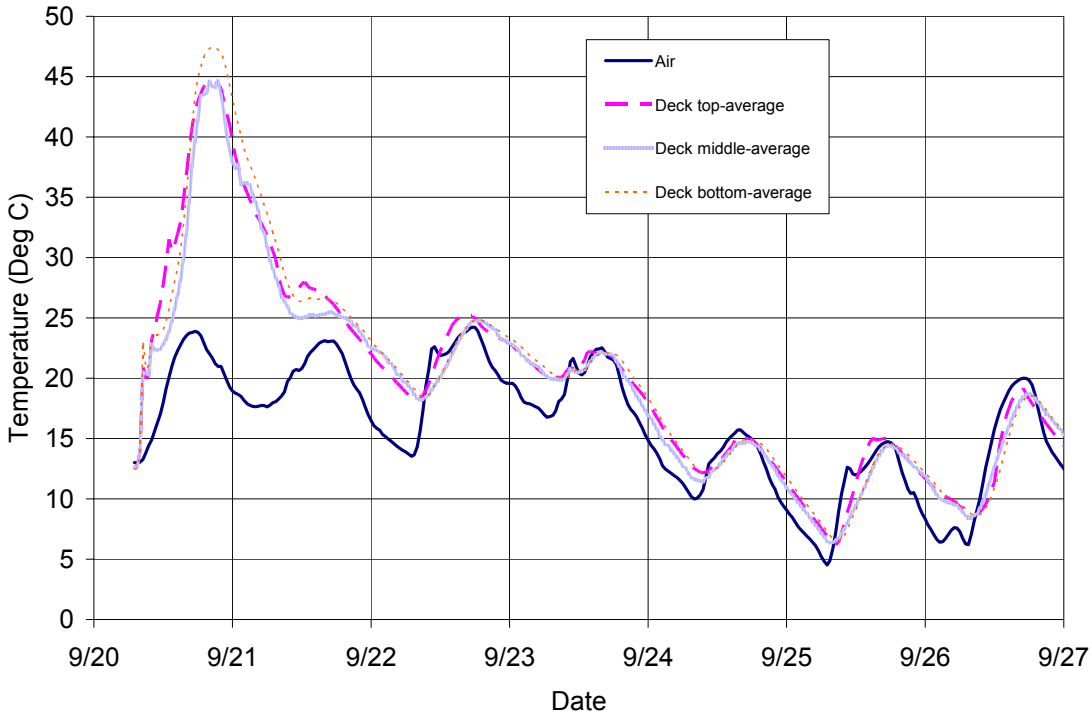

Figure 212. Measured temperatures after 1 week, Duncan Rd

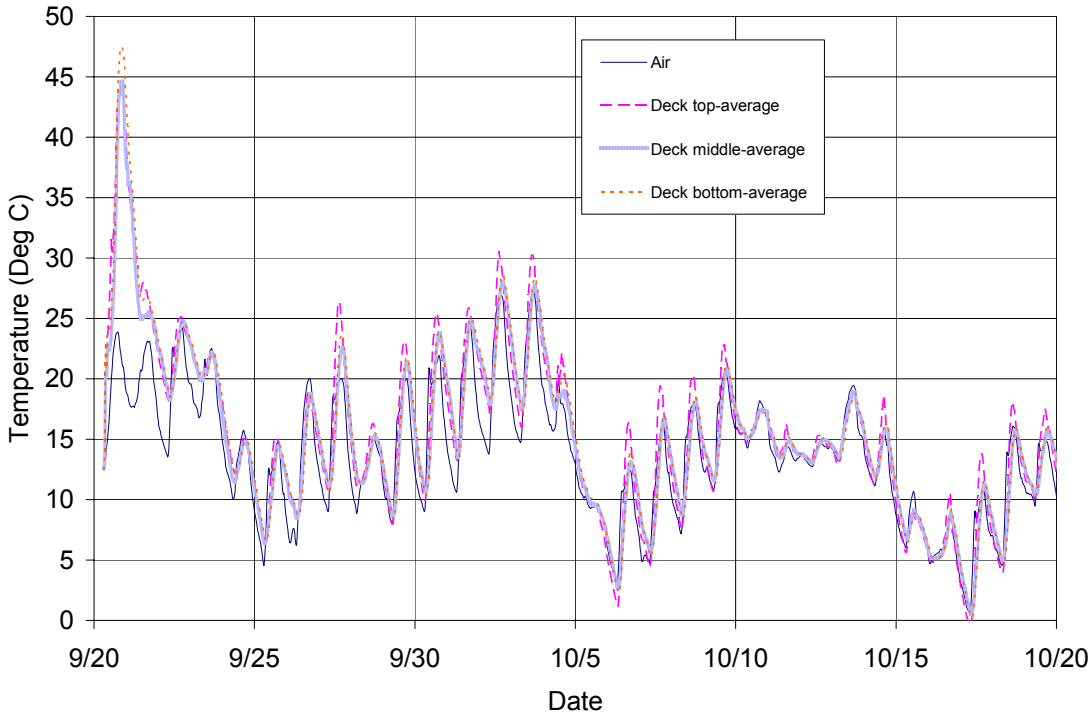

Figure 213. Measured temperatures after 1 month, Duncan Rd

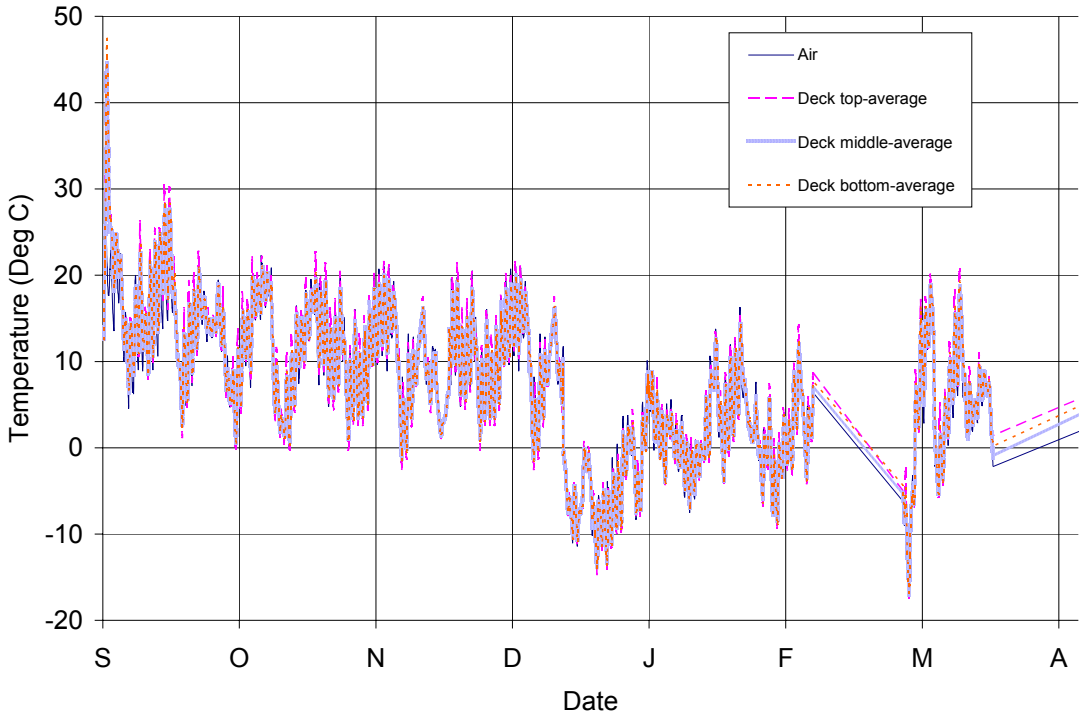

Figure 214. Measured temperatures after 6 months, Duncan Rd

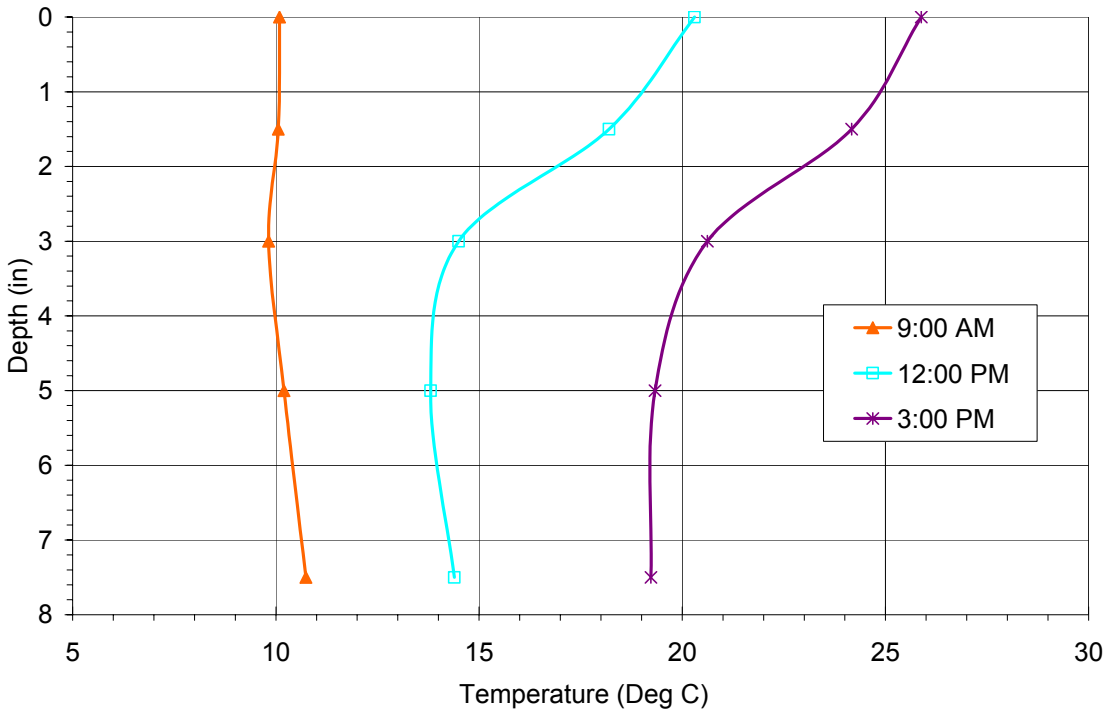

Figure 215. Temperature gradient in the deck during early afternoon heating, Duncan Rd.

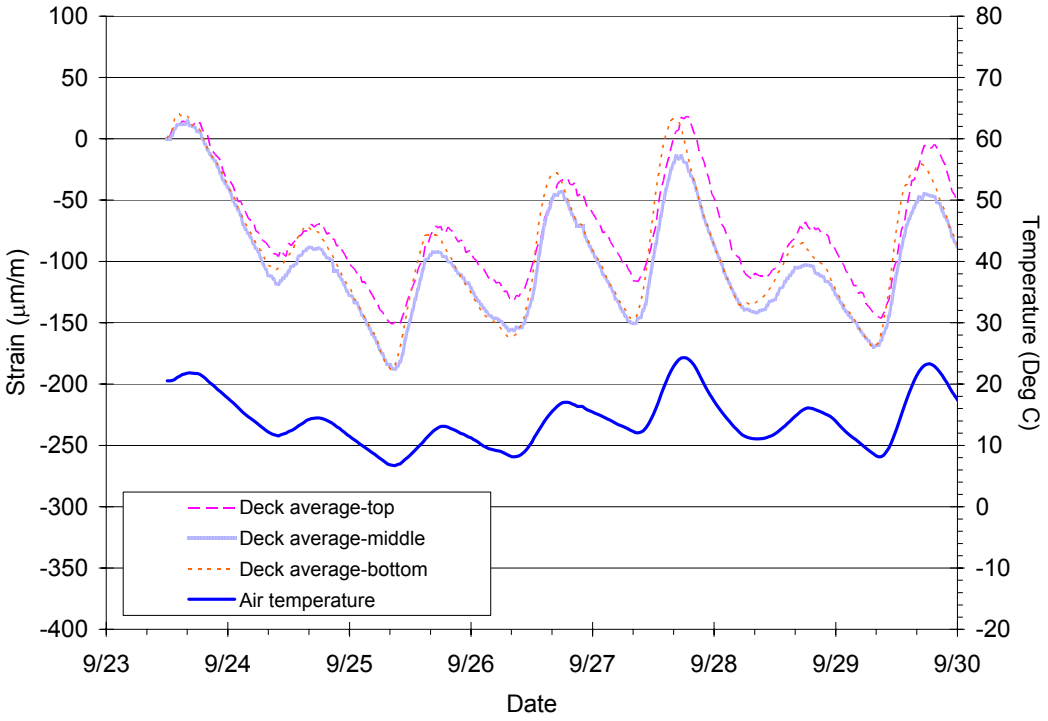

Figure 216. Measured strain after 1 week, Duncan Rd

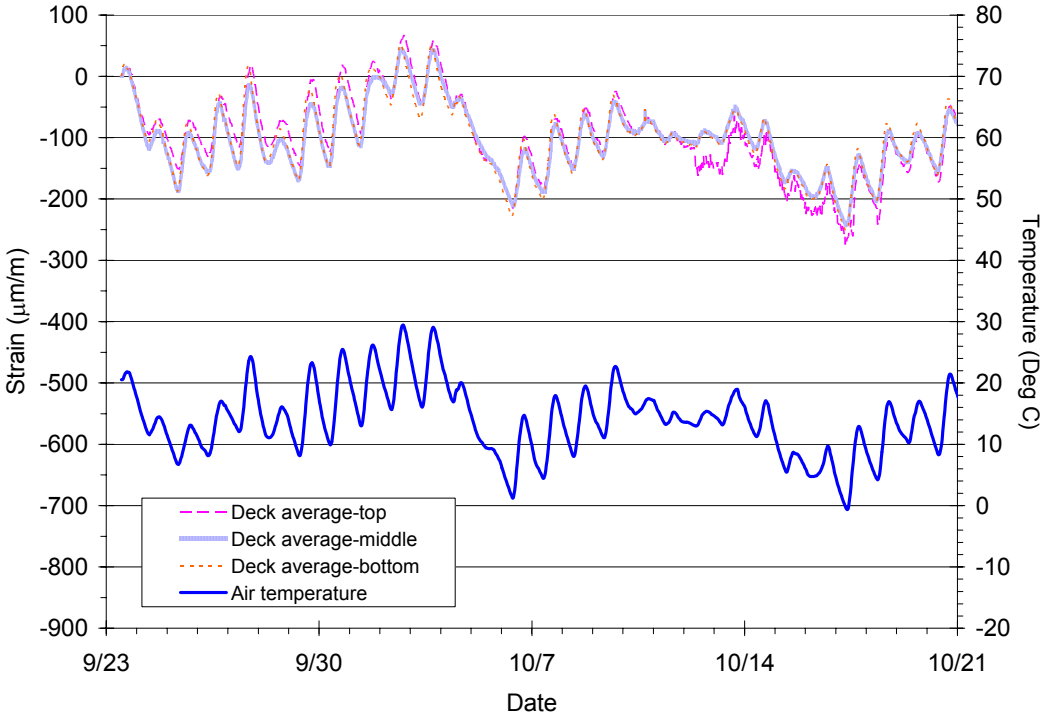

Figure 217. Measured strains after 1 month, Duncan Rd

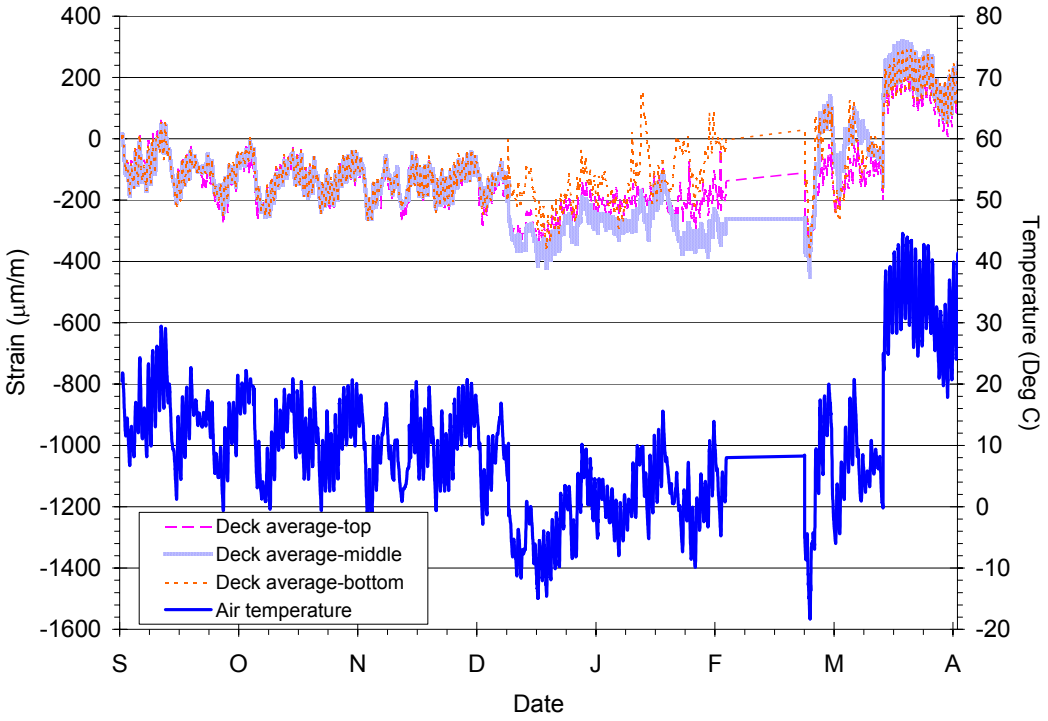

Figure 218. Measured strains after 6 months, Duncan Rd

Appendix D – I-55 / Lake Springfield District 6 (Springfield, IL)

- This deck was instrumented on September 24, 2001. UIUC and IDOT personnel performed the instrumentation with IDOT equipment. Data collection ended on March 14th, 2002
- I-55 Southbound lanes, Segment 9 the sequentially placed deck was instrumented in two locations (A and B). Each location consisted of three strain gages and five thermocouples. Free shrinkage beams were not used for this project due to limitation in strain channels.
- Only one strain gage was damaged leaving 5/6 or 83%
- Maximum temperature differential of 9.7° C occurred on March 9 at 2:30 pm. The largest differentials during the measurement period were usually 5-7° C and occurred during late morning/early-afternoon heating of the deck.

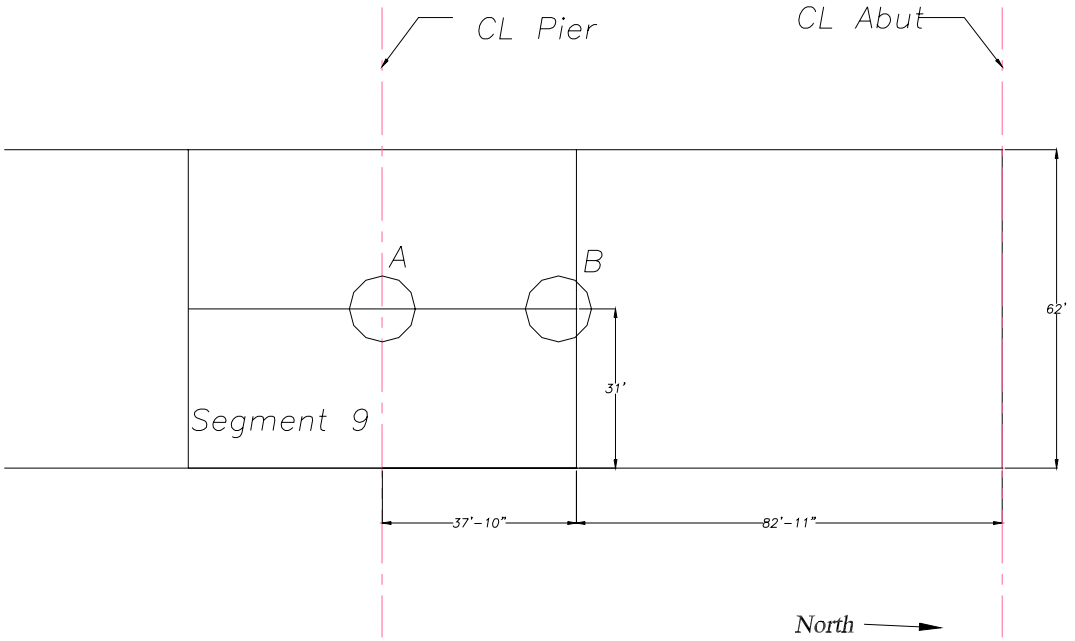

Figure 219. Sensor location map for Lake Springfield, southbound lanes

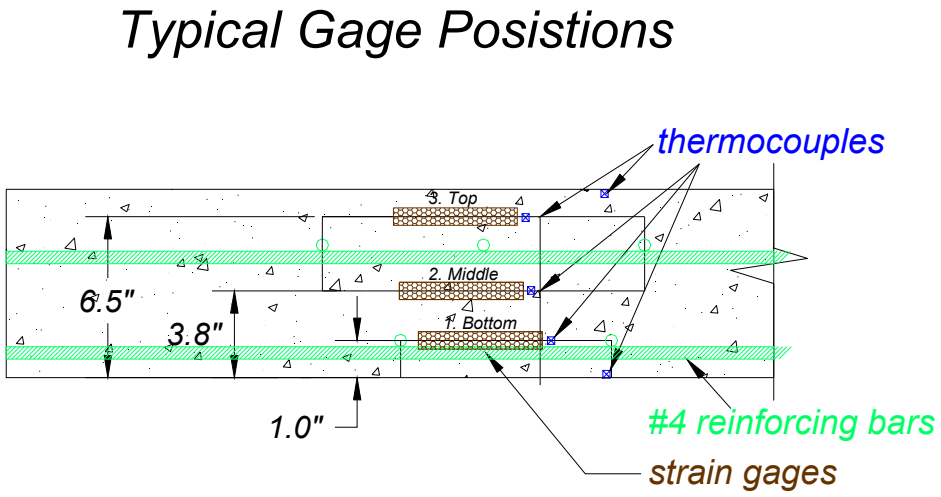

Figure 220. Sensor positions at Lake Springfield

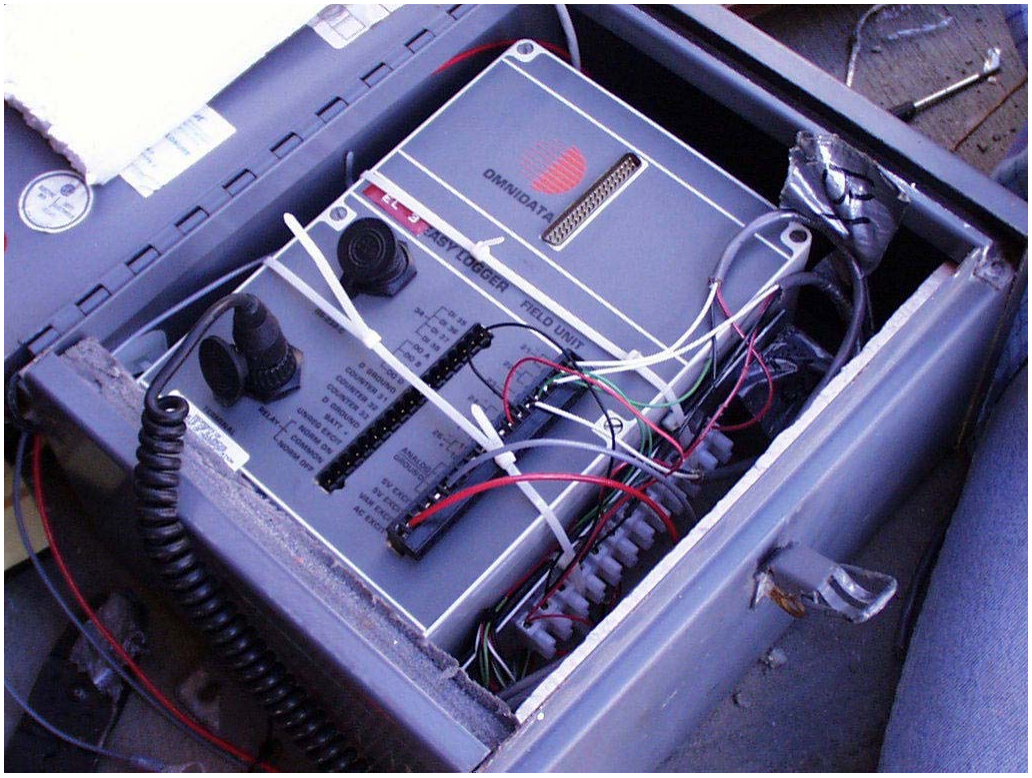

Figure 221. Data collection equipment used at Lake Springfield

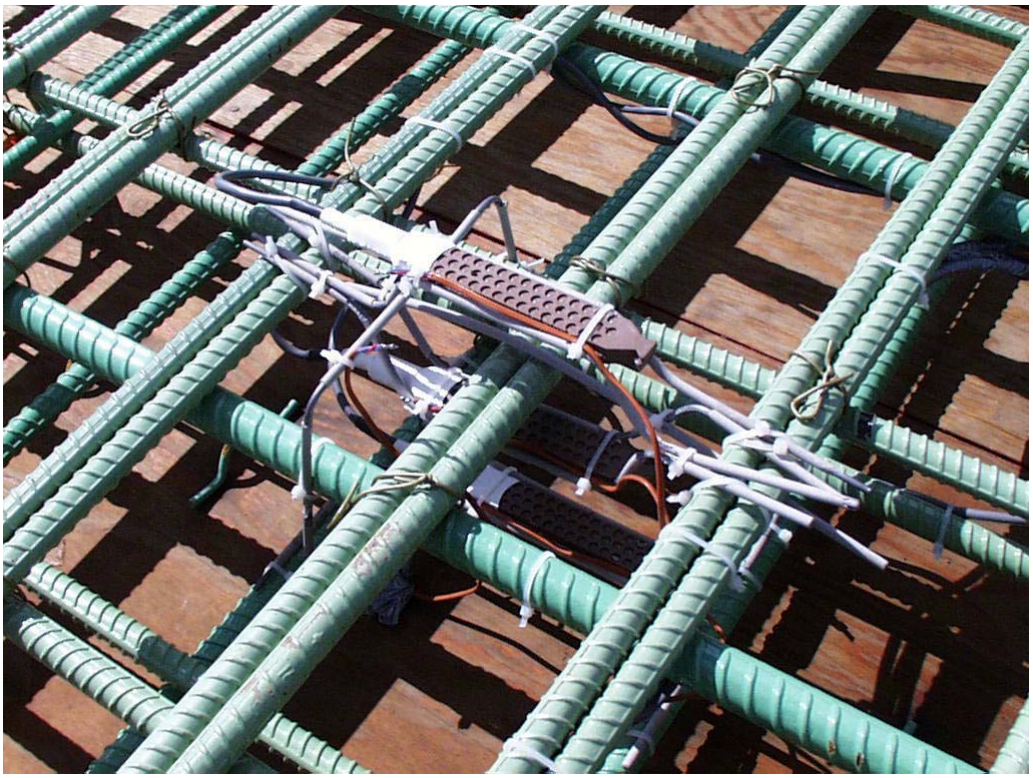

Figure 222. Sensor location A, over pier No. 4, center of deck, L. Springfield

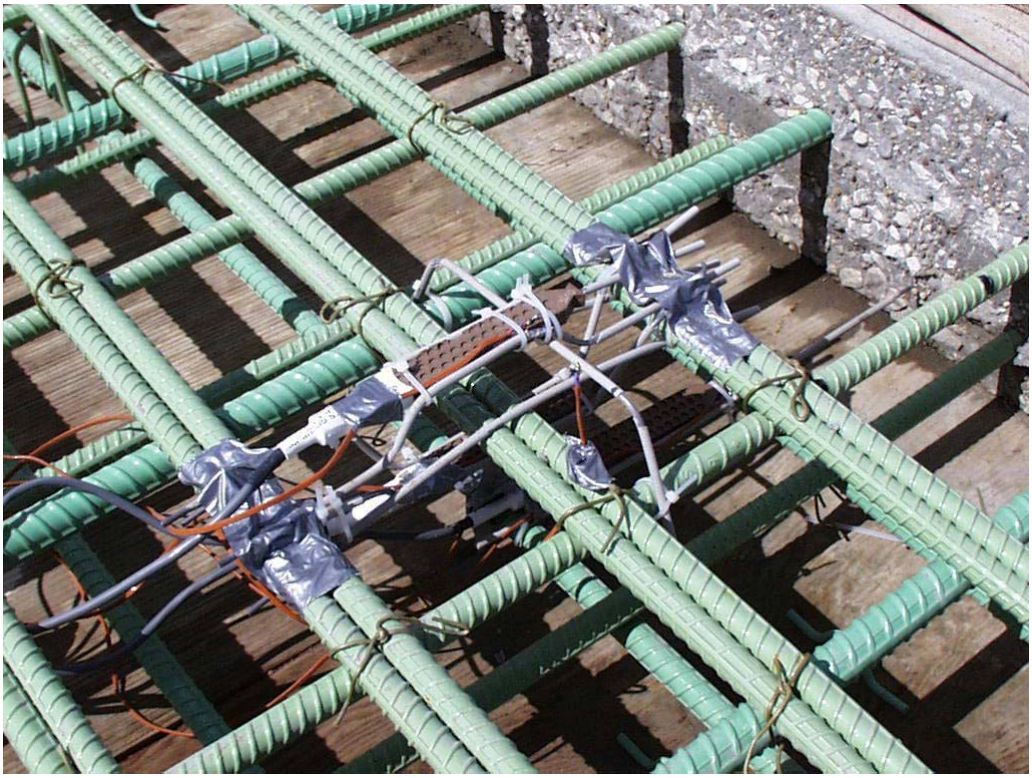

Figure 223. Sensor location B, third point final span, end of segment 9, L. Springfield

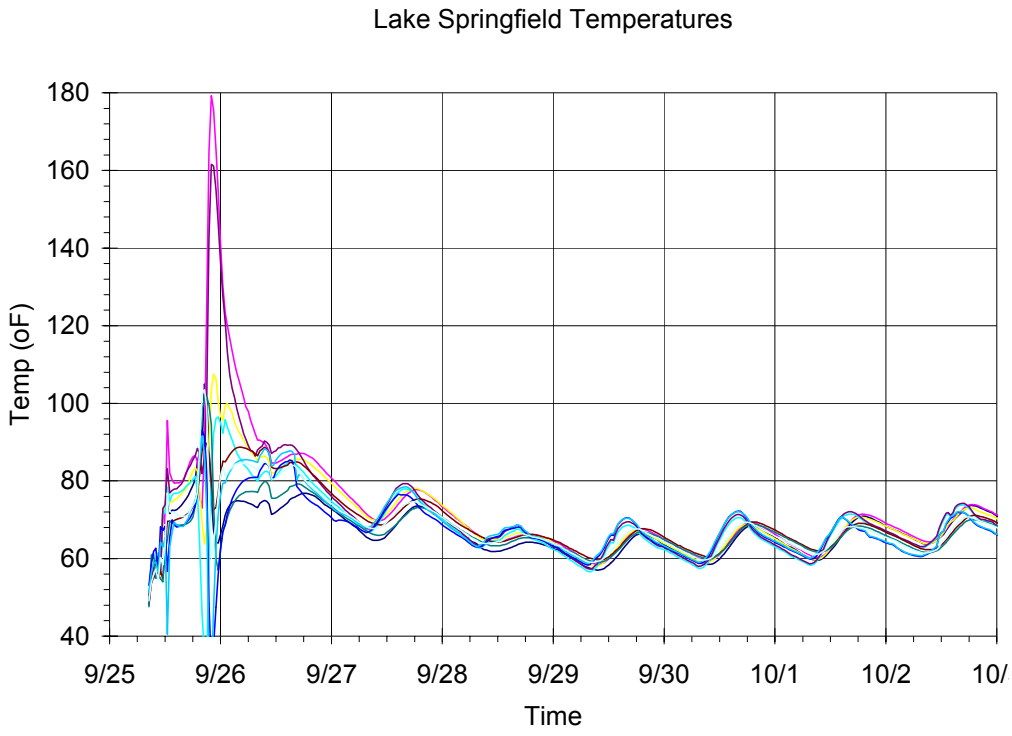

Figure 224. Measured 1st week temperatures for Lake Springfield, segment 9, SB

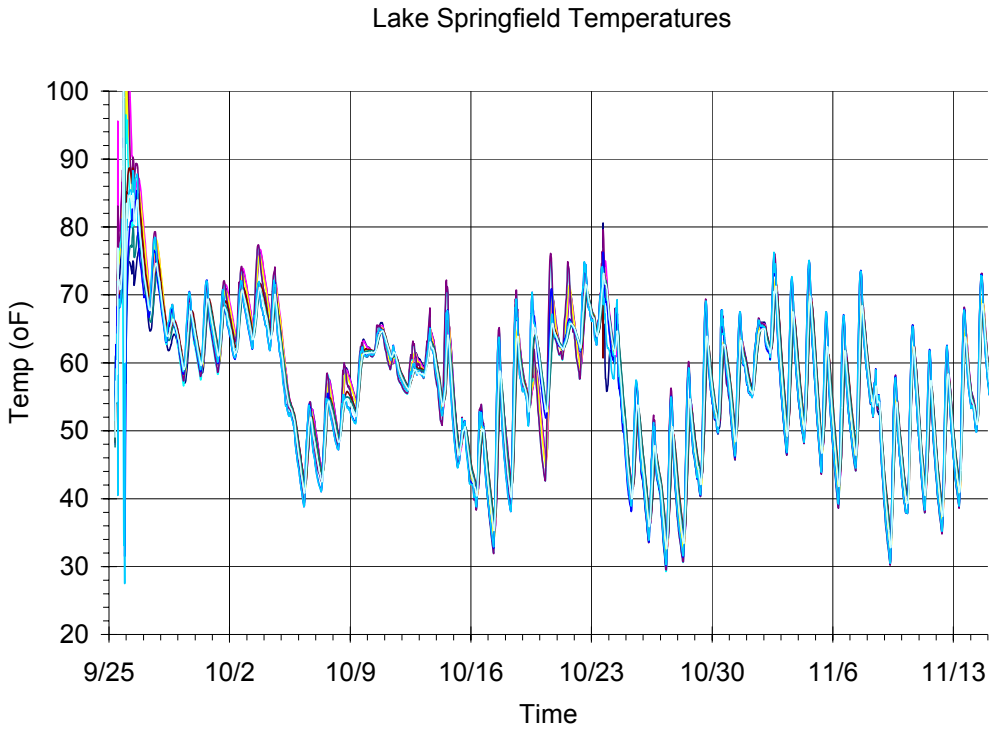

Figure 225. Measured 1st month temperatures for Lake Springfield, segment 9, SB lanes

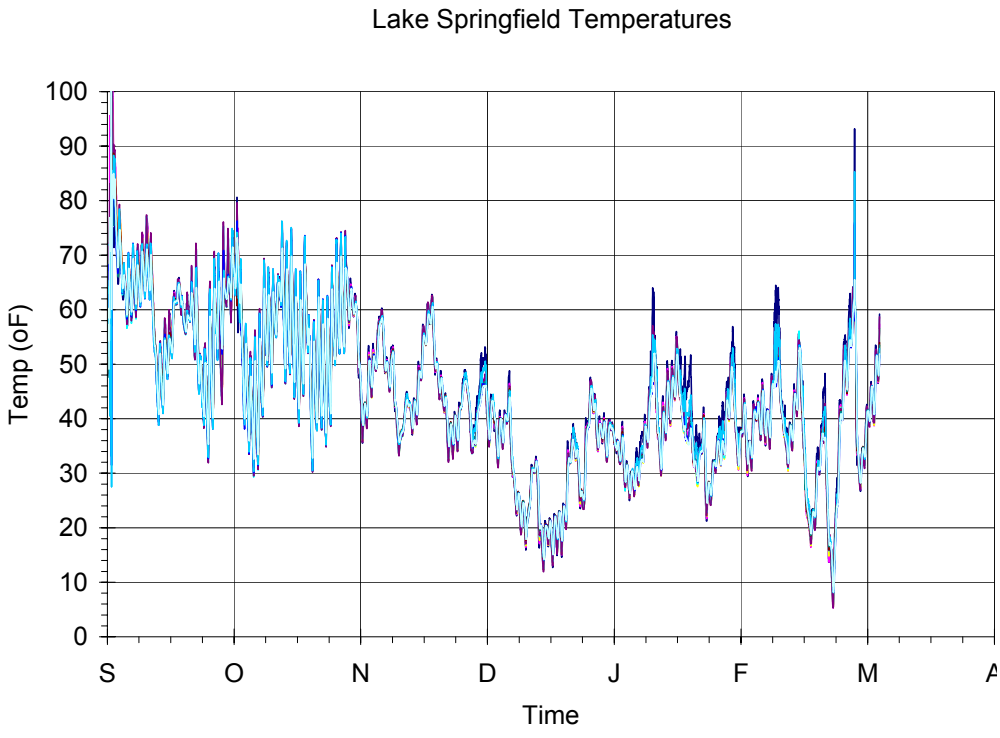

Figure 226. Measured temperatures for Lake Springfield, segment 9, SB lanes

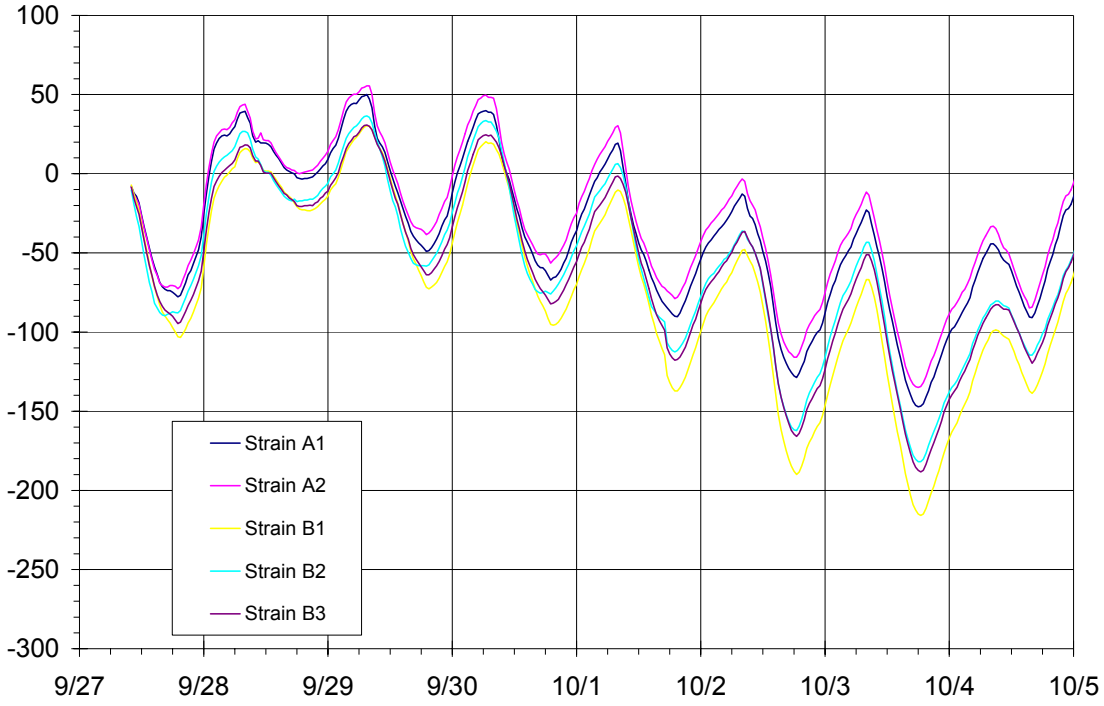

Figure 227. Measured 1st week strains for Lake Springfield, segment 9, SB lanes

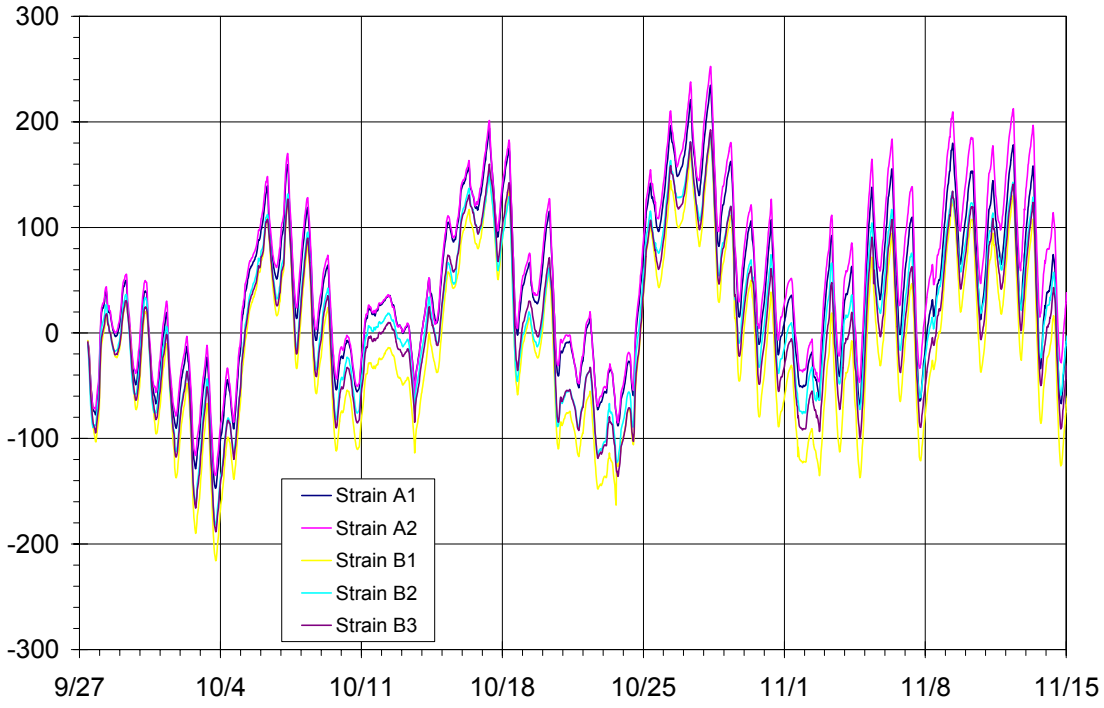

Figure 228. Measured 1st month strains for Lake Springfield, segment 9, SB lanes

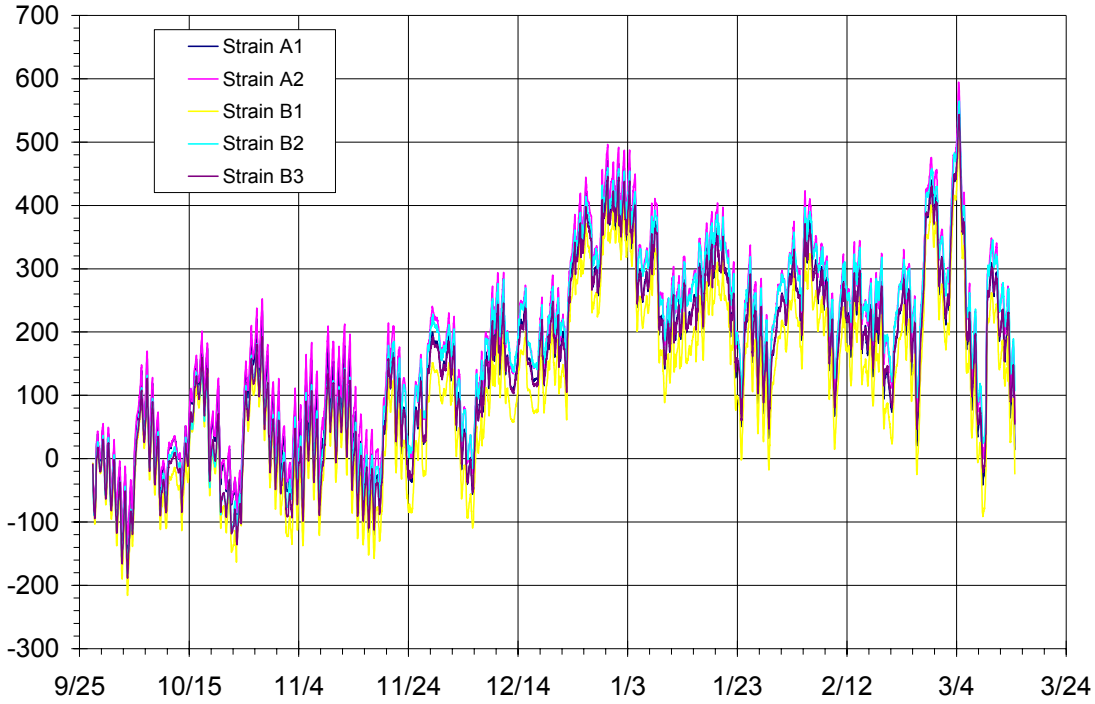

Figure 229. Measured strains for Lake Springfield, segment 9, SB lanes

Appendix E – I-70 / Big Creek District 5 (Marshall, IL)

The Big Creek project consisted of a two-lane bridge deck for westbound traffic on Interstate 70 near Marshall, IL. UIUC provided the data collection equipment and performed the instrumentation for this deck with assistance from IDOT personnel. The deck was instrumented at three locations based on the predicted maximum and minimum stress points in the deck as shown in Figure 128. It was decided based on previous experience that the locations corresponding to the zero, maximum positive, and maximum negative moment regions in the deck were not as critical. Locations each have four embedment strain gages and five thermocouples. One embedment gage was used to measure transverse strain at these positions. Two free shrinkage beams were constructed and each contained three strain gages and 4 thermocouples. Three additional thermocouples were installed in the parapet on top of the deck. The 350-ohm strain gages were manufactured by Measurement Group, Inc. and had an active gage length of 4 inches. Type T thermocouple wire (22 AWG) with Teflon insulation was used. Figure 129 shows a longitudinal cross section displaying the individual gage orientation. Figure 130 shows the data collection equipment during installation and Figure 131 through Figure 135 show the sensors installed at various locations. In Figure 136, the data collection system and the free shrinkage beams are shown. Figure 137 through Figure 139 are of the concrete placement operation. The figures are typical of all the bridge deck installation projects.

The instrumentation work was performed on August 21, 2001 and the deck was placed on August 27, 2001 starting at 6:30 am. The concrete mixture is shown in Chapter 4, Table 4-1. The material was an HPC deck mixture with optimized aggregate gradation. The concrete was pumped during placement followed by finishing of the deck with a paving machine. Following placement, wet cotton mats were applied to the concrete surface as seen in Figure 139.

Temperature Data

The strain gage and thermocouple data span a period of eleven months. Air temperature was measured at the project location. Temperature data for the first week after placement are shown in Figure 151 through Figure 153. Internal concrete temperatures followed the measured air temperature with a slight lag. This is expected as the concrete conducts heat slowly and adjusts to ambient conditions. Measured temperatures reached almost 60°C (140°F) during hydration, but the temperature gradient through the thickness of the deck was only 10°C. Hydration temperatures were the highest over the pier location. The deck was placed monolithically with the diaphragm and thus had a greater mass of concrete leading to higher heat evolution. Temperature measurements in the parapet are shown in Figure 246. The maximum parapet temperature during hydration was 54°C and the temperature gradient between the top and bottom of the parapet was about 6°C. The free shrinkage beams developed lower heat, as was expected due to their smaller size compared to the deck. The complete temperature history is shown in Figure 146. The maximum temperature gradient in the deck during daily temperature cycles usually occurred during the late morning/early-afternoon heating of the top of the deck on sunny days. The gradient often reached 9-10°C, but did not exceed 10.5°C. A model was developed to describe heat transfer in this bridge deck and is described further in Chapter 4.

Strain Data

The general trends of the strain data correspond to both daily cycles of temperature and weekly temperature variation. The data are shown in Figure 248 through Figure 259. Strain measurements were corrected for thermal output as discussed in Chapter 2. Most of the strain sensors survived concrete placement for this bridge. Magnitudes of the transverse strain sensors are similar to longitudinal sensors. No significant differences were noticed between locations in the deck. The strain varies with temperature at each location, and bending deflections are seen during morning heating and evening cooling cycles. These warping deflections are also seen in the free shrinkage beams at locations D and E as shown in Figure 160 and Figure 161. Warping in the free shrinkage beams is well behaved during heating and cooling, where the top strain elongates as it heat and there is almost a linear relation to depth. In the bridge deck however, the warping strain is not always evenly spaced. This indicates a higher level of restraint against bending in the deck is changing the strain distribution. This is expected since the bridge girders are not heated directly by solar radiation and do not have the same tendency to warp. It should be noted that measured strains reflect the amount of displacement in the bridge and should not be confused with the strain associated with stress. The two additional factors that control stress in the bridge deck are the level of structural restraint and the creep capacity of the material. The level of restraint is less for temperature deformation than it is for shrinkage. The beams supporting the bridge are changing with temperature along with the deck, although the coefficient of thermal dilation is not the same, the restraint will not be significant. The only restraint to temperature deformation is from the pier. However, shrinkage of the concrete deck is highly restrained by the steel beams. The strain measurements reflect only temperature changes in the deck, but a finite element model in Chapter 4 was combined with shrinkage and creep

models in Chapter 5 of the laboratory section to understand the stress that develops in this bridge deck.

Internal Relative Humidity Measurements

In addition to the embeddable strain gages and thermocouples already being implemented in the bridge deck field experimentation, internal relative humidity sensors were installed. The internal RH measurement system used in the field research was a preliminary system developed at UIUC prior to the system used in the laboratory research. The system consisted of a G-Cap2 capacitive RH sensor manufactured by General Eastern enclosed in a 1/2" PVC tube. The end of the tube was covered in Gore-Tex to allow moisture vapor transmission while blocking liquid water and solid particles. Figure 260 shows the internal RH sensors ready to be cast in the concrete bridge deck on I-70 near Marshall, IL (Big Creek). The data was collected every 10 minutes with the Campbell Scientific datalogger system

The RH sensors appeared to function properly for a couple of weeks after the bridge deck was cast before going out of range. It is unclear at this time why the sensors went out of range, but it may be due to eventual water infiltration. The end of the PVC tube that had the lead wire exit (opposite from the end covered in Gore-Tex) was plugged with duct-seal, which is a sealing putty. It is possible that this seal developed leaks over time and the sensor became exposed to liquid moisture and dissolved salts from the pore solution.

Before the RH sensors went out of range, the internal RH gradient was measured in the concrete bridge deck. The data for the six-day period is shown in Figure 261. The most interesting observation to make from the data is that the internal RH varies synchronously with the internal temperature. This is opposite from intuition. Relative humidity is defined as the partial vapor pressure (the actual amount of moisture in the air) relative to the maximum possible

vapor pressure at a given temperature. In an open environment, when the temperature goes down the saturation vapor pressure goes down, which means the RH goes up with constant partial vapor pressure. This means that normally there is an inverse relationship between RH and temperature.

The observation that RH varies synchronously with temperature means that in partially saturated concrete where capillary menisci are present, capillary tension decreases as temperature increases. In other words, there is a relaxation of shrinkage stresses as the temperature is increased, allowing an additional expansion of the material shown in Figure 262. Furthermore, this indicates a dependence of the coefficient of thermal dilation (CTD) on the state of moisture in concrete. The highest increase in the CTD occurs in concrete that has an internal RH of about 50%, which is the lowest internal RH before capillary menisci become unstable. Figure 263 illustrates the dependence of the CTD on the state of internal moisture.

In concrete that is exposed to drying on the top surface (i.e. has an internal RH gradient) there will be a thermal stress gradient induced. Different layers throughout the depth of the material will have different coefficients of thermal dilation. This could potentially exacerbate the thermal cracking potential of drying concrete.

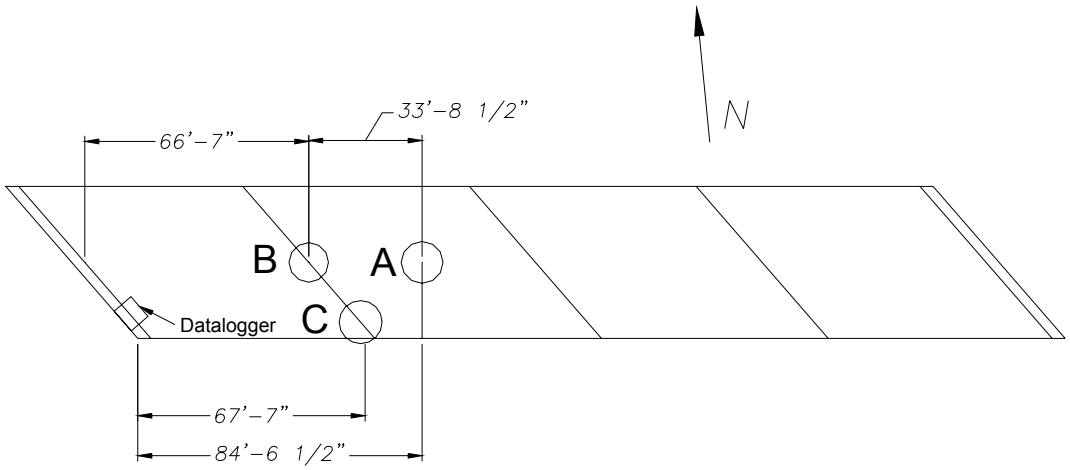

Figure 230. Big Creek sensor location map

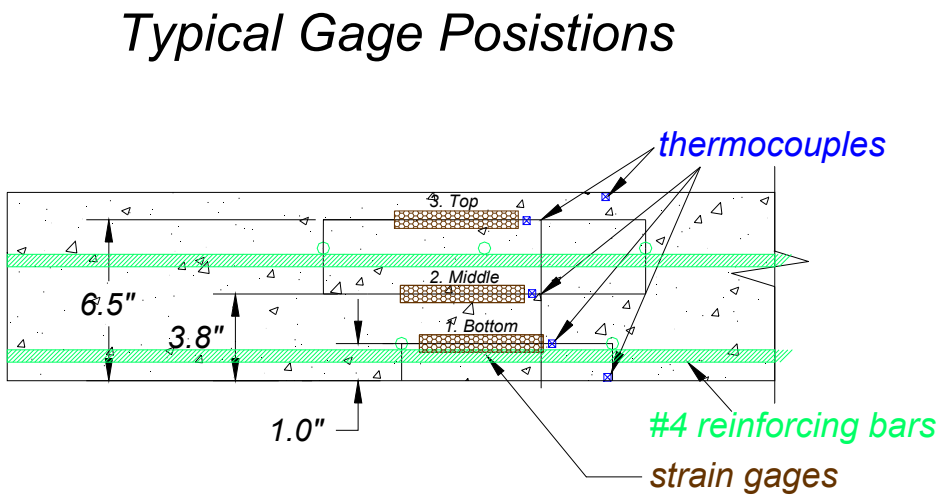

Figure 231. Big creek sensor positions

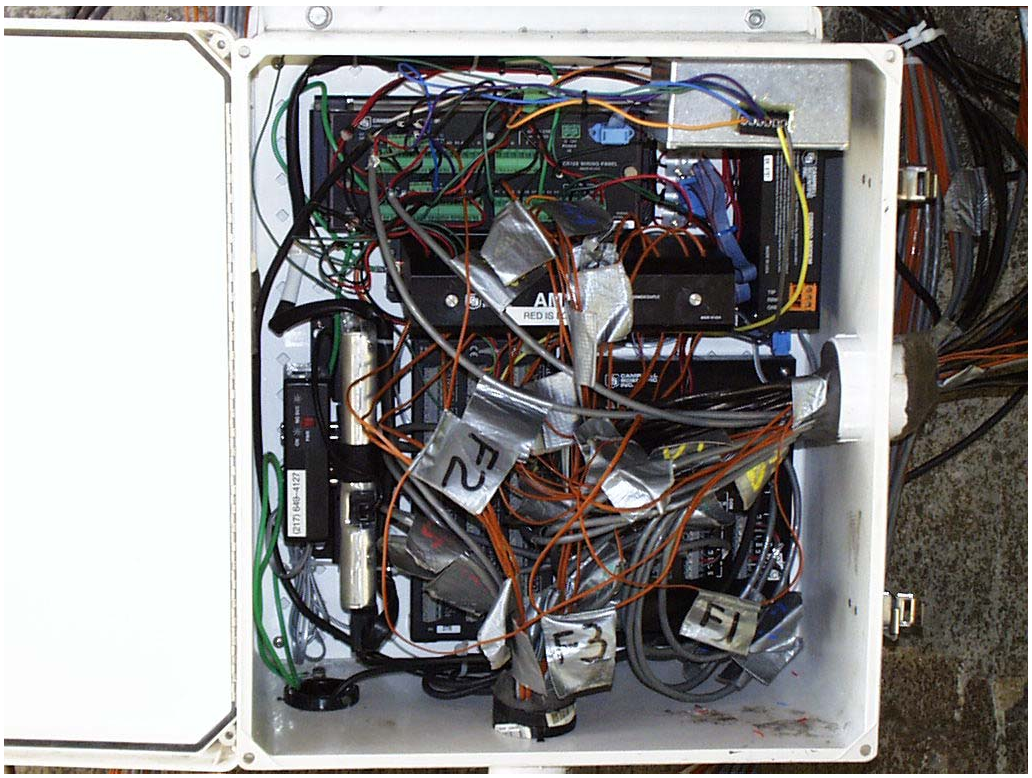

Figure 232. Data collection system during installation, Big Creek

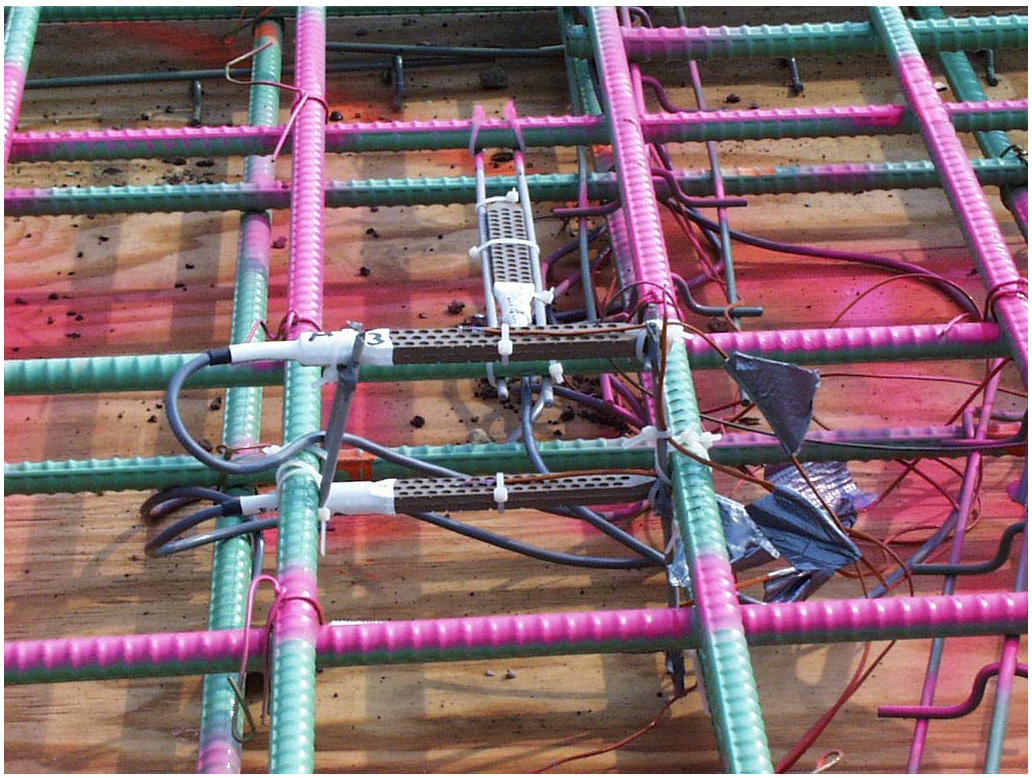

Figure 233. Sensors installed at location A, midspan, center of deck, Big Creek

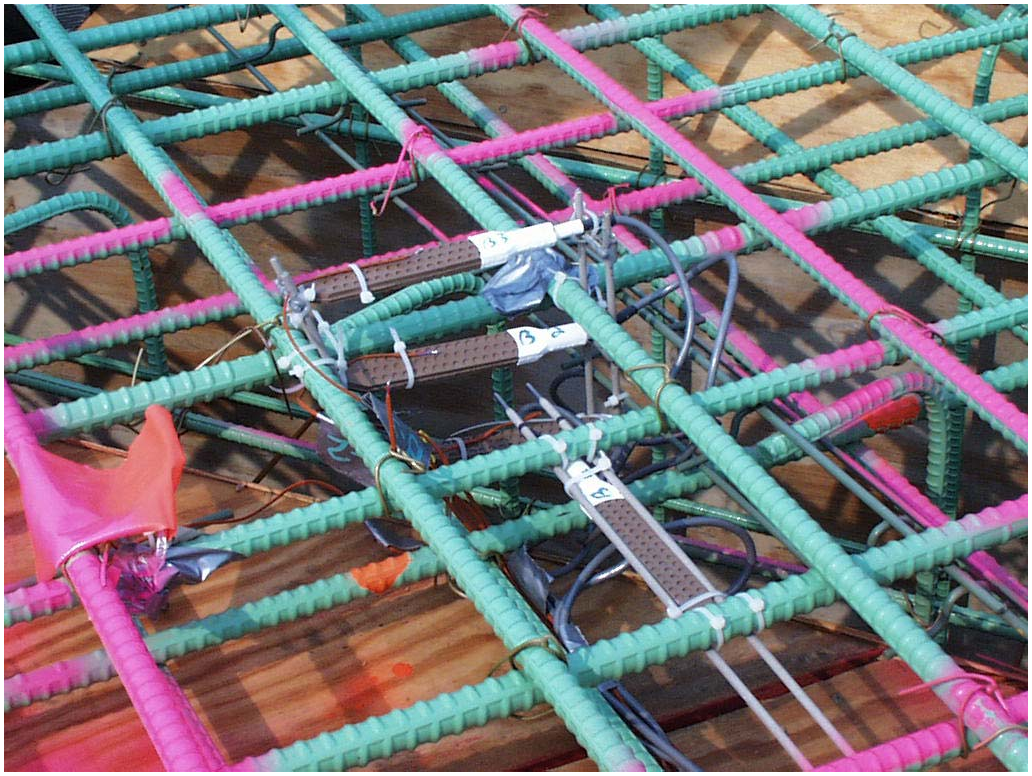

Figure 234. Sensors installed at location B, over pier, center of deck, Big Creek

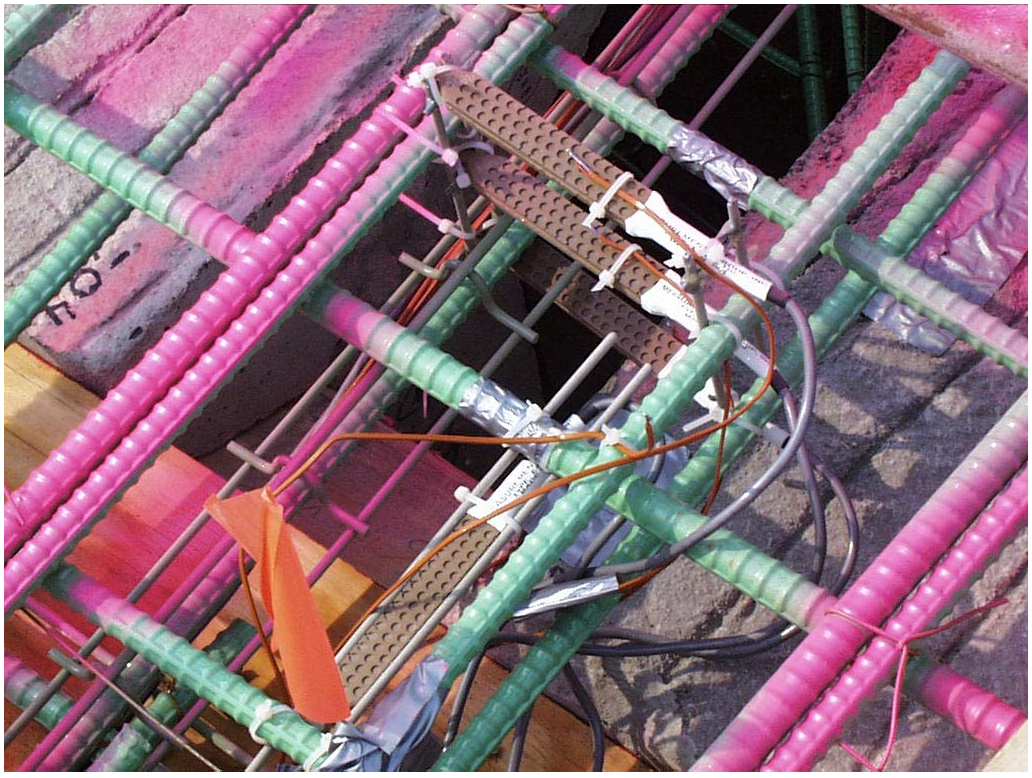

Figure 235. Sensors installed at location C, over pier, edge of deck, Big Creek

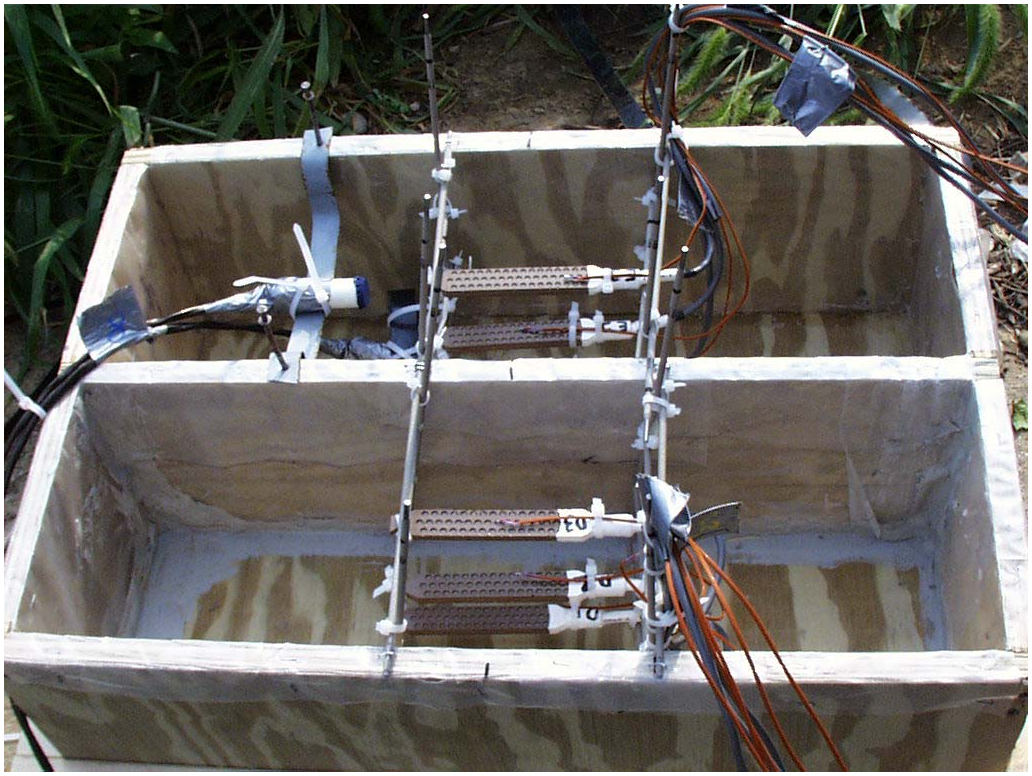

Figure 236. Sensors installed in free shrinkage beams, Big Creek

Figure 237. Sensors installed in parapet wall, Big Creek

Figure 238. Data collection system and free shrinkage beams, Big Creek

Figure 239. Concrete pumping operation, Big Creek

Figure 240. Placing and finishing concrete, Big Creek

Figure 241. Applying wet cotton mats for curing, Big Creek

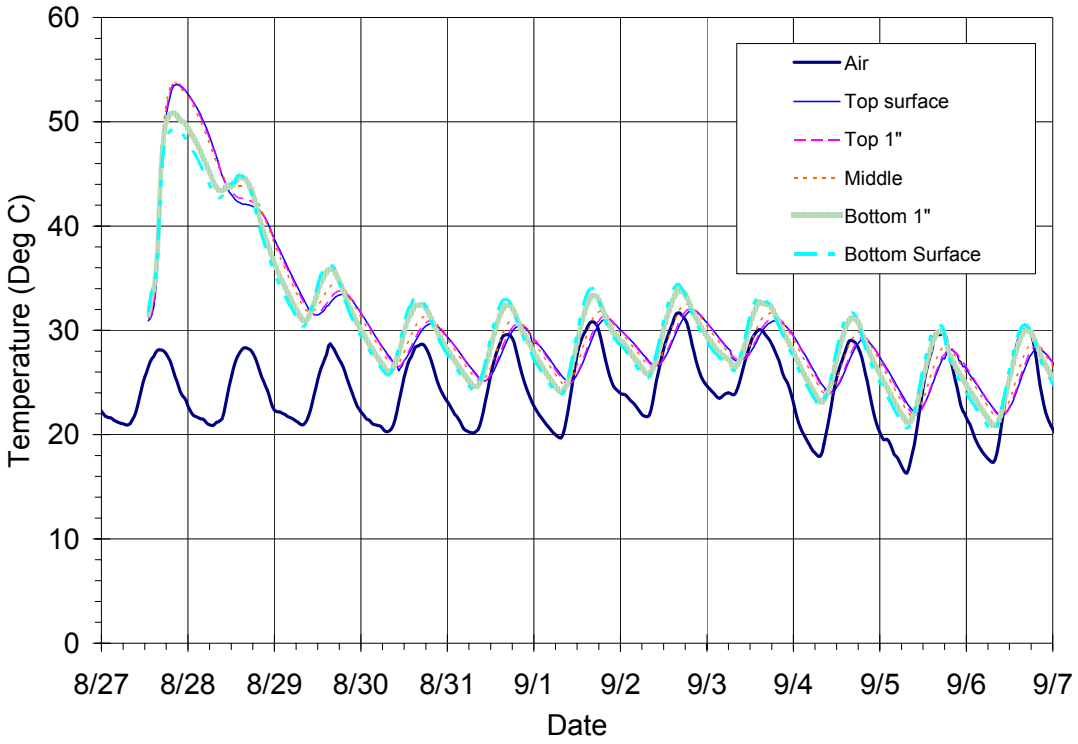

Figure 242. Temperature measurements at location A, midspan, center of deck, Big Creek

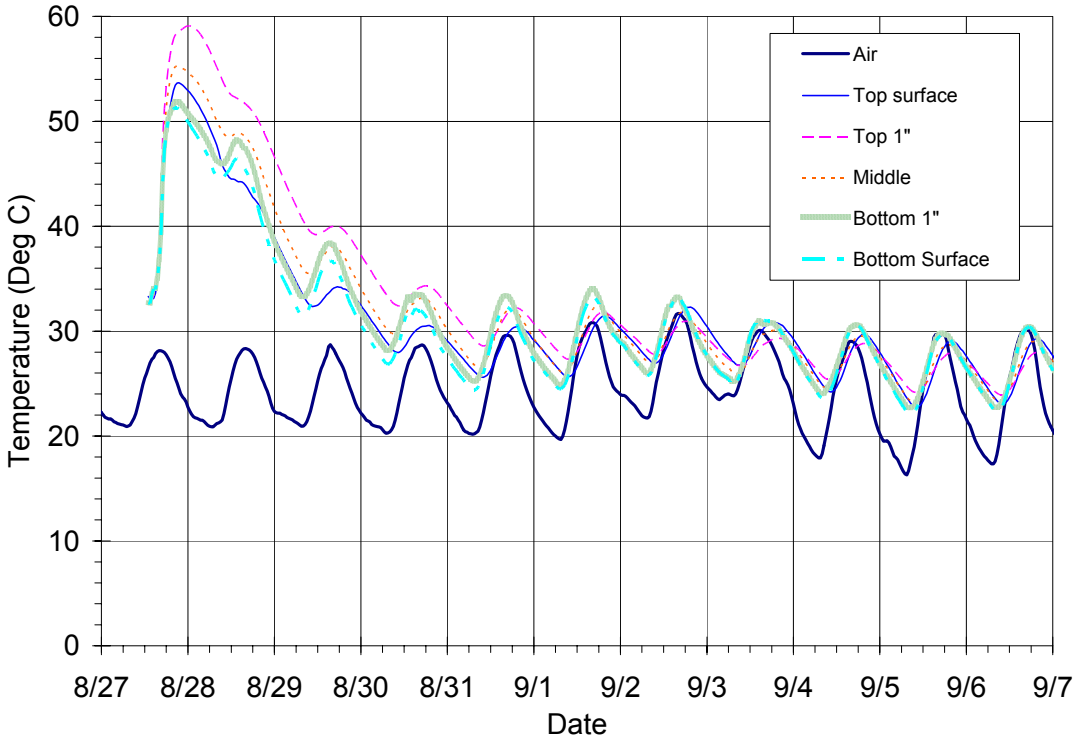

Figure 243. Temperature measurements at location B, over pier, center of deck, Big Creek

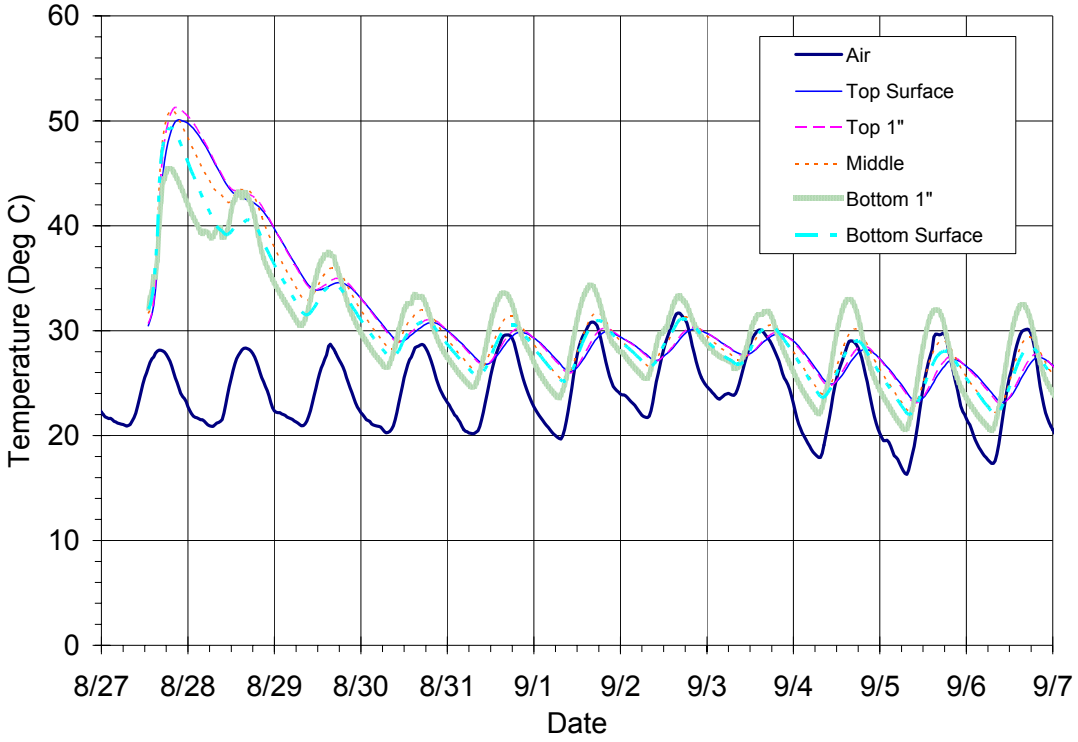

Figure 244. Temperature measurements at location C, over pier, edge of deck, Big Creek

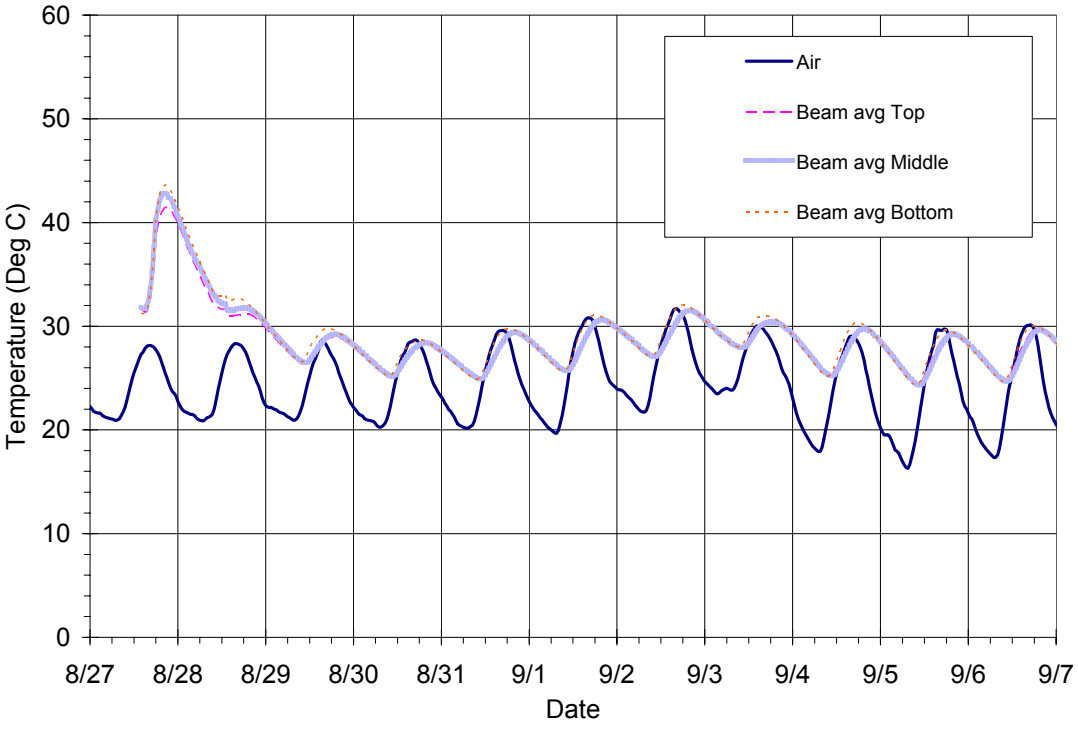

Figure 245. Temperature measurements in free shrinkage beams, Big Creek

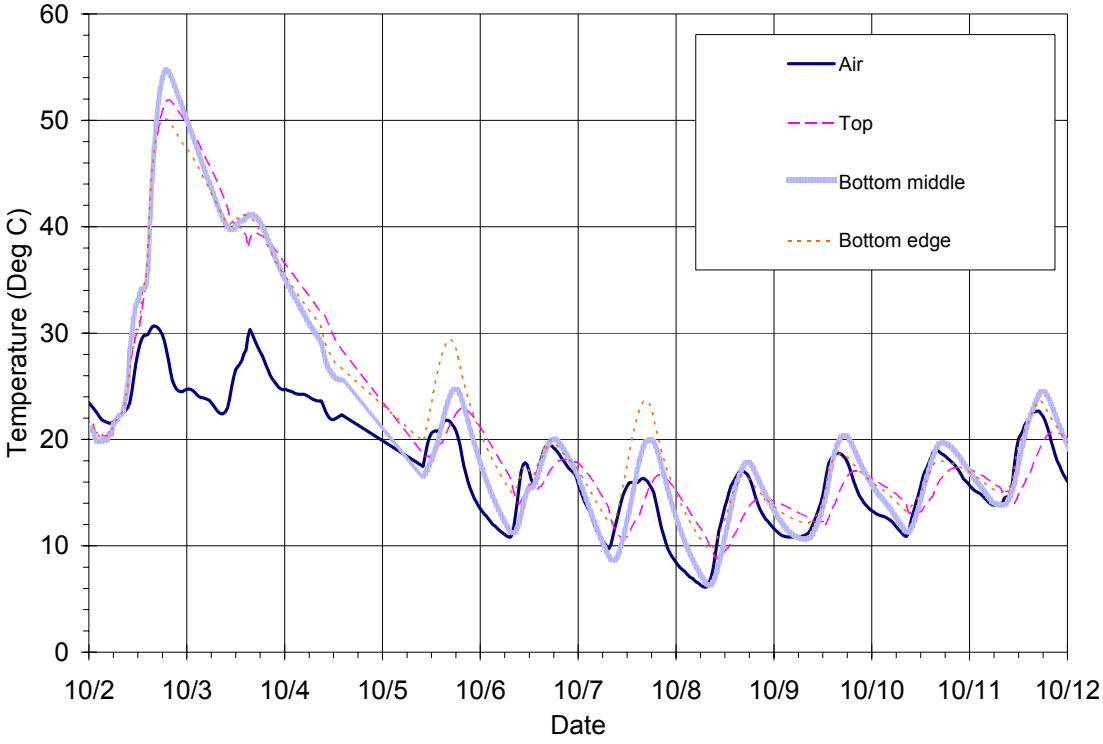

Figure 246. Temperature measurements in parapet wall after 1 week, Big Creek

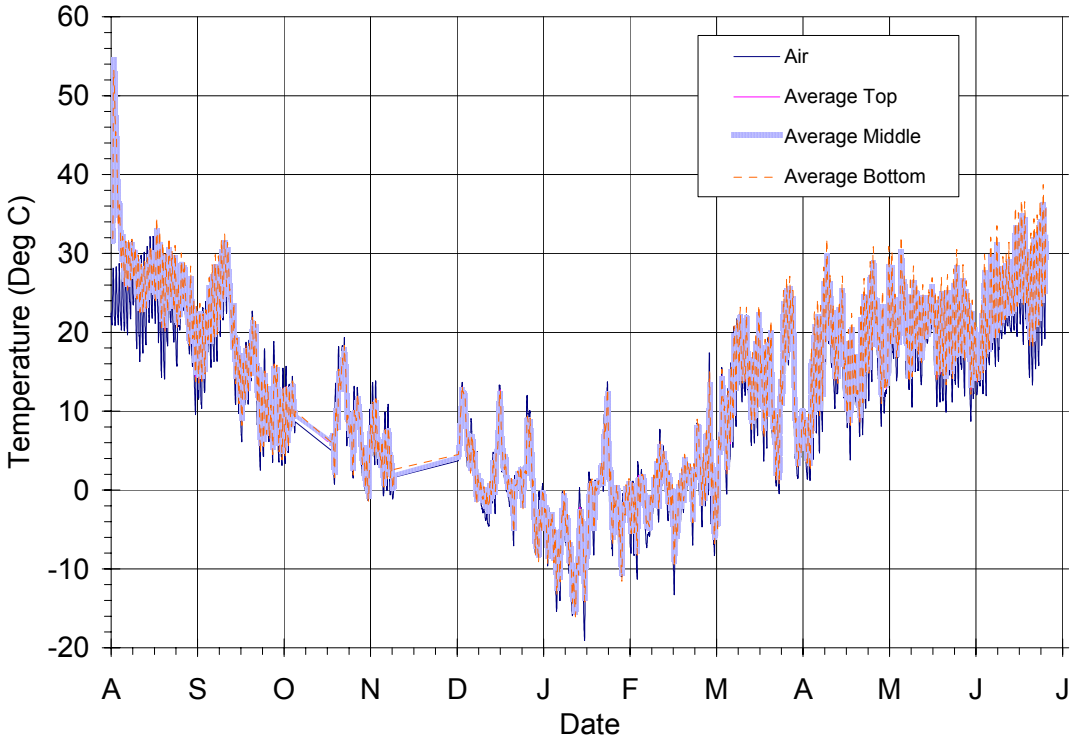

Figure 247. Average temperature history for Big Creek bridge deck for one year, Big Creek

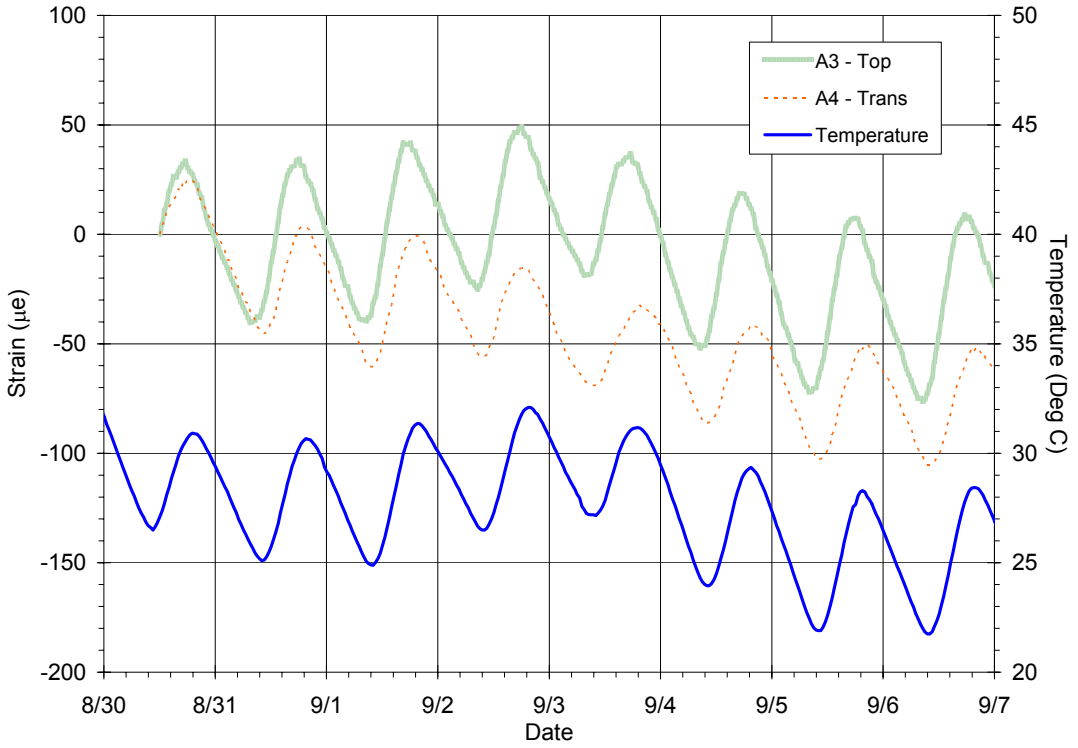

Figure 248. Strain measurements at location A, midspan, center of deck, Big Creek

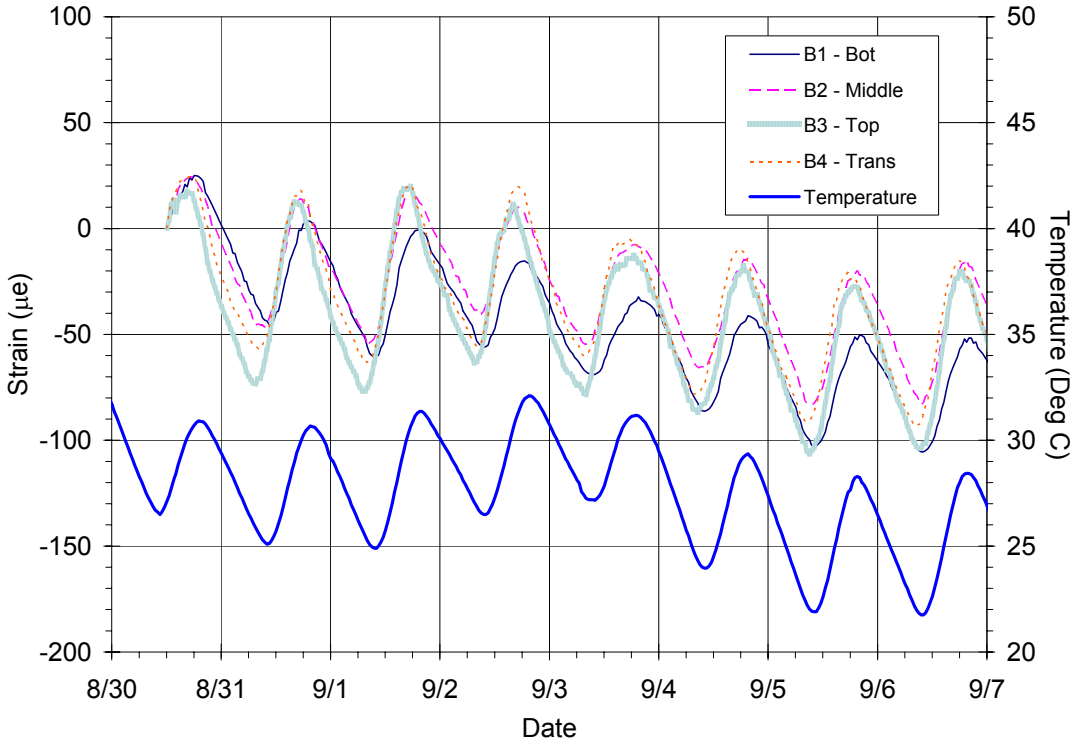

Figure 249. Strain measurements at location B, over pier, center of deck, Big Creek

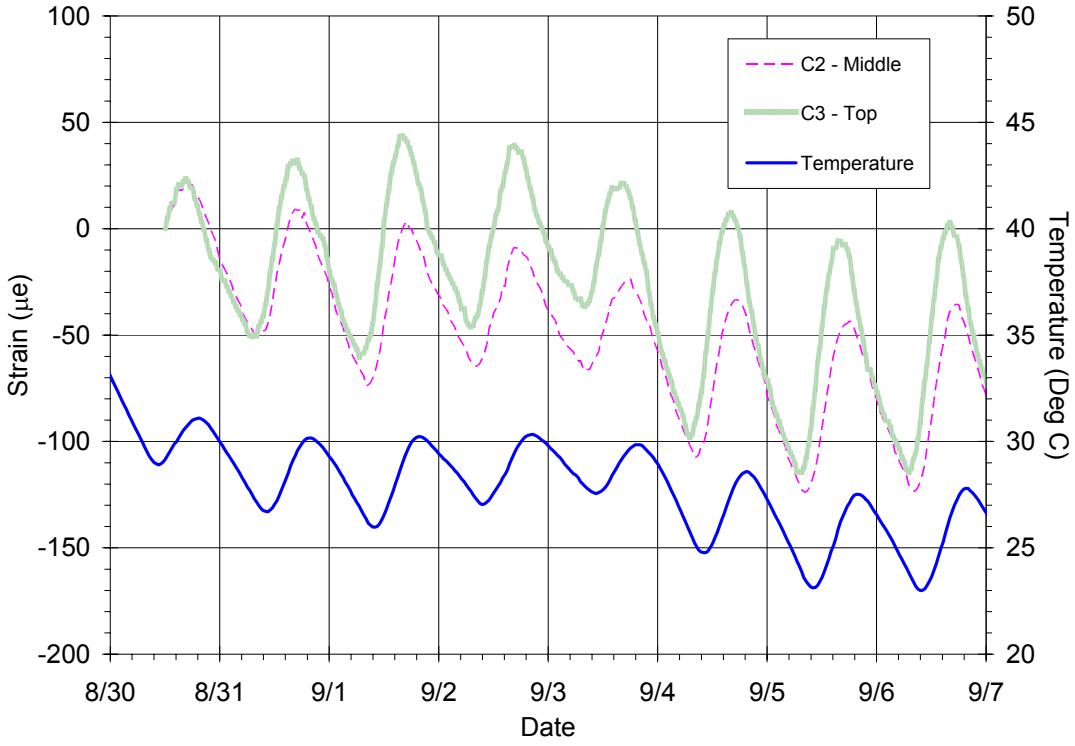

Figure 250. Strain measurements at location B, over pier, edge of deck, Big Creek

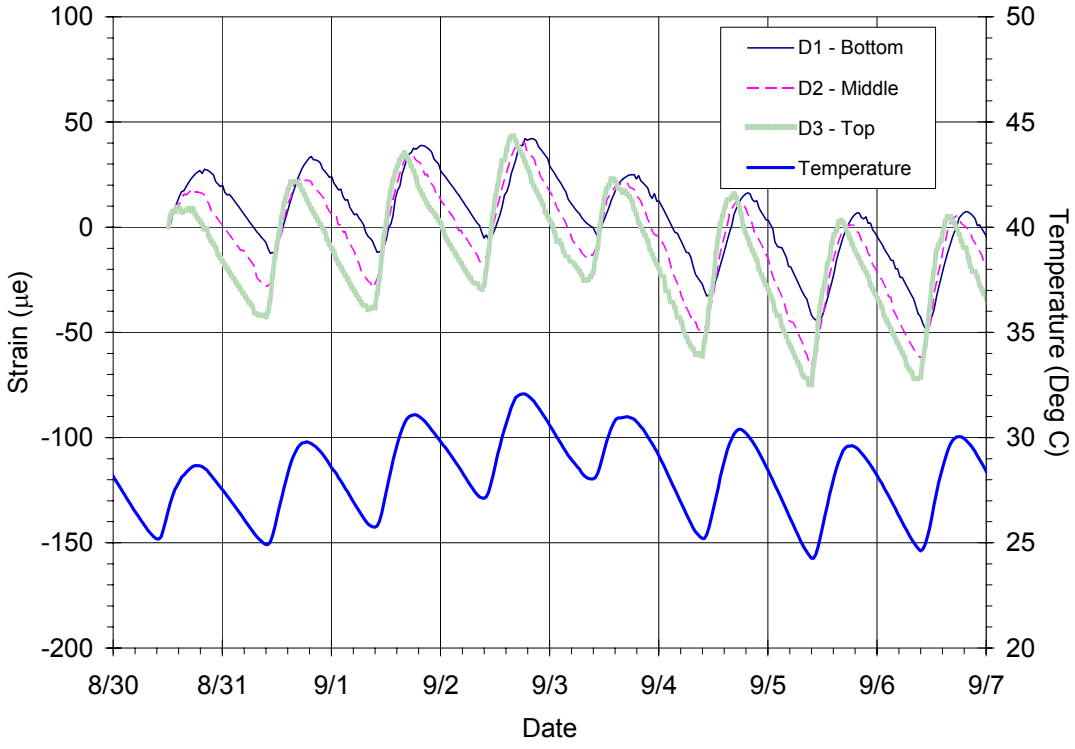

Figure 251. Strain measurements at location D, free shrinkage beam 1, Big Creek

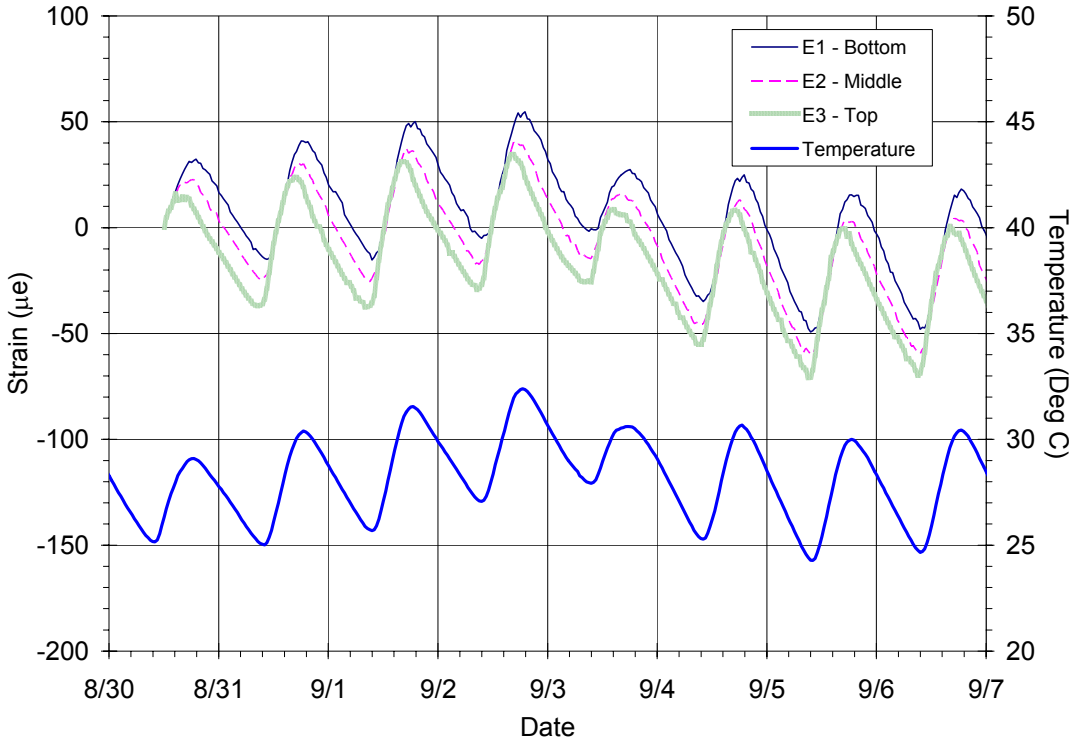

Figure 252. Strain measurements for location E, free shrinkage beam 2, Big Creek

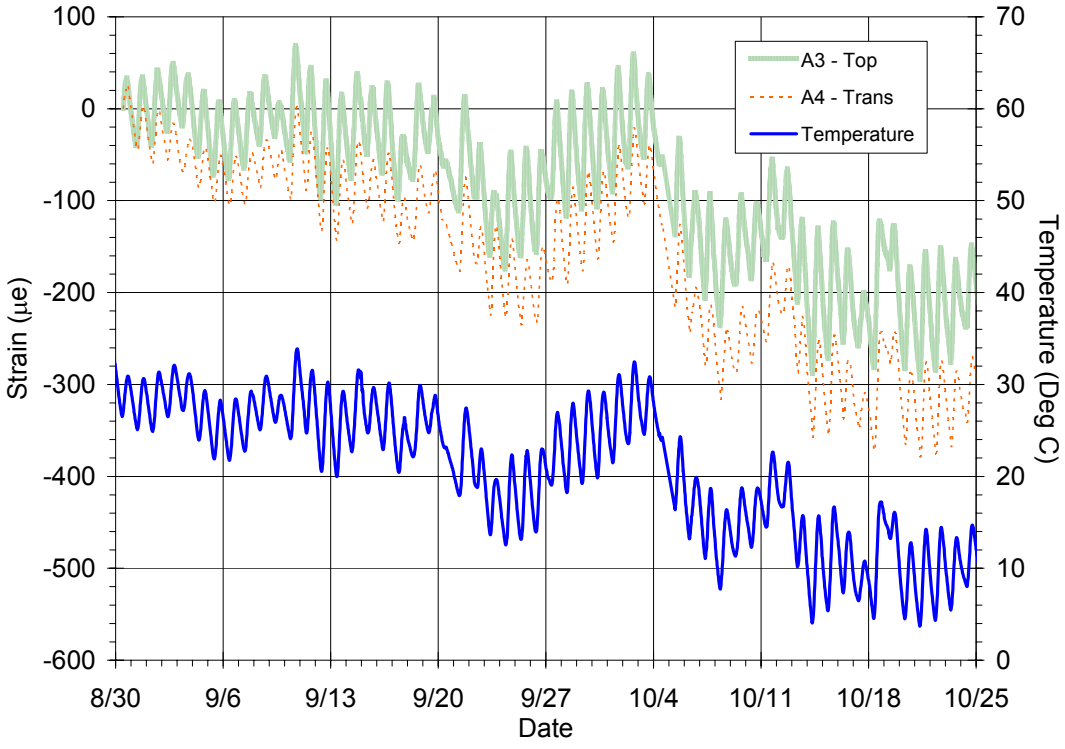

Figure 253. Strain measurements at location A, midspan, center of deck, Big Creek

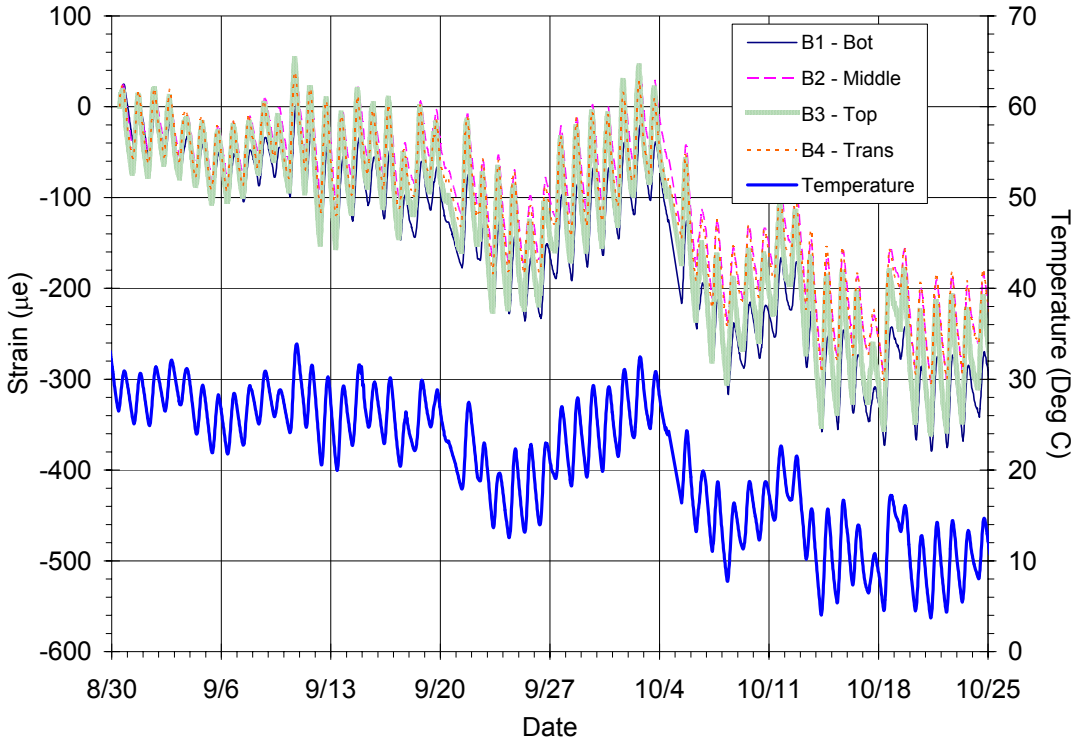

Figure 254. Strain measurements at location B, over pier, center of deck, Big Creek

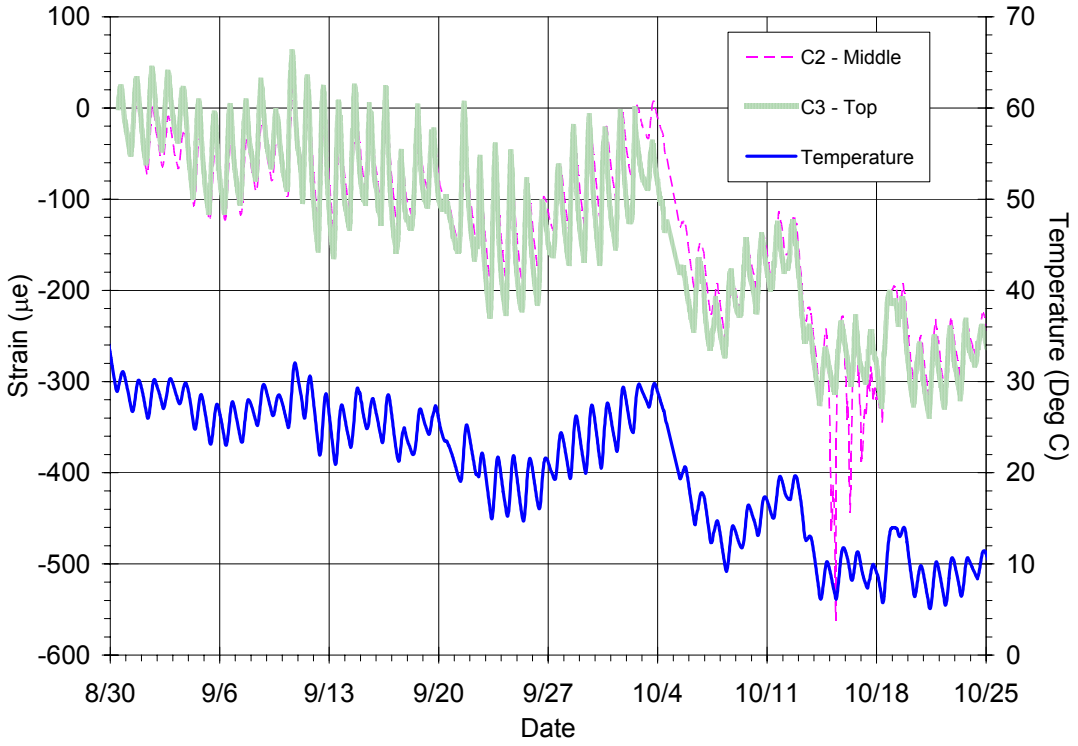

Figure 255. Strain measurements at location C, over pier, edge of deck, Big Creek

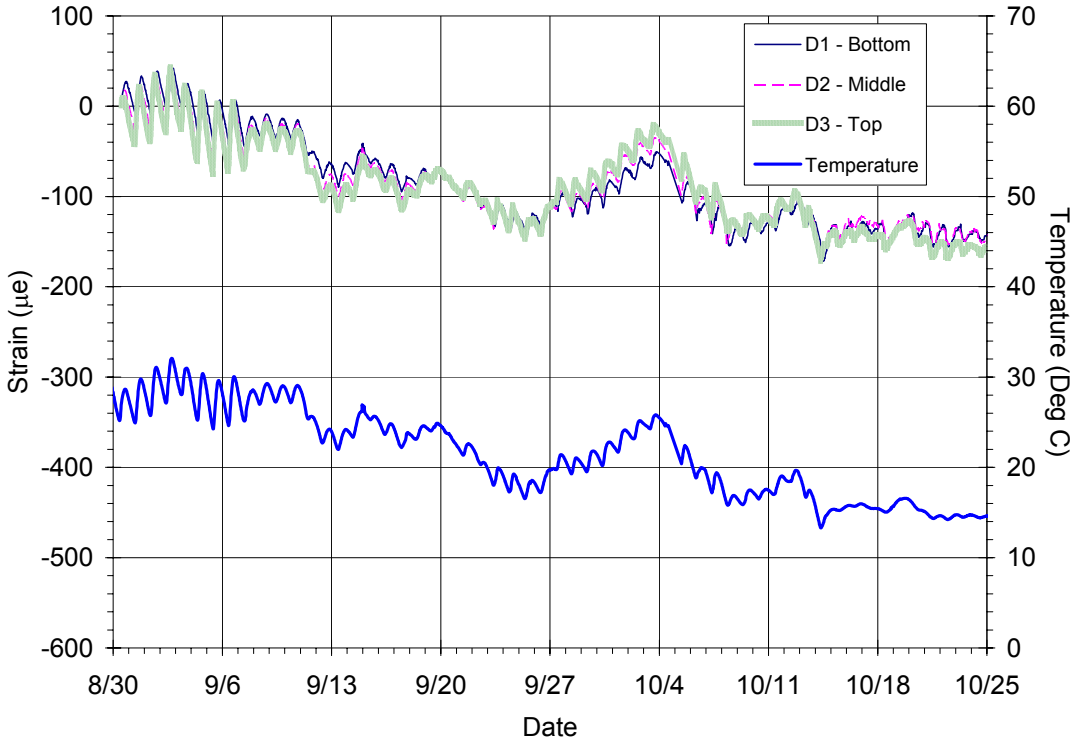

Figure 256. Strain measurements at location D, free shrinkage beam 1, Big Creek

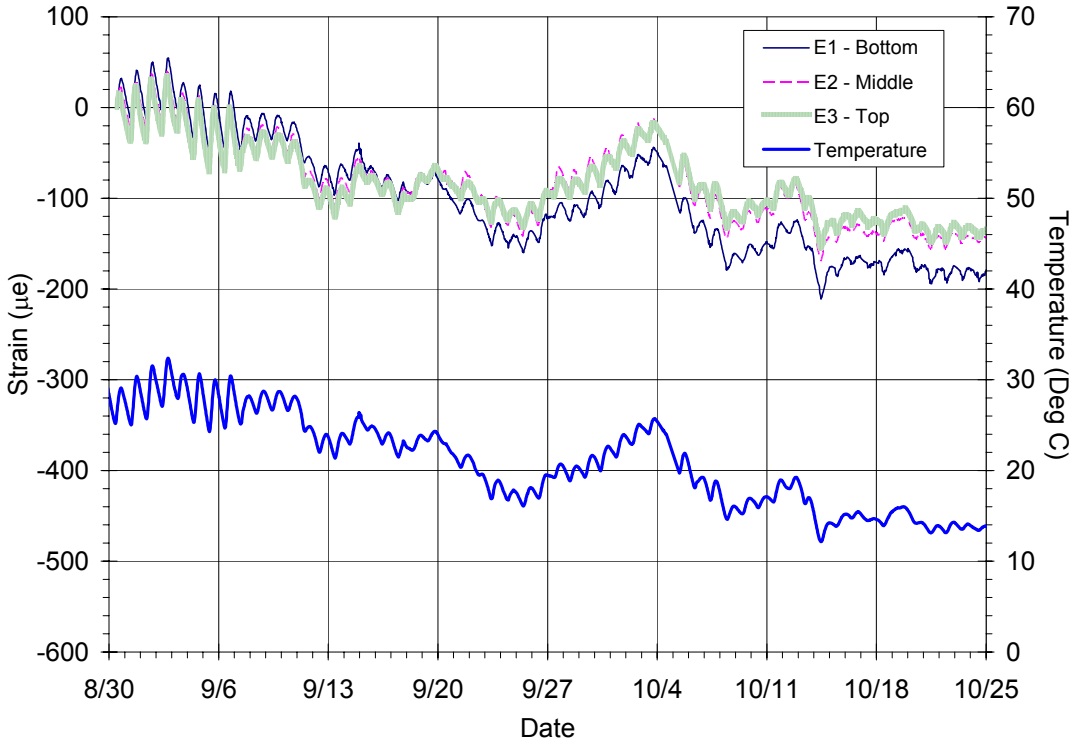

Figure 257. Strain measurements at location E, free shrinkage beam 2, Big Creek

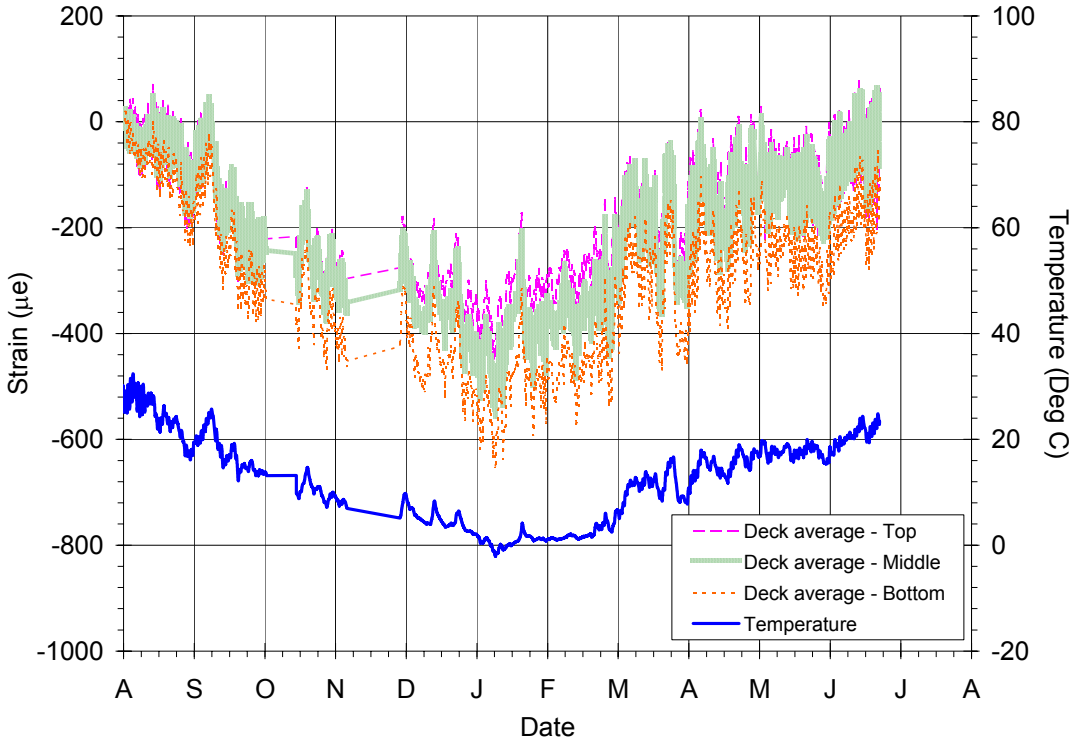

Figure 258. Average long term strain measurements of the bridge deck, Big Creek

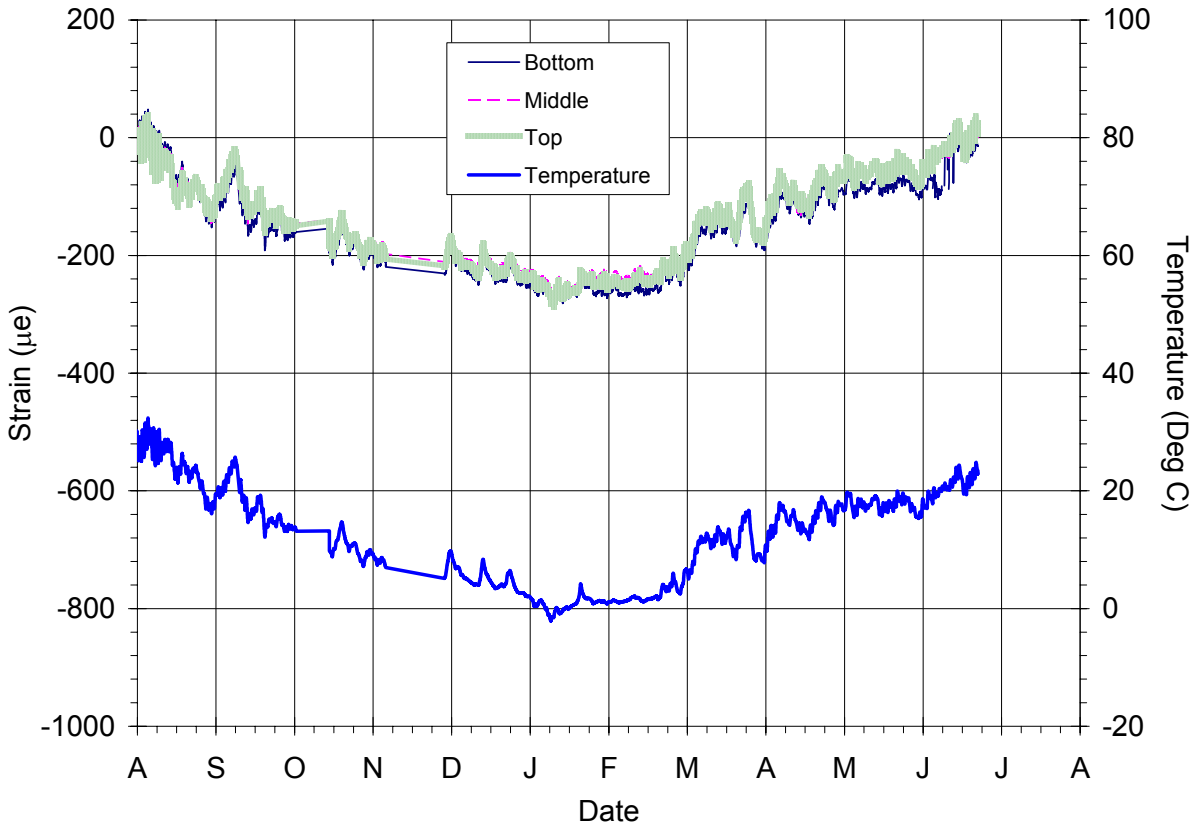

Figure 259. Average long term strain measurements of free shrinkage beams, Big Creek

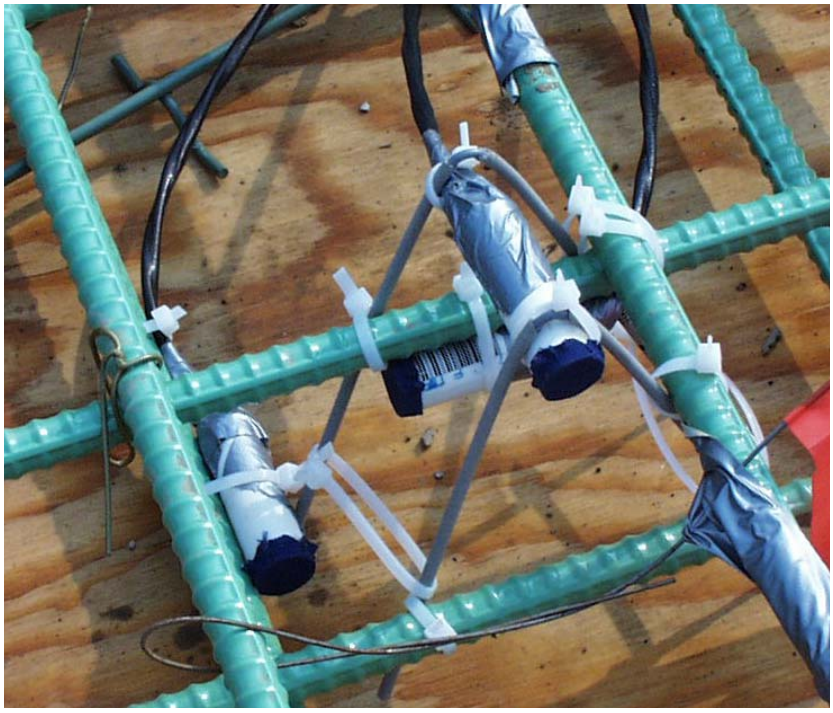

Figure 260. Internal RH sensors mounted for casting in concrete bridge deck, Big Creek

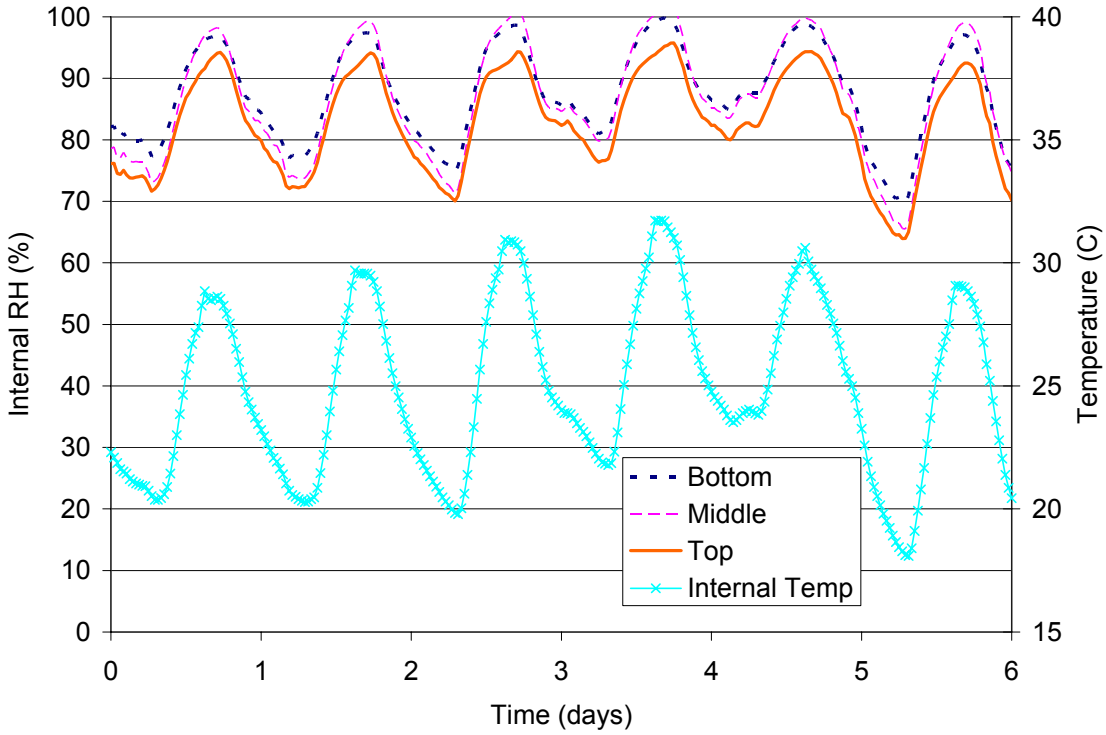

Figure 261. Internal RH and temperature cycles in concrete bridge deck, Big Creek

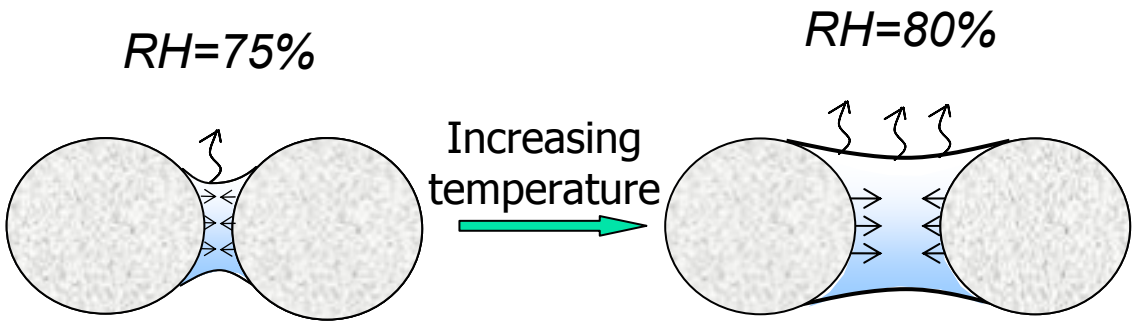

Figure 262. Effect of increasing temperature on capillary shrinkage pressure

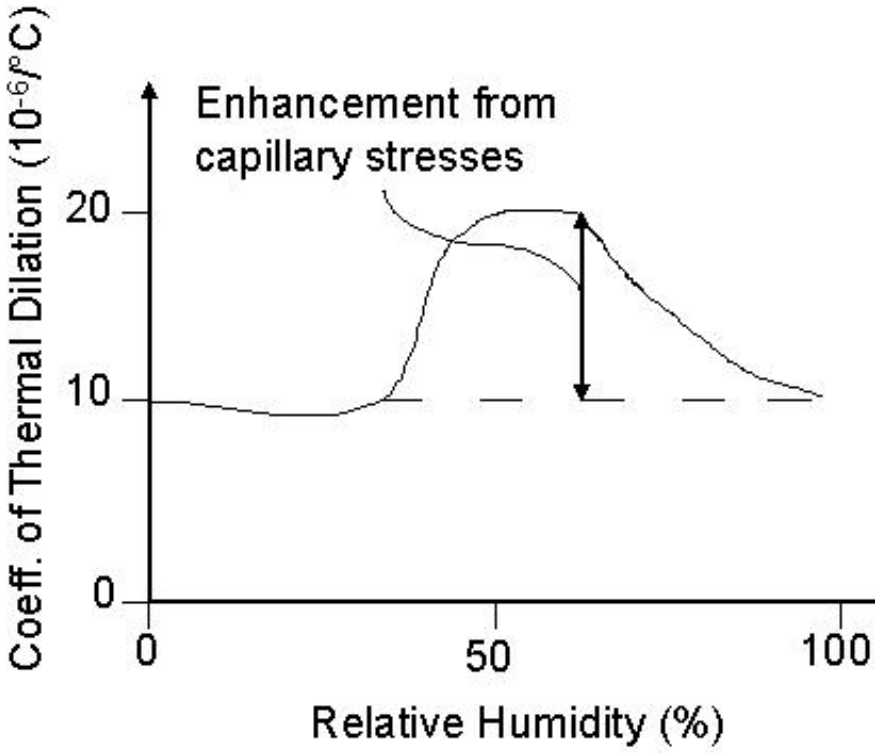

Figure 263. Dependence of CTD on state of internal moisture [1]

Appendix F – US-51 / Kaskaskia River District 7 (Vandalia, IL)

- Survival rate of strain sensors was low (5/16 or 30%) for this deck. Many sensors failed prior to placement. The reason is not clear for the electrical problems with sensors.
- Relative humidity sensors were installed in the bridge deck and in free shrinkage beams, but the sensors did not respond to voltage input and were immeasurable. Water possibly infiltrated the sensors and caused their voltage output to exceed the range of measurement for the data collection system
- Measurement period for Oct 17th placement date until January 20th, but data collection was interrupted by power loss and measurement problems
- Power system stopped charging on Oct. 23. This was six days after placement. Solar panel possibly damaged during form removal. Data was obtained after system failure and battery was changed, but the charging problem could not be resolved. Ultimate system failure occurred in January.
- Maximum temperature differential of 4.6° C occurred on January 4 at noon. The largest differentials fall and winter were usually 3-4° C and occurred during late morning/early-afternoon heating of the deck. No warm weather data was obtained for this deck.

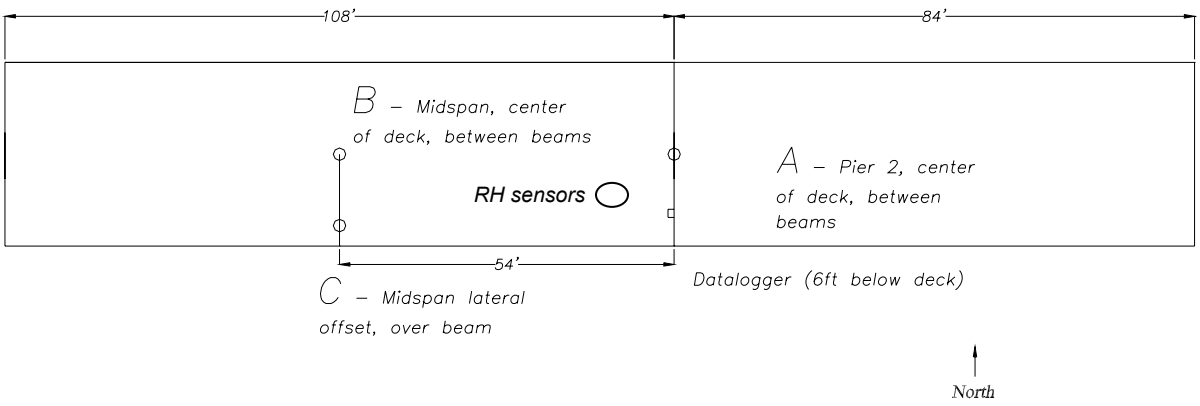

Figure 264. Kaskaskia bridge deck sensor locations

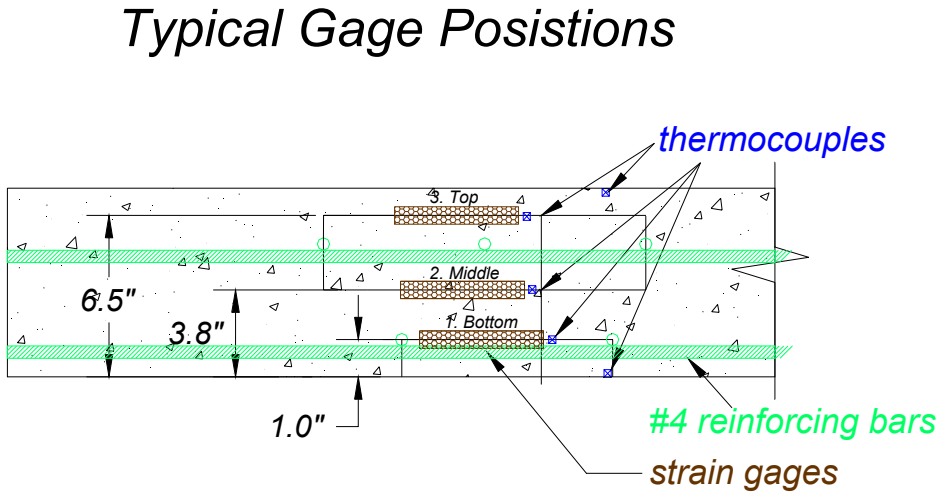

Figure 265. Kaskaskia sensor positions in deck, RH sensors had the same spacing

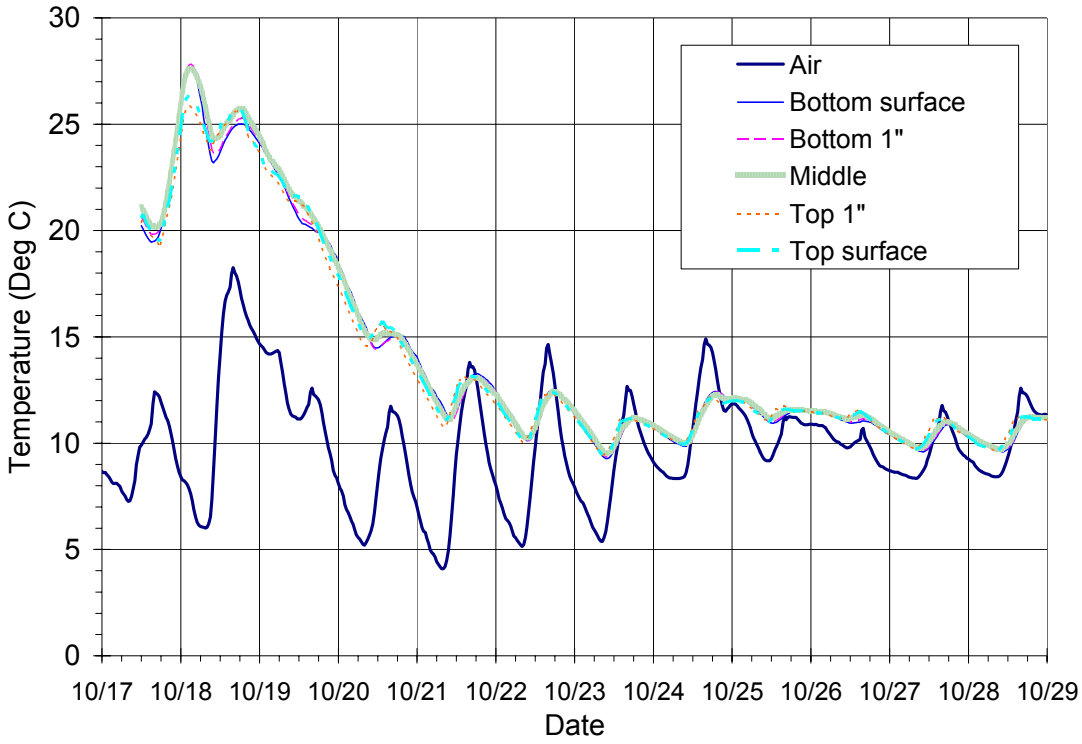

Figure 266. Temperature measurements at A, over pier, center deck, Kaskaskia

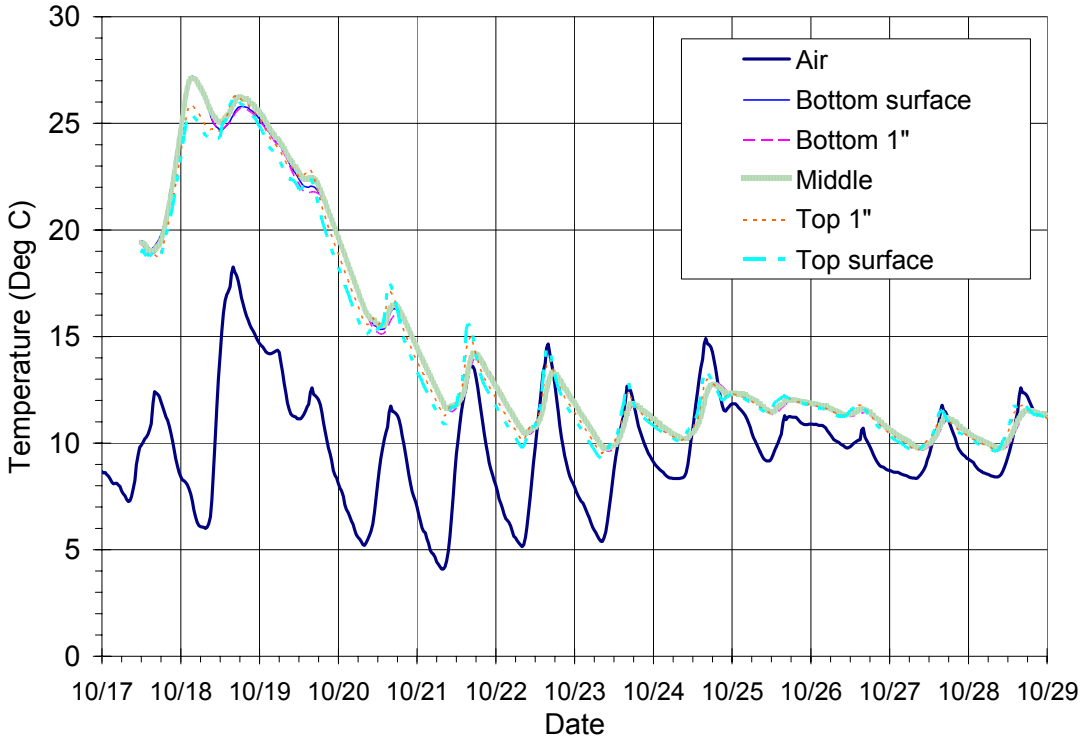

Figure 267. Temperature measurements at B, midspan, center deck, Kaskaskia

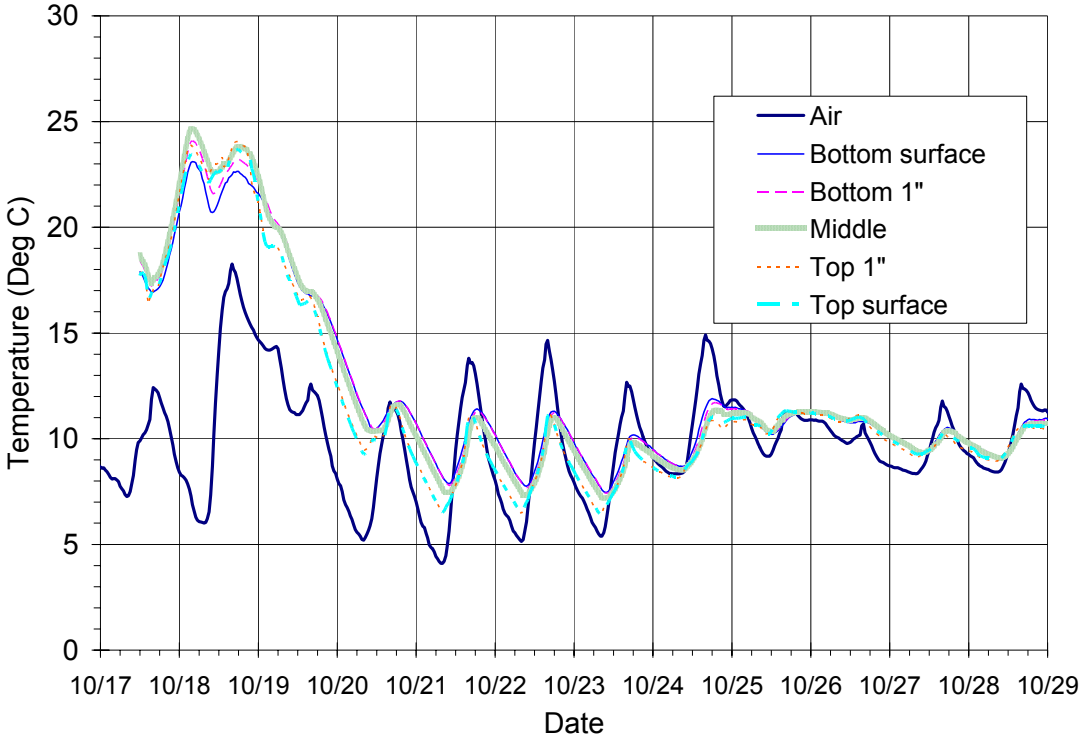

Figure 268. Temperature measurements at C, midspan edge of deck, Kaskaskia

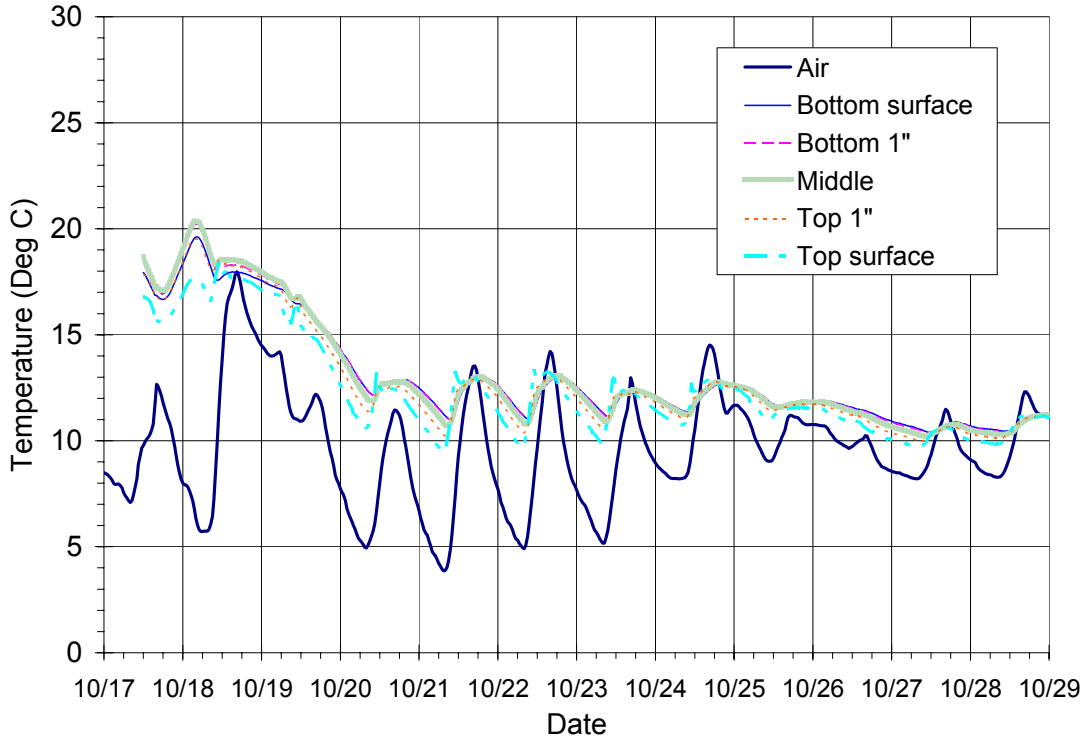

Figure 269. Temperature measurements in free shrinkage beams, Kaskaskia

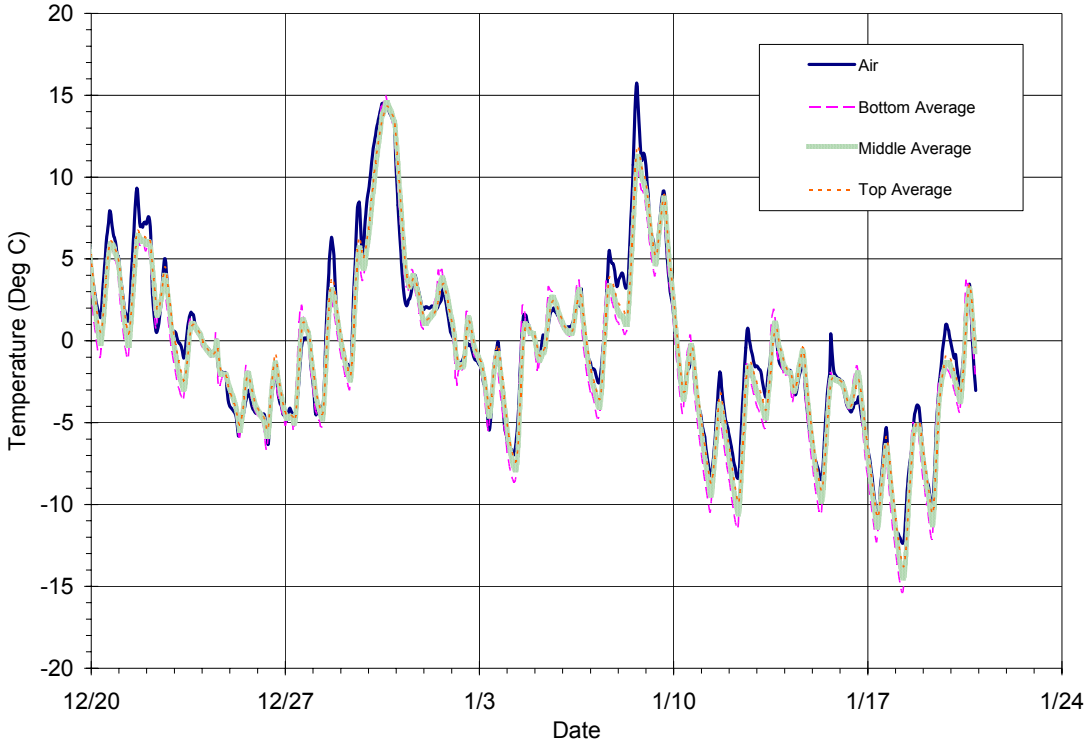

Figure 270. Temperature measurements during Dec-Jan, averaged data, Kaskaskia

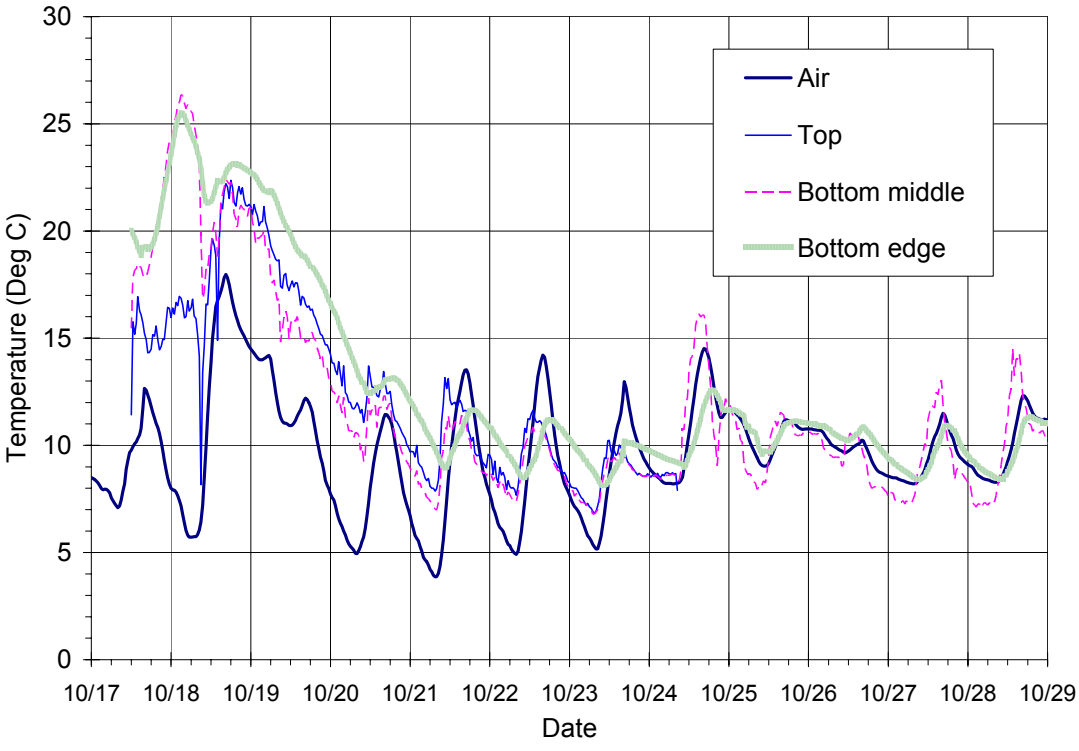

Figure 271. Temperature measurements of parapet wall, Kaskaskia

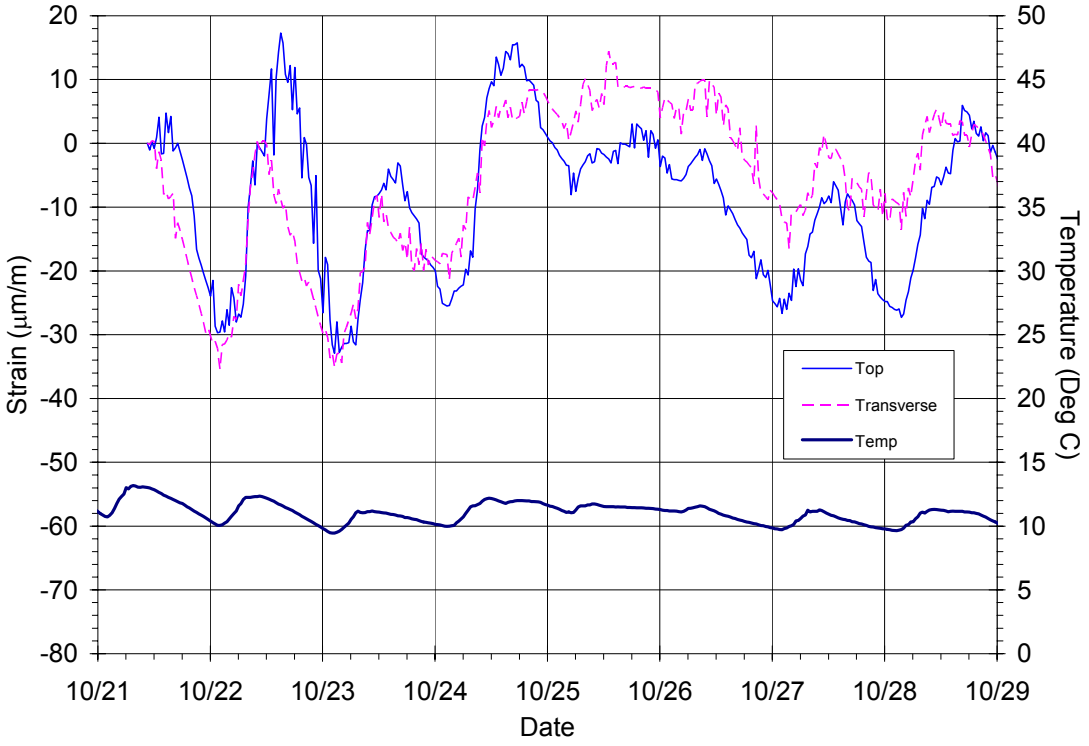

Figure 272. Strain measurements after 1 week in bridge deck, Kaskaskia

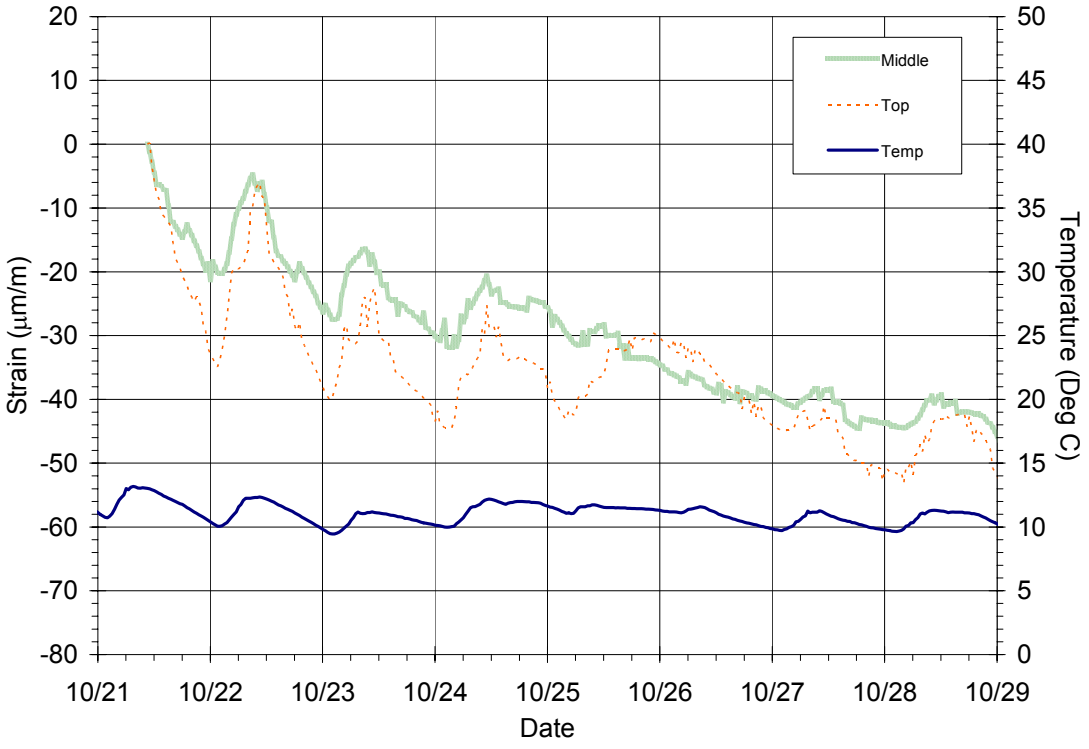

Figure 273. Strain measurements after 1 week in free shrinkage beams, Kaskaskia